Abstract

An array of diagnostic techniques was used to study anode phenomena in quasi-steady self-field MPD thrusters operated at power levels between 150 kW and 7 MW with argon and helium propellants. Spatially resolved anode heat flux measurements were made by embedding thermocouples to the inner surface of a hollowed section of the anode. These measurements indicate that at a thruster power level of 1 MW over 40% of the input power was deposited into the anode while at 7 MW this fraction decreased to less than 20%. The peak measured anode heat flux was approximately 10 kW/cm^2. Electron temperature and anode current densities were measured via Langmuir and magnetic probes, respectively, which with heat flux measurements permitted an estimate of the anode fall to be made. In addition, floating probes, which were used to measure the anode fall, served as a second means of estimating the anode heat flux. Comparison of anode fall data acquired through either method showed excellent agreement. Anode falls varied between 4 and 50 V for both argon and helium propellants. Furthermore, the anode fall was found to correlate well with electron Hall parameters calculated from triple Langmuir and magnetic probe data collected near the anode. Two possible explanations for this result are proposed: the establishment of large electric fields at the anode to maintain current conduction across the strong magnetic fields; anomalous resistivity resulting from the onset of microturbulence in the plasma. To investigate the latter hypothesis, electric field, magnetic field, and current density profiles measured in the vicinity of the anode were incorporated into Ohm's law to estimate electrical conductivity. Results of this analysis show a substantial deviation of the measured conductivity from that calculated with classical formulae. These results imply that anomalous effects are present in the plasma near the anode. In an attempt at reducing the anode fall by decreasing the local electron Hall parameter, a proof-of-concept test was conducted in which thirty six permanent magnets were imbedded within an anode to counteract the ambient magnetic field. The results of this experiment were promising, with a reduction of the anode fall of up to 15 V (37%) with argon and 20 V (50%) with helium.

Chapter I

Introduction and Motivation for the Work

I.1 Background Information

Propulsion systems having high exhaust velocity (U_e >10 km/s) are desirable for interplanetary space missions. A review of the rocket equation shows that in order for a propulsive system not to require an inordinate amount of propellant, its exhaust velocity should be of the same order as the characteristic velocity increment (Delta-V) required for a given space mission. Studies have shown that even for modest interplanetary missions, a characteristic velocity increment of a few tens of kilometers per second is necessary[1, 2, 3, 4]. Chemical rockets, which rely on the intrinsic energy available from chemical reactions of their constituent propellants, are inherently limited to exhaust velocities of perhaps 5 km/s, a value far short of those desired for planetary missions.

In an effort to remove the limitation placed on performance by chemical reactions, a scheme has been developed whereby propellant is heated via passage through an active nuclear reactor. By heating propellant independently of internal chemical reactions, the limitation of energy available for conversion into gas enthalpy from the chemical energy of the propellant has been removed and the performance of the engine is now dictated by the thermal and structural limitations of engine components (e.g. nozzle throat, reactor core elements). As such, solid core nuclear thermal rockets are capable of providing exhaust velocities in excess of 8 km/s with hydrogen propellant. Low

pressure solid core nuclear rockets as well as exotic systems with reactor elements in the form of particles, liquids, and gases offer theoretical exhaust velocities as high as 60 km/s [2, 5]. The feasibility of these systems, however, have yet to be demonstrated.

To achieve exhaust velocities in excess of 10 km/s, a propulsion system must accelerate its propellant gas without relying on energy addition through chemical reactions or heat transfer from a solid heating element. One approach is the application of electrical energy to a gas stream in the form of electrical heating and/or electric and magnetic body forces. This type of propulsion system is commonly known as electric propulsion.

Electric propulsion can be categorized into three groups[6]:

1. *Electrothermal Propulsion*: electrical energy is used to heat propellant which is subsequently expanded through a nozzle. This electrical energy can be delivered through an arc which traverses the propellant stream.

2. *Electrostatic Propulsion*: ionized propellant is accelerated through the application of electrostatic body forces.

3. *Electromagnetic Propulsion*: ionized propellant is accelerated by the interaction of an electric current, driven through the propellant, with magnetic fields that are induced by the current and/or supplied from external sources.

Electrothermal systems that rely on resistive heating elements suffer from the same thermal and structural limitations described above for solid core nuclear thermal rockets and are thus limited to exhaust velocities below 10 km/s [6]. Electrothermal devices which use arcs to heat propellant, although alleviating part of the material limitation problem by removing resistive heating elements, are still constrained by heat transfer to the nozzle walls and frozen flow losses. As such, electrothermal arc engines (arcjets) are limited to exhaust velocities of 15 km/s with hydrogen and thrust efficiencies of approximately 0.5 [7, 8, 9].

Thrust efficiency (η_{th}) is defined as the fraction of the total input power that is converted into directed thrust power;

$$\eta_{th} = \frac{\dot{\mathrm{m}} U_e^2}{2P_t} \tag{I.1}$$

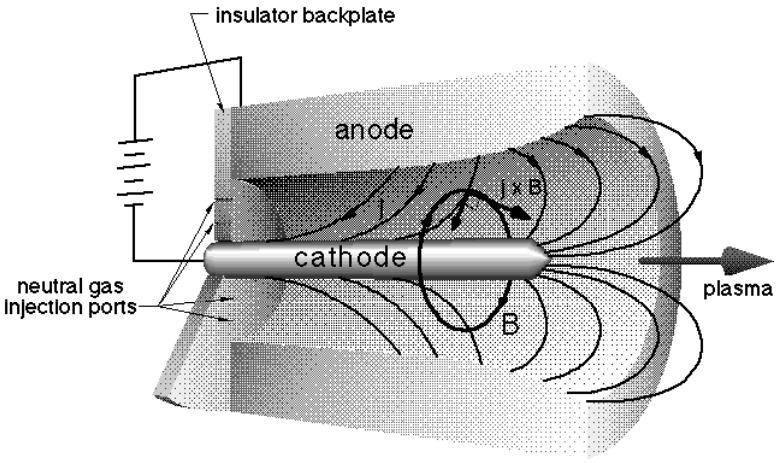

Figure I.1: MPD Thruster.

where $\dot{m}$ is the propellant mass flow rate, U_e is the propellant exhaust velocity and P_t is the total input power.

Electrostatic engines (e.g. ion engines), which can achieve large exhaust velocities (U_e > 50 km/s) at high thrust efficiencies (> 0.7), have demonstrated efficient performance only at power levels below 30 kW, with thrust densities on the order of 10 N/m^2 [6, 10, 11]. Studies have shown that an electrically propelled unmanned cargo vessel for lunar or mars basing requires a propulsion system capable of producing at least one megawatt of thrust power at thrusts in excess of 50 N[3, 12, 13]. Even though attempts to develop 100 kW ion engines that use mercury as propellant have met with limited success[14], still higher individual thruster power is necessary in order to maintain a manageable level of propulsion system complexity.

By virtue of the fact that electromagnetic engines such as the MPD (*magnetoplasma-dynamic*) thruster, do not rely on body forces which entail macroscopic space charge to accelerate particles and, therefore, are not "space-charge" limited in propellant throughput, this class of engines offers large exhaust velocities (5–100 km/s) at thrust densities up to 10^5 N/m^2 [15]. The MPD thruster (cf. Figure I.1) uses two concentric electrodes, an annular anode and a central cathode, to drive current through a flowing propellant

stream. The current rapidly heats the propellant to a high degree of ionization. The propellant plasma is accelerated through the interaction of the current with a magnetic field (Lorentz Force) that is either induced by the current (self-field thrusters) or supplied through external means (applied-field thrusters). Thrust is further enhanced through the conversion of propellant enthalpy to directed kinetic energy.

In addition to self and applied-field thrusters, MPD thrusters can be further categorized into steady and quasi-steady modes of operation. To test a steady multi-megawatt MPD thruster in an environment of sufficiently low background pressure, $\sim$0.04 Pa, (to minimize the influence of the ambient gas in the vacuum tank on thruster operation) would require a pumping system equivalent to several hundred 81 cm diameter hydrocarbon oil diffusion pumps[15]. In quasi-steady mode, the thruster operates in pulses of sufficient duration ($\sim$1 msec) such that over most of the pulse steady propellant acceleration is achieved at constant thruster current and terminal voltage. Thus, transient processes (e.g. current sheet formation) take place over a relatively small portion of the pulse. The benefits of operating in this mode are threefold: it greatly reduces the pumping requirements of a vacuum test facility, it decreases the thermal loads subjected to thruster components, and it allows for the application of intrusive plasma diagnostics (e.g. Langmuir probes) within the thruster.

MPD thrusters have been operated over a spectrum of power levels between one kilowatt (steady mode) and several hundred megawatts (quasi-steady mode). Although these devices offer high exhaust velocities for a variety of propellants, they suffer from low thrust efficiencies. The highest thrust efficiency obtained with non-liquid metal propellants is 0.45 with hydrogen[16][1]. For piloted planetary missions, studies have shown that utilization of MPD thrusters with thrust efficiencies in excess of 0.5 can reduce the initial spacecraft mass to levels significantly below those of chemically propelled vehicles.[12].

[1]This reference, the most extensive review of the state-of-the-art in MPD thruster technology (outside of the Soviet Union), excluded performance data with ambiguous experimental conditions (e.g. high background tank pressure).

I.2 Motivation for the Study

Two major loss mechanisms limit MPD thruster performance: frozen flow losses, which are dominant at high thruster power (above 1 MW), and anode losses. At thruster power levels below one megawatt, a majority of the engine input power is deposited into the anode[17, 18, 19]. Although the fraction of thruster power that is deposited into the anode substantially decreases at multi-megawatt power levels (e.g. ∼10%)[17], the heat flux to the anode is sufficient to pose a formidable thermal management problem for spacecraft designers. In addition, such intense heating may severely limit anode lifetime, which for many proposed space missions must exceed several thousand hours[12].

Since the invention of the MPD thruster (circa 1964[6]), a great deal of literature has been devoted to the study of anode phenomena in these devices. From its inception, it was known that an understanding of the physical processes involved in anode power deposition is essential for the eventual design of efficient MPD thrusters. However, because of the complexity of the processes involved, theoretical modeling of anode phenomena has been quite limited. As such, researchers have been forced to use careful experimentation for insight.

Much of the early work (1964-1971) focussed on characterizing the modes of anode energy transfer in steady-state devices at power levels of 50 kW or less[20, 21, 22, 23]. Since these devices were water cooled, anode power fractions could be easily determined through water calorimetry. These studies found that between 30 to over 80% of the total thruster power is consumed by the anode, and that this fraction decreases with increasing thruster power. The anode power fraction may be written as[24]

$$\eta_a \equiv \frac{\mathrm{P_a}}{\mathrm{V}J} = \frac{1}{\mathrm{V}J} \oint_{\mathcal{S}} \dot{\mathrm{q}}_\mathrm{a} \cdot d\mathcal{S} \tag{I.2}$$

where $\mathrm{P_a}$ is the total power absorbed at the anode, V is the total thruster voltage, J is the discharge current, and $\dot{\mathrm{q}}_\mathrm{a}$ is the local anode heat flux. The integration in Equation I.2 is performed over the entire current conducting surface of the anode. The integrand of Equation I.2, defined as

$$\dot{\mathrm{q}}_\mathrm{a} = \mathrm{j_a}\,(\mathrm{V_a} + \frac{5}{2}\frac{\mathrm{kT_e}}{e} + \phi) + \dot{\mathrm{q}}_\mathrm{c} + \dot{\mathrm{q}}_\mathrm{r} \tag{I.3}$$

where $\mathrm{j_a}$ is the local anode current density, represents the contribution to anode heating

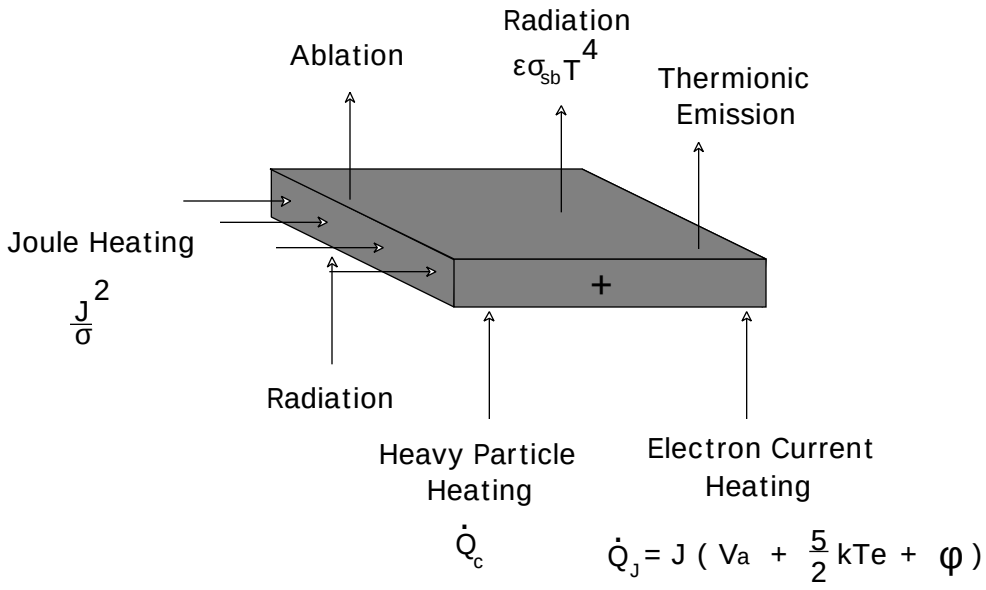

Figure I.2: Anode Power Balance.

from the kinetic energy that current carrying electrons gain from the potential difference between the anode and the local plasma, known as the anode fall (V_a), the random electron thermal energy ($\frac{kT_e}{e}$), the heat liberated due to the work function of the anode material (ϕ), and contributions from plasma convection ($\dot{q}_c$) and radiation ($\dot{q}_r$). As is appropriate for most thruster operating conditions, contributions from Joule heating and ablation cooling are neglected in this model. Equation I.3 also represents the local anode heat flux to a small region of the anode where plasma properties (i.e. V_a and $\frac{kT_e}{e}$) do not change appreciably. At equilibrium, barring regenerative or liquid cooling, the power deposited to the anode is balanced by cooling mechanisms, such as heat conduction to a thermal reservoir, surface radiation, ablation, and thermionic current emission (cf. Figure I.2).

I.3 Review of Prior Art

Many anode studies conducted prior to 1971 were performed on steady-state water cooled MPD thrusters with discharge power levels of less than 50 kW. Studies with a 20 kW thruster (Reference [20]) showed that the anode heat flux and anode power fraction decreased with increased thruster chamber pressure and propellant mass flow rate. Anode power was also found to increase linearly with discharge current (cf. Equation I.3). Similar trends were observed with a 30 kW thruster, with an anode comprised of eight independent segments (axially stacked rings), which was tested to determine axial anode current and heat flux profiles[21]. This thruster, which operated at argon mass flow rates of 17 to 34 mg/s with currents between 150 to 500 A, was found to have current and heat flux profiles consistent with the heat flux model of Equation I.3. Convection and radiation was found to account for 15% to 45% of the total anode heat flux.

In Reference [22], the results of anode heat transfer studies in a 3 kW thruster with an anode composed of eight azimuthally sectioned (pie sections) segments is presented. In addition to calorimetric determinations of the anode heat flux (and anode fall), the researchers inserted a small Langmuir probe between two adjacent segments to measure the electron temperature and the plasma potential near the anode surface. Anode falls determined from direct measurements and through use of Equation I.3 with calorimetry data were in good agreement with each other, ranging from small negative values (electron repelling) to equally small positive values ($\pm$2V). Further justification of Equation I.3 is offered in Reference [23] in which 70% to 80% of the total anode power was deposited by the current carrying electrons for the low power device described in Reference [22]. Furthermore, below a specific mass flow rate, current attachment to the anode changed from a diffuse character to a spot mode.

Although useful in the characterization of anode heat transfer, most of the early anode work was conducted with thrusters of power levels two to three orders of magnitude lower than devices required for most space missions. By the early 1970's, anode studies were conducted on multi-megawatt quasi-steady devices with maximum anode heat fluxes in excess of ten kilowatts per square centimeter[17, 25]. In contrast to low

powered devices in which nearly 50% of the anode heat flux can be due to convection and radiation, convective and radiative heat transfer to the anode of high powered devices have been shown to account for less than 10% of the total heating rate[17, 25, 26, 27]. Furthermore, for typical operating conditions, the contribution to anode heating from the anode fall, which can exceed 20 V, is much greater than those due to electron random thermal energy ($\frac{kT_e}{e} \simeq$2 eV), or the work function ($\sim$4 eV) (cf. Equation I.3). Therefore, understanding the underlying physics of the anode fall is necessary for the reduction of anode losses.

Oberth [25] used Langmuir probes to measure the difference in potential between the anode and the plasma some 0.1 cm from the anode surface. This quantity (taken as the anode fall) was found, in limited operating conditions, to decrease with increasing current density. In addition, when the thruster was operated with high currents at low mass flow rates, a condition desired for high specific impulse, the anode fall and thruster terminal voltage increased rapidly with increasing current. This condition also resulted in large terminal voltage oscillations and enhanced insulator and electrode ablation. It was theorized that when the mass flow rate is too low for a given current ("underfed"), the flux of electrons from the adjacent plasma due to their thermal motion is inadequate to maintain the prescribed discharge current density. In this situation, argues Oberth, large electric fields (i.e. anode falls) form near the anode to enhance current conduction by both increasing the number of available current carriers through Joule heating induced ionization, and by increasing the effective anode surface area (or conversely decreasing the prescribed current density). This effect, know as "anode starvation" has been described by other researchers as well[28, 32].

Saber [17] employed thermocouples attached to the inner surface of a hollowed shell anode to measure incident plasma heat flux to a quasi-steady device. The shell anode had a wall thickness of 1 mm and an external shape and dimension that matched the standard solid anode used by Oberth[25]. In addition, he measured local plasma potentials, current densities, and electron temperatures with an array of probes. Over the range of currents (5.5 to 44 kA) and argon propellant flow rates (1 to 48 g/s) studied, the anode power fraction decreased from 50% at 200 kW to 10% at 20 MW. Saber concluded that electric fields in the quasi-neutral portion of the plasma, over a

length on the order of the electron-ion "energy-exchange" mean free path, significantly contribute to the kinetic energy (i.e. the anode fall) which current carrying electrons deliver to the anode. For certain thruster operating conditions (e.g. low thruster power), this region extends approximately 1 cm from the anode surface; well beyond the sheath thickness. At multi-megawatt power levels, however, he found that the measured heat fluxes were in good agreement with those estimated from floating probe data collected 2 mm from the anode (cf. Equation I.3).

Vainberg et al. performed experiments that clearly demonstrated the effect of anode starvation on thruster operation[28]. These authors used Langmuir probes to measure the anode fall as well as ion and electron number densities, and electron temperatures a few millimeters from the anode of a 20 kW MPD thruster. They found that for a given propellant mass flow rate, at sufficiently low currents the anode fall assumed small negative values. As the current was increased the anode fall changed sign and became increasingly large, reaching 10 V out of a total terminal voltage of 25 V. Simultaneously, the electron number density near the anode decreased while the electron temperature and anode surface temperature increased in a manner mimicking that of the anode fall. Further increase in discharge current resulted in significant anode ablation. The authors evoked anode starvation to explain their results. They argue that as the current is increased, the magnetic field and electron temperature near the anode also increased, leading to large currents parallel to the anode surface. These axial currents lead to radial components of the Lorentz body force known as the pumping force. This pumping force reduces the number density of charged particles by displacing both electrons and ions radially toward the thruster axis. If severe, this effect may result in anode surface material ablation and subsequent ionization to create new charge carriers to replace those displaced by the Lorentz pumping force.

Almost identical trends were observed in both high pressure stationary arcs and MPD thrusters studied by Dyuzhev et al.[29, 30]. These authors and others (Reference [31]) observed that the current conduction at the anode transitions from a diffuse mode with electron repelling falls, to a destructive spot mode with large positive anode falls when the local anode current density equals or exceeds that naturally supplied by the thermal motion of the electrons. This transition leads to significant evaporation and

ionization of anode surface material as noted in Reference [28].

Similar results were obtained by Hügel in studies with water cooled, 250 kW MPD thrusters in which the anode fall was found to increase from small negative values (-2 V) to large positive values (30 V) with increasing current at constant propellant flow rate[32]. He also found that the anode fall data correlated well with the ratio $J^2/\dot{m}$, a scaling parameter for exhaust velocity. In addition, calculations by a fluid dynamic (2-D) computer model of the discharge plasma indicated that the surface pressure at the anode decreases monotonically with $J^2/\dot{m}$. This computer code also predicted zero anode surface pressure at values of $J^2/\dot{m}$ that corresponded to conditions of thruster operation (J and $\dot{m}$) in which the terminal voltage and anode fall were observed to abruptly increase with discharge current ($(J^2/\dot{m})_{crit}$).

Attempts to model anode processes have largely evolved from a desire to predict thruster conditions which result in the onset of unstable operation and excessive electrode and insulator ablation. Baksht et al.[33] developed an expression for the "limiting" current as a function of thruster geometry, propellant mass flow rate, propellant species mass, and electron temperature. The authors defined this current as the point at which a further increase in discharge current results in a rapid increase of the terminal voltage, anode heating, and thruster ablation. The results, which compare quite favorably with experiments, show that at this critical current the anode fall changes from negative to positive values.

Shubin[34], who similarly was in search of an expression for this transition current, performed an analysis evoking plasma microturbulence from wave-particle interactions. He derived an expression for the critical current that differs from that of Baksht only by a numerical constant of approximately two. Shubin's definition of the critical current was that at which electrostatic oscillations in the plasma near the anode are driven unstable. He argued that this condition exists when the drift velocity of the electrons reaches a certain threshold and cited possible instabilities which he felt could be excited near the anode. Excitation of these instabilities are expected to result in anomalously high resistivity in the local plasma; a mechanism which may explain the intense electric fields found near the anode.

The fact that two analyses using different mechanisms produce such similar results

follows from the observation that the plasma conditions necessary to cause classical anode starvation effects (Lorentz pumping) and anomalous resistivities from plasma turbulence are the same. As will be show in the thesis, this is due to large Hall parameters.

The Hall parameter (Ω), defined as the ratio of the electron gyrofrequency (ω_e) to the electron collision frequency (ν_e), is a measure of the tendency of current to flow perpendicular to both the electric and magnetic fields. For plasmas characterized by Hall parameters much less than one, the current flows generally parallel with the electric field. Thruster operation with large axial currents, which lead to the Lorentz pumping force, are characterized as having Hall parameters much greater than one. Thus, the the role of the Hall parameter as a major scaling parameter for anode power deposition should be anticipated.

This behavior was observed in an atmospheric pressure MHD accelerator (generator) where anode voltage drops of 20 to 50 volts correlated well with estimated electron Hall parameters[35]. This trend has been observed with multi-megawatt pulsed plasma injectors operating at significantly less pressure ($\sim$1300 Pa)[36] as well as in applied-field MPD thruster operating at 100 kW or less[37]. Experimental results of this thesis which show that the Hall parameter is a major scaling parameter for the anode fall are presented later.

Although several mechanisms have been evoked to explain large anode falls including anode starvation and anomalous resistivity[38, 39, 40, 41], no definitive theoretical or experimental work linking the Hall parameter to anode power deposition in plasma thrusters exists. Recently (1991) a two-dimensional two fluid non-equilibrium computer code which includes viscosity, heat conduction, and variable electrical conductivity, predicted large voltage drops at the anode of an axisymmetric multi-megawatt MPD thruster as a result of anode starvation[42]. Large Hall parameters near the anode were shown to cause highly skewed (axial) current profiles resulting in the depletion of charge carriers from Lorentz pumping. Numerical results exhibit trends that are in good agreement with experiment.

Choueiri et al. have recently shown that a strong correlation exists between anomalous resistivity, due to turbulence in the plasma, and the electron Hall parameter[43, 44].

They predict electrical conductivities that are thirty times lower than classical values for Hall parameters of twelve[44]. Their model also predicts other experimentally observed trends in thruster plasma properties that have not been exhibited by classical models (e.g. $T_i > T_e$).

Another mechanism which might be responsible for the large voltage drop near the anode is the presence of a sheath. When a solid body such as a wall or a probe electrode is in contact with a plasma, the potential drop between the ambient plasma and the surface is confined primarily within a narrow region (usually a few Debye lengths thick) called a sheath. In general, quasi-neutrality is not maintained throughout the sheath, allowing for large electric fields to be established. Sheaths may form near the anode to maintain current continuity by enhancing electron current collection (via large electric fields) or by creating new charge carriers through field enhanced electron impact ionization.

The question of whether anode power deposition is due to classical (e.g. sheath) and/or anomalous phenomena is still open to debate. Evidence that anomalous effects are present near the anode is given in Appendix A in which electrical resistivity near the anode (i.e. effective electron collision frequency) is found to be more than an order of magnitude larger than classically predicted values.

I.4 Thesis Outline

Although a variety of work on anode processes in MPD thrusters has been performed over the past twenty five years, these devices are still plagued by excessively large anode losses. A clearer understanding of anode power processes is needed if the MPD thruster is to serve as a primary propulsion system for interplanetary missions. This need has motivated this research effort.

The goals of this thesis are as follows:

- To investigate the influence of local plasma characteristics such as electron temperature and number density, anode current density, and magnetic field strength on anode power deposition.
- To obtain relevant scaling parameters for anode power dissipation.

- To develop methods of reducing anode heating.

The remaining portion of the thesis is composed of the following parts:

1. Chapter 2 describes the experimental facilities and associated diagnostic techniques.

2. Chapter 3 describes the characterization of anode power deposition of the benchmark thruster in terms of global thruster operating conditions.

3. Chapter 4 illustrates the role of the Hall parameter as an important factor of anode power deposition.

4. Chapter 5 details a first experimental attempt to reduce anode power deposition by the modification of the local magnetic fields through the use of permanent magnets embedded within the anode of a benchmark thruster.

5. Chapter 6 draws conclusions and suggests future direction of research.

Appendices at the end of the thesis present several detailed calculations in support of this work. Appendix A presents calculations that estimate the electrical conductivity near the anode. Appendix B summarizes anode power deposition experiments conducted on a 100 kW applied-field continuously operating MPD thruster. Appendix C presents an estimate of convective heat transfer to the anode and Appendix D outlines the 1-D anode sheath model developed in support of this work.

Chapter II

Experimental Facility for the Quasi-Steady MPD Thruster

II.1 Introduction

The facility used for this study has been in operation for more than 25 years. Throughout its existence, it has undergone several modifications which are documented in several reports[45, 46, 47]. The thruster design, facility description, and diagnostics used in the thesis are presented in this chapter.

II.2 Experimental Facilities

II.2.1 The Quasi-Steady MPD Thruster Design

The MPD thruster studied in this thesis has been in operation at Princeton University for more than fifteen years. Designated as the "benchmark" thruster, the device consists of an aluminum cylindrical thrust chamber 5 cm deep with an inner diameter of 15.0 cm and an outer diameter of 18.8 cm (cf. Figure II.1). The inner surface of the thrust chamber is insulated from the discharge by a Pyrex tube with a wall thickness of approximately 1 cm. Mylar tape is used to insulate the outer surface of the thruster column. The cathode, made of 2% thoriated tungsten, is 10 cm long and 1.8 cm in diameter.

Propellant is injected through a boron-nitride backplate via twelve 3 mm diameter

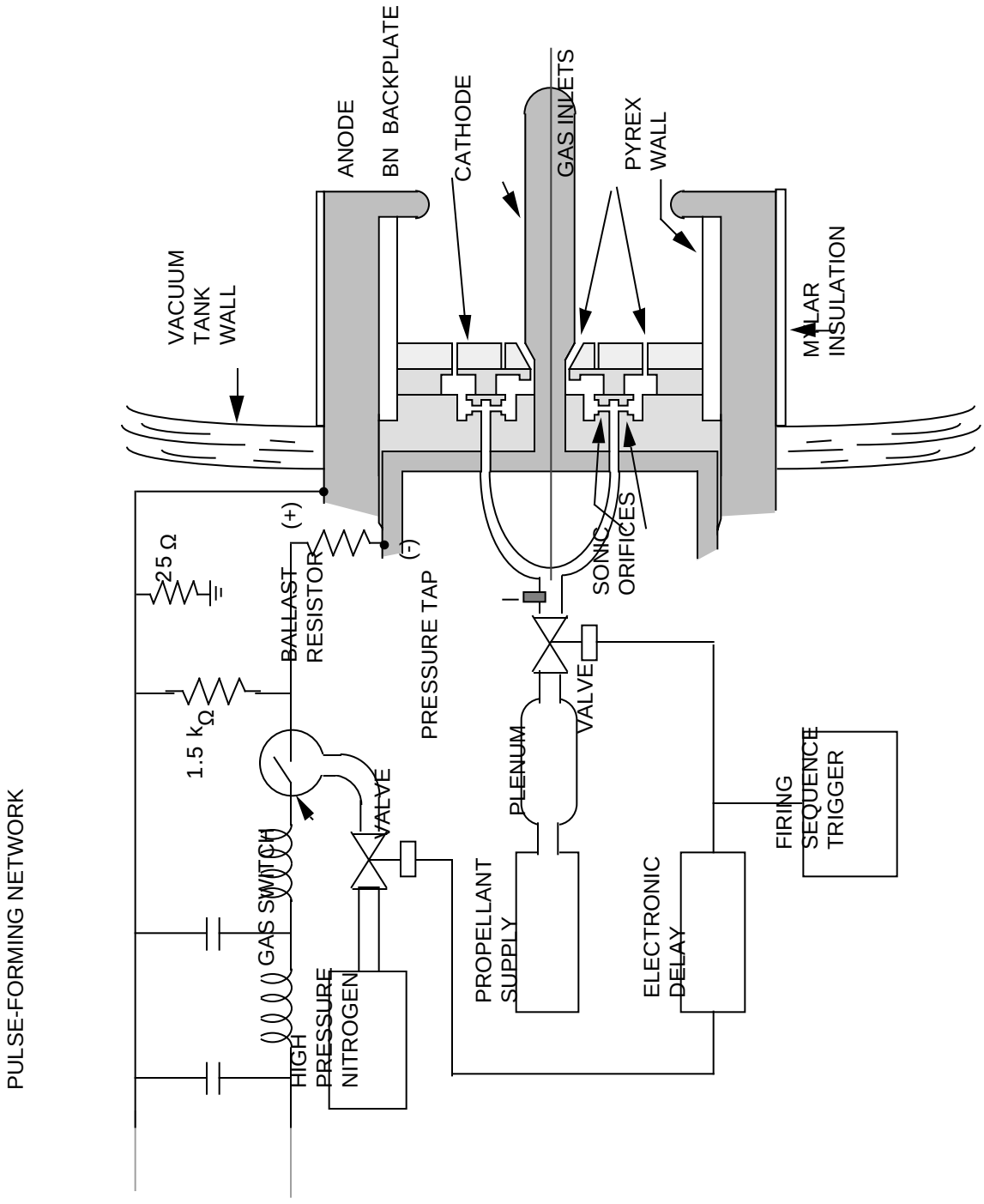

Figure II.1: Experimental Apparatus.

holes at a radius of 3.8 cm, and through an annulus at the base of the cathode. An equal amount of propellant flows through the holes and the annulus. Mass flow is distributed to the holes and annulus by two sets of six sonic orifices (one for the annulus the other for the holes) located in a Plexiglass distribution plate just aft of the backplate. Since the propellant flow through the orifices is choked, the mass flow rate is proportional to the pressure in the plenum upstream of the distribution plate. Details of the mass flow rate calibration are presented in Appendix A of Reference [46]. The standard deviation in propellant flow rates among the injection holes has been measured at 2% [46]. The uncertainty in the mass flow rate is estimated to be 8%.

The anode of the thruster, which is located at the exit plane of the thrust chamber, is constructed out of a 1 cm thick aluminum ring of outer diameter 19 cm and with an inner diameter of 10 cm. The inner radius of the ring has been machined to a semi-circular lip (cf. Figure II.1). Argon and helium are used as propellants for all quasi-steady thruster experiments.

II.2.2 Vacuum Facility

All experiments have been conducted in a Plexiglass vacuum tank 1.83 m long with an inner diameter of 0.92 m. The total interior volume of the tank is estimated at 1.12 m^3. Tank pressure is maintained to less than 0.01 Pa (1×10^{-4} Torr) between thruster firings by a 15 cm oil diffusion pump and two mechanical backing pumps. The tank contains an electronically controlled probe positioning table with three degrees of freedom as well as angular freedom in the horizontal plane.

II.2.3 Power Supply

Thruster power is supplied by a 160 kJ pulse-forming network (capacitor bank) capable of delivering a rectangular current pulse of up to 52 kA for a duration of approximately 1 msec. The network consists of 80 stations, each with four 26 μF capacitors connected in parallel. The bank can be configured to produce a 0.5, 1, or 2 msec pulse at a current of 16, 8, and 4 amperes for every charging volt, respectively. All data reported herein were collected with the 1 msec pulse length.

The firing sequence begins by charging the pulse-forming network to a predetermined

voltage via a Del high voltage power supply. Once the voltage is reached, the firing mechanism is triggered which first opens a solenoid valve allowing the propellant to flow through the thruster. Once a steady propellant flow rate has been achieved (typically in 20 msec), a second solenoid valve is triggered, allowing nitrogen to enter a gas switch situated in series between the pulse-forming network and the thruster (cf. Figure II.1). Breakdown of the nitrogen completes the circuit between the thruster and the pulse forming network. Once breakdown of the propellant has occurred, the capacitor bank drives the thruster to the desired operating condition. The thruster operates in a quasi-steady mode for approximately 800 of the 1000 μsec pulse. Charging voltage is varied between 500 and 3000 V which corresponds to currents between 4 and 24 kA, respectively.

Thruster current is measured with a 240 mΩ copper sheet shunt located between the bank and thruster anode. Terminal voltage and current shunt voltage are measured with Tektronix 1000:1 high voltage probes and Tektronix AM501 operational amplifiers. Terminal voltage and current measurements are accurate to with 5%.

II.3 Thruster Diagnostics

II.3.1 Anode Heat Flux Experiment

A section of the anode described above was hollowed to form a cavity with a wall thickness of 1 mm (cf. Figure II.2). The azimuthal extent of the shell is approximately 30 degrees. To measure anode heating rates, a technique first implemented in Reference [17] for an almost identical thruster is used in which a heat conduction model is employed to ascertain the incident heat flux to the exposed outer surface of the anode shell from the plasma, from the measured rise in temperature of the inner surface. To measure shell wall temperatures, several copper-constantan thermocouples (#36 gauge) are attached to the inner wall of the cavity. Thermocouple temperature measurements are made with a Keithley System 570 analog-to-digital unit containing an AIM 7 thermocouple board, which is controlled by an AT&T PC 6300 computer. To minimize noise, thermocouple lines are routed through the tank via electrically shielded cables. The cable shields, which are connected to the Keithley ground, are isolated from the

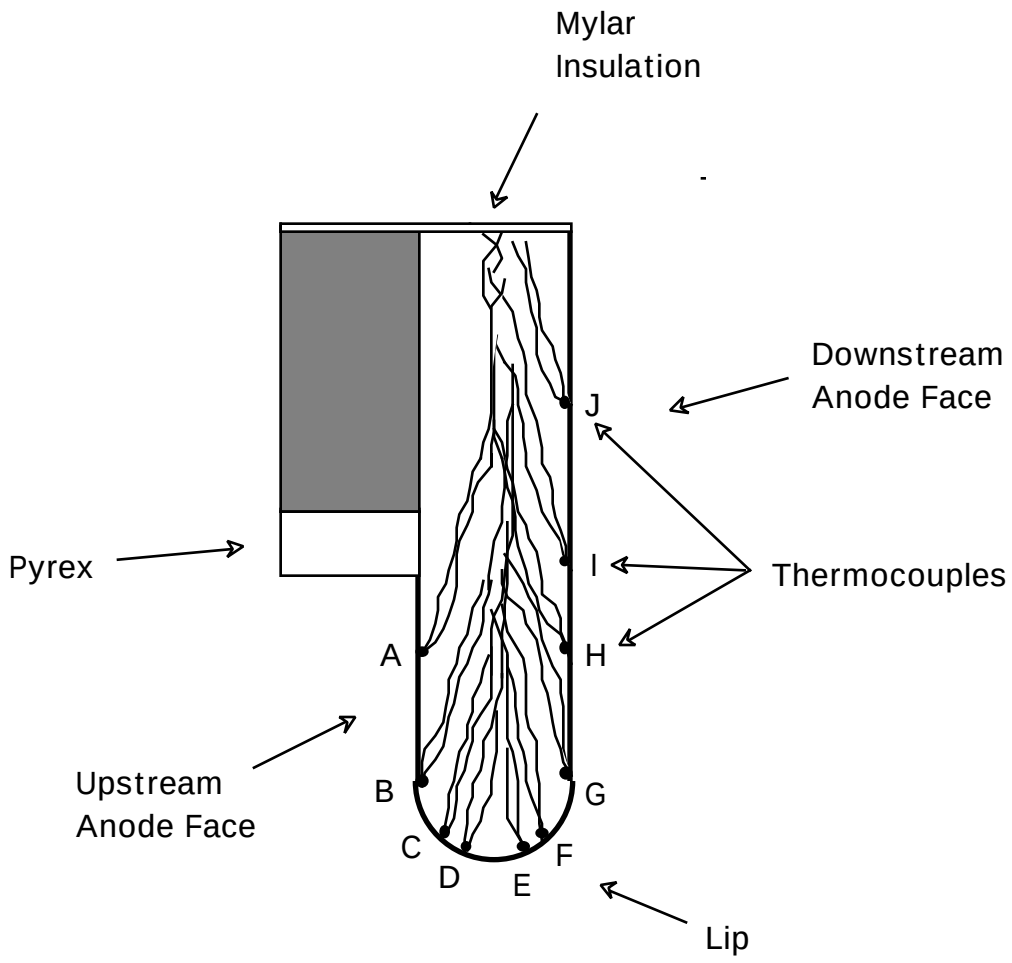

Figure II.2: Anode Shell.

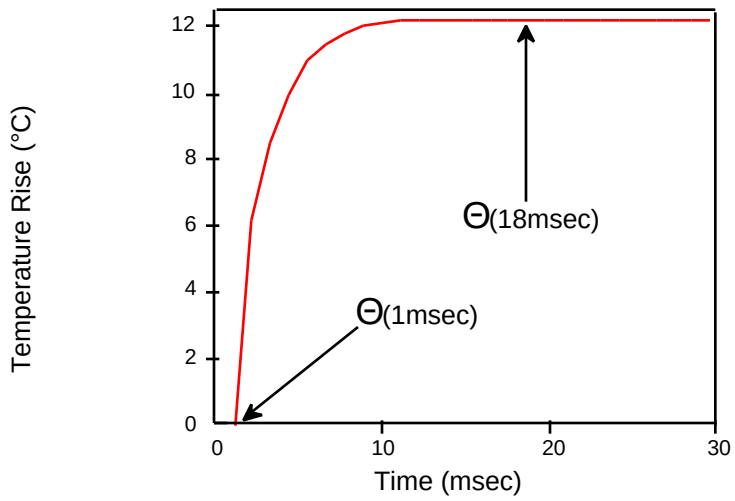

Figure II.3: Thermocouple Temperature Response.

discharge with shrink tube and mylar tape. All instrumentation is housed in a Faraday cage connected to the experiment (Keithley) ground. To protect the computer equipment from the large voltage spikes produced at the anode during breakdown, a special epoxy (Omegabond 200) is used to attach the thermocouples to the anode shell. This epoxy was selected on the basis of its high thermal conductivity (1.4 W/m-K) and high electrical resistivity ($10^{13}\Omega$). The Keithley system takes two measurements per thermocouple; one approximately a millisecond after the discharged ends (before the thermal input has had time to diffuse through the shell wall) and one approximately 18 milliseconds later. The length of time between measurements was experimentally determined to coincide with the plateauing of the inner shell temperature. By comparison, the temperature rise due to transverse conduction along the shell generally occurs thirty or more milliseconds after the initiation of the discharge.

Figure II.3 shows the typical response of the thermocouples to the incident anode heat flux where thermocouple temperature rise is shown as a function of time. Zero on the abscissa corresponds to the end of the discharge. As the figure shows, there is a

negligible temperature rise of the the inner anode shell at the time the first thermocouple measurement is taken (t=1 msec). However, by the time the second measurement is taken (t=18 msec) the inner shell temperature has plateaued to its maximum value.

Analysis of transient heat conduction through the shell involves the application of a fixed heat flux to one end of a uniform slab at t=0 and a second flux of opposite magnitude at t=τ. The net result is a rectangular heat flux pulse that begins at the initiation of the thruster discharge (t=0) and ends at the extinction of the thruster discharge (t= τ $\approx$1 msec)[17, 48]. Each applied heat flux can be modeled by a series solution representing the temperature at a certain depth within the slab at a specific time. Since the problem is linear both solutions can be added resulting in the temperature at any depth within the slab as a function of time for the heat flux pulse described above. By setting the depth equal to the wall thickness of the shell we obtain the following (t $> \tau$),

$$\Theta(\mathcal{L},t) = \frac{\dot{\mathbf{q}}\tau}{\rho c\mathcal{L}} + \frac{2\dot{\mathbf{q}}\mathcal{L}}{\pi^2\kappa}\sum_{n=1}^{n=\infty}\frac{(-1)^n}{n^2}[exp(-\frac{\mu n^2\pi^2(t-\tau)}{\mathcal{L}^2}) - exp(-\frac{\mu n^2\pi^2 t}{\mathcal{L}^2})] \qquad \text{(II.1)}$$

where $\Theta(\mathcal{L}$,t) is the temperature rise at the unheated end of the shell (thermocouple site), τ is the duration of heat input ($\sim$1 msec), κ is the thermal conductivity of the shell material (aluminum: 237 W/m-K), μ is the thermal diffusivity of the shell material (aluminum: 8.23×10^{-5} m^2/s), c is the heat capacity of the shell material (aluminum: 900 J/kg-K), ρ is the density of the shell material (aluminum: 2699 Kg/m^3), $\mathcal{L}$ is the shell thickness (1 mm), and $\dot{\mathbf{q}}$ is the heat flux (W/m^2). Equation II.1 can be written as

$$\Theta(t) = \dot{\mathbf{q}}\hat{\mathcal{F}}(t) \qquad \text{(II.2)}$$

where $\hat{\mathcal{F}}(t)$ represents the temperature rise per unit heat flux at the unheated side of the shell. By inverting Equation II.2 we obtain

$$\dot{\mathbf{q}} = \Theta(t)/\hat{\mathcal{F}}(t). \qquad \text{(II.3)}$$

Thus, the incident heat flux ($\dot{\mathbf{q}}$) is determined by dividing the temperature rise obtained at each thermocouple site ($\Theta(t)$) by $\hat{\mathcal{F}}(t)$ once the inner shell temperature has plateaued to its maximum value (at t>15 msec (cf. Figure II.3)). An AT&T personal computer is used to calculate $\hat{\mathcal{F}}(t)$ to terms of order 10^{-8} relative to that which preceded it.

However, once the temperature has plateaued, the contribution of the exponentials to $\hat{\mathcal{F}}(t)$ is nil.

The assumptions of the heat flux model are as follows:

- Heat flux is constant during the discharge and zero at all other times.
- Heat conduction along the shell is negligible.
- Ohmic heating in the aluminum is negligible.
- The anode is locally flat (to approximate a slab).
- Anode ablation is negligible.

The first assumption is generally satisfied by the nearly rectangular form of the quasi-steady thruster voltage and current profiles. For the conditions of this experiment, ohmic heating within the shell proves to be negligible[17][1]. The anode can be assumed to be locally flat if the radius of curvature of the anode's outer surface is much larger than the shell wall thickness. This is only compromised at the lip where the surface radius of curvature is 5 mm and the wall thickness is 1 mm. Given the accuracy of the experiment, this amount of curvature is not expected to significantly effect the results[17]. Lastly, ablation of anode material in a diffuse current attachment mode has been estimated to be negligible[17].

Errors in the calculation of heat transfer are introduced by heat conduction along the anode shell, inaccuracy of the thermocouples, and variation in shell wall thickness. Analysis has shown that under the most extreme conditions encountered in this experiment, heat conduction along the shell results in, at most, a 10% uncertainty in heat flux[17]. The thermocouples used for these experiments are accurate to 0.5 °C and introduce an uncertainty of ∼130 W/cm^2 in heat flux estimates. Nonuniformity of wall thickness do not significantly alter the results[17].

[1]The experimental conditions assumed in the analyses of Reference [17] are applicable to this thesis.

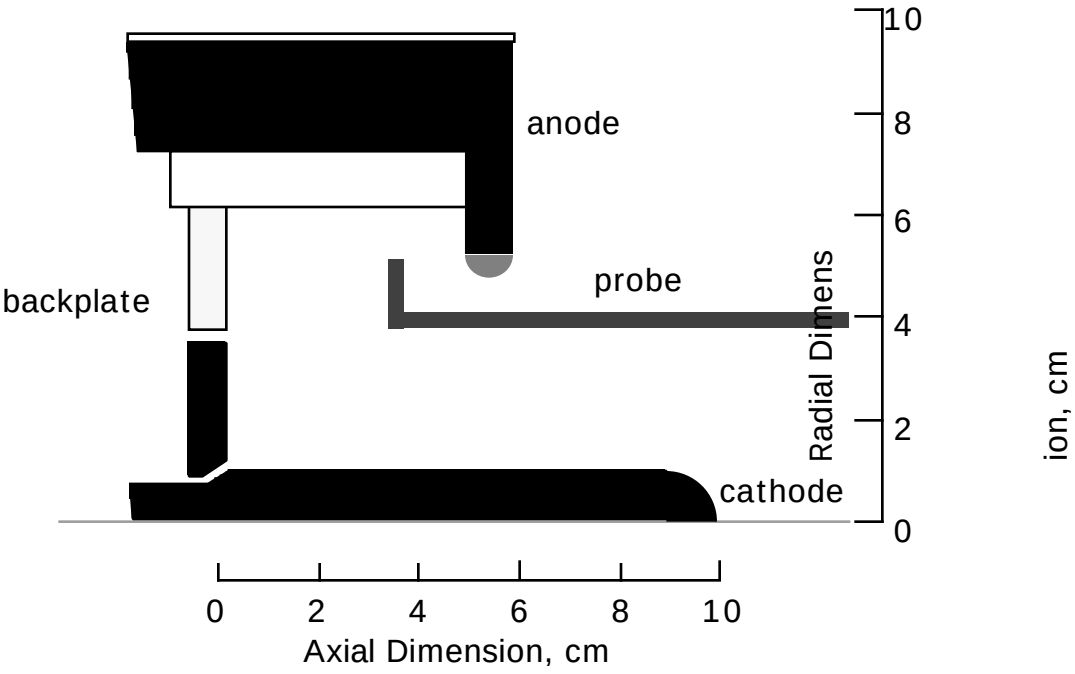

Figure II.4: Magnetic Induction Probe.

II.3.2 Magnetic Induction Probes

Two magnetic induction probes are used to obtain anode current density profiles (via Amperes Law) as well as magnetic field strengths near the anode. One probe was formed in the shape of an "L" in order to conduct measurements along the upstream anode face (cf. Figure II.4). The arm of the probe that contains the coil is 2.5 cm long. The probe coil consists of 20 turns of #38 Formvar coated copper wire wrapped around a 1.27 mm diameter Lucite core. For protection against the discharge, the coil is inserted into a quartz tube of inner diameter 3 mm and outer diameter 4 mm. One end of the quartz tube is sealed by heating with an oxy-acetylene torch forming a hemisphere around the coil. The major arm of the probe is 55 cm long and is enclosed in quartz tubing of identical O.D. as well. Structural stability is maintained through the use of

stainless steel tubes which enclose the probe wires just inside the quartz tubes. Two #26 Formvar coated copper wires run the entire length of the major arm of the probe (55 cm) and connect the two leads of the coil to a RG 58 coaxial cable.

The other probe was originally constructed to investigate asymmetries in the thruster discharge[46]. The core of this probe consists of a coil with thirty turns of #44 Formvar coated copper wire on a 0.15 cm diameter lucite rod. The core and probe signal lines are enclosed in a quartz tube 61 cm long with an outer diameter of 4 mm. Again, one end of the quartz tube terminates to form a hemisphere for protection of the core. Further details of the construction of the probe can be found in Reference [46]. To prevent the cables from outgassing, coaxial cables for both probes are routed to the exterior of the tank through Tygon tubing.

To measure magnetic fields, the probe output signal is time integrated with an electronic integrator. A 50 Ω terminator is used to match the impedance of the coaxial cable line with that of the integrator. This ensures that error associated with signal reflections are minimized[49, 50].

The probes were calibrated with a Helmholtz coil powered by a small bank of capacitors. Current through the Helmholtz coil is controlled via a manually triggered function generator. The magnetic field produced by the coil is nominally a square pulse (40 msec long) with a magnitude proportional to the capacitor bank charging voltage. The Helmholtz coil was calibrated with a Hall effect probe and Gaussmeter. Both probes agree to within approximately 1%, with the total uncertainty in magnetic field measurements estimated to be 2%[46].

II.3.3 Double and Triple Langmuir Probes

Double and triple probes were used to measure electron temperatures and ion number densities near the anode. A bias voltage applied between the two electrodes (cf. Figure II.5) of the double Langmuir probe permits the electron temperature as well as the ion number density to be estimated from the corresponding current response of the probe[51, 52]. The asymmetric electrodes of the probe, 0.6 cm (250 mils) long with diameters of 0.13 mm (5 mils) and 0.25 mm (10 mils), separated by a 0.3 cm gap, permit the electron distribution function to be sampled with higher precision then can

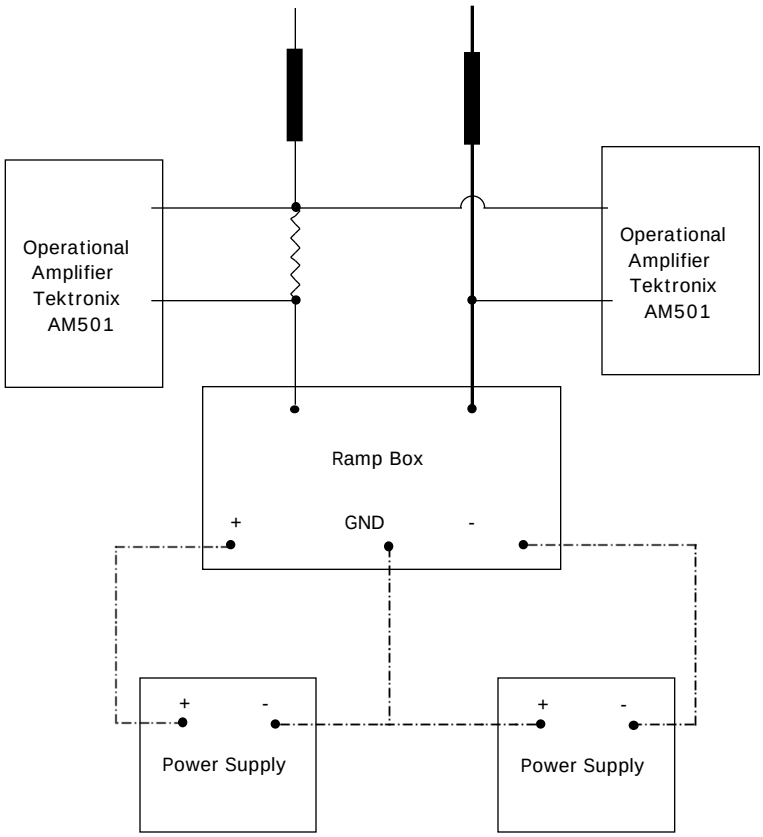

Figure II.5: Double Probe Apparatus.

be achieved by symmetrical probes, thus reducing uncertainty in electron temperature measurements[51, 52]. The probe was designed to have sufficiently high aspect ratios (electrode length/electrode radius) to minimize errors due to "end" effects, which can be significant in the plasma conditions that exist in MPD thrusters[53].

The electrodes are attached to two parallel 1 mm diameter and 5 cm long quartz tubes. A small brass clamp is used to connect each tungsten probe electrode to the core of a RG 174 coaxial cable. The two coaxial cables run through a 48 cm long brass tube (O.D. 5 mm) which is connected to the shields of both coaxial cables. The brass tube is enclosed in a 47 cm long and 0.8 cm diameter G-10 (Fiberglass-epoxy composite) tube. Tygon tubing feeds the coaxial cables from the G-10 tube to the exterior of the tank through a port, thus preventing the cables from outgassing inside of the tank. All elements of the probe are held together with high temperature epoxy (Duralco 4525).

The probe voltage is biased by an electronic ramp box which is triggered by the delay (via delay box) of the 5 volt pulse used to initiate thruster propellant flow (cf. Section II.2.3). By adjusting the delay, ramping, which occurs over a span of some 50 microseconds, is programmed to take place only during the quasi-steady portion of the discharge. The electrodes are biased from -21 volts to +21 volts during ramping. Tektronix AM 501 operational amplifiers are used to measure probe voltages, while a 1 Ω shunt is used to measure probe current. Probe current and voltage are displayed on a Nicolet 320 digital oscilloscope. Oscilloscope traces are transferred to the AT&T computer for analysis. Probe currents obtained at fixed biases at selected points along the voltage ramp are identical to the corresponding currents of the continuous ramp.

The electrons are assumed to have a Maxwellian velocity distribution. Consequently, electron temperature can be estimated with the following relation[52]:

$$\frac{kT_e}{e} = \frac{\mid I_{1+} \mid\mid I_{2+} \mid}{(\mid I_{1+} \mid + \mid I_{2+} \mid)[\frac{dI}{dV}]_{I=0}} \tag{II.4}$$

where I and V are probe current and voltage respectively, e is the elementary charge, $\mid I_{1+} \mid$ and $\mid I_{2+} \mid$ are absolute values of probe saturation currents for either probe electrode, and $[\frac{dI}{dV}]_{I=0}$ is the slope of the probe voltage-current characteristic in the vicinity of I=0 amperes. Once the electron temperature is obtained the ion number density is

determined from the following equation, by assuming Bohm ion current collection[52],

$$n_i = \frac{2I_+}{e\mathcal{A}\sqrt{\frac{kT_e}{M_i}}} \tag{II.5}$$

where I_+ is the saturation current of either probe electrode, $\mathcal{A}$ is the corresponding electrode area, and M_i is the ion mass. Given the conditions that exist in the thruster, these formulas yield electron temperatures that are accurate to 15% and number densities accurate to within a factor of two[51, 52].

The ramp box proved to be so sensitive to interference produced by the thruster discharge that it was not possible to obtain data above 19 kA. This necessitated the implementation of the triple probe system. The triple probe employs three electrodes, one of which is allowed to float in the plasma while the remaining two probes are biased at a constant voltage with respect to each other (cf. Figure II.6). The major benefit of this method is its ability to obtain plasma properties without the need to ramp voltages. With the electrode configuration shown in Figure II.6 the formulas for obtaining T_e and n_i are

$$T_e = \frac{-eV_{d1}}{k\ln(0.5 + 5exp[-\frac{eV_{d3}}{kT_e}])} \tag{II.6}$$

$$n_i = \frac{exp[0.5]I}{e\mathcal{A}\sqrt{\frac{kT_e}{kM_i}}(exp[-\frac{e(V_{d1}-V_{d3})}{kT_e}] - 1)} \tag{II.7}$$

where k is the Boltzmann constant, I is the probe current, and $\mathcal{A}$ is the probe surface area. These formulas assume a Maxwellian electron distribution and a thin collisionless sheath (i.e. $r_p \gg \lambda_d$ and $\lambda_e \gg \lambda_d$ where λ_d is the electron Debye shielding length). The additional requirement that the electron mean free path be much larger than the probe radius ($\lambda_e \gg r_p$) may not be satisfied in the quasi-steady MPD thruster where charged particle densities can approach 1×10^{21} m^{-3}. This effect is expected to have only minor effect on ion current collection of the probe[54, 55].

In an effort to obtain the most accurate interpretation of data possible, curve fits of Laframboise's exact solution of current collection by a cylindrical probe of infinite length in a quiescent plasma have been applied to the triple probe and are used to reduce all probe data in the thesis[56, 57, 58, 59]. The corrections to the Bohm model (Equations II.6 and II.7) introduced by Laframboise's solution take into account phenomena

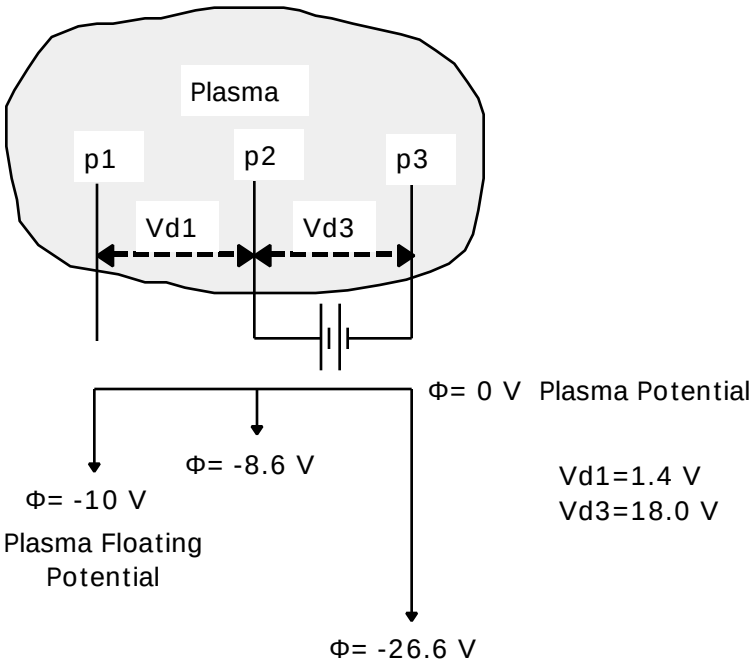

Figure II.6: Triple Probe Electrode Potentials.

which affect ion collection such as finite ion temperature and sheath thickness. For the dense plasma of the pulsed thruster, these corrections prove to be minimal, changing T_e and n_i by only 3 and 10%, respectively. These measurements, however, are now expected to be accurate to within 5% for T_e and 60% for n_i [58, 59].

Application of Laframboise's solution to a flowing plasma may yield erroneous data if special care is not taken. The probe axis should be aligned parallel with the flowing plasma to minimize the convective ion current contribution which would result in measuring artificially high number densities. Also, the minimum probe aspect ratio (L/r_p) for which Laframboise's infinite cylinder results can be applied has been estimated to be twenty for a quiescent plasma[51, 58, 59]. For a flowing plasma where $r_p \gg \lambda_d$, (λ_d Debye length) the additional current due to the convection of ions through the end of

a probe aligned with the flow is

$$\frac{I(L)}{I(\infty)} = 1 + \frac{r_p}{L}\frac{U_p}{\sqrt{\frac{kT_e}{M_i}}} \tag{II.8}$$

where the ratio $\frac{I(L)}{I(\infty)}$ is the finite length correction to Laframboise's currents[59]. For typical conditions near the thruster axis ($kT_e \approx 2$ eV, $U_p \approx 10{,}000$ m/s, $L/r_p = 50$) this correction predicts only a 9% increase in current. Because of uncertainties in flow velocity near the anode however, this correction was not used in the analysis of data.

The triple probe used for this work is composed of three tungsten wire electrodes, each of which are 0.026 cm (10 mils) in diameter and 6.4 cm (250 mils) long ($L/r_p = 50$). The electrodes, which are supported by three parallel quartz tubes of outer diameter 0.1 cm and 5.5 cm in length, are spaced approximately 0.1 cm apart from each other. The quartz tubes are supported by a nylon rod 1 cm in diameter and 15 cm long. The quartz tubes are fastened to the nylon rod with high temperature epoxy (Duralco 4525) which is also used to seal the end of the quartz tube containing the wire electrodes. The nylon tube houses three BNC cables which are connected to the probe electrodes. Again, to prevent outgassing, Tygon tubing (O.D.$\sim$2 cm) feeds the BNC cables from the nylon tube to the exterior of the tank.

Figure II.7 shows a schematic diagram of the triple probe experiment. The potential of the floating probe (p1) relative to the anode (thruster ground) and relative to the adjacent probe electrode (p2) are measured with calibrated 10:1 and 1:1 Nicolet M12 voltage probes respectively. Tektronix AM501 operational amplifiers accept the probe signals and provide an output that is displayed either on a Nicolet 2090 or 320 digital oscilloscope. The potential between active probe electrodes (p2 and p3), which is maintained by a Kepco power supply, is measured with a standard benchtop digital voltmeter. Although V_{d3} was generally maintained at 18 volts, temperature and number density measurements proved to be insensitive to its value. Probe current is measured both with a 1 Ω shunt and by a Tektronix AM503 current probe. Discrepancies in measured current were usually within 10%. All BNC cable shields are maintained at the same potential as the Faraday cage which itself is at the ground potential of the equipment within (e.g. oscilloscope).

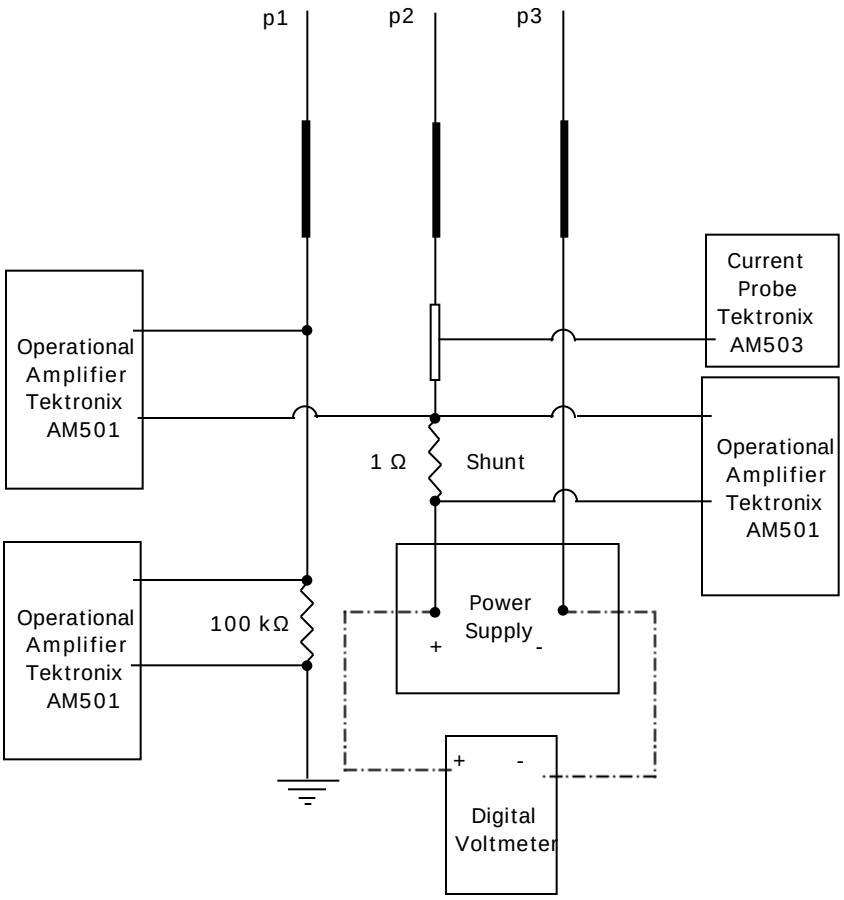

Figure II.7: Triple Probe Apparatus.

The probe was ion impact cleaned by filling the tank with argon to a pressure of 25×10^3 Pa (∼200 microns) and biasing the probe electrodes several hundred volts negative with respect to the thruster anode. Testing showed that reliable data could only be obtained if the probes were cleaned after, at most, every two shots.

As mentioned above, the values obtained with the probe aligned with the flow are expected to be accurate to within 5% for T_e and 60% for n_i. Values obtained with the probe misaligned with the flow obviously will not be as accurate. Errors in number densities can be roughly estimated by the following analysis from Reference [60]. For $C_i \ll U_p \ll C_e$, where C_i and C_e are the ion and electron thermal speed, respectively, and U_p is the plasma flow velocity (bulk velocity), the total current to a probe is approximately

$$I(\theta) = I_{p\|} + (I_{p\perp} - I_{p\|}) \sin\theta \tag{II.9}$$

where θ is the angle of the probe axis with respect to that of the bulk flow and $I_{p\|}$ and $I_{p\perp}$ are measured probe currents when the probe axis is parallel with and perpendicular to the flow, respectively. These currents are defined as

$$I_{p\|} \simeq \mathcal{K} q \mathcal{A}_{\|} n_i \sqrt{\frac{kT_e}{M_i}} \tag{II.10}$$

$$I_{p\perp} \simeq q \mathcal{A}_{\perp} n_i U_p \tag{II.11}$$

where $\mathcal{A}_{\|}$ and $\mathcal{A}_{\perp}$ are effective probe areas for either extreme in probe orientation, and $\mathcal{K}$ is a dimensionless proportionality constant (∼0.5). Assuming for the moment that $\mathcal{A}_{\|} \simeq 2\pi r_p L$ and $\mathcal{A}_{\perp} \sim 2 r_p L$, then

$$\frac{I_{p\perp}}{I_{p\|}} \simeq \frac{2U_p}{\pi\sqrt{kT_e/M_i}}. \tag{II.12}$$

For the typical thruster operating conditions, ($C_i \simeq$2,200 m/s, $U_p \simeq$10,000 m/s, and $C_e \simeq$590,000 m/s), Equation II.12 estimates $I_{p\perp}/I_{p\|} \simeq 3$ which is consistent with the experimental results cited in Reference [60]. Thus, alignment of the probe with the flow can greatly reduce the uncertainty in ion number density measurements.

II.3.4 Floating Probe

Floating probe measurements were conducted at the anode region of the thruster to measure the anode fall and the anode power fraction. These measurements serve as an

independent check on the heat flux technique. The floating probe used for all measurements is shaped in the form of an "L" to permit probing within the thrust chamber behind the anode. The probe has a major arm 54 cm long and a minor arm 1.4 cm long. The probe electrode is tungsten wire 0.26 mm (10 mils) in diameter and 0.17 cm (65 mils) long. Construction of the probe is similar to the Langmuir probes (cf. Section II.3.3). Probe and anode potentials are measured with Tektronix P6015 1000:1, Nicolet M12 10:1, and Nicolet M12 1:1 voltage probes. Voltage probe outputs are measured with a Tektronix AM501 operational amplifier with matched impedance (10^8 Ω) connected to either a Nicolet 2090 or 320 digital oscilloscope. Oscilloscope traces are transferred to the AT&T personal computer for processing.

As the name suggests, the potential measured by the floating probe is the potential of the tungsten wire (plasma floating potential). To obtain the actual plasma potential, the floating potential must be adjusted, usually by adding a term that is proportional to the electron temperature[52]. To obtain an accurate interpretation of floating probe data, Laframboise's results[56], embodied in a curve fit developed by Peterson and Talbot[57], were applied assuming that the probe collects zero net current (floats). This results in a correction term that is a function of T_e, n_e, and T_i. T_e and n_e were obtained from double and triple probe measurements where n_e was assumed to equal n_i (assuming only singly ionized argon ions are present). Fortunately, the correction term, which is solved iteratively, is not strongly dependent on T_i, thus T_i was set equal to T_e. Based on the accuracy of the electron temperature measurements, plasma potentials obtained from floating probe measurements should be accurate to within ± 2 volts.

Chapter III

Anode Studies with the Benchmark Thruster

III.1 Introduction

Direct measurements of anode heat flux obtained using the calorimetric technique described in Chapter 2, were made at argon mass flow rates of 4 and 16 g/s and with thruster currents of 8, 16, and 24 kA, spanning thruster power levels between 200 kW and 6 MW. In addition, anode current density and electron temperature data, obtained with the diagnostics also reviewed in Chapter 2, are presented as well. By manipulating the anode heat transfer equation introduced in Chapter 1 (cf. Equation I.3), an expression for the anode fall, as a function of measured heat flux, current density, and electron temperature, is obtained. Floating probe data, collected throughout the anode region, serve as a second means of determining the anode fall and anode heating rates.

III.2 Heat Flux Measurements

Ten thermocouples were mounted inside of a modified full-scale benchmark MPD thruster anode as described in Chapter 2 (cf. Figure II.2). The heat flux, calculated by the temperature rise of each thermocouple, is assumed to be constant over each associated site, which extends from midpoints of adjacent thermocouples. Thermocouples "A" and "J", which are located near insulated portions of the thruster (cf. Figure II.2), are assumed

to have areas which extend to those boundaries. Azimuthal symmetry is assumed for all sites. The validity of this assumption was investigated by using four magnetic induction probes and a multi-probe rake developed by Hoskins[46] to investigate asymmetries in thruster discharges. The four probes were attached to an acrylic ring that is placed on the probe positioning table. The sensing elements of the probes (cores) are positioned at the same axial location but are placed 90 degrees apart in the azimuthal direction. The probe cores are aligned with the azimuthal direction at a radius of approximately 4.5 cm (0.5 cm from the anode lip). Probe measurements were made at several axial locations over a wide range of thruster operating conditions. For the thruster operating conditions of interest, magnetic fields measured by the probes were within 7% of each other.

A typical thermocouple temperature response is shown in Figure III.1. As shown, the temperature at the thermocouple site reaches its final maximum value in approximately 10 milliseconds. Anode heat fluxes, measured at each thermocouple site, are shown in Figures III.2 through III.4, with the data presented on these figures being averaged over fifty or more shots. The abscissa of the plots represents a coordinate system that linearly maps onto the anode surface, with the extreme left (-2.0 cm) of the axis representing the upstream anode face near the thrust chamber Pyrex insulating tube, the middle portion representing the lip region (-0.8 to +0.8 cm), and the remaining portion representing the downstream anode face (cf. Figure III.5). The junction of the anode face and the mylar insulation on the outer diameter of the thruster column is located at approximately +4.8 cm.

Anode heat fluxes vary from 300 to 5500 W/cm^2. Maximum heating rates are measured just downstream of the anode lip 6 o'clock (anode midplane: 0.0 cm) position. As the figures illustrate, anode heat flux appears to be independent of mass flow rate. At 8 kA the anode heat flux is approximately 250 W/cm^2 along the upstream anode face (Chamber). The heat flux increases along the lip until a peak value of 1100 W/cm^2 is measured just downstream of the midplane. Along the downstream face, the heat flux drops to 200 W/cm^2. At 16 kA, a similar pattern is evident, however, the heating rates are considerably larger with a minimum heat flux of $\sim$1000 W/cm^2 and a maximum of 3500 W/cm^2. The anode heating rates decrease rapidly outside of the lip region. At

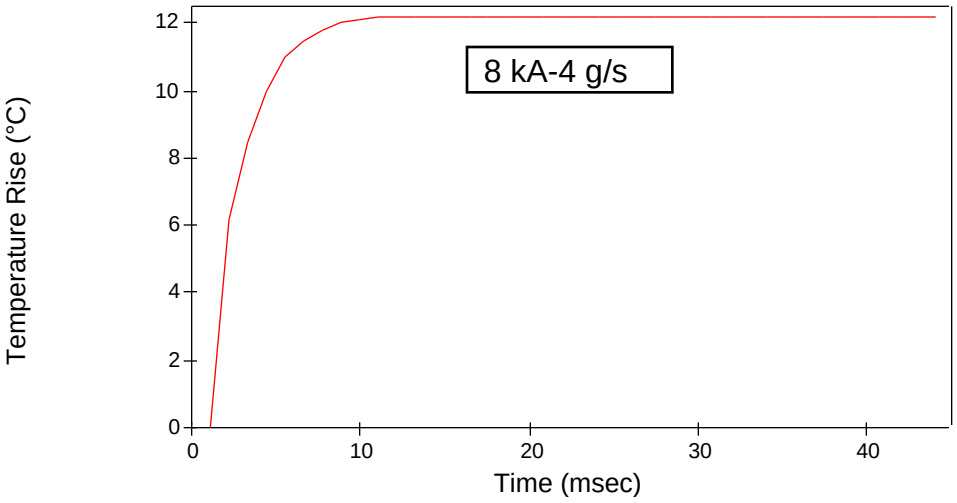

Figure III.1: Thermocouple Temperature Response (8 kA-4 g/s).

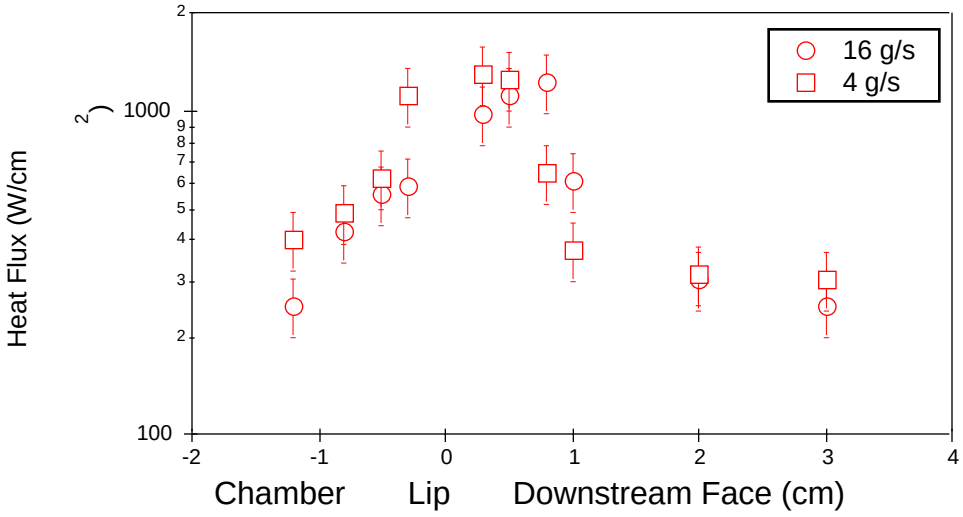

Figure III.2: Anode Heat Flux Profile (8 kA).

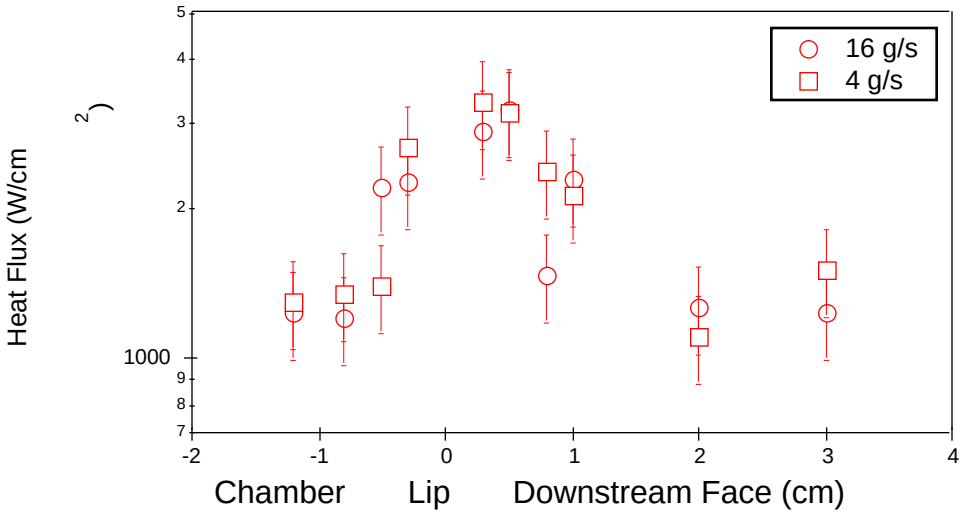

Figure III.3: Anode Heat Flux Profile (16 kA).

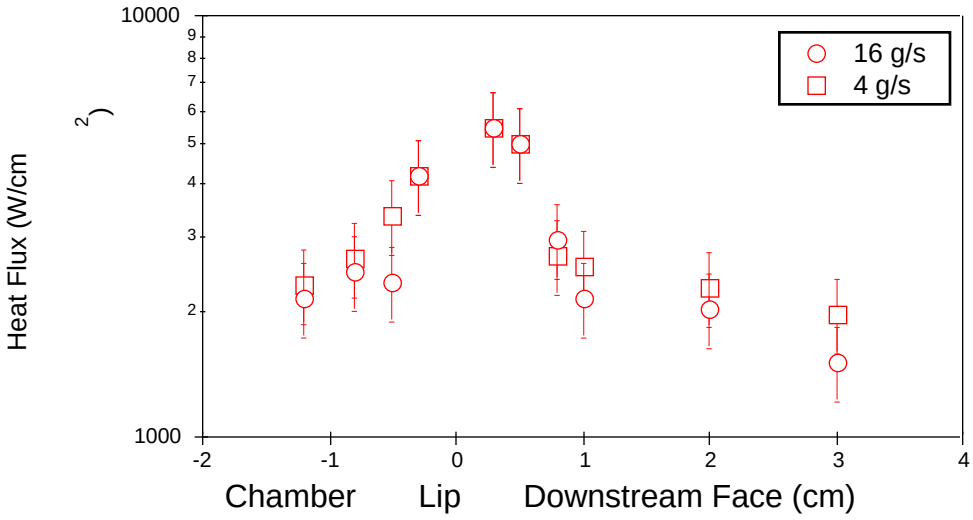

Figure III.4: Anode Heat Flux Profile (24 kA).

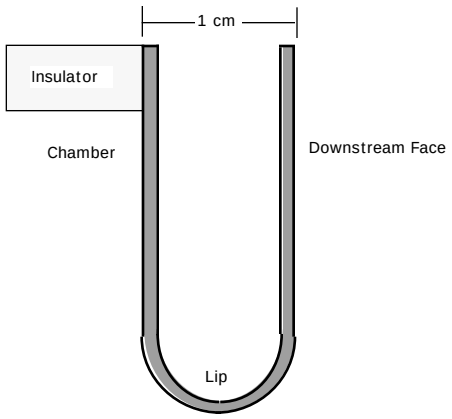

Figure III.5: Anode Heat Flux Coordinate Reference.

24 kA, the heat flux along the upstream face is approximately 2000 W/cm^2. Along the lip, this values reaches the maximum measured heat flux of ∼5500 W/cm^2. Along the downstream face, the anode heat flux decreases to less than 2000 W/cm^2.

The results described above are in general agreement with trends observed by Saber[17], who took a similar approach in determining anode heating rates. Although the peak heat fluxes measured by Saber are higher than those measured here, heat fluxes recorded along the upstream and downstream faces of his anode are lower than those obtained in these experiments. While the anode designs used in both experiments are very similar, Saber used a conical cathode (2% thoriated tungsten) with a base diameter of 1.9 cm and a length of 2.7 cm. The smaller cathode of Reference [17] may have changed the discharge pattern in the thruster, resulting in an increased concentration of current and anode heating at the lip region. This conclusion is supported by Saber's current density measurements as well.

III.3 Anode Current Density Measurements

Current contours near the anode are acquired through the incorporation of magnetic field data, obtained throughout the anode region, into Ampere's law. Figures III.7 through III.12 show the current profiles and their corresponding anode current density

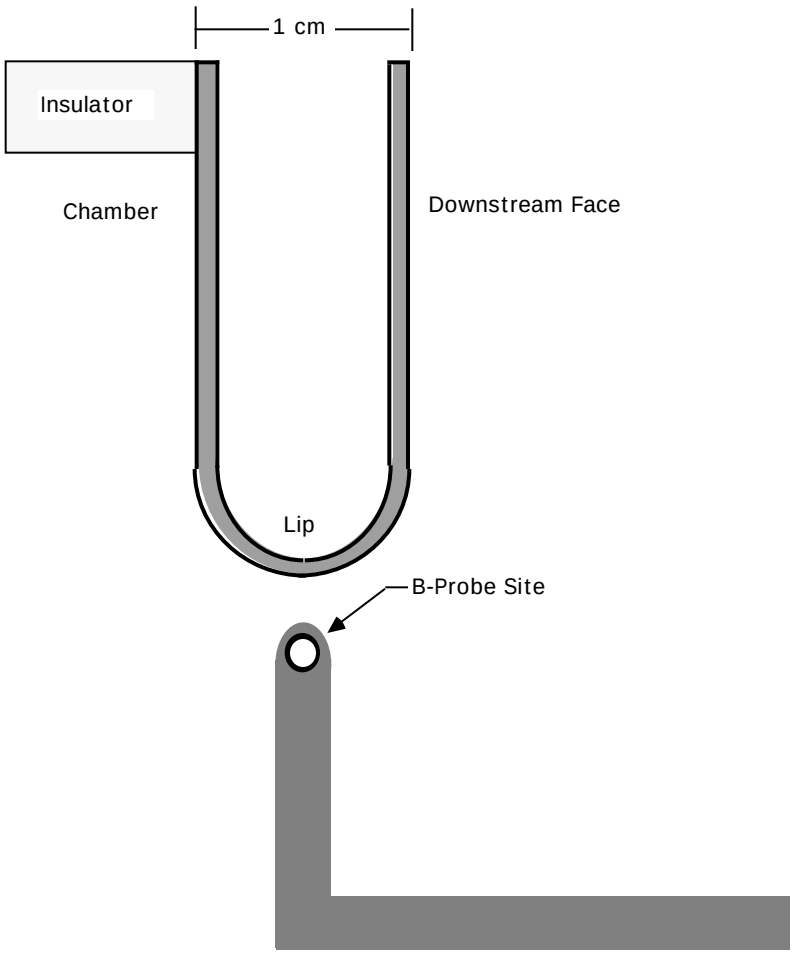

Figure III.6: Magnetic Induction Probe Site.

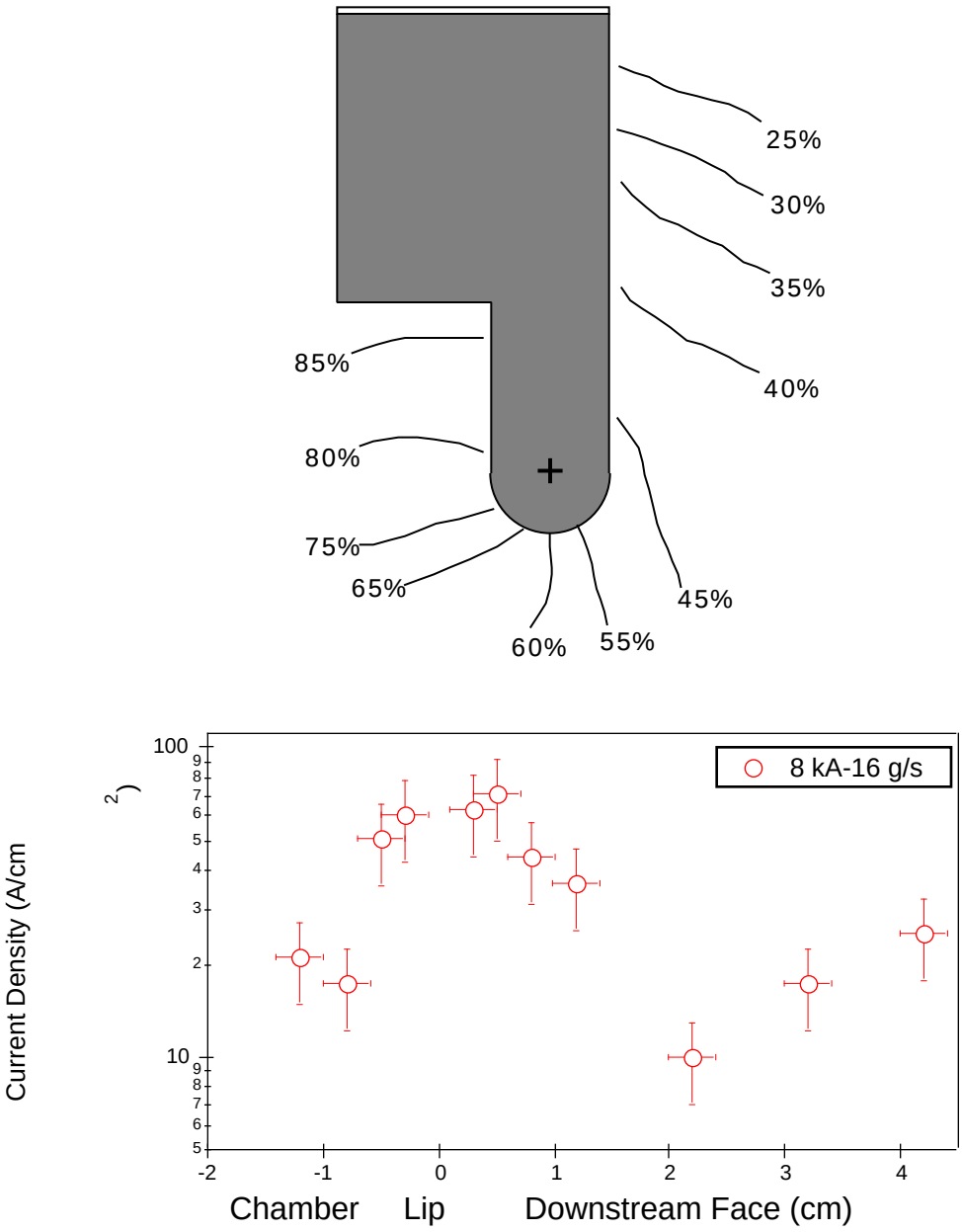

Figure III.7: Anode Current Profile (8 kA-16 g/s).

distributions for the operating conditions in which anode heat fluxes were measured (cf. Figure III.6). In general, the current density distribution pattern mimics that of heat flux, with extreme values measured at the lip. Significant axial currents are measured along both anode faces. The Lorentz body force is directed radially inward along the upstream face, axially along the lip, and radially outward along the downstream face. The abscissa of the plots are the same as those used in Section III.2.

The probe surveyed a region near the anode that extends 3 to 15 mm from the anode in grids whose size varies from 1 mm by 2 mm (axial by radial) at the lip, to 3 mm by 5 mm near the downstream anode face. Anode current densities are estimated by extrapolating measured current contours and calculating the amount of current absorbed at the anode between two adjacent current streamlines. The maximum length of extrapolation is usually less than 3 mm. Each current density measurement site was allocated a specific surface in the manner used for the heat flux measurements. Summing the products of local current density and its associated anode surface area resulted in a total anode current that differed from the total discharge current by less than 5%. Error in these measurements is estimated to be between 30 and 50%.

The anode current distribution for the thruster operating at a current of 8 kA with a propellant flow rate of 16 g/s is shown in Figure III.7. The highest current densities (45 to 75 A/cm^2) are measured along the lip region, with the peak current density (75 A/cm^2) located just downstream of the 6 o'clock position of the anode lip. A sharp drop in current density is observed on either face of the anode with current densities of 20 A/cm^2 along the upstream face (side enclosing chamber) and 10 to 25 A/cm^2 along the downstream face. The steady increase in current density observed along the downstream face is inconsistent with trends at any other operating condition. This implies that a large fraction of the current that is blown downstream of the anode plane attaches near the junction of the downstream face with the mylar insulation. At this operating condition, however, examination of the mylar insulation revealed no charring or damage indicative of significant ablation. At the same current (8 kA) but with a mass flow rate of 4 g/s (cf. Figure III.8), the peak anode current density (90 A/cm^2) is observed just upstream of the anode midplane. Current densities of 35 A/cm^2 and 15 A/cm^2 are measured along the upstream and downstream faces, respectively.

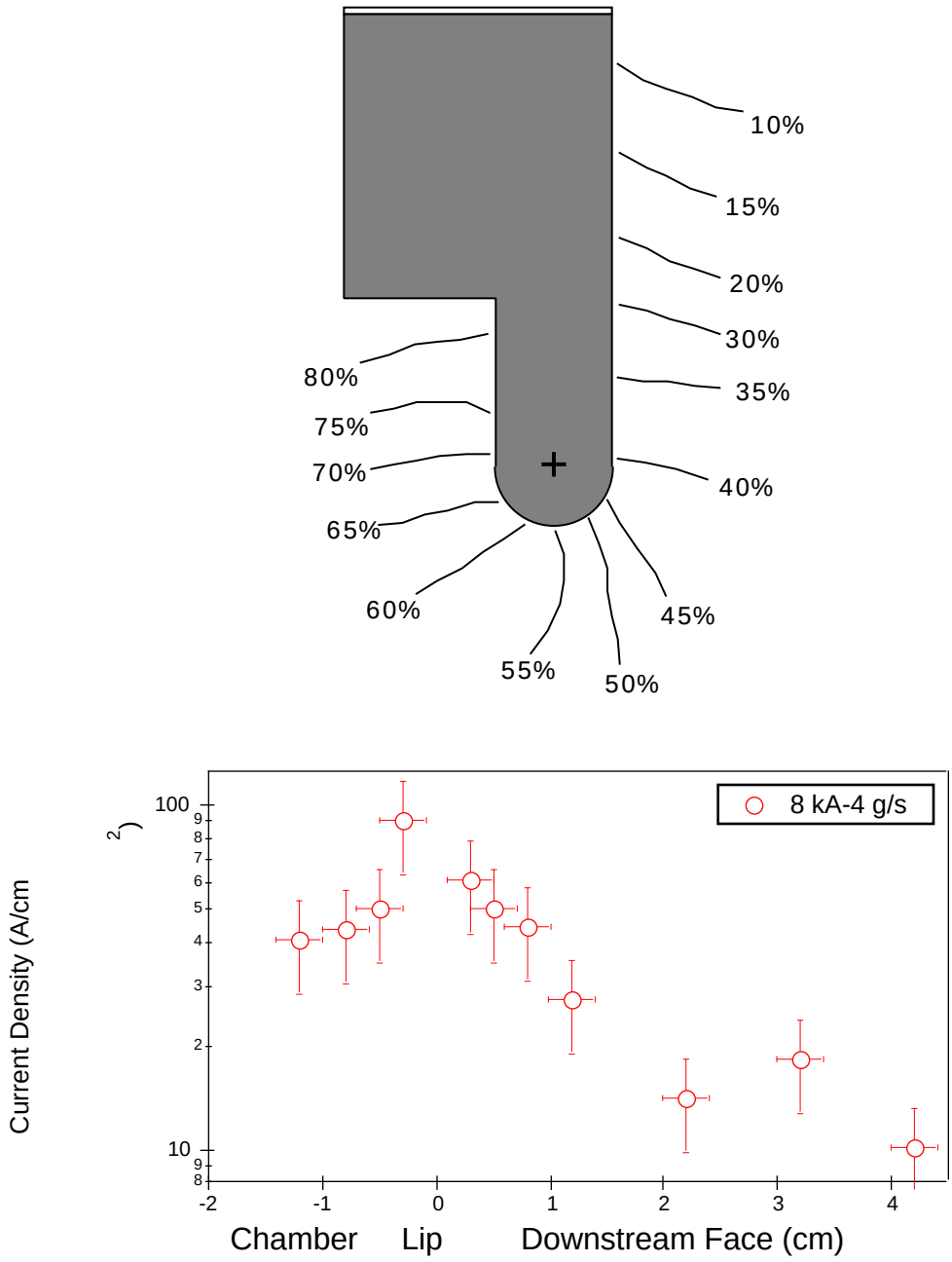

Figure III.8: Anode Current Profile (8 kA-4 g/s).

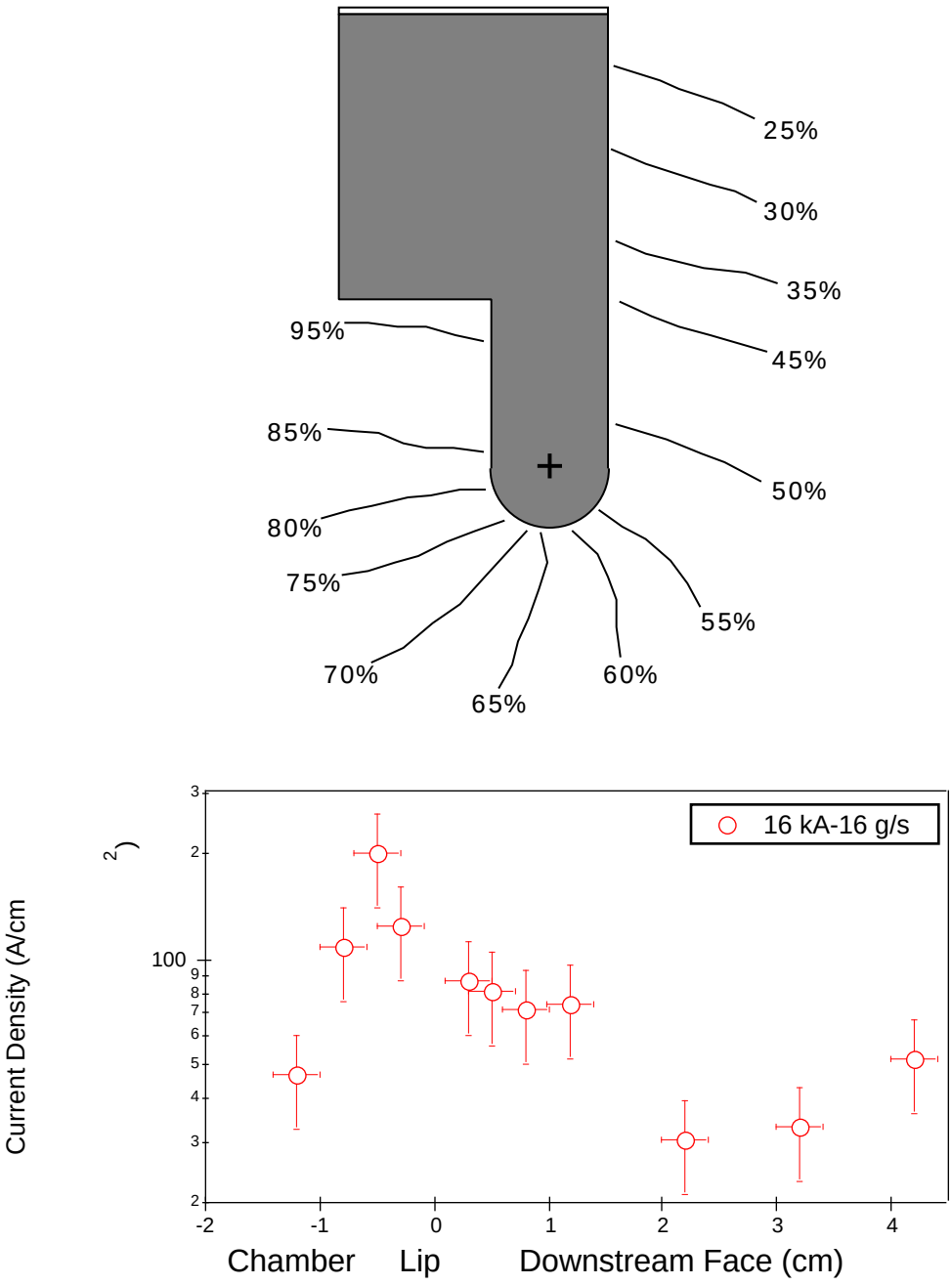

Figure III.9: Anode Current Profile (16 kA-16 g/s).

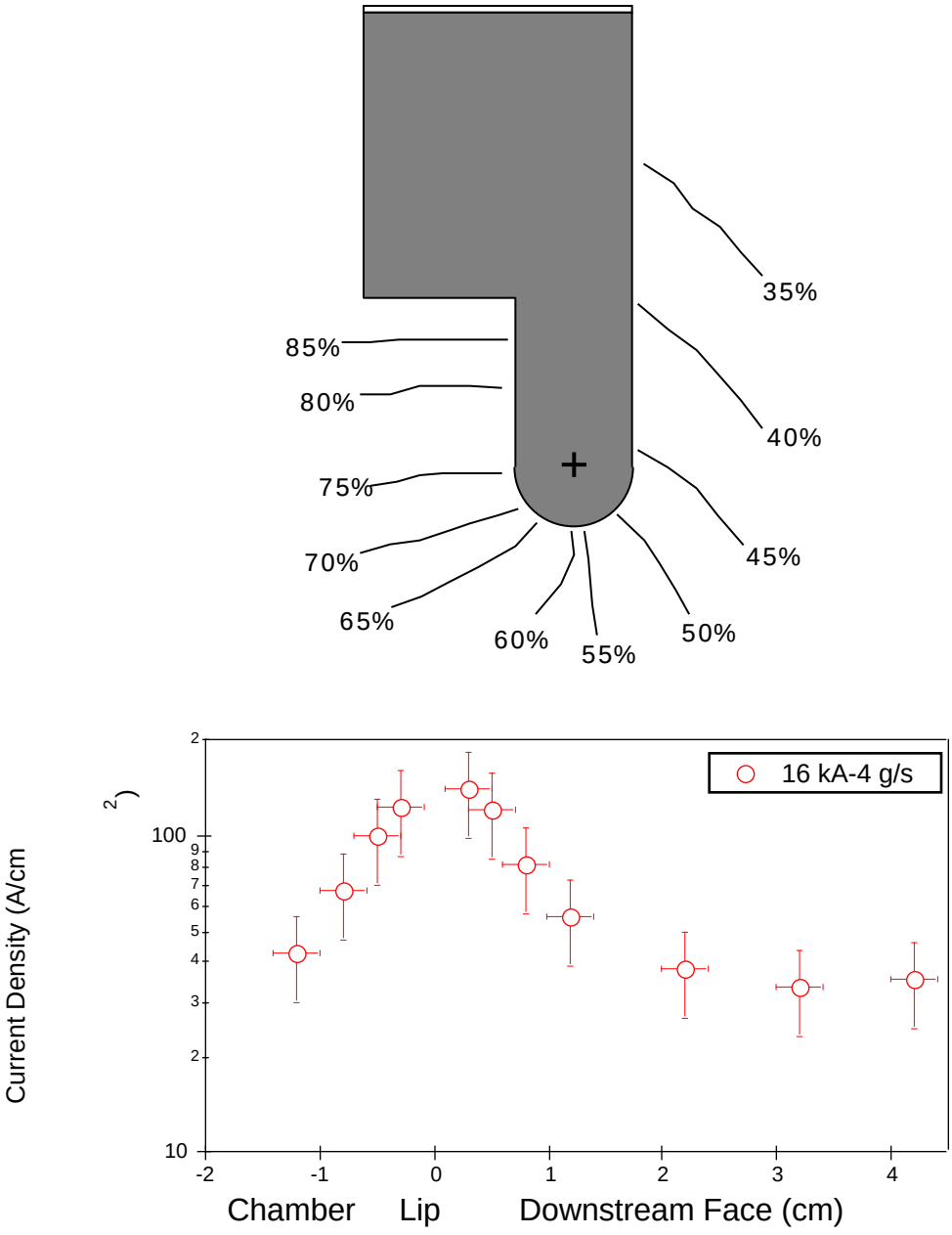

Figure III.10: Anode Current Profile (16 kA-4 g/s).

Figures III.9 and III.10 show data collected at a discharge current of 16 kA with mass flow rates of 16 and 4 g/s, respectively. At a mass flow rate of 16 g/s, the current density along the upstream face is approximately 45 A/cm^2. Current densities between 100 and 200 A/cm^2 are measured at the lip, with the peak current density ($\sim$200 A/cm^2) upstream of the center of the lip. Downstream of the lip, the current density increases from 20 to 40 A/cm^2 along the face. Although similar trends and magnitudes are observed, the current profile at 4 g/s is somewhat more diffuse than at 16 g/s. The peak current density for the former operating condition is approximately 140 A/cm^2. In comparing Figures III.8 and III.9 where each condition corresponds to a $J^2/\dot{m}$ of 16 kA$^2-$s/g, we see that the peak current density occurs at almost the same position on the anode lip. However, at 16 kA-16 g/s a larger fraction of the current is blown outside of the thruster than at 8 kA-4 g/s.

Figures III.11 and III.12 show the results at 24 kA for mass flow rates of 16 and 4 g/s, respectively. The peak current density for both conditions is measured downstream of the anode midplane ($\sim$250 A/cm^2). As the figures illustrate, a significant portion of the discharge current is blown outside of the thruster. Current densities within the chamber for both conditions are approximately 100 A/cm^2. Current densities along the downstream face for the thruster operating at a current of 24 kA and a mass flow rate of 16 g/s vary from 70 A/cm^2 just downstream of the lip to approximately 15 A/cm^2. With the mass flow rate at 4 g/s, the current density along the downstream faces varies between 30 and 60 A/cm^2.

In summary, the anode current density varies from ten to several hundred Amperes per square centimeter, with the highest current densities at the lip. The large axial currents measured along the anode faces are indicative of significant Lorentz pumping. The fact that the current streamlines near the lip are almost entirely radial implies that the Hall parameter in this region is near unity. However, as is shown in Appendix A, the Hall parameter, calculated from electron temperature, number density, and magnetic field data, is significantly larger than one near the lip.

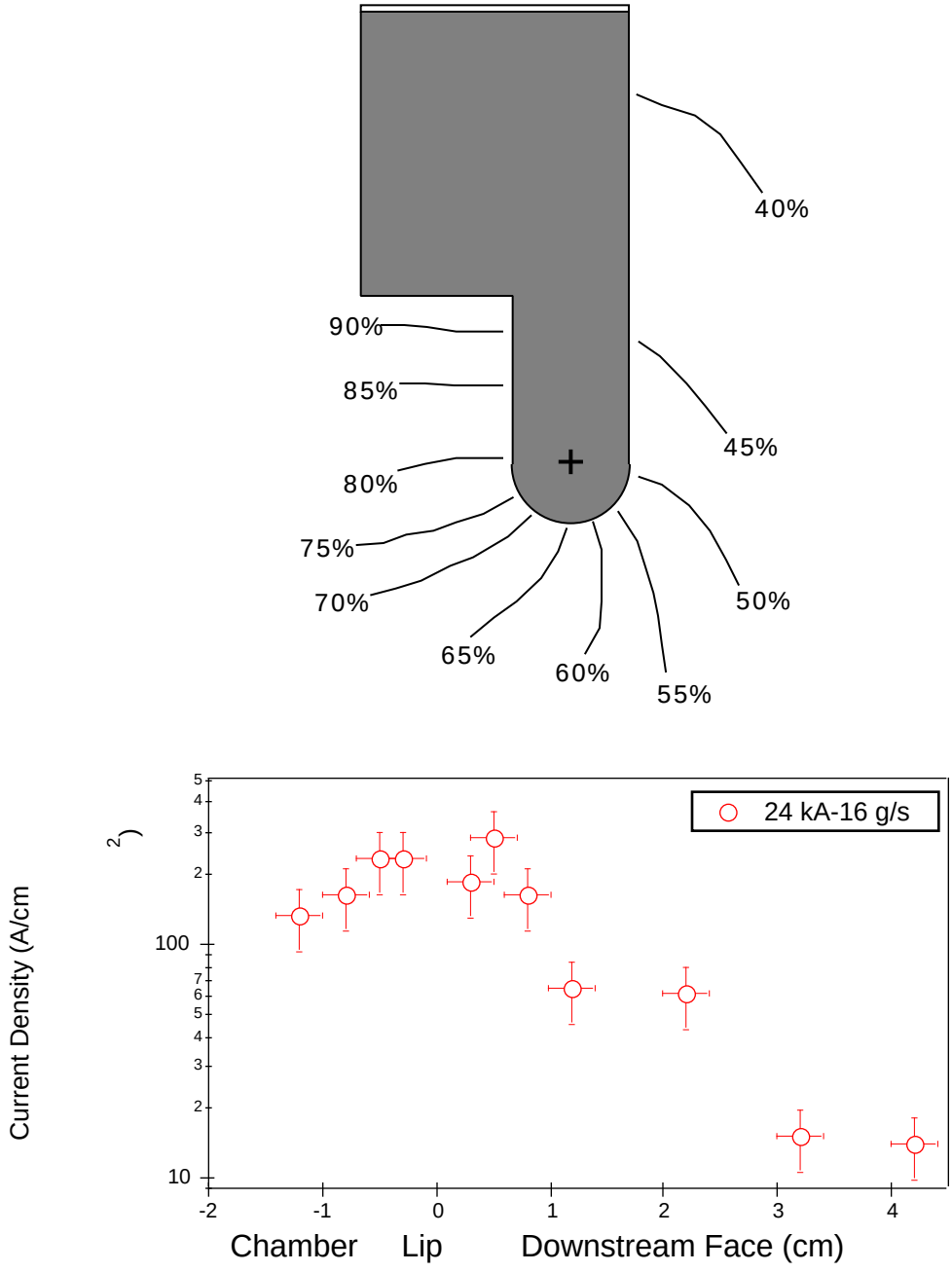

Figure III.11: Anode Current Profile (24 kA-16 g/s).

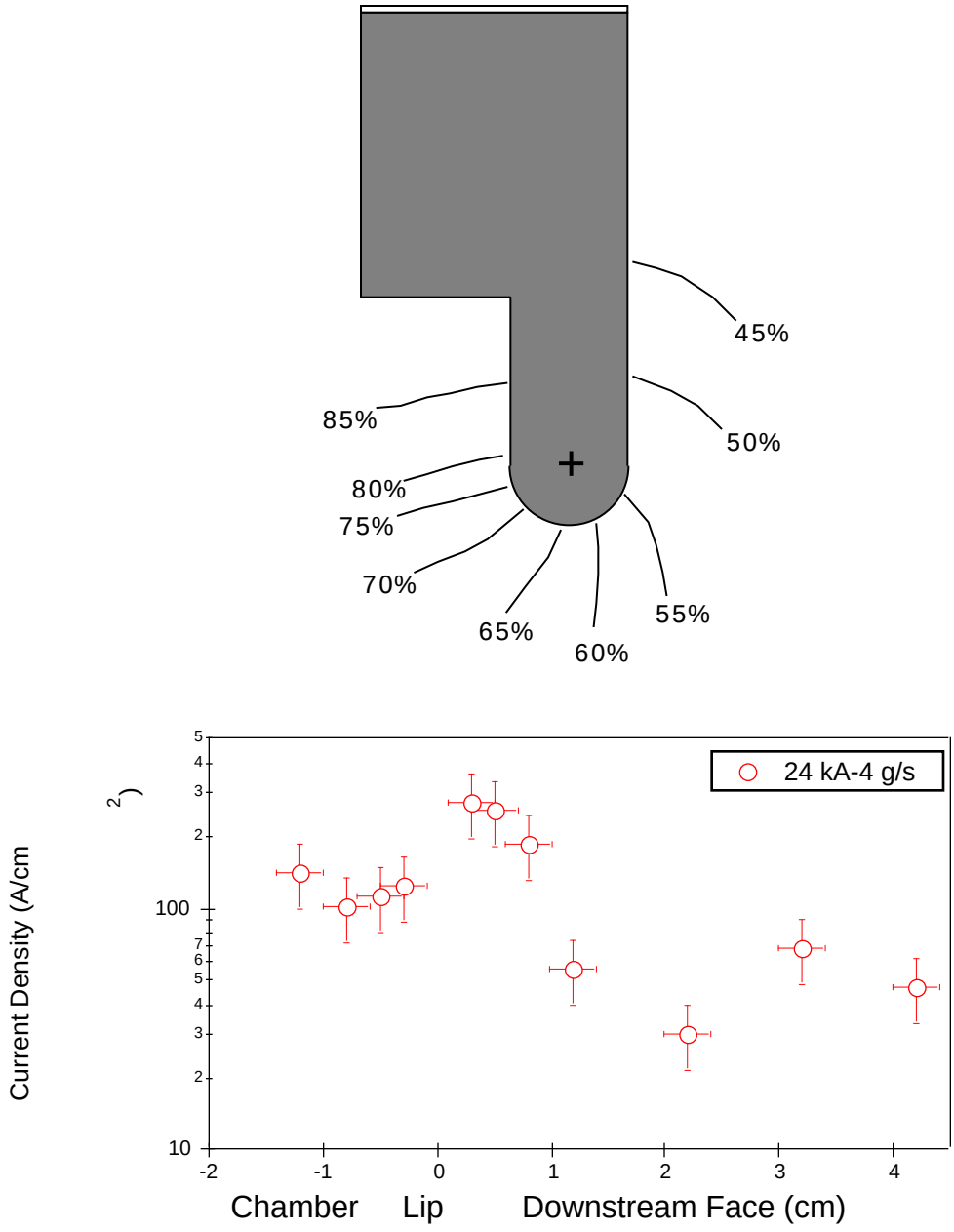

Figure III.12: Anode Current Profile (24 kA-4 g/s).

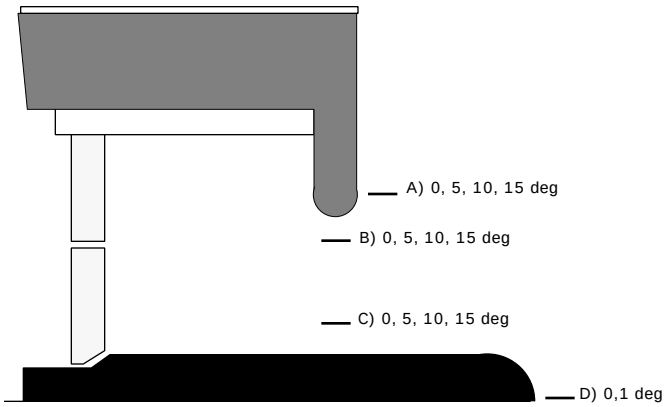

Figure III.13: Langmuir Probe Sites.

III.4 Electron Temperature and Ion Density Measurements

Knowledge of the electron temperature near the anode is necessary to extract the anode fall from measured anode heat fluxes (cf. Equation I.3). Furthermore, electron temperature and number density measurements are important for the characterization of plasma conditions that lead to large anode falls.

III.4.1 Double Langmuir Probe Measurements

Figure III.13 shows the position in the thruster where electron temperature and ion number density measurements were made with the double Langmuir probe described in Chapter 2. Position "A" is located 0.5 cm downstream of the anode face. Positions "B" and "C" are both located in the anode exit plane, 1 and 3 cm from the anode lip, respectively. Position "D" is located 2.5 cm downstream of the cathode surface along the axis of symmetry. This arrangement was selected to obtain plasma data near the anode and to look at radial variations in temperature and density throughout the region. The numbers next to each position represent the angles through which the probe was rotated with respect to the cathode axis for alignment with the flowing plasma. Only

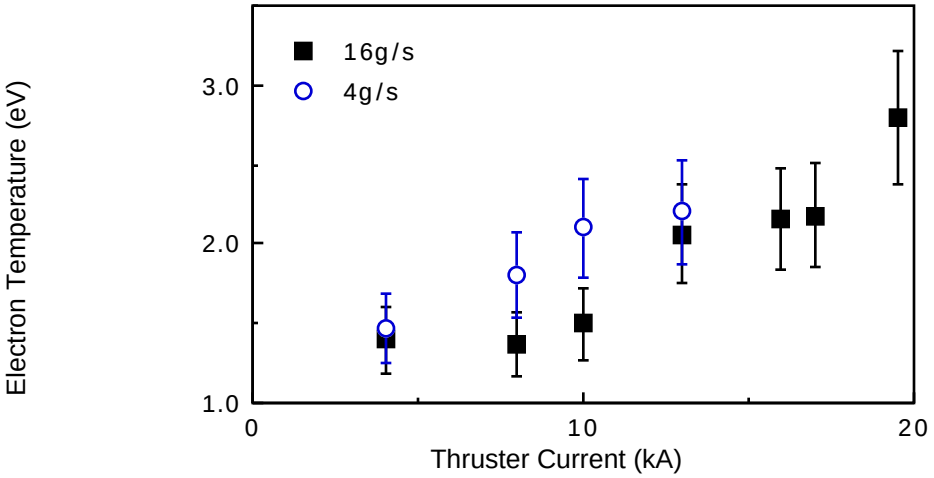

Figure III.14: Electron Temperature vs. Thruster Current.

data collected at the angle of minimum saturation current, presumably when the probe axis is approximately parallel with the flow, are used.

Figures III.14 and III.15 show the variation in electron temperature and ion number density near the anode lip as a function of thruster current at 4 and 16 g/s (position B in Figure III.13). As the figures illustrate, there is a steady increase in both electron temperature and ion number density near the anode lip as the thruster current is increased. Electron temperature varies from 1.5 to 2.5 eV between currents of 4 and 19 kA. Over the same range of current, the ion number density ranges from 5×10^{19} to 5×10^{20} m^{-3}. As the figures illustrate, over these thruster operating conditions, electron temperature and ion number density are weakly dependent on mass flow rate. This observation is further illustrated in Tables III.1, III.2, and III.3, which present Langmuir probe data obtained at a current of 8 kA for mass flow rates of 16, 8, and 4 g/s. Not only is there little change in plasma properties with mass flow rate, but there does not appear to be a strong number density variation with radial position. This is

Position	Probe Angle (deg)	kT_e (eV)	n_i ($10^{20}m^{-3}$)
A	5	1.66	2.9
B	5	1.37	0.7
C	5	2.43	4.8
D	0	2.76	5.2

Table III.1: Double Langmuir Probe Data (8 kA-16 g/s).

Position	Probe Angle (deg)	kT_e (eV)	n_i ($10^{20}m^{-3}$)
A	5	1.27	3.9
B	5	1.29	1.8
C	5	2.81	3.3
D	0	2.34	3.5

Table III.2: Double Langmuir Probe Data (8 kA-8 g/s).

Position	Probe Angle (deg)	kT_e (eV)	n_i ($10^{20}m^{-3}$)
A	0	1.48	3.1
B	5	1.83	1.4
C	0	2.87	3.9
D	0	2.64	2.6

Table III.3: Double Langmuir Probe Data (8 kA-4 g/s).

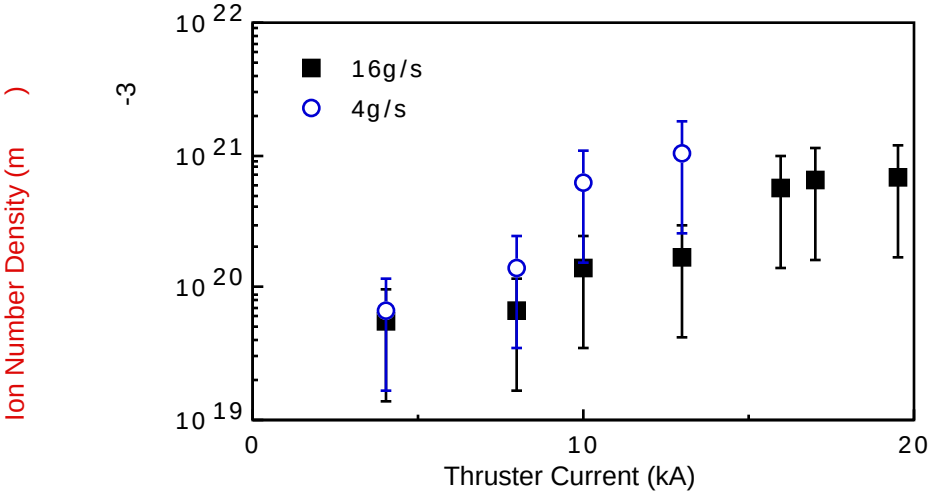

Figure III.15: Ion Number Density vs. Thruster Current.

not surprising since at these low values of $J^2/\dot{m}$, where the plasma acceleration is dominated by electrothermal effects, diffusion processes may dominate over electromagnetic phenomena such as Lorentz pumping. As mentioned in Chapter 2 however, the ramp box proved to be so sensitive to thruster conditions that it was not possible to obtain data above 19 kA, necessitating the implementation of the triple probe system.

III.4.2 Triple Langmuir Probe Data Collection Process

As with the double probe, the triple probe was positioned at several sites near the anode lip with its axis oriented to various angles with respect to the thruster centerline. Only data from the angle which corresponds to minimum probe current is used. To insure that all measurements are averaged over the gradient of plasma properties that exist at each measurement site, the probe electrode configuration was periodically rearranged (e.g. in one shot the center electrode is allowed to float, in the next shot an end electrode is set to float etc.). Variation of the electrode configuration resulted

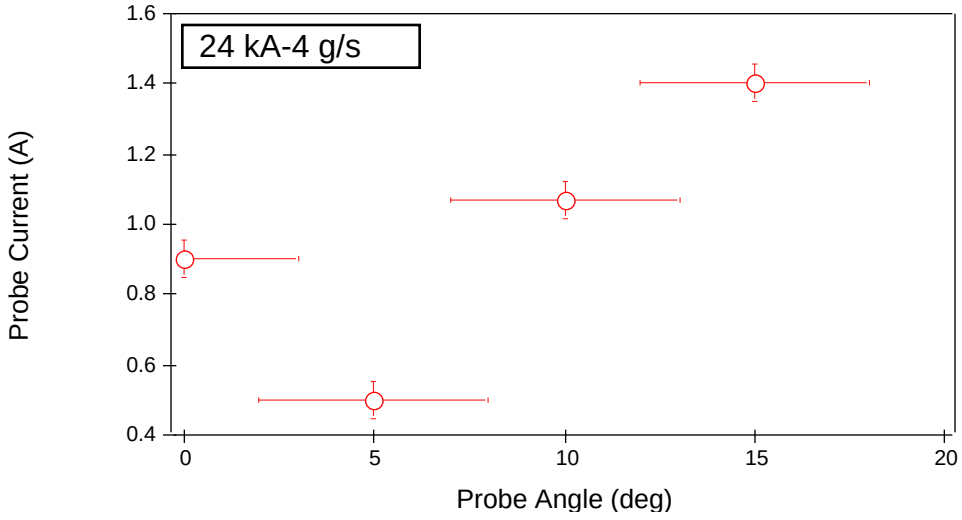

Figure III.16: Probe Current vs. Probe Angle (24 kA-4 g/s).

in a negligible change (5%) to the probe data. Electron temperature and ion number density measurements obtained by the triple and double probes are in good agreement. Although temperatures and number densities measured from either method are generally within 15% and 50%, respectively, plasma properties obtained via triple probe are more accurate since Laframboise's analysis was used to reduce only triple probe data (cf. Chapter II). In addition, the triple probe is easier to implement over a wider range of thruster operating conditions. Thus for consistency, only triple probe data is used to calculate plasma properties.

Figure III.16 shows the variation of probe current with probe orientation angle. As the figure shows, when the thruster is operating at large values of $J^2/\dot{m}$, large errors in the measurement of probe saturation current (i.e. n_i) can be incurred if the probe is not aligned with the flow. For this condition, misalignment of the probe with the flow results in an artificially large ion saturation current that is almost three times larger than that obtained with the probe aligned with the flow. This observation agrees with analysis on the influence of probe misalignment on ion number density measurements

that was presented in Chapter 2 (cf. Section II.3.3, Equation II.8). The strong variation of probe current seen in Figure III.16 was not observed at any other thruster operating condition, presumably because of lower flow velocities. This implies that alignment of the probe with the flow may not be crucial when the thruster is operating at low exhaust velocities.

Figures III.17-III.22 show the measured n_i and T_e values at respective sites. Numbers in brackets indicate the probe angle with respect to the cathode axis, that corresponds to minimum probe current. Because of the physical constraints of the vacuum tank, it was not possible to align the probe parallel with the flow at all sites along the anode face. Thus, along portions of the downstream anode face (i.e. sites without bracketed numbers) the probe was kept parallel with the cathode. Because of the relatively low flow velocities expected in the vicinity of the downstream face of the anode, the electron temperature is expected to be insensitive to probe alignment and should be accurate to within 20%. The number density measurements in this region are accurate to within a factor of three (see discussion in Section II.3.3 of Chapter 2). Figures III.18, III.20, and III.22 are missing data near the cathode because the probe was found to be covered with tungsten after just a few shots at these conditions.

The results of these measurements indicate that the electron temperature near the anode lip varies between 1.7 and 3.7 eV (cf. Figures III.17-III.22) with corresponding number densities of 8×10^{19} to 5×10^{20} m^{-3}. The measurements along the anode face indicate a strong radial gradient in number density, with values changing by an order of magnitude over a distance of less than 4 cm. As the figures show, the peak electron temperatures are measured either at the lip or at the junction of the lip with the downstream face. The electron temperature decreases radially outward.

If the electrons near the anode are assumed to be governed by a Maxwell-Boltzmann distribution, in the absence of strong electro-magnetic fields, the electron current density at the anode surface due to random motion is

$$j_e = \frac{1}{4} q n_e \bar{C}_e \tag{III.1}$$

where $\bar{C}_e$ is the electron thermal speed ($\sqrt{kT_e/(2\pi m_e)}$) and n_e is the electron number density.

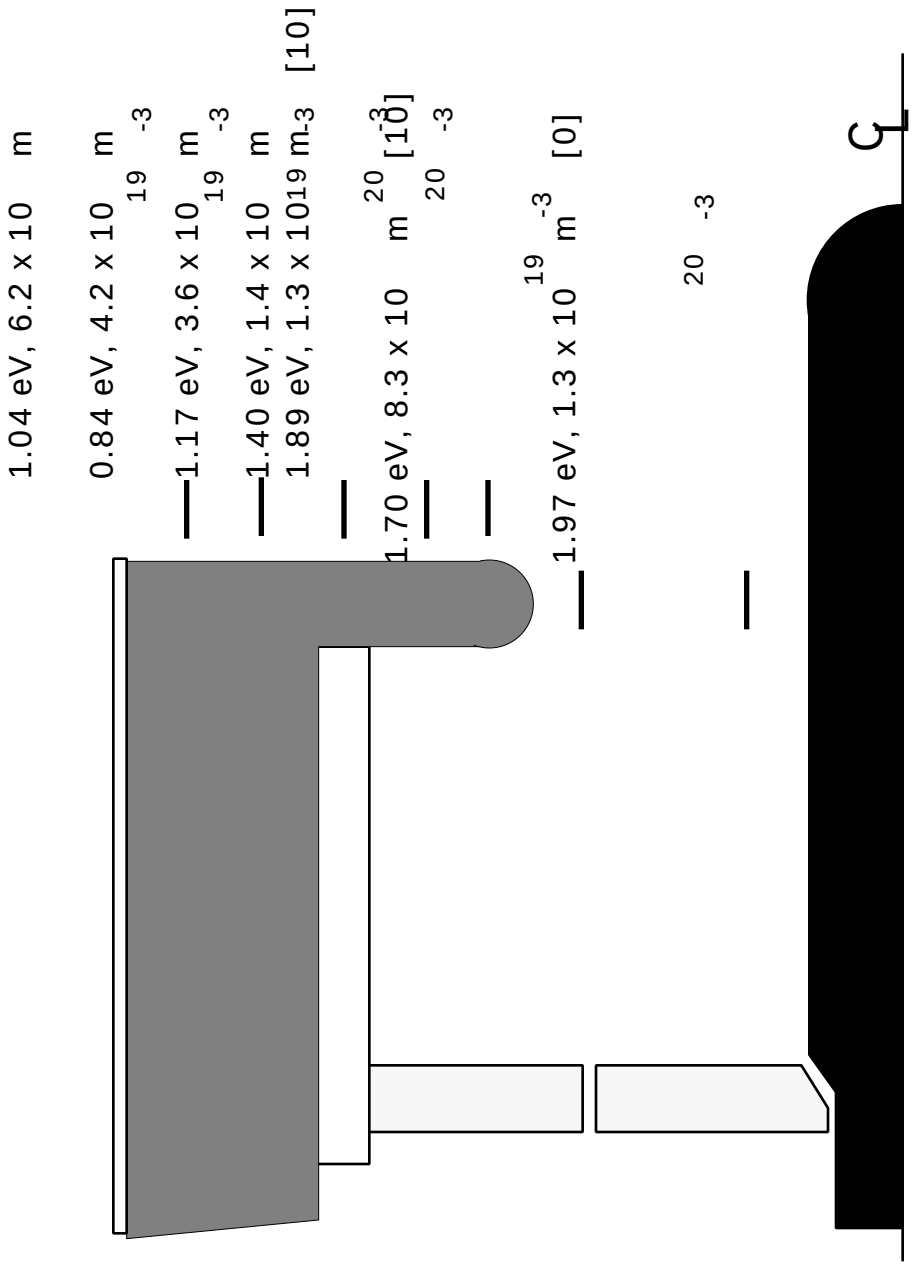

Figure III.17: Electron Temperature and Ion Number Density Profile (8 kA-16 g/s).

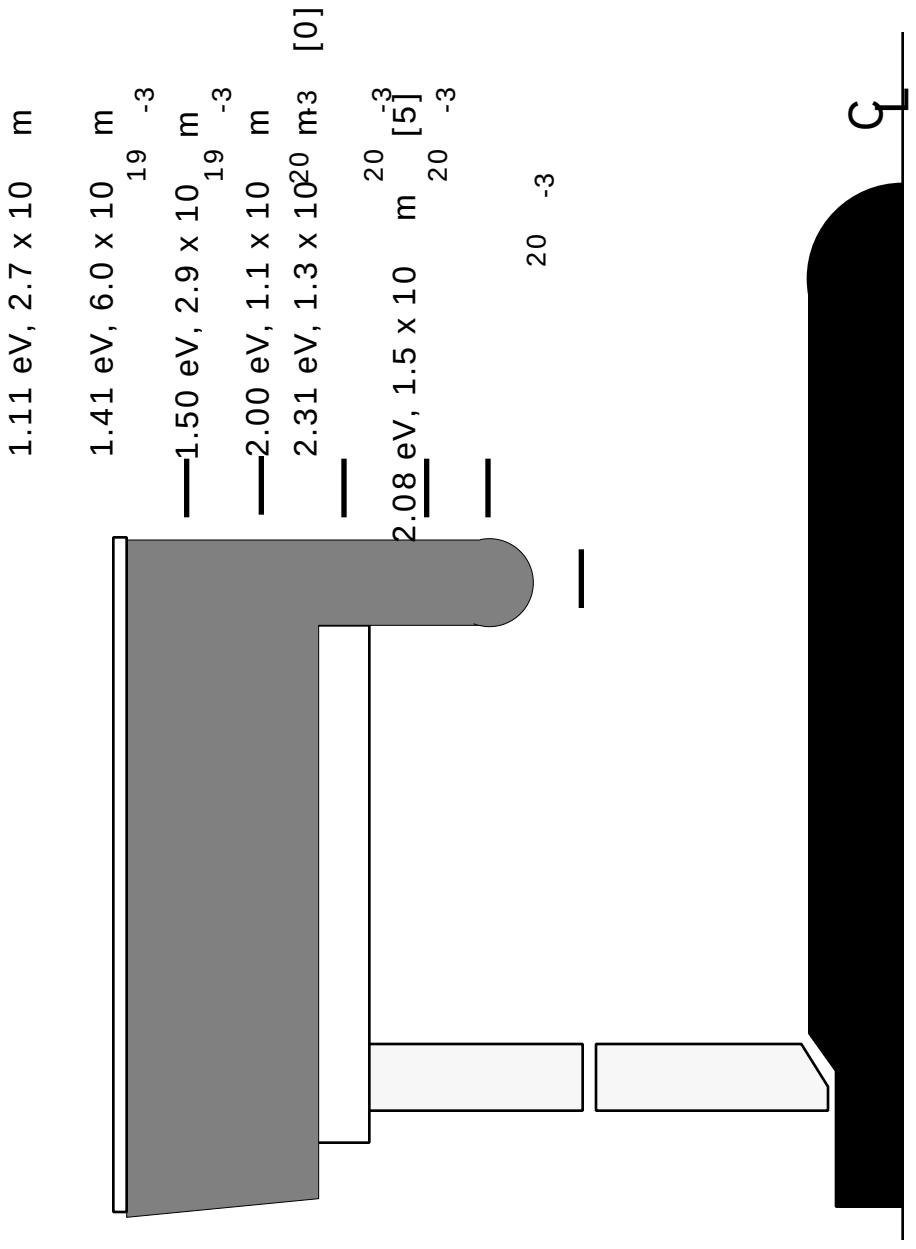

Figure III.18: Electron Temperature and Ion Number Density Profile (8 kA-4 g/s).

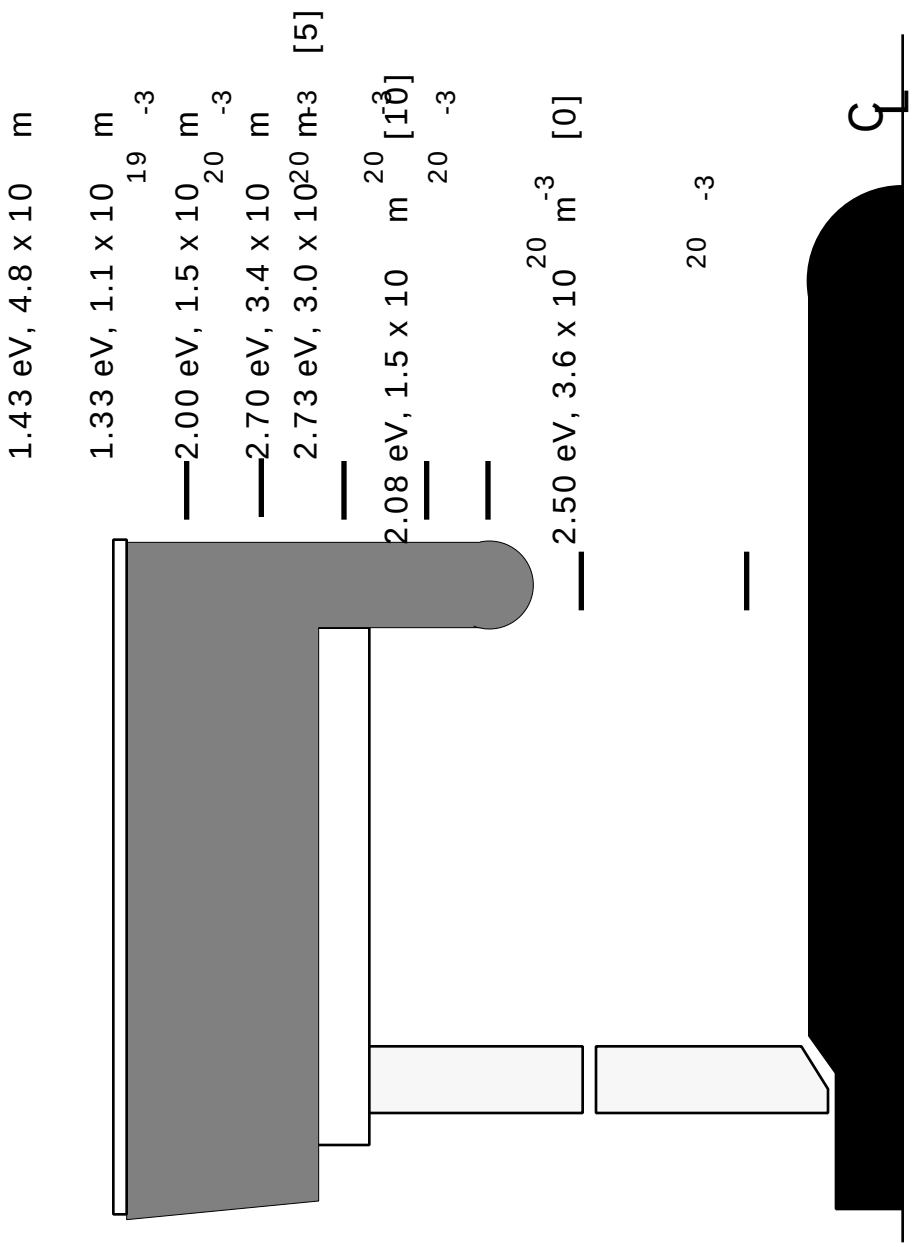

Figure III.19: Electron Temperature and Ion Number Density Profile (16 kA-16 g/s).

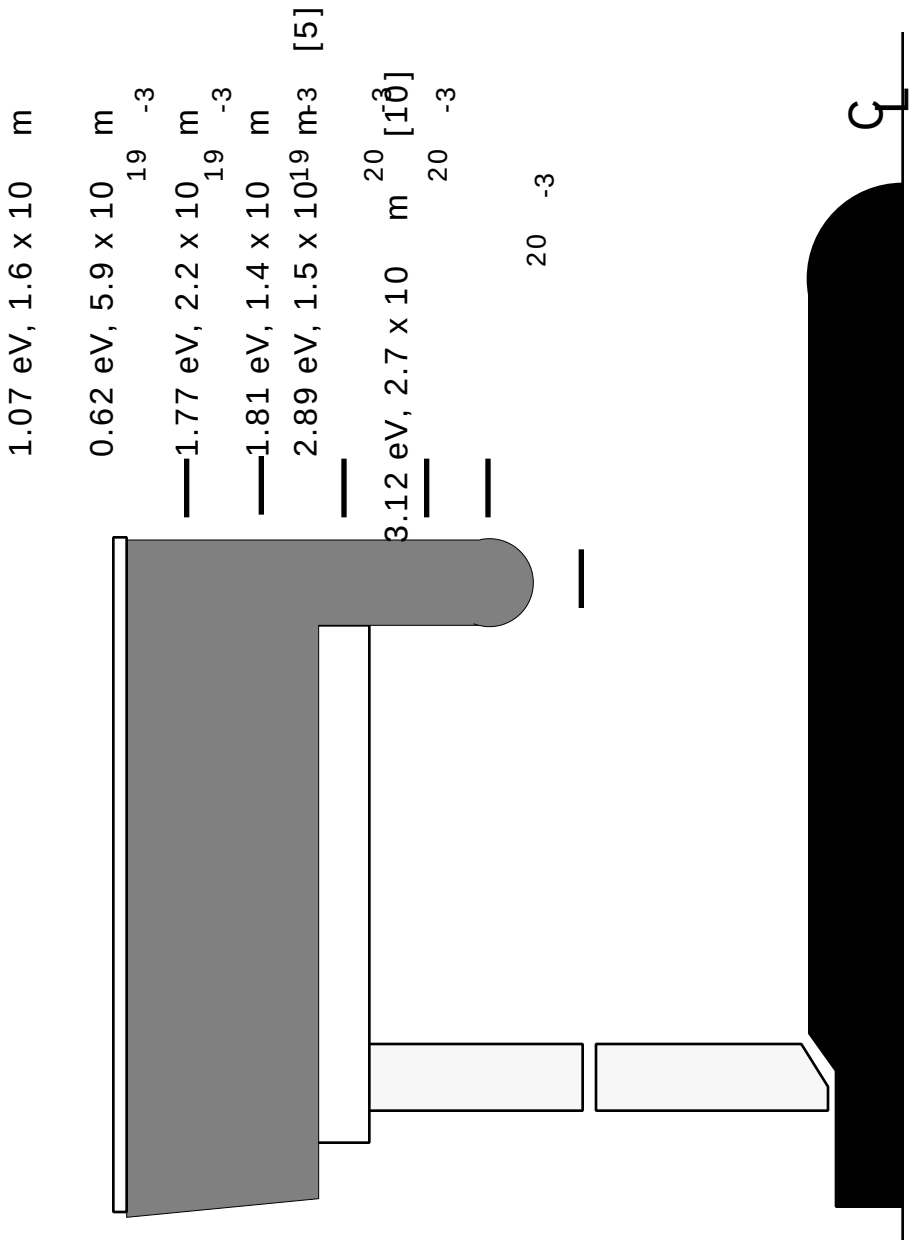

Figure III.20: Electron Temperature and Ion Number Density Profile (16 kA-4 g/s).

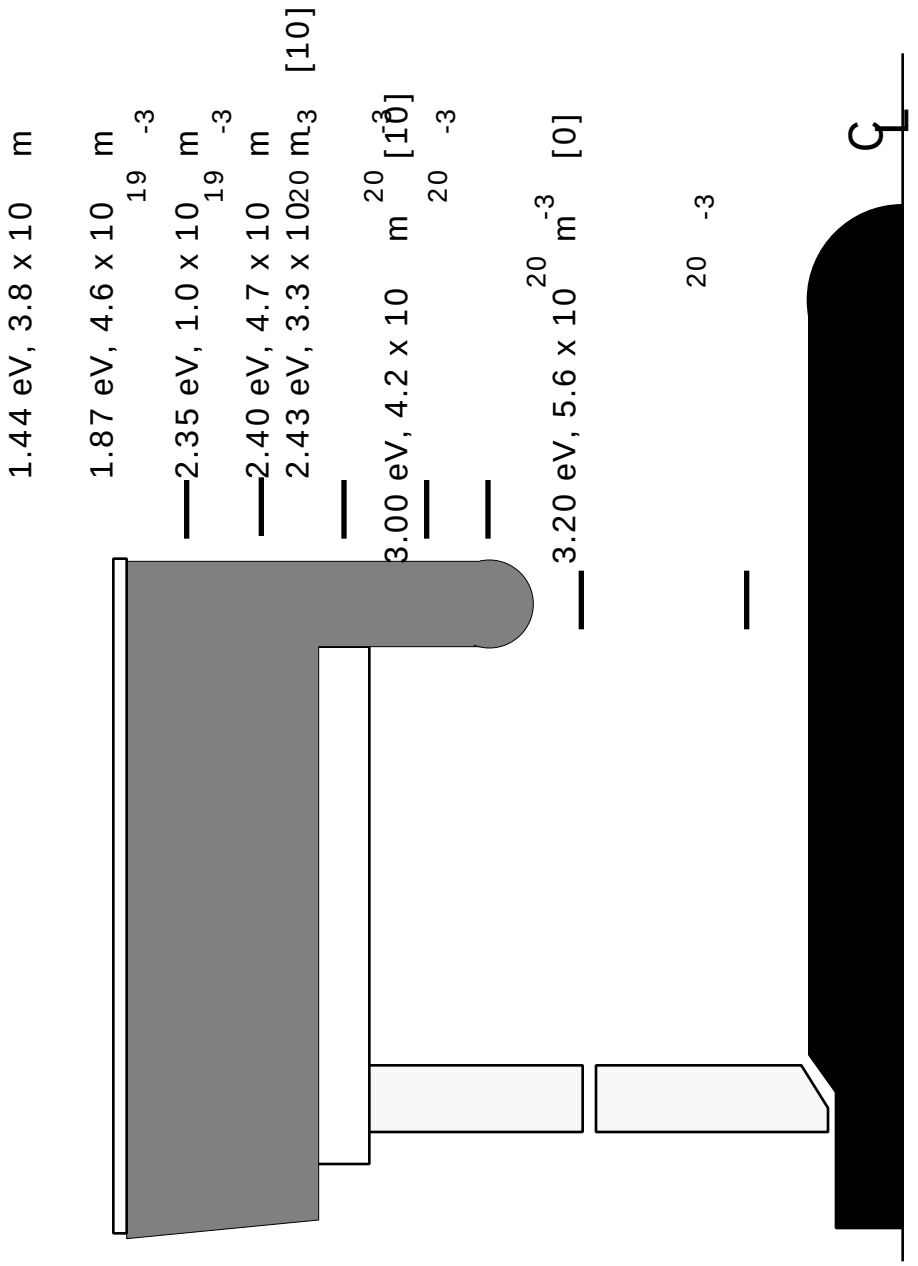

Figure III.21: Electron Temperature and Ion Number Density Profile (24 kA-16 g/s).

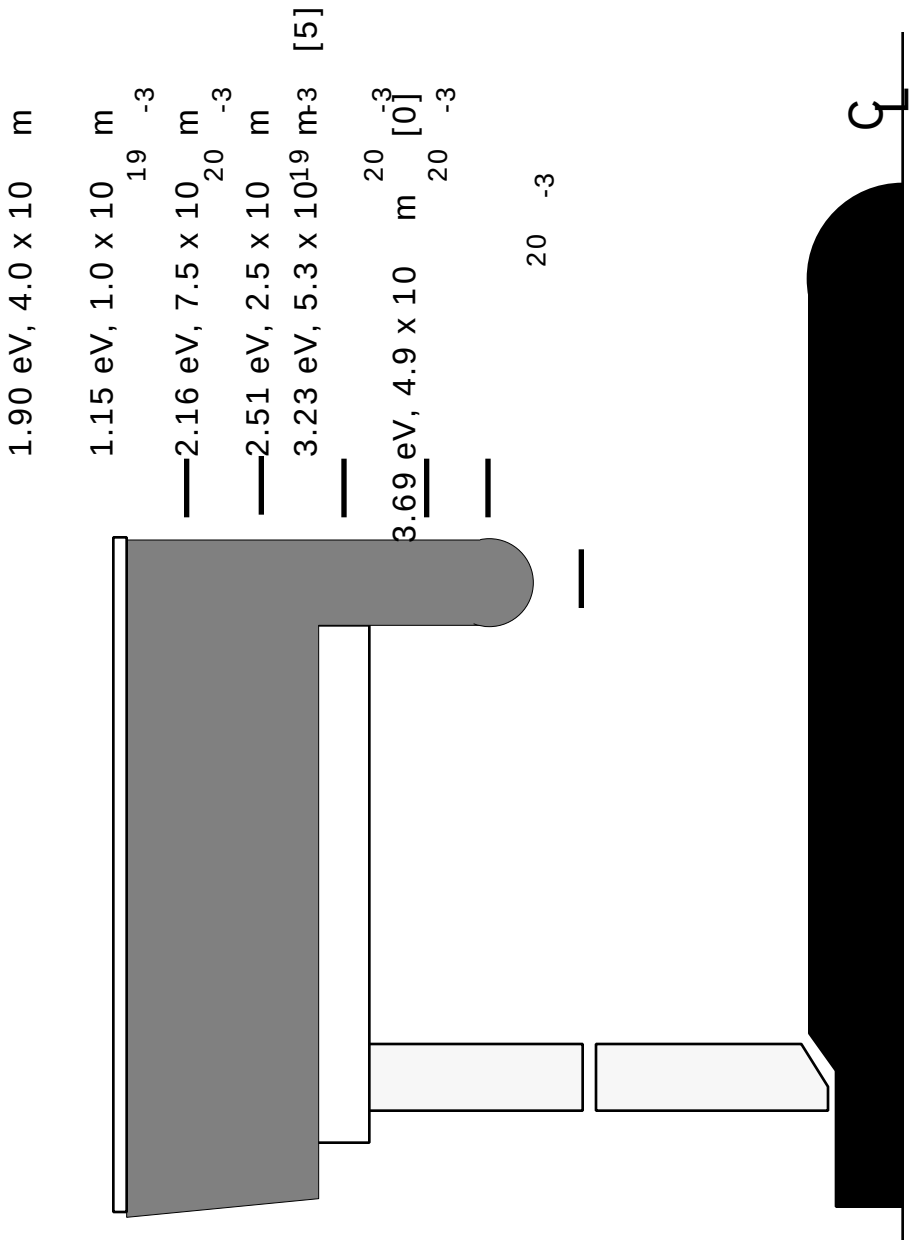

Figure III.22: Electron Temperature and Ion Number Density Profile (24 kA-4 g/s).

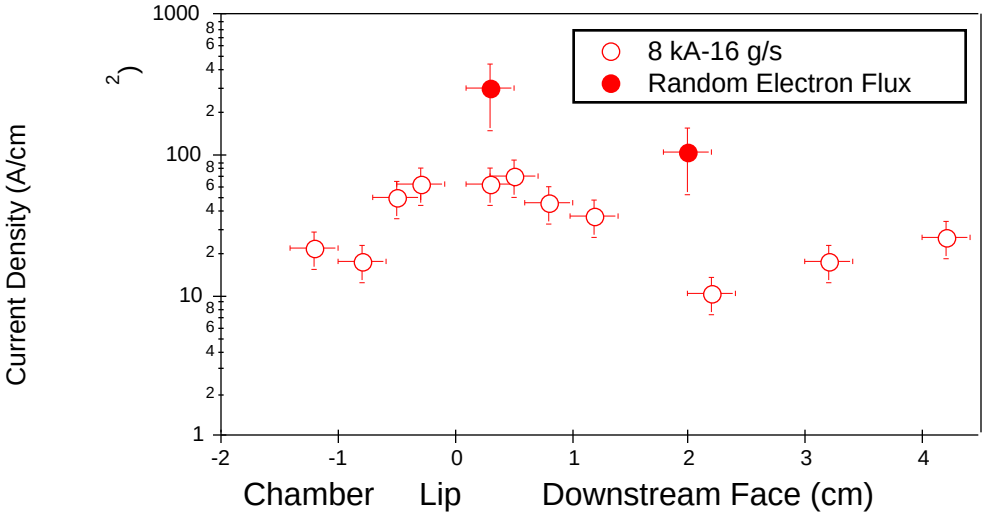

Figure III.23: Anode Current Density Distribution with Estimated Random Electron Current (8 kA-16 g/s).

Figures III.23 and III.24 show comparisons between the current density due to the random electron flux to the anode, estimated from triple probe data (assuming n_i=n_e), with current density measurements made by the magnetic induction probe survey for the conditions 8 kA-16 g/s and 24 kA-4 g/s. As is evident from the figures, the electron flux required by the thruster for current conduction is easily supplied by the ambient plasma. In all cases studied, the random electron flux at any site is drastically larger than the current density measured by the magnetic induction probe survey. According to Langmuir probe theory, this should result in a negative (electron repelling) anode fall. However, all floating probe and heat flux measurements have indicated that the anode fall is positive at all conditions studied. In fact, an electron repelling anode fall has never been measured in any MPD thruster at Princeton. Caution must be used in assuming that the plasma conditions that exist several millimeters from the anode surface are the same as those at the sheath-plasma interface (pre-sheath). Various models have estimated the thickness of a boundary layer at the anode to be on the order of 10 mm[25, 26] and have calculated electron number densities at the base of the

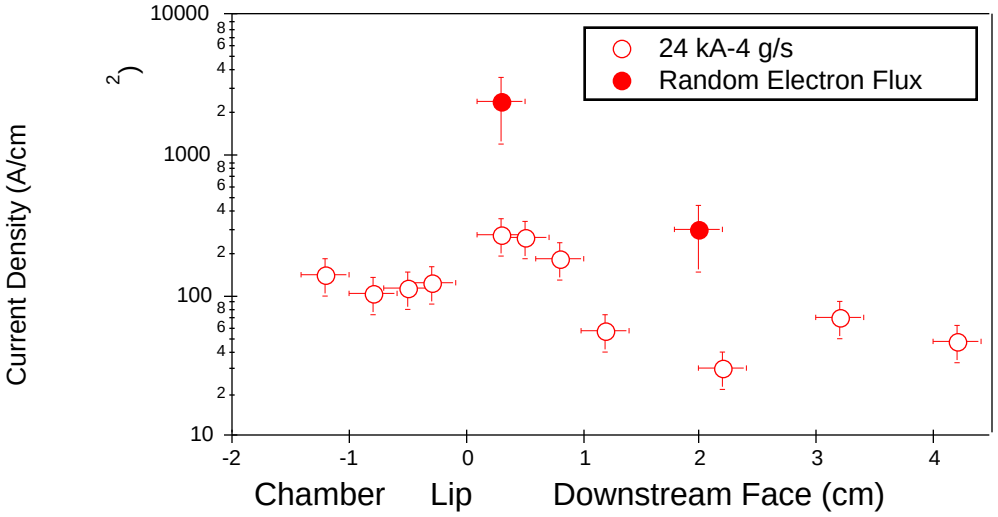

Figure III.24: Anode Current Density Distribution with Estimated Random Electron Current (24 kA-4 g/s).

boundary layer that are quite different from those in the ambient plasma. Studies have shown that although the electron and ion number densities vary considerably throughout the boundary layer, the electron temperature remains constant[26, 65].

The discrepancy between measured current density and estimated electron random flux current density may also be explained by the highly non-isotropic nature of current conduction in a magnetized plasma. The presence of a strong magnetic field tends to inhibit the flow of current carrying electrons across field lines, making the analysis of anode current conduction on the basis of the unrestricted random flux of electrons to a surface inappropriate. The observation that magnetization of the electrons may be a significant feature of anode current conduction is qualitatively justified by the fact that the Hall parameter at the anode has been calculated from probe data to be between 3 and 10 (cf. Appendix A).

III.5 Plasma Potential Measurements

The anode fall is frequently estimated by measuring the potential of the adjacent plasma with respect to the anode through the use of floating Langmuir probes. Because of the size of the probe, however, most of these measurements are made ∼1 mm or more from the anode surface. The anode fall has therefore been assumed to coincide with the measured difference in potential between the anode and the plasma a few millimeters away. Comparison of anode falls estimated from heat flux measurements with those measured with the Langmuir probe, allows for the determination as to whether the drop in potential over a span of a few millimeters near the anode corresponds to the potential energy that current carrying electrons deliver to the anode (i.e. anode fall). The "L" shaped floating probe described in Section II.3.4 was used to make the floating potential measurements.

Figures III.25 and III.26 show equipotential profiles (floating potentials) near the anode at a current of 8 kA for mass flow rates of 16 and 4 g/s, respectively. The small cross in each figure represents the uncertainty of the probe location (±1 mm). The survey from which these results are obtained is similar to that used to generate current contours in Section III.3. As is apparent from the figure, the electric fields near the anode surface are much larger than those in the bulk of the plasma. Separation of the equipotential profiles is greatest at the lower density portion of the discharge along the downstream anode face.

Figures III.27 and III.28 show equipotential profiles near the anode when the thruster is operating at 16 kA with mass flow rates of 16 and 4 g/s, respectively. For this discharge current, the potential gradients are markedly larger at 4 g/s than at 16 g/s. This implies that at some thruster operating conditions, substantial energy dissipation takes place near the anode as a result of the highly resistive plasma in this region.

Figures III.29 and III.30 show equipotential profiles at 16 and 4 g/s with the thruster operating at 24 kA, respectively. The floating potential near the anode becomes noticeably larger with increasing thruster current. At a current of 24 kA, electric fields in the quasi-neutral portion of the plasma near the anode (i.e. outside of the anode sheath) reach values in excess of 7000 V/m. Models that rely on classical transport mecha-

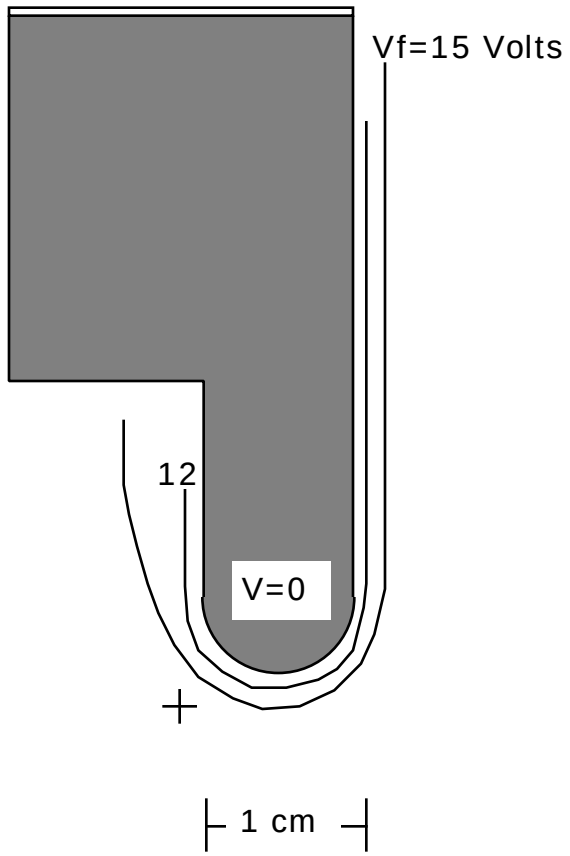

Figure III.25: Floating Potential Profiles (8 kA-16 g/s).

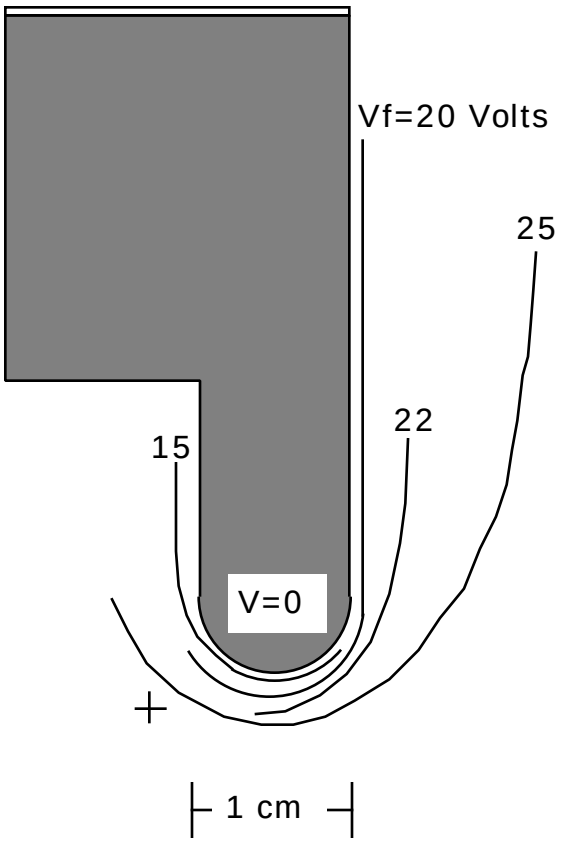

Figure III.26: Floating Potential Profiles (8 kA-4 g/s).

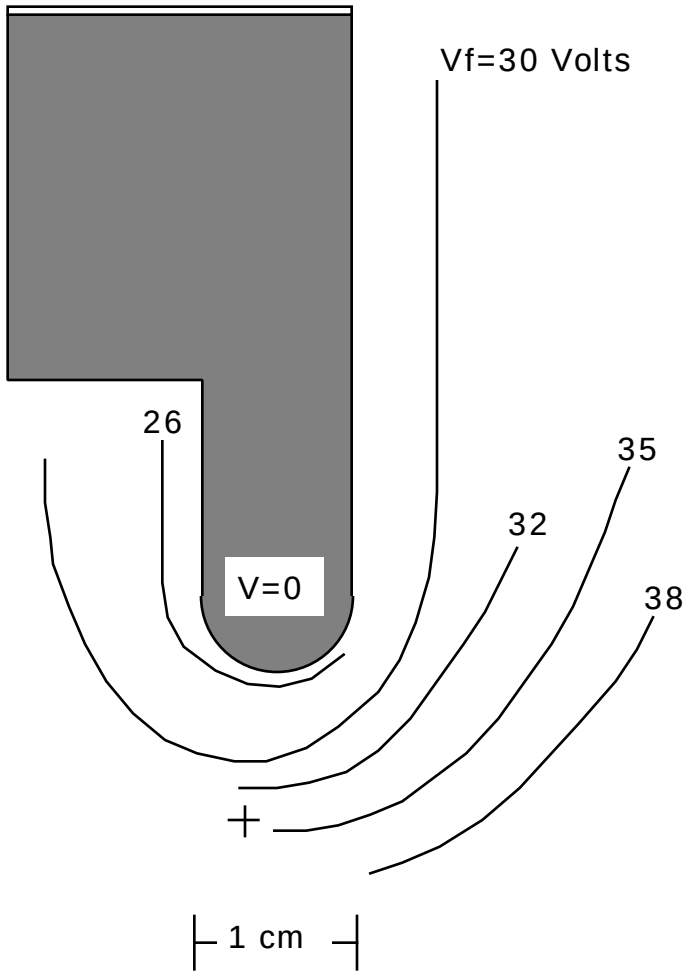

Figure III.27: Floating Potential Profiles (16 kA-16 g/s).

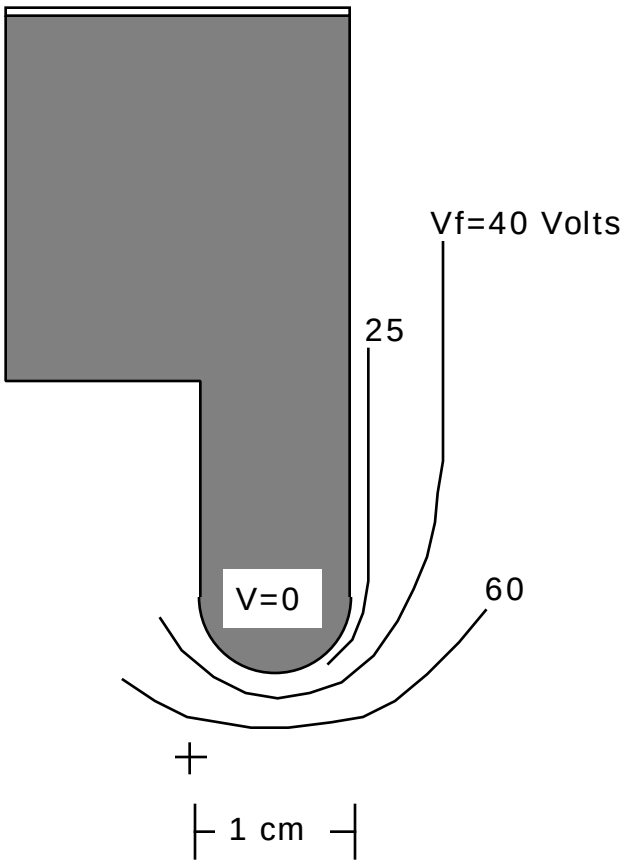

Figure III.28: Floating Potential Profiles (16 kA-4 g/s).

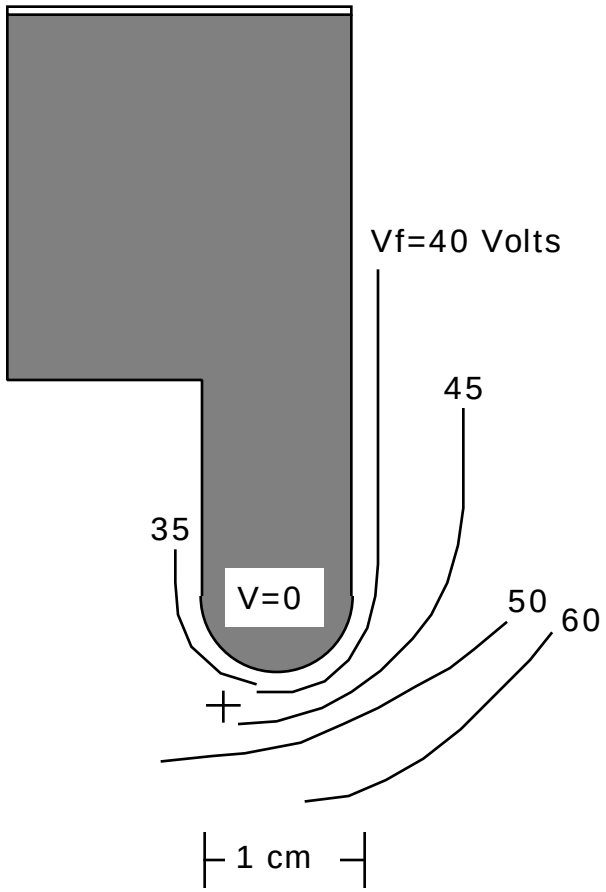

Figure III.29: Floating Potential Profiles (24 kA-16 g/s)).

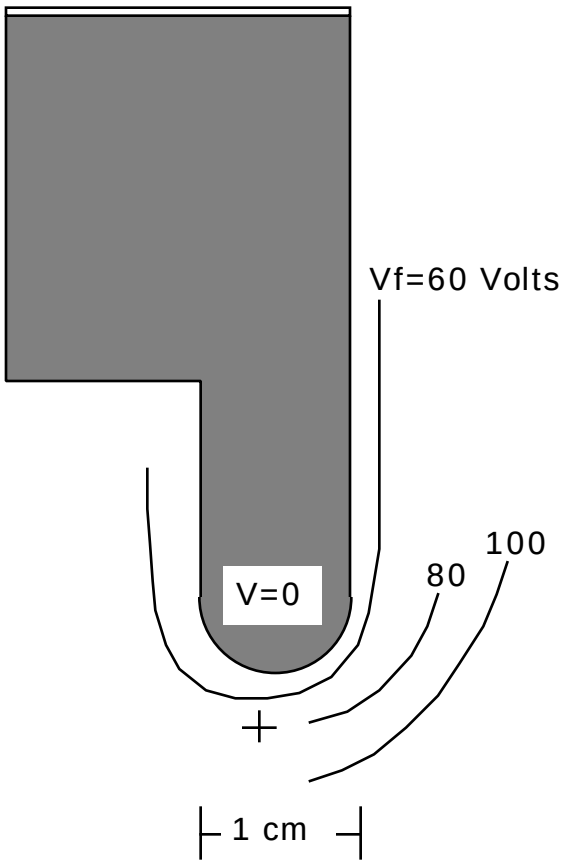

Figure III.30: Floating Potential Profiles (24 kA-4 g/s).

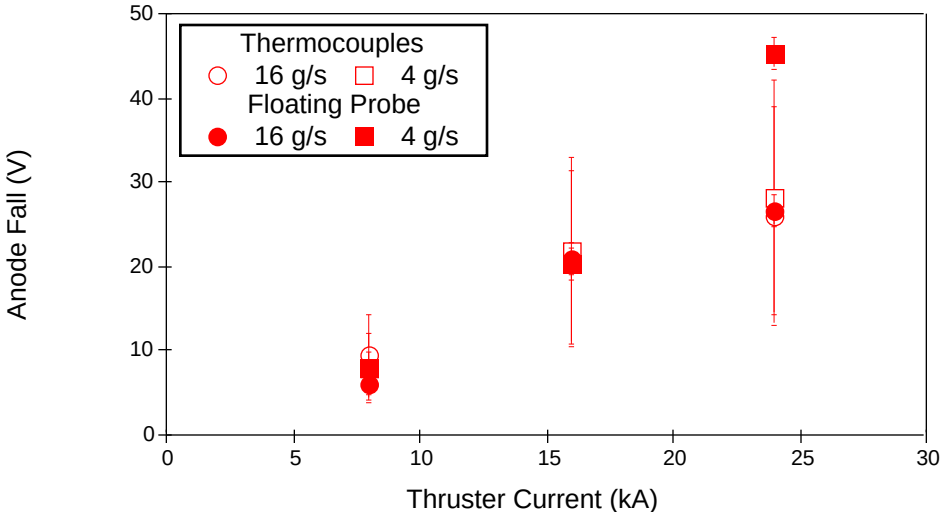

Figure III.31: Anode Fall vs. Thruster Current.

nisms have not been successful in predicting the large voltages seen in the quasi-neutral portion of the plasma. Calculations presented in Appendix A show that the electrical resistivity of the plasma near the anode is between three and thirty times larger than classically predicted values.

In the following section, triple probe measurements of the electron temperature are used to convert measured floating potential to the actual plasma potential. The difference in potential between the anode and adjacent plasma, as determined through floating probe measurements, will be compared to the anode fall inferred from heat flux measurements.

III.6 Determination of the Anode Fall

By measuring the anode heat flux, current densities, and electron temperature, through use of Equation I.3 (neglecting ($\dot{q}_c$) and ($\dot{q}_r$)) we are able to obtain an estimate of the anode fall. By neglecting radiation and convection, we obtain a lower bound for the power that is deposited to the anode. However, several studies have shown

that convection contributes negligibly to anode power deposition of high power MPD thrusters[25, 17, 26]. Recent estimates of the convective heat transfer rate to the anode of high powered MPD thrusters (cf. Appendix C) further corroborate those findings. Although often ignored, the contribution to anode heating from radiation emanating from the plasma has only recently been treated rigorously. Randolph[27] applied his non-equilibrium multi-step ionization model to estimate the power of radiation emitted from the plasma. The results of his work show that for argon propellant, the radiative heat flux that is absorbed by the anode is at most a few watts per square centimeter. This value is not expected to change significantly with propellant.

Figure III.31 shows the anode fall, obtained from both heat flux and floating probe measurements, as a function of thruster current for propellant mass flow rates of 16 and 4 g/s. The values from the heat flux measurements are obtained by weighting the measured heat flux for each individual thermocouple site by its appropriate fraction of total current. Floating probe measurements of the anode fall are obtained by placing the probe electrode to within 0.1 cm of the anode surface and using local triple probe measurements of the electron temperature to the convert probe potential to the actual potential of the plasma. Probe measurements are weighted in the same manner as the heat flux data. With the exception of the data collected at 24 kA-4 g/s, there is excellent agreement between both methods of measuring the anode fall. Comparing results of both techniques, again with the exception of floating probe data at 24 kA-4 g/s, we see that the anode fall increases monotonically with current and is independent of mass flow rate. The reason for the discrepancy at 24kA-4g/s has not been fully established. Given the agreement between floating probe and heat flux fall estimates at all other conditions, one may be tempted to hold the probe data suspect. However, no known flow or magnetic field effects can account for such a drastic error ($\sim$20 V) in floating potential measurements. Although the reason for this discrepancy remains unknown, two possible explanations for this difference that are discussed in the following paragraphs are anode ablation and the fact that part of the voltage drop measured by the floating probe may be due to the resistivity of the plasma.

It has been suggested that anode ablation at high $J^2/\dot{m}$ ($>$100 kA^2-s/g) may result in artificially low measurements of the anode heat flux[17]. Given the short duration

of the discharge, the total energy deposited to the anode from the heat flux predicted by floating probe (40 V anode fall), current density, and electron temperature measurements at this condition, although larger than that measured with the thermocouples, is insufficient to cause significant anode evaporation. The anode surface is not expected to exceed a temperature of 130°C[17]. However, inspection of the anode surface reveals regions along the anode lip were local melting has occurred. This is presumably due to spot-mode current attachment at the anode which has been observed once a threshold value of $J^2/\dot{m}$ for stable thruster operation is exceeded[28, 31].

Another explanation for the discrepancy may be that the drop in voltage between the anode and the plasma 1 mm away does not correspond to the anode fall for all operating conditions. If the electron experiences inelastic collisions between the floating probe and the anode, the kinetic energy that the electron delivers to the anode surface will not equal the difference in potential between the plasma at the floating probe site and the anode. Additionally, the presence of anomalous effects illustrated in Appendix A imply that significant scattering of the electrons due to wave-particle interactions takes place near the anode. Thus, part of the kinetic energy that the current carrying electrons receive from the ambient electric fields may be absorbed in enhancing local plasma instabilities.

Figure III.32 shows the anode power fraction, obtained from both heat flux and floating probe measurements, as a function of thruster power. Each data point on this plot was obtained by summing the product of the estimated heat flux and the appropriate anode surface area of the measurement site. The figure shows that the anode power fraction depends on thruster power, current, and mass flow rate. The exhibited behavior is due both to the variation of the voltage drop through the bulk of the plasma (resistivity and back emf) as well as to the changing anode fall. At power levels below 1 megawatt, 28 to 44% of the total input power is deposited into the anode. As power is further increased, anode power fraction decreases with increasing thruster power. At 6 MW, the anode power fraction predicted by heat flux and floating probe measurements is down to approximately 10 and 20%, respectively. These trends are consistent with those observed by Saber[17]. Figure III.33 shows the same data plotted against $J^2/\dot{m}$. As the figure shows, above a $J^2/\dot{m}$ of approximately 20 kA^2-s/g, the

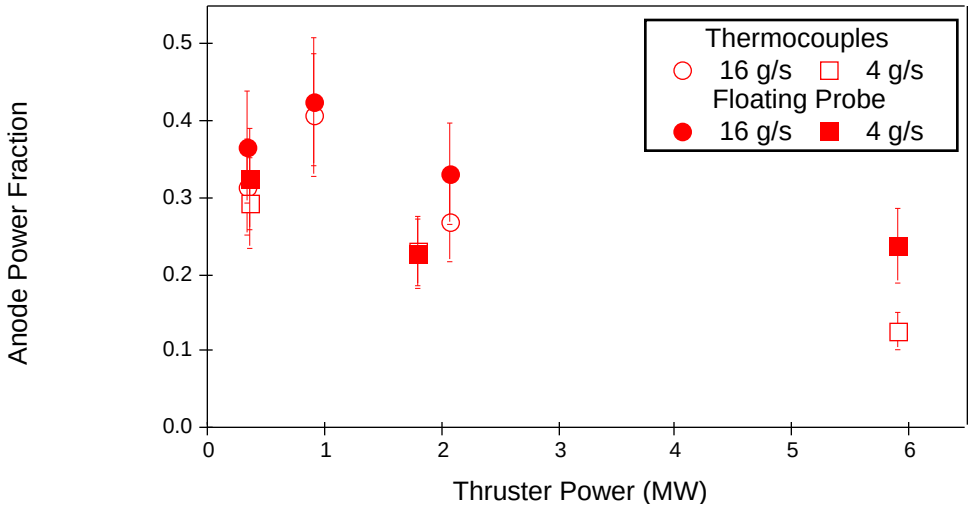

Figure III.32: Anode Power Fraction vs. Thruster Power.

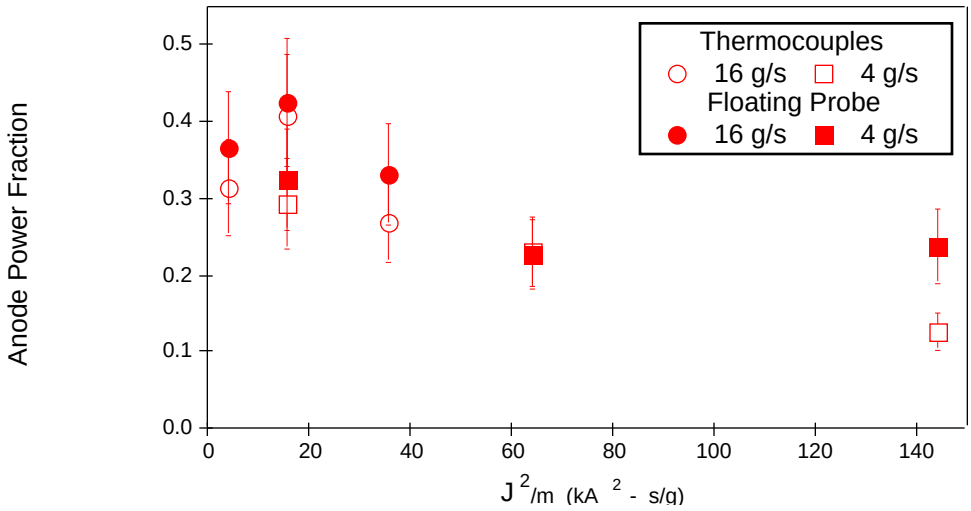

Figure III.33: Anode Power Fraction vs. $J^2/\dot{m}$.

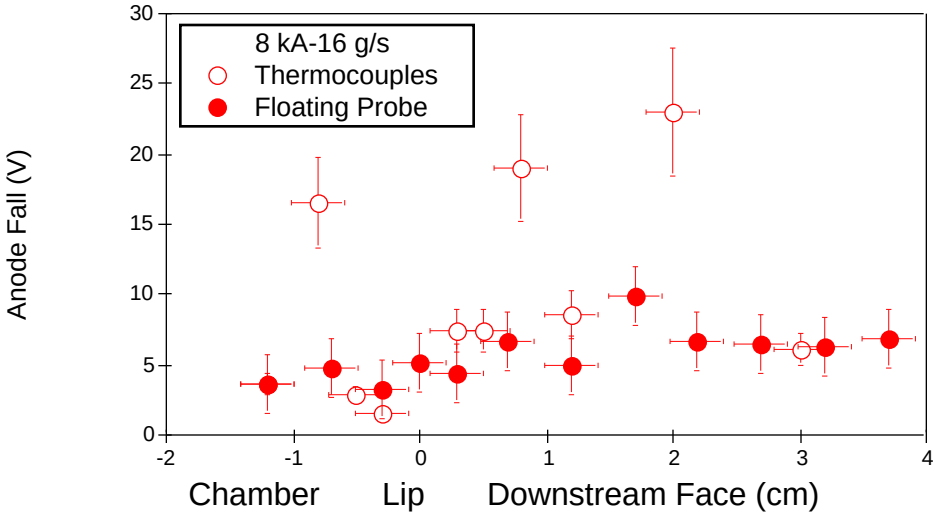

Figure III.34: Anode Fall Profile (8 kA-16 g/s).

fraction of power deposited to the anode decreases monotonically with increasing $J^2/\dot{m}$.

Figures III.34-III.39 show the variation of the anode fall, obtained from floating probe and heat flux measurements, along the anode surface. As the figures show, the anode falls estimated from either method usually fall within the respective error bars. This tendency, however, is not displayed in Figure III.39 (24 kA-4 g/s) which shows that the anode falls measured with the floating probe are significantly larger than those obtained through heat flux measurements (cf. Figure III.31) over most of the anode surface; an exception being along the downstream face. Again, the discrepancy between the thermocouple data and floating probe data collected along the anode face may be due to the anomalously resistive plasma that is present near the anode. The figures also show a tendency for the anode fall to be lowest at the lip region where the current density is highest, a behavior which has been observed in other anode studies as well[17, 25]. This observation is the impetus for experiments described in the next chapter in which current attachment is restricted to only the lip of the anode.

Figures III.40-III.42 show anode falls, determined through floating probe measure-

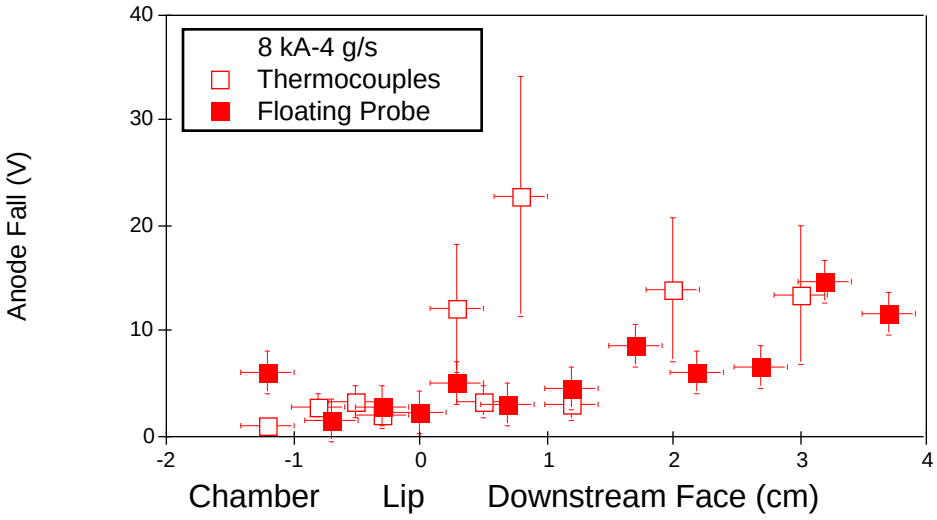

Figure III.35: Anode Fall Profile (8 kA-4 g/s).

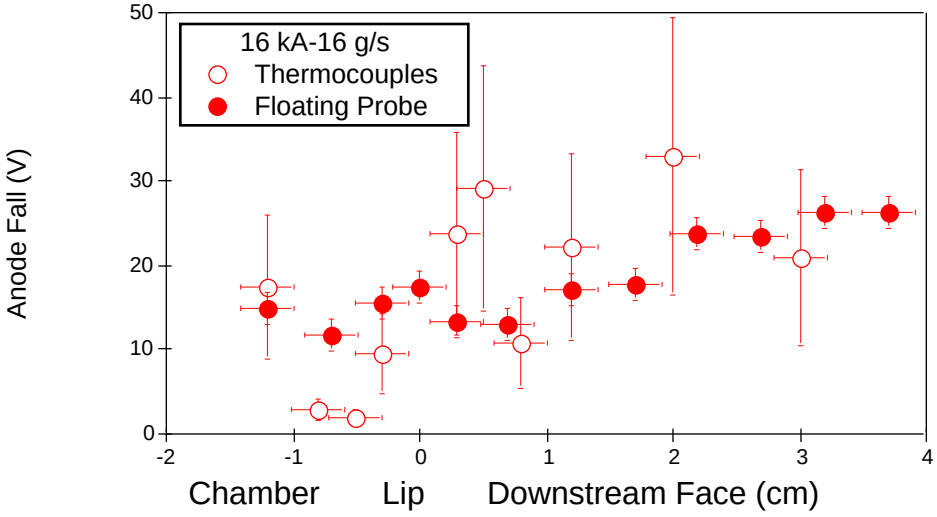

Figure III.36: Anode Fall Profile (16 kA-16 g/s).

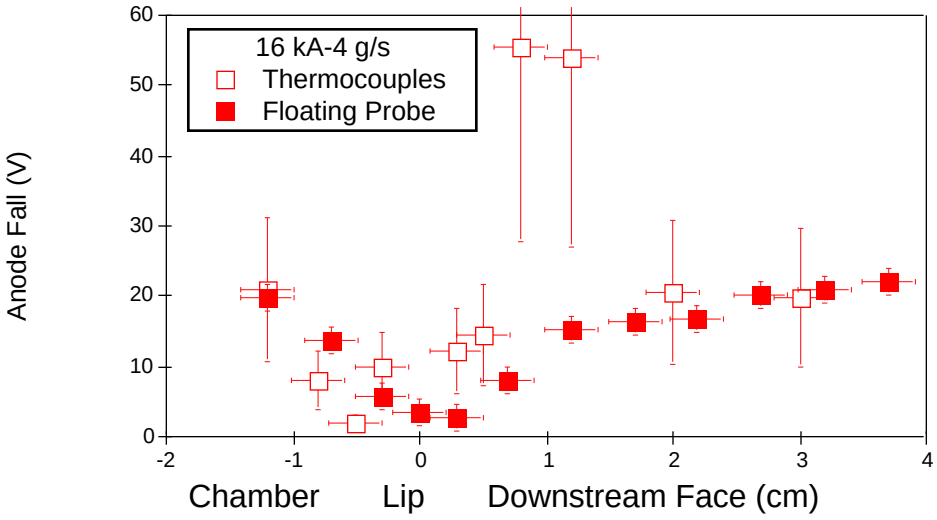

Figure III.37: Anode Fall Profile (16 kA-4 g/s).

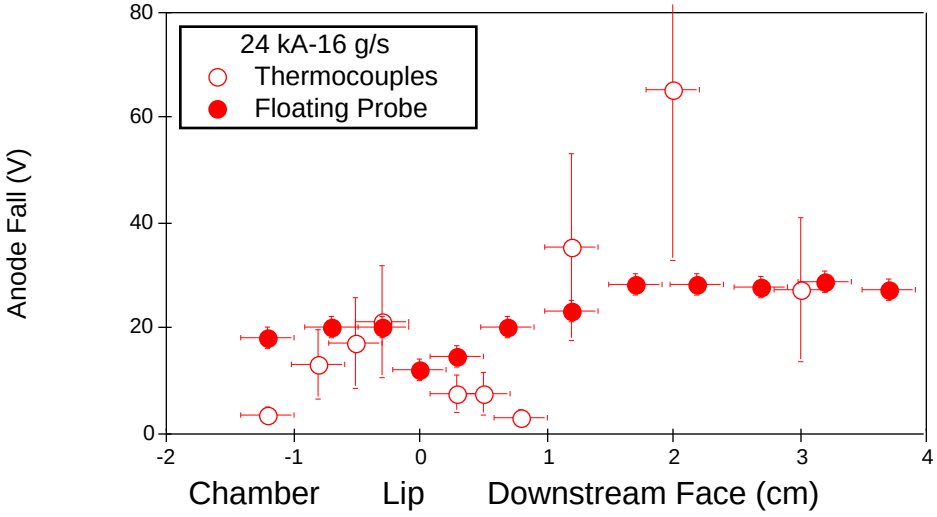

Figure III.38: Anode Fall Profile (24 kA-16 g/s).

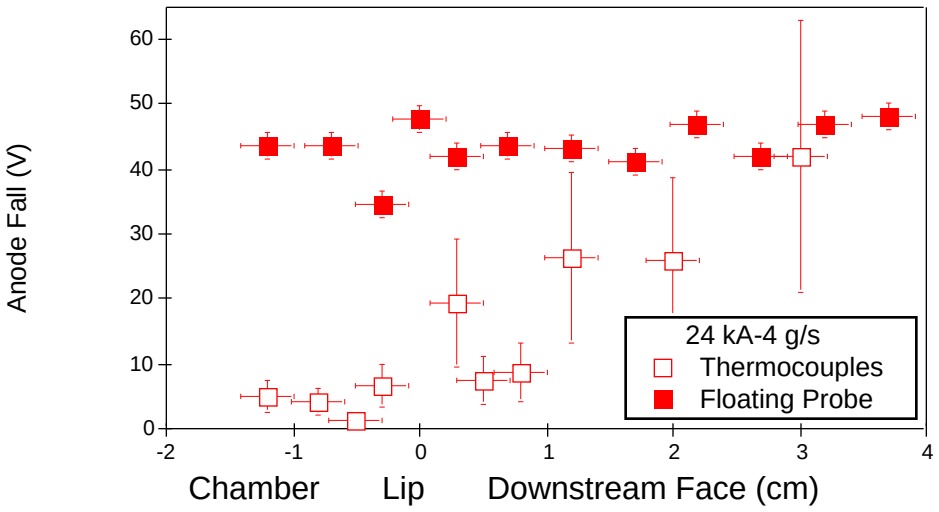

Figure III.39: Anode Fall Profile (24 kA-4 g/s).

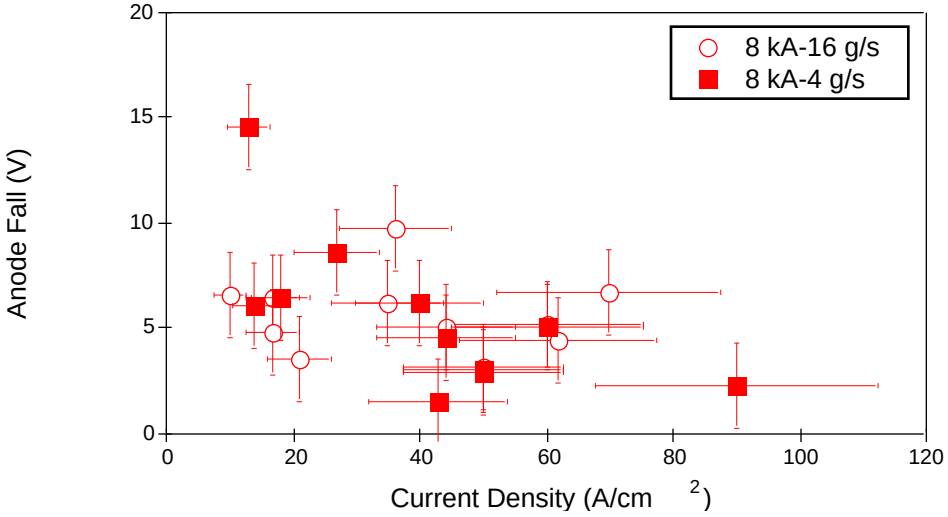

Figure III.40: Anode Fall vs. Current Density (8 kA).

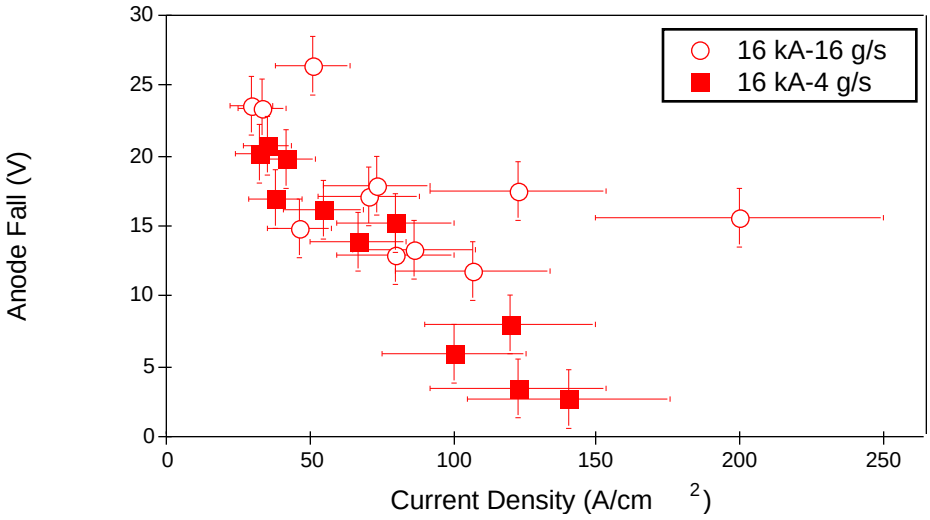

Figure III.41: Anode Fall vs. Current Density (16 kA).

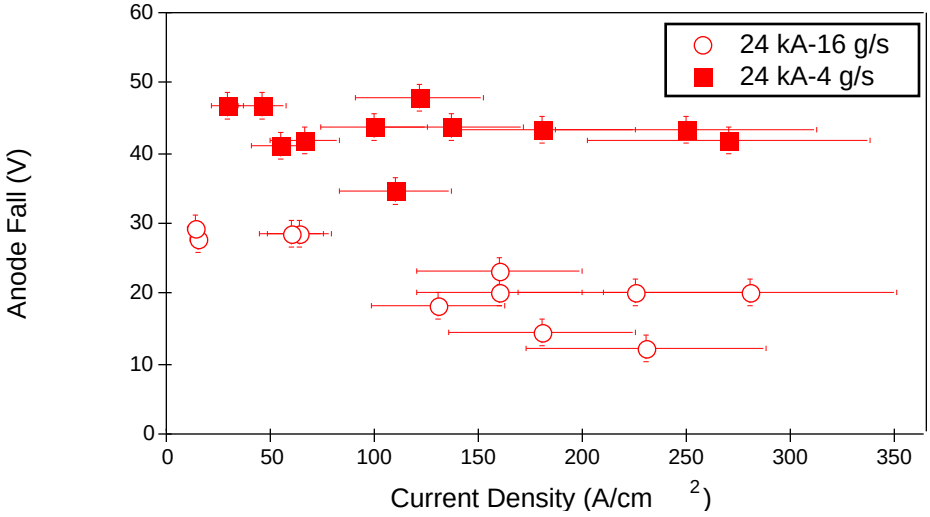

Figure III.42: Anode Fall vs. Current Density (24 kA).

ments, as a function of current density for the operating conditions studied in this experiment. The inverse dependence of the anode fall with current density displayed in these figures has been noted by other anode researchers as well[17, 25]. To explain this observation, Oberth[25] evoked theories that were developed by Bez and Höcker[63, 64] in their studies of anode phenomena in atmospheric pressure carbon arcs in air. According to these authors, the primary purpose of the anode fall is to produce ions which, through diffusion away from the anode, replenish those lost at the cathode.

One process which the authors claim produces ions in the anode fall is "Field Ionization." In this mechanism, ions in the anode fall region are generated from impact ionization by free falling electrons. Thus, in order for the colliding electrons to have sufficient energy to ionize neutrals, the anode fall must exceed the ionization potential of the ambient gas. The anode falls predicted by this model compare favorably with experimental data for temperatures below 9000 °K. Above this temperature, however, this model fails to reproduce experimental results.

At large electron temperatures, Bez and Höcker suggest that ion production in the anode fall is dominated by a mechanism called "Thermal Ionization" whereby electrons undergo several elastic collisions within the anode fall and become thermalized. A sufficient number of high energy electrons are produced in this thermalization process to insure that the necessary rate of ionizing collisions is maintained. This model predicts that the anode fall decreases with increasing electron temperature. Since joule heating of the plasma is a quadratic function of current density, Oberth argues that the transition from "Field" to "Thermal" ionization modes, which is usually associated with a threshold electron temperature, may also be related to a critical current density. He postulates that the inverse dependence of the anode fall with current density may be a result of the transition between anode fall modes.

In general, however, the theories of Bez and Hocker predict trends that are counter to what is observed experimentally in MPD thrusters. Although their models produce the observed trend that the anode fall decreases with increasing current density, they also predict that the anode fall decreases with increasing electron temperature, which is contrary to experimental results (cf. Section III.4). Careful observation of the figures will show, however, that anode current density is not the only scaling parameter. Although

the minimum anode fall for each operating condition is usually measured at the location of maximum current density, the anode fall for a given current density yet depends on thruster operating condition.

In summary, this chapter has shown anode power deposition to be a complicated function of various plasma parameters as well as thruster operating conditions. The results presented in this chapter corroborate those obtained in other studies with similar apparatus[17] wherein the most intense heating rates and highest current densities are seen at the lip. Good agreement is seen between heat flux and floating probe estimates of the anode fall except at high $J^2/\dot{m}$. Furthermore, electron accelerating anode falls are always observed although the thermal electron flux is consistently larger than the local current density. Thus the magnetization of electrons is an important feature of the current conduction at the anode of MPD thrusters. This may be the primary reason why anode models which have been successful in high pressure arcs are not able to predict trends observed in MPD thrusters. And finally, the anode fall is seen to vary inversely with local current density. This behavior, which has been documented in other studies with MPD thrusters, is the motivation for the modifications made to the anode for experiments described in the next chapter.

Chapter IV

Determination of Anode Fall Scaling Parameters

IV.1 Introduction

The results of Chapter 3 as well as those from previous experiments [17, 18, 25] show that a correlation between current density and the anode fall may exist. In experiments in which the anode current conduction area was restricted to a 2 mm band along the lip by covering the remaining surface with mylar tape, the thruster operated with decreased anode falls, lower thruster voltages, and in some cases, reduced anode power fractions[18]. The impetus for that experiment was the observation that the anode fall was smallest at the regions along the anode of largest current density; as noted previously. To investigate further the role of current density on the anode fall, 85% of the surface area of the anode used in the experiments detailed in Chapter 3 was insulated with a coating of alumina. Most of the experiments performed on the standard thruster were repeated for the modified thruster. In addition, an extensive series of anode fall measurements with argon and helium propellants were also made, the results of which show that a strong correlation exists between the anode fall and the electron Hall parameter.

IV.2 Experiments with a Reduced Area Anode

To investigate what effect current density may have on anode power deposition, the hollowed "benchmark" quasi-steady MPD thruster anode that was used in the experiments of the previous chapter was further modified by plasma-spraying a 0.013 cm (5 mils) thick layer of alumina on over 85% of its outer surface (cf. Figure IV.1). Alumina insulation was selected on the basis of its resistance against ablation. By forcing the current to the lip the local anode current density was increased by at least a factor of four.

Spatially resolved anode heat flux measurements were made, in accordance with the description of Chapter 2, by embedding five thermocouples to the inner surface of the hollowed thruster anode. Floating probe measurements were made as a second means of estimating the magnitude of the anode heat flux.

Figure IV.2 shows the voltage-current characteristics of both the "Standard" and "Modified" benchmark thrusters. As the figure shows, at any given thruster current the reduction of the anode current conduction area by a factor of six resulted in a change in the terminal voltage of less than 10%, suggesting that the mechanisms which govern anode power dissipation may not be sensitive to moderate increases in current density.

IV.2.1 Heat Flux Measurements

Figure IV.3 shows anode heat flux measurements from thermocouple data as a function of anode shell position for both the standard and modified benchmark thrusters. The abscissa of the figure represents a coordinate that linearly maps onto the surface of the anode, the extreme left (-2.0 cm) and right (+4.0 cm) ends of the plot approximately representing the extent of the upstream and downstream faces of the anode, respectively. The anode surface is exposed (uninsulated) within a coordinate range of ± 0.8 cm. As the figure shows the peak heat flux of the modified anode is over ten kilowatts per square centimeter. In comparison, the maximum heat flux measured at the same operating condition with the standard anode is 3500 W/cm^2. In contrast to the heat flux profile of the standard anode, little variation in the heat fluxes measured by the three thermocouples situated behind the lip of the modified anode is seen. This implies

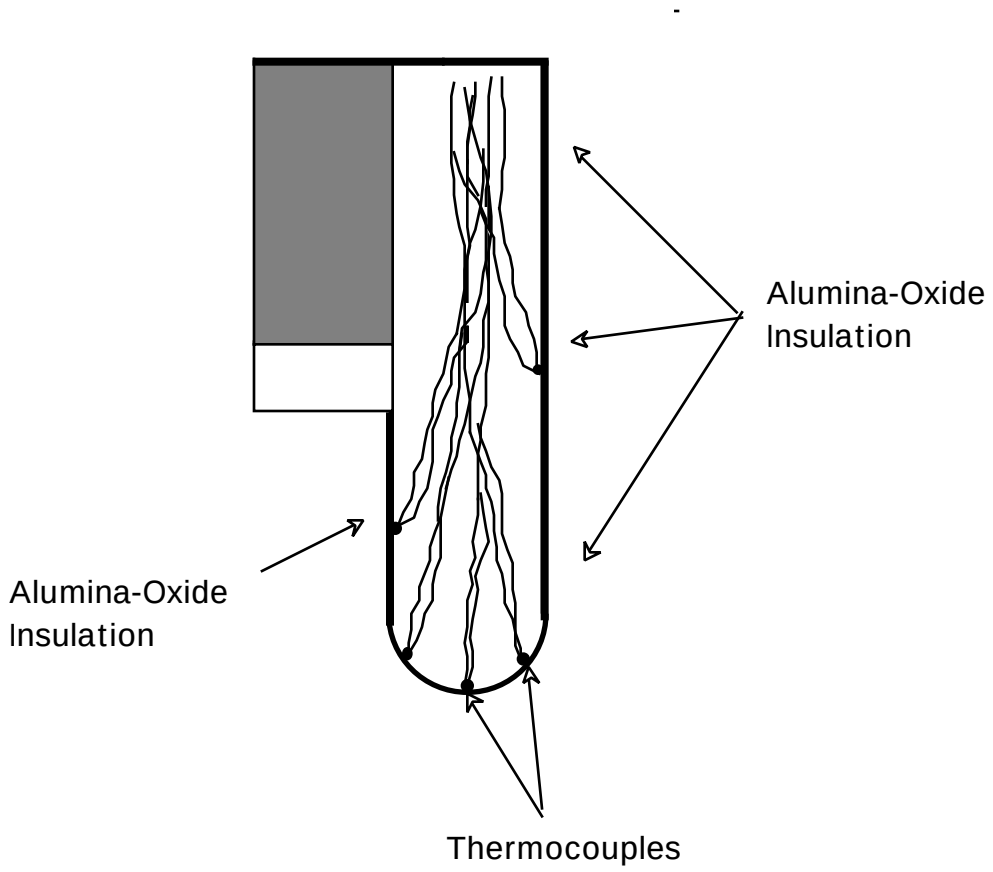

Figure IV.1: Alumina Coated Anode Shell.

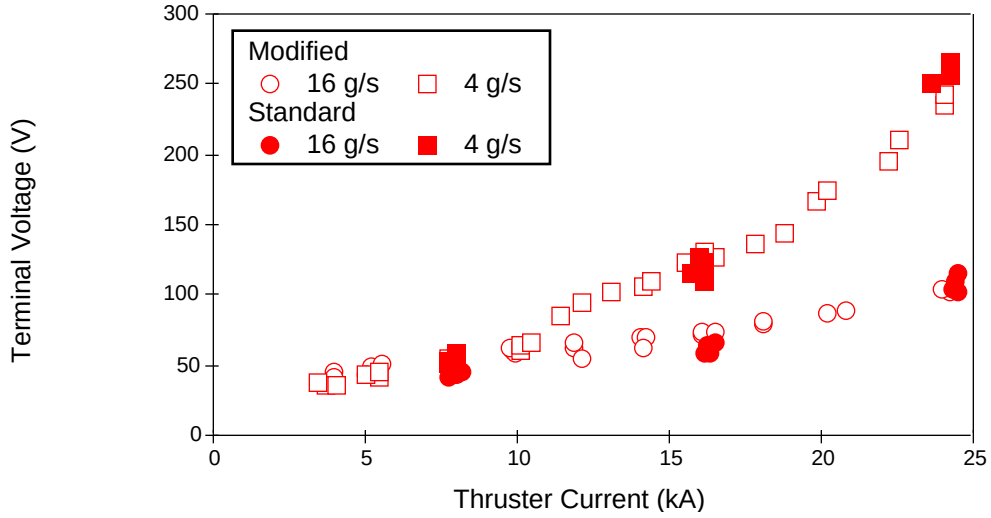

Figure IV.2: Thruster Voltage-Current Characteristics.

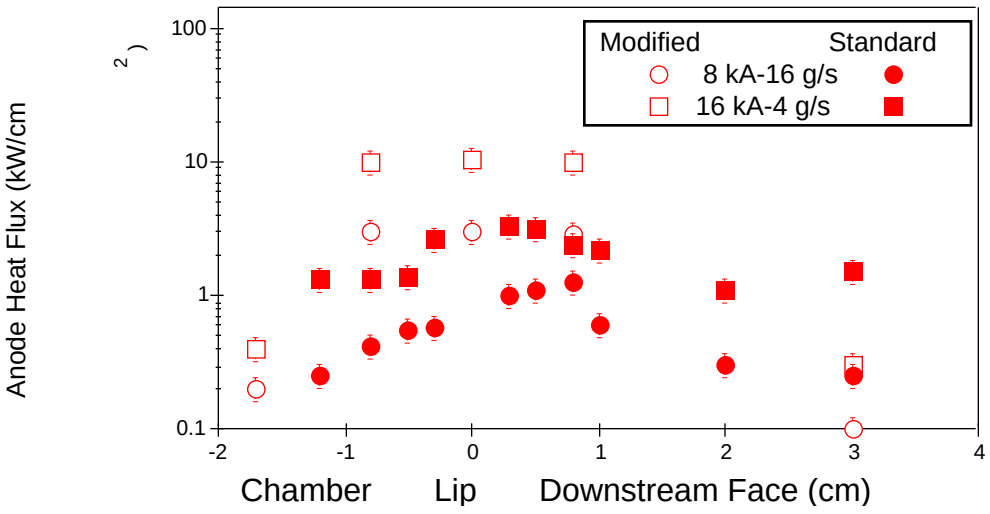

Figure IV.3: Anode Heat Flux Profile.

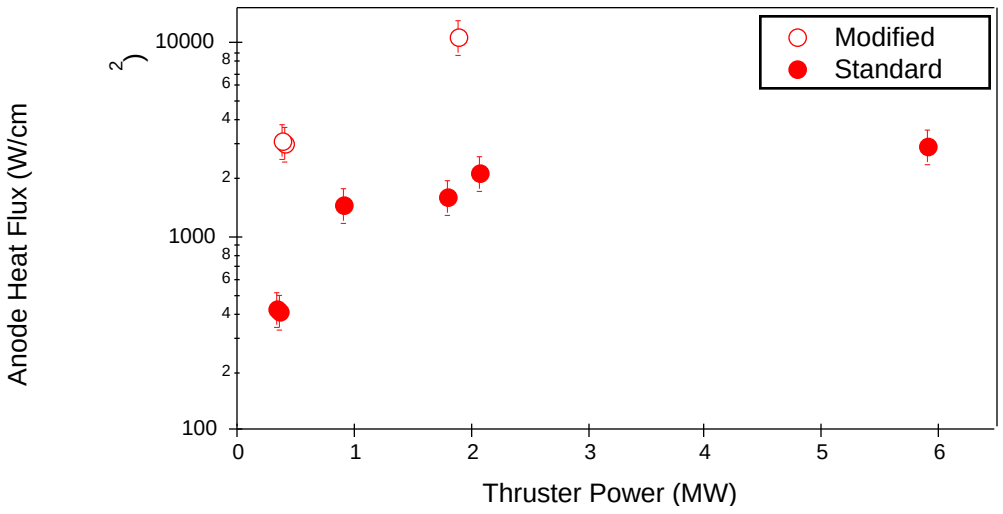

Figure IV.4: Average Anode Heat vs. Thruster Power.

that forcing the current to the lip results in a more uniform, albeit intense, current distribution. The minimal response of the thermocouples at the insulated sites support the assumptions that joule heating within the shell and transverse heat conduction along the shell are negligible, and can be neglected. Figure IV.4 shows the average anode heat flux (weighted by current density (cf. Chapter 3)), measured with thermocouples, as a function of thruster power for both thrusters. The intense heat fluxes of the modified engine are due to the increased mean anode current density as a result of the decreased conducting anode surface area.

IV.2.2 Plasma Potential Contours

The floating probe described in Chapter 2 serves as a second means of determining the anode fall by making floating potential measurements near the anode. Figures IV.5 through IV.7 show equipotential profiles near the anode at the operating conditions 8kA-16g/s, 8kA-4g/s, and 16kA-4g/s for the benchmark thruster and the thruster with the modified anode, with the small cross in each figure indicating the extent of uncertainty in positioning the probe (±1 mm). At 8 kA-16 g/s, the floating potential measured

a) Standard Benchmark Thruster

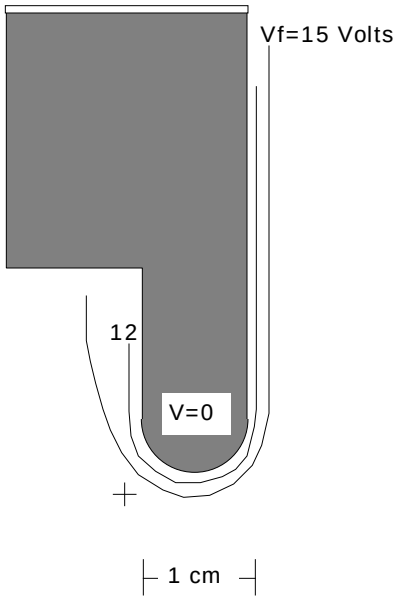

b) Modified Benchmark Thruster

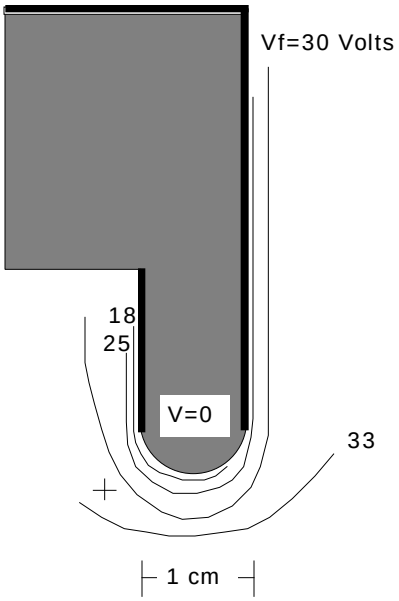

Figure IV.5: Floating Potential Profiles (8 kA-16 g/s).

1 mm from the modified anode surface is approximately 6 volts higher than that of the standard anode, while at 8 kA-4 g/s, the floating potentials measured 1 mm from the surface of either anode are virtually identical. Furthermore, at the former condition (8 kA-16 g/s), the floating potential gradients are larger for the modified anode than for the standard anode.

Figure IV.7 shows equipotential profiles near the anode of the standard and modified benchmark thrusters at 16 kA and 4 g/s. As is evident from the figure, the gradients of floating potential for the modified benchmark thruster are larger than those of the standard thruster. The floating potential measured 1 mm from the modified anode is approximately 7 volts higher than that of the standard anode. Again, the floating potential gradients extending several millimeters from the modified anode are larger than those of the standard benchmark thruster.

The triple Langmuir probe described in Chapter 2 was used to measure electron temperatures and ion number densities near the modified anode. The electron temperature is needed both to convert floating potentials to actual plasma potentials and to estimate the anode fall from measured heat flux. The triple probe was placed in the anode exit plane, 0.5 cm from the from the lip. To the accuracy of the measurement (10% for T_e and 60% for n_i), reduction of anode conduction surface area had virtually no effect on either the electron temperature or ion number density near the anode.

Figures IV.8 and IV.9 show the "average" anode falls obtained from both heat flux measurements and from the floating probe measurements taken 1 mm from the anode surface, respectively. To obtain the "average" fall values, anode falls for each thermocouple or floating probe measurement site were again weighted by the local current density. By entering the average anode fall into the anode heat transfer equation introduced in Chapter 1 (cf. Equations I.2 and I.3), neglecting convection and radiation, the total measured power to the anode (and anode power fraction) is obtained. Anode falls estimated from heat flux measurements are accurate to within 30% and 15% for the standard and modified benchmark thrusters, respectively. The difference in error of the two thrusters is due to the large error (30-50%) associated with the extrapolated current density profiles of the standard benchmark thruster. Because current conduction was restricted to a small portion of the modified benchmark thruster, a constant current

a) Standard Benchmark Thruster

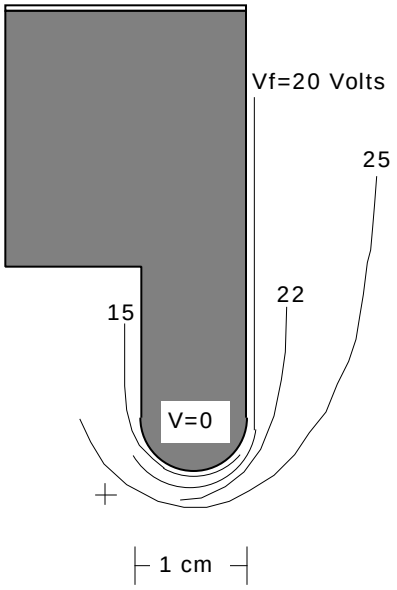

b) Modified Benchmark Thruster

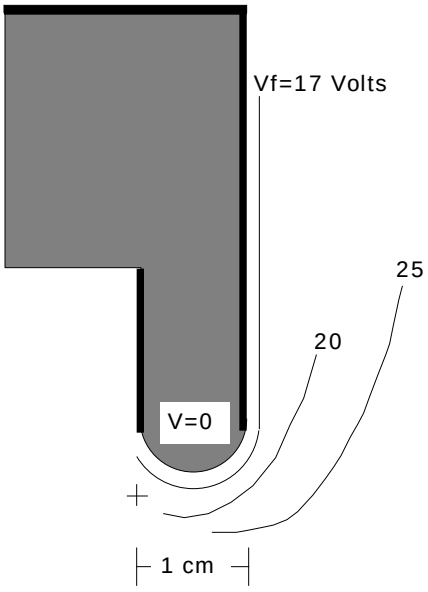

Figure IV.6: Floating Potential Profiles (8 kA-4 g/s).

a) Standard Benchmark Thruster

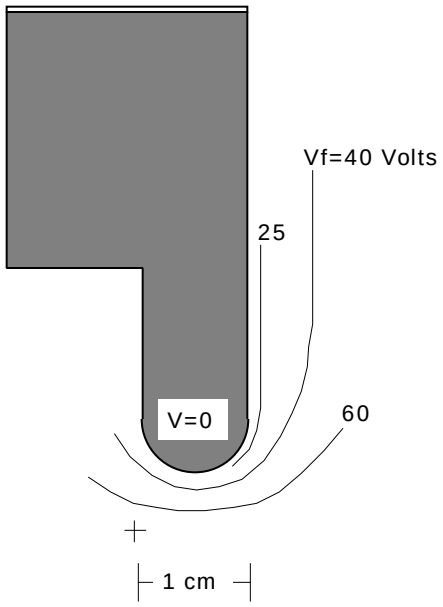

b) Modified Benchmark Thruster

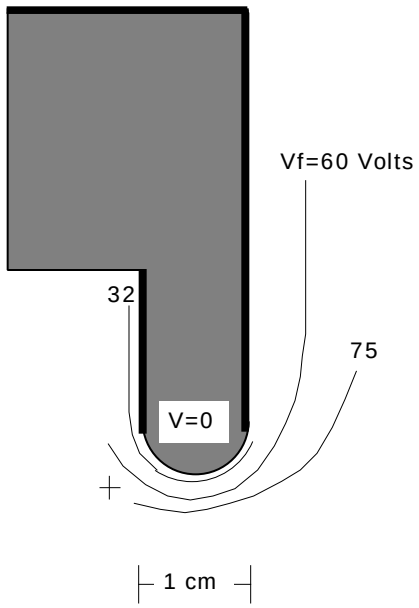

Figure IV.7: Floating Potential Profiles (16 kA-4 g/s).

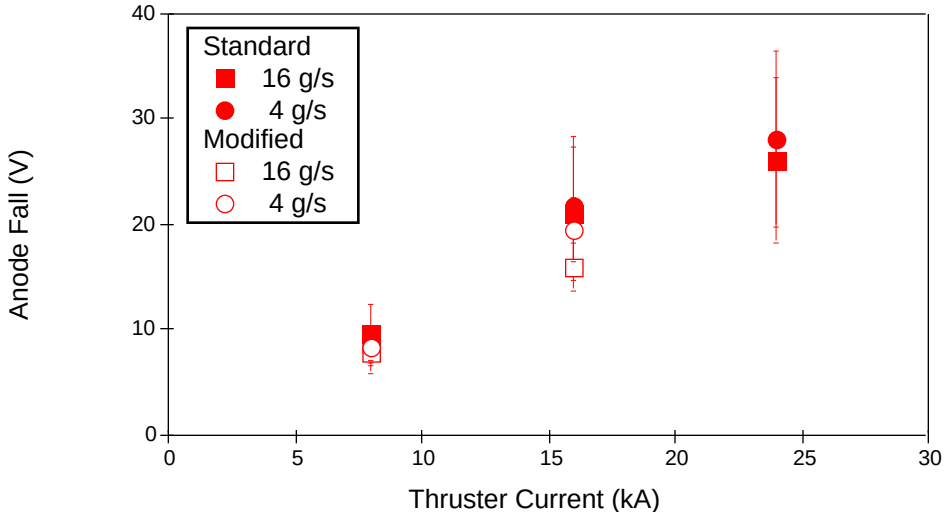

Figure IV.8: Anode Fall vs. Thruster Current (Thermocouple).

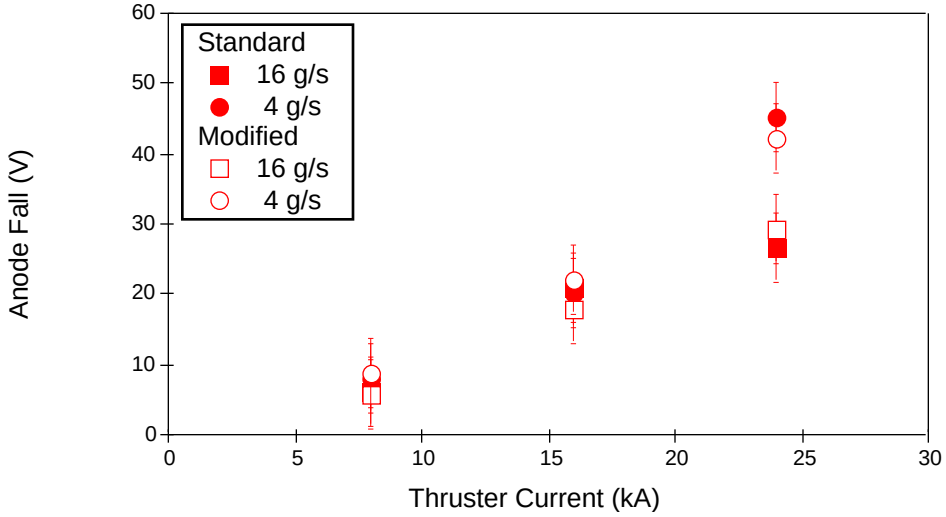

Figure IV.9: Anode Fall vs. Thruster Current (Floating Probe).

density (total thruster current divided by the lip surface area) can be assumed at each of the appropriate thermocouple sites. The validity of this assumption is partly supported by the constant heat flux measured by the three thermocouples at the lip of the modified anode (cf. Figure IV.3).

The figures above illustrate two important points: there is little difference between the "average" anode falls of either thruster, and that anode fall values from thermocouple and floating probe data are in good agreement with each other except at large values of $J^2/\dot{m}$, where larger anode falls are inferred from floating probe measurements than from measured heat fluxes. This discrepancy had at one time been attributed solely to ablation of the anode surface material, resulting in an energy sink not accounted for in the heat conduction model. Considering the measured electric fields near the anode at this operating condition, however, some of this disagreement may also be due simply to a voltage drop through the highly resistive plasma near the anode.

Given the fact that the terminal voltages, electron temperatures, and anode falls are virtually unchanged, the anode power fractions of the two thrusters are almost identical. Thus, the reduction of anode surface area has minimal effect on the operating characteristics of the MPD thruster. The failure of this experiment to reproduce the results reported in References [17] and [18] may be attributed to the following factors:

- The reduction of anode surface area may not have been enough. The anode used in Reference [18] reduced the conduction area by a factor of forty by limiting current conduction to a 2 mm band around the anode lip, compared to our factor of six.
- The mylar tape used to insulate 98% of the anode surface in Reference [18] may have ablated, introducing mass to the local plasma.

IV.3 Anode Fall Scaling Parameter

IV.3.1 Experiments with Argon Propellant

It was shown in the previous section that the reduction of the anode surface area had negligible effect on local plasma properties (T_e and n_i) and the anode fall. Furthermore,

it is seen that the anode falls predicted from anode heat flux measurements agree with those measured with the floating probe except at high $J^2/\dot{m}$. By insulating 85% of the anode surface, we have, in a sense, limited the physical domain of the "local" anode plasma to the lip region of the thruster. This allows for the study of anode power deposition to become more amenable to intrusive diagnostic techniques such as floating and triple probes. Since floating probes are considerably simpler to implement than the heat flux apparatus, it was decided that a series of floating probe measurements of the anode fall, for a variety of currents and mass flow rates, would be useful in further establishing trends in anode power deposition.

The floating electrode of the triple probe was used to measure the plasma floating potential 1 mm from the anode surface. Floating potentials were converted to the plasma potentials through use of electron temperatures measured by the triple probe, allowing for the instantaneous measurement of plasma potential. The "L" shaped floating probe, previously described, was also employed in several anode fall measurements at the lip. The floating potentials measured with the triple probe agree to within 5% of those obtained with the floating probe. Support apparatus for floating potential measurements are described in Chapter 2.

This series of experiments was conducted with the modified benchmark thruster for argon propellant at mass flow rates of 4, 6, 8, 12, and 16 g/s at thruster currents between 4 and 25 kA. Figures IV.10 and IV.11 show the the terminal voltage and anode fall characteristics of the modified benchmark thruster, respectively, with the anode fall equated to the voltage drop measured 0.1 cm from the anode midlip. As Figure IV.11 shows, above a current of 20 kA, the anode fall becomes highly sensitive to mass flow rate. Anode falls of almost 50 V are measured at 25 kA (4 g/s). Between 4 and 10 kA, the anode fall increases slightly with current. However, above 10 kA, a steeper rise in the anode fall characteristic is observed.

Figure IV.12 shows anode power fraction as a function of thruster power for various mass flow rates. As is evident from the figure, anode power fraction is strongly dependent on mass flow rate. Below a power level of 2.5 MW, significant scatter is present for the different mass flow rates and no consistent trend is evident. Between power levels of 1 and 2.5 MW two distinct branches appear: a low anode power fraction branch for

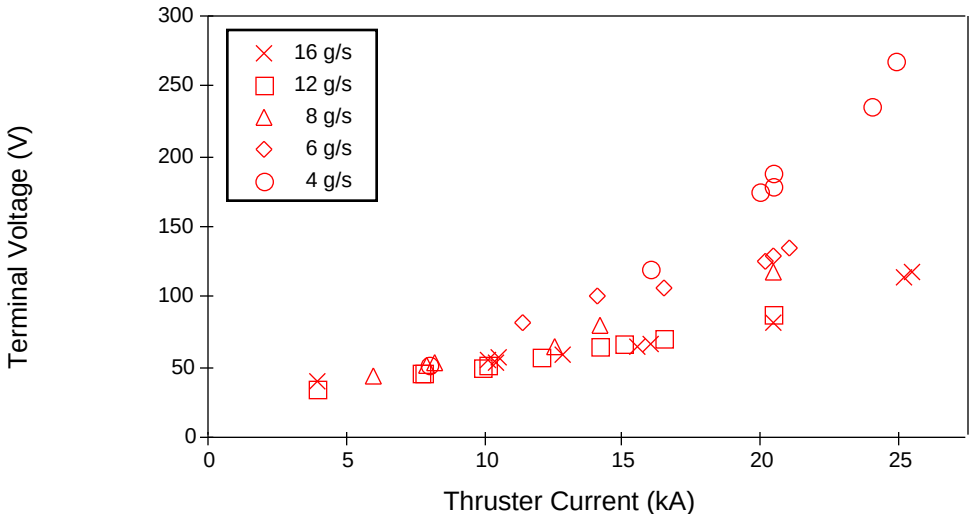

Figure IV.10: Terminal Voltage vs. Thruster Current.

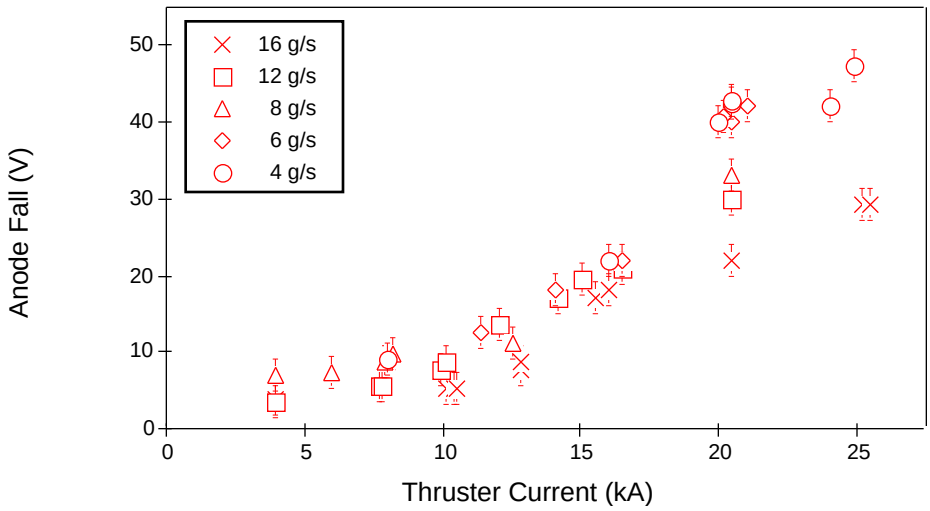

Figure IV.11: Anode Fall vs. Thruster Current.

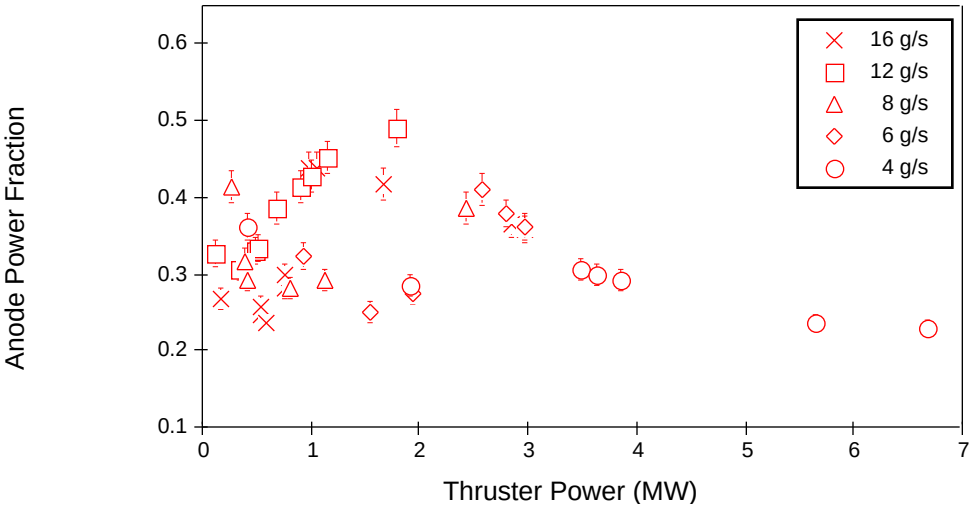

Figure IV.12: Anode Power Fraction vs. Thruster Power.

low propellant flow rates and a high anode power fraction branch at high flow rates.

When the same data are categorized by $J^2/\dot{m}$ (Figure IV.13), however, some coherent structure appears in the data. A $J^2/\dot{m}$ of 54 kA^2-s/g corresponds (through the bJ^2 thrust law[1])[6] to an exhaust velocity equal to the Alfvén critical velocity for argon (~8.7 km/s). The figure further illustrates the fact that for exhaust velocities above the Alfvén critical velocity, the anode power fraction tends to decrease with increasing thruster power. The minimum anode power fraction of 0.23 (23% input power) is measured at a thruster power level of almost 6 MW. Figure IV.14 shows anode power fraction as a function of $J^2/\dot{m}$. Again it is seen that at large values of $J^2/\dot{m}$ the fraction of power that is deposited to the anode becomes relatively small.

Figure IV.15 shows the anode fall as a function of $J^2/\dot{m}$ for the various mass flow rates. As seen in previous studies[32] there is a strong increase in the anode fall with $J^2/\dot{m}$. Beyond a $J^2/\dot{m}$ of approximately 60 kA^2-s/g, however, the anode fall approaches an asymptote of approximately 50 V. This behavior is quite different from results seen in Reference [32] which exhibited no leveling off of the anode fall. It should be pointed

[1] "b" is a scaling factor solely dependent on the geometry of the thruster.

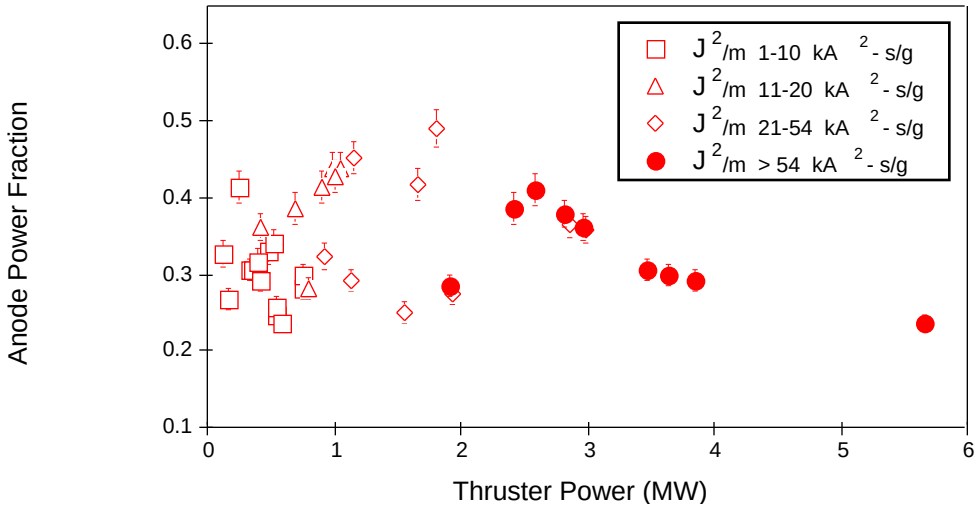

Figure IV.13: Anode Power Fraction vs. Thruster Power.

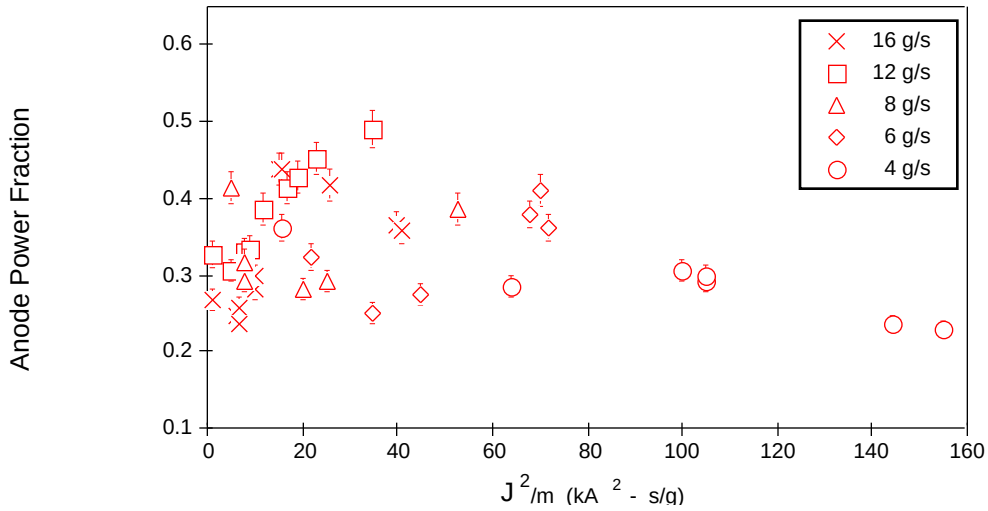

Figure IV.14: Anode Power Fraction vs. $J^2/\dot{m}$.

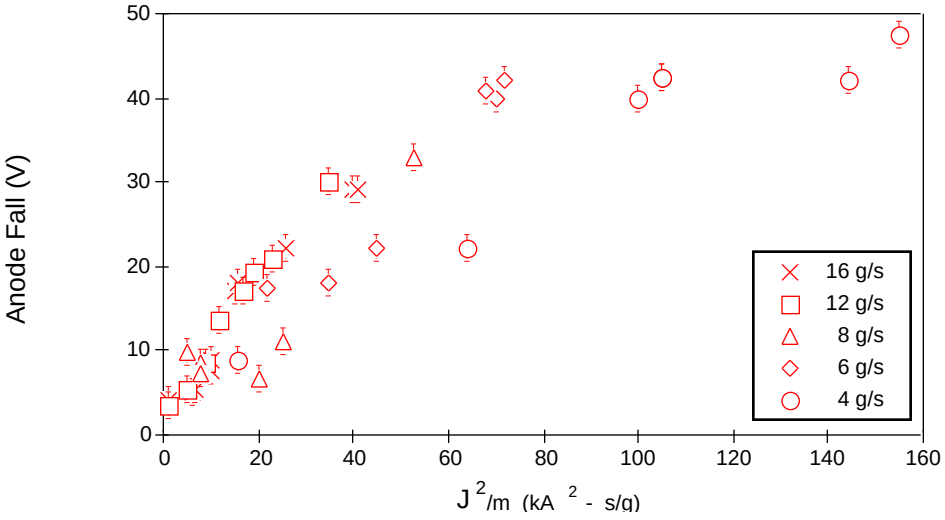

Figure IV.15: Anode Fall vs. $J^2/\dot{m}$.

out, however, that the range of $J^2/\dot{m}$ investigated in the study mentioned above (Reference [32]) corresponds to the regime observed in the present work in which the anode fall increases rapidly with $J^2/\dot{m}$ ($J^2/\dot{m} \leq 30$ kA^2–s/g). Within this range, both studies measure equivalent values of the anode fall. Large amplitude high frequency oscillations in the terminal voltage ($\geq$100 kHz at 10% of the signal magnitude) are seen for thruster operation above a $J^2/\dot{m}$ of approximately 65 kA^2–s/g.

Another way of casting the dependence of the anode fall on exhaust velocity that shows some insight to the physical processes involved is to present the anode fall data above as a function of ξ^2 (cf. Figure IV.16), where ξ is a dimensionless current defined by[66]:

$$\xi = \frac{J}{J_{fi}}. \tag{IV.1}$$

J_{fi} , the minimum thruster current for full ionization of the propellant, is defined through the following equation[2]:

$$J_{fi} = \sqrt{\frac{\dot{m}}{\frac{\mu}{4\pi} ln\frac{r_a}{r_c}} \sqrt{\frac{2E_i}{M}}}. \tag{IV.2}$$

[2]evoking Alfvén's hypotheses of critical ionization[67]

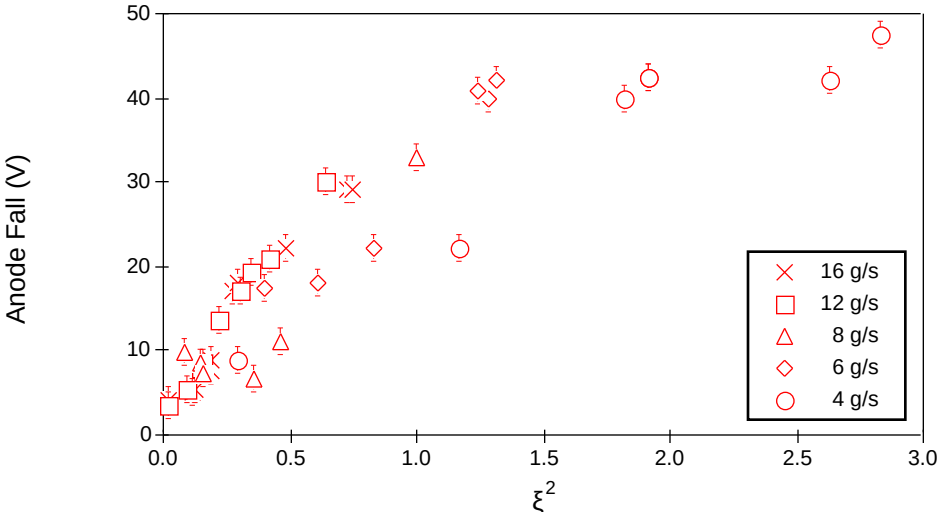

Figure IV.16: Anode Fall vs. ξ^2.

In Equation IV.2, μ is the permeability of free space, r_a and r_c are the anode and cathode radii, respectively, and E_i and M are the ionization potential and mass of the propellant atoms, respectively. Thus, thruster operation with a partially ionized plasma corresponds to $\xi \leq 1$ and with a fully ionized plasma to $\xi > 1$. A value of unity for ξ has also been shown to be the transitional region for MPD thruster operation from an electromagnetic-electrothermal mode to a pure electromagnetic mode[68], where the thrust is accurately described by the relation bJ^2 mentioned above. In argon, $\xi > 1$ corresponds to $J^2/\dot{m} > 54 kA^2-s/g$.

As is expected, the dependence of the anode fall on ξ^2 is similar to the anode fall dependence shown in Figure IV.15. The anode fall increases rapidly with ξ^2 for $\xi^2 \leq 1$. However, for ξ^2 above 1, the anode fall levels off at approximately 45 V.

Figure IV.17 shows anode power fraction as a function of ξ^2. For $\xi^2 > 1$, the thruster operates in a regime of relatively low anode dissipation (in comparison to thruster power). This can be partially attributed to the leveling off of the anode fall seen in Figure IV.16 as well as to the rapid increase in terminal voltage with current that is characteristic of a fully ionized thruster. For $\xi^2 \leq 1$ the terminal voltage of the

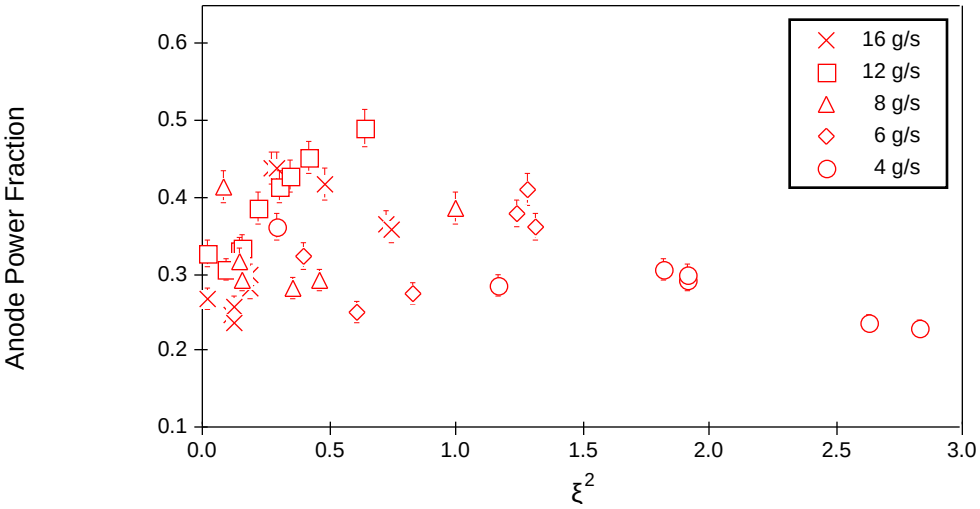

Figure IV.17: Anode Power Fraction vs. ξ^2.

thruster has been shown to increase linearly with current while for $\xi^2 > 1$, the voltage increases with current raised to the third power. Thus, in a partially ionized mode of thruster operation, with varying degrees of ionization, one would expect scatter of anode power fraction data since both the anode fall and the terminal voltage increase rapidly with current, with only the terminal voltage strongly sensitive to propellant mass flow rate. With a fully ionized plasma, however, as the terminal voltage increases rapidly with current, the anode fall remains constant. Thus the fraction of thruster power deposited to the anode decreases with increasing ξ.

IV.3.2 Correlation of the Anode Fall with the Hall Parameter

Work in the past has linked large voltage drops at the anode of various devices to large electron Hall parameters predicted to exist in the adjacent plasma[35, 36]. In all of these cases, the ambient magnetic field is predominantly parallel with the anode. Thus, current conduction to the anode requires electrons to diffuse across magnetic field lines. The electron Hall parameter (Ω), defined as the ratio of the electron gyrofrequency (ω_e) to the electron collision frequency (ν_e), is a measure of the response of electrons to

electric and magnetic fields. For plasmas characterized as having low Hall parameters, electrons, in general, flow parallel with the electric field. For plasmas with large electron Hall parameters, electrons tend to migrate in a direction that is perpendicular to both the electric and magnetic fields.

As was mentioned in Chapter I, studies with a variety of plasma producing devices have found that the anode fall increases with Hall parameter[35, 36, 37]. Anode starvation[28, 42, 69], and plasma turbulence[34, 38, 39, 40, 41] have been evoked to explain the correlation between anode power deposition and the Hall parameter. Anode starvation refers to the depletion of current carriers from the anode region as a result of a radial component of the Lorentz force (pumping force). At large Hall parameters, significant axial Hall currents exist which create radial components of the Lorentz force that drive charged particles away from the anode region. In response to this depletion of charge carriers, large electric fields are needed near the anode to maintain the radial current density at the necessary level. This effect can be shown by manipulation of Ohm's law:

$$\mathbf{j} = \sigma_o(\mathbf{E} + \mathbf{v} \times \mathbf{B}) - \frac{\Omega}{|\mathbf{B}|}(\mathbf{j} \times \mathbf{B} - \nabla p_e) \tag{IV.3}$$

where $\mathbf{j}$ is the current density vector, σ_o is the electrical conductivity, $\mathbf{E}$ and $\mathbf{B}$ are the electric and magnetic fields, respectively, $\mathbf{v}$ is the streaming velocity of the plasma (bulk velocity), and p_e is the electron pressure. The "z" axis is selected to align with the magnetic field, which is assumed to be purely in the azimuthal direction (parallel with the anode), and the "x" and "y" coordinates are chosen to be in the axial and radial directions, respectively. The "z" components of $\mathbf{E}$, $\mathbf{v}$, and $\mathbf{j}$ can be neglected if the discharge is assumed to be axisymmetric. Estimates of ∇p_e from Langmuir probe data presented in Chapter 3 show it to be negligible in comparison to the other terms in Equation IV.3. The radial electric field can be calculated from the radial and axial current densities through the following equation:

$$E_y = \frac{(\Omega^2+1)(j_y - j_x\Omega) - \sigma_o(\Omega^2+1)B_z v_x}{\sigma_o(\Omega^2+1)} \tag{IV.4}$$

where j_y, j_x, E_y, and E_x are the radial and axial current densities, and the radial and axial electric fields, respectively. v_y and v_x represent the radial and axial flowing speed of the plasma, respectively. The axial electric field is related to current density and the

radial electric field through the following equation:

$$E_x = \frac{j_x(\Omega^2 + 1)}{\sigma_o} + E_y\Omega - B_z(v_x\Omega + v_y). \tag{IV.5}$$

The radial current density, electron temperature, and electron number density are assumed constant. The electrical conductivity is calculated with the Spitzer-Härm formula presented in Appendix A. Equations relating j_x and j_y to axial and radial electric fields are presented in Appendix A as well. The magnetic field is calculated by selecting a Hall parameter through the following equation:

$$B_z = \frac{qn_e\Omega}{\sigma_o}. \tag{IV.6}$$

The "bJ^2" thrust law was used to estimate the magnitude of the plasma flowing speed near the anode. Based on Langmuir probe data presented in Chapter 3, the flow angle ($\sim (v_x/v_y)$) was set to ten degrees. Because of the relatively low magnetic field near the anode, the analysis proved to be insensitive to the flowing speed of the plasma.

Figures IV.18 and IV.19 show the calculated radial electric fields necessary to draw a set level of radial current as a function of electron Hall parameter at an electron temperature of 2 eV and electron number densities of 1×10^{20} and 1×10^{19} m^{-3}, respectively. As the Hall parameter increases, a larger electric field is required to maintain the radial current density through the quasi-neutral plasma at the specified level. The effect of reduced electron number density can also be seen by the fact that the electric field needed to draw a specific level of current density at a given Hall parameter increases with decreasing number density (cf. Figures IV.20). From these calculations we can surmise that the Hall parameter should be a major scaling parameter for anode power deposition, a behavior which has been observed in a variety of current carrying devices[35, 36, 37].

In an effort to investigate the connection between the Hall parameter and the anode fall, the triple probe data described above, in conjunction with a series of magnetic field measurements taken at the anode lip, were employed to obtain an estimate of the local electron Hall parameter. The Hall parameter is defined as

$$\Omega \equiv \omega_e/\nu_e \tag{IV.7}$$

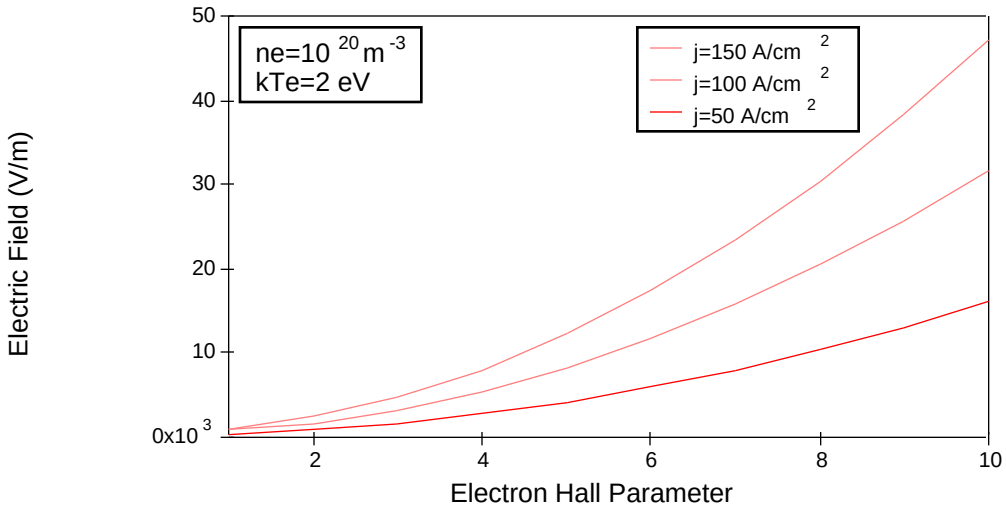

Figure IV.18: Electric Field vs. Electron Hall Parameter.

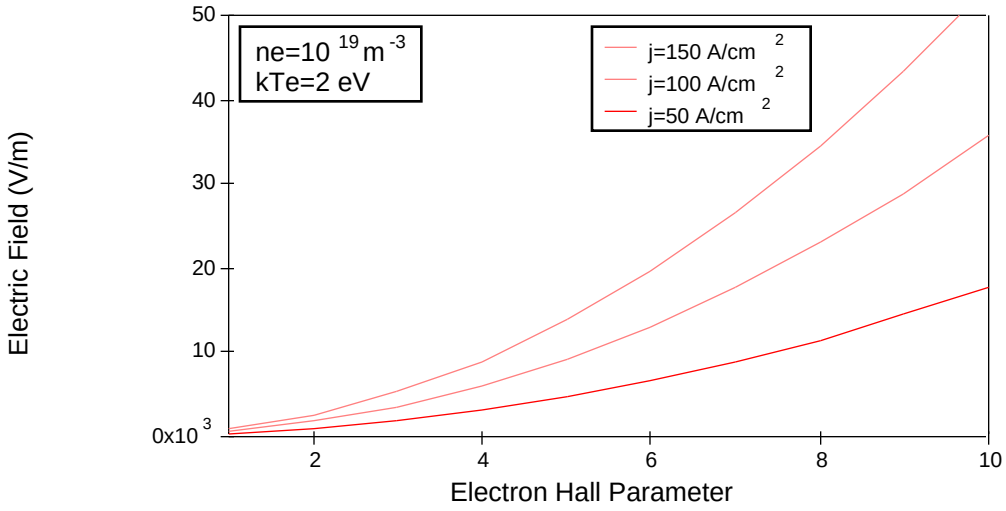

Figure IV.19: Electric Field vs. Electron Hall Parameter.

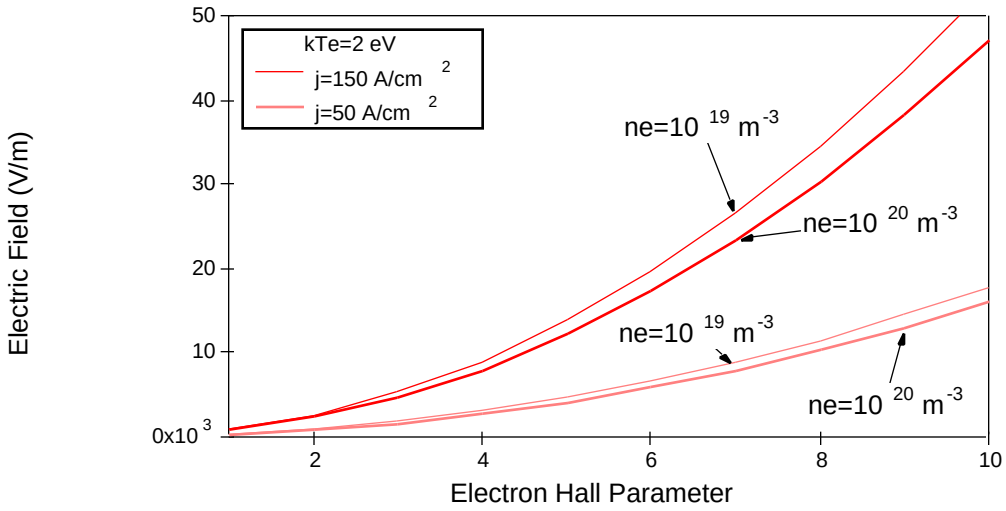

Figure IV.20: Electric Field vs. Electron Hall Parameter.

where the gyrofrequency is calculated by the following equation:

$$\omega_e = qB/m_e. \tag{IV.8}$$

The electron collision frequency is given by

$$\nu_e = \sum_k n_k Q_{ek}^p \overline{v}_{ek} \tag{IV.9}$$

where the index "k" refers to the species with which electrons experience momentum-transfer collisions (i.e. ions and neutrals), n_k is the number density of species "k," Q_{ek}^p is the momentum-transfer collision cross section of the electrons with species "k," and $\overline{v}_{ek}$ is the mean relative speed of the electrons with respect to species "k" particles. Because the electrons are much lighter than the neutrals and ions and move at much greater thermal speeds, the difference in speed between the electrons and the heavy particles is essentially the thermal speed of the electrons. Therefore, as an approximation, the relative speed between the electrons and the heavy particles is usually taken as the thermal speed of the electrons.

Equation IV.9 can be written as

$$\nu_e = n_i Q_{ei}^p \overline{v}_{ei} + n_n Q_{en}^p \overline{v}_{en} \tag{IV.10}$$

where subscript "i" refers to the ions and subscript "n" refers to the neutrals. For ionization fractions greater than 1%, the electron-ion coulomb collisions are much more frequent than electron-neutral collisions[6]. Therefore, for the highly ionized plasmas of MPD thrusters where electron-neutral collisions can be ignored, Equation IV.10 can be written as

$$\nu_e \simeq \nu_{ei} = \frac{q^4 (\ln \Lambda) n_e}{3(2\pi)^{3/2} \sqrt{m_e} \varepsilon_o^2 (kT_e)^{3/2}} \tag{IV.11}$$

where ν_{ei} is the electron-ion collision frequency, and ε_o is the permittivity of free space. The plasma parameter (Λ) is given by

$$\Lambda = 9(\frac{4}{3})\pi n_e \lambda_e^3 \tag{IV.12}$$

where the electron Debye length (λ_e) is calculated from

$$\lambda_e = \sqrt{\frac{\varepsilon_o k T_e}{n_e q^2}}. \tag{IV.13}$$

Equation IV.7 can now be simplified to

$$\Omega = \frac{3(2\pi)^{3/2} \varepsilon_o^2}{\sqrt{m_e} \ln \Lambda} \frac{(kT_e)^{3/2} B}{q^3 n_e} \tag{IV.14}$$

which shows that the Hall parameter is proportional to $T_e^{3/2}$ and magnetic field strength and inversely proportional to electron number density [3]. Thus, to experimentally determine the Hall parameter, the electron temperature, electron number density, and the local magnetic field must be measured. The magnetic field probe (B-probe) originally constructed to investigate asymmetries in the thruster discharge[46] (see Chapter 2) was used for this experiment. The core of the probe was aligned with the azimuthal magnetic field lines at a distance of approximately 0.3 cm from the anode midlip. Triple probe measurements were used in obtaining the electron temperature and the electron number density (assuming n_e=n_i).

[3] Ignoring the weak dependence of $\ln \Lambda$ on n_e

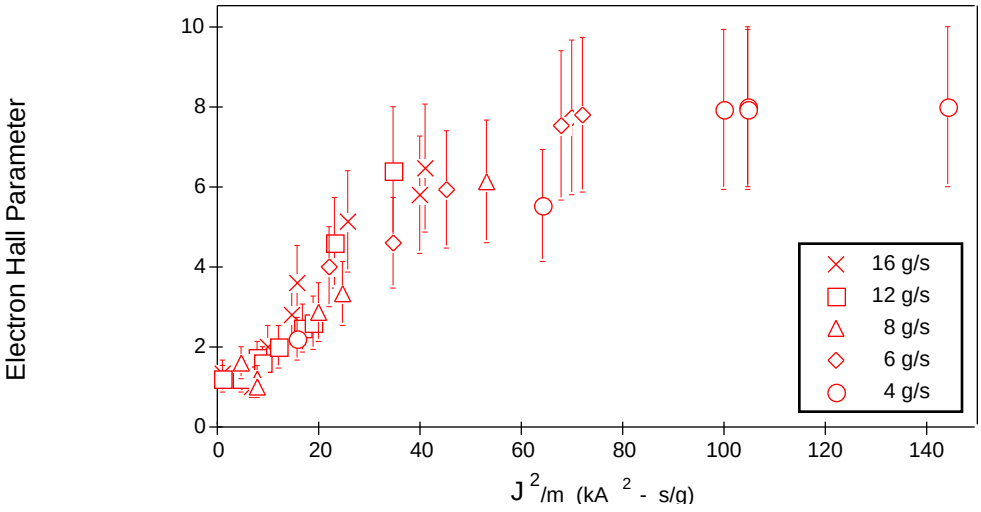

Figure IV.21: Electron Hall Parameter vs. $J^2/\dot{m}$.

Figures IV.21 and IV.22 show the electron Hall parameter as a function of $J^2/\dot{m}$ and ξ^2, respectively, at a distance of 0.3 cm from the anode midlip using Equation IV.14 The accuracy of the electron Hall parameter estimate is limited by that of the number density measurement ($\sim$60%). The most striking features of these figures are the fact that for values of $J^2/\dot{m}$ and ξ^2 less than 60 kA^2-s/g and 1, respectively, the data fall on straight lines with little scatter. Above the the values mentioned above, however, the electron Hall parameter reaches an asymptote of approximately eight.

The anode fall is plotted as a function of the Hall parameter for various mass flow rates and values of $J^2/\dot{m}$ in Figures IV.23 and IV.24, respectively. The anode fall increases with increasing Hall parameter irrespective of mass flow rate. This trend, which is in total agreement with previous work mentioned above, is further corroborated by data collected with a 100 kW steady applied-field MPD thruster (see Appendix B).

IV.3.3 Experiments with Helium Propellant

In the previous section the electron Hall parameter was shown to be a key scaling parameter for the anode fall. The battery of diagnostics applied to the MPD thruster

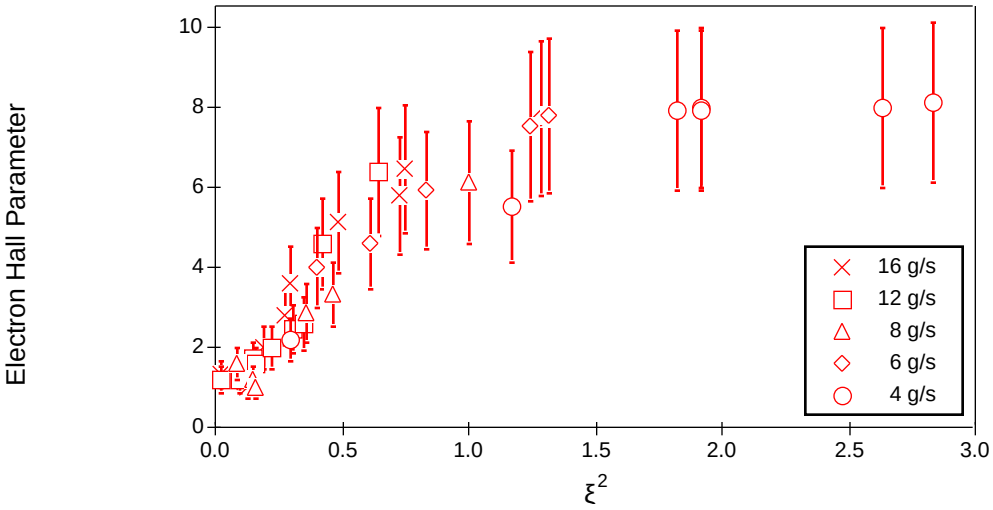

Figure IV.22: Electron Hall Parameter vs. ξ^2.

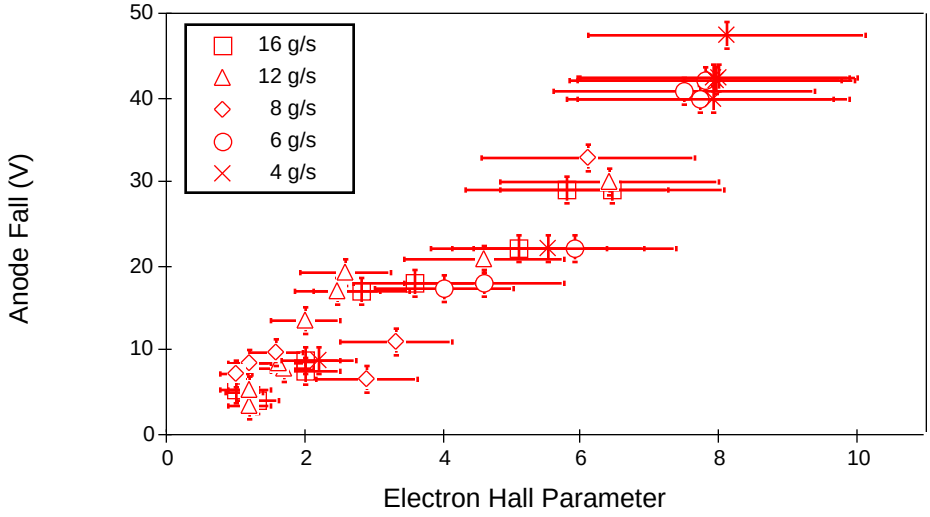

Figure IV.23: Anode Fall vs. Electron Hall Parameter.

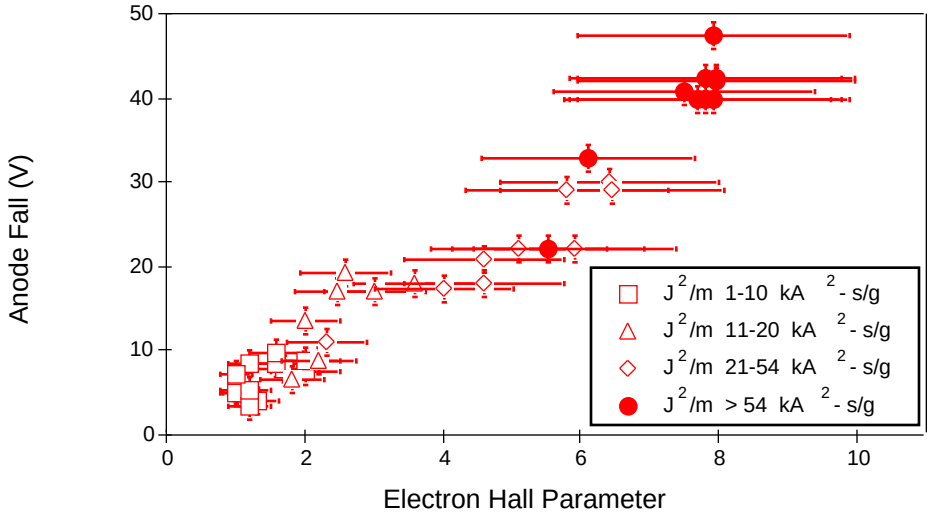

Figure IV.24: Anode Fall vs. Electron Hall Parameter.

in this thesis has, for the first time, allowed for such a quantitative correlation to be made. To investigate this correlation further, the series of experiments described above with argon propellant was repeated for the thruster operating with helium propellant.

Figures IV.25 and IV.26 show terminal voltage as a function of thruster current and ξ^2, respectively, for helium propellant flow rates of 1, 2, 4, and 6 g/s. Based on the results of previous studies[68], the terminal voltage of the thruster operating with either propellant should scale with ξ^2. As the figures show, the terminal voltages range from about 40 to 170 V for thruster currents between 4 and 24 kA and ξ^2 up to 1.5. Although there is some scatter present in Figure IV.26, the voltage scales reasonably well with ξ^2 for both argon and helium (Figure IV.27).

Floating plasma potentials were measured to within 0.1 cm from the anode surface with the floating probe. Electron temperatures, obtained by triple probe, are used to convert the measured floating potentials to the actual plasma potentials. Figure IV.28 shows the anode fall as a function of thruster current for various mass flow rates. As with the argon, the data fall within the range between 5 and 50 V. The helium data exhibits less coherence with propellant flow rate than the argon data. Although the

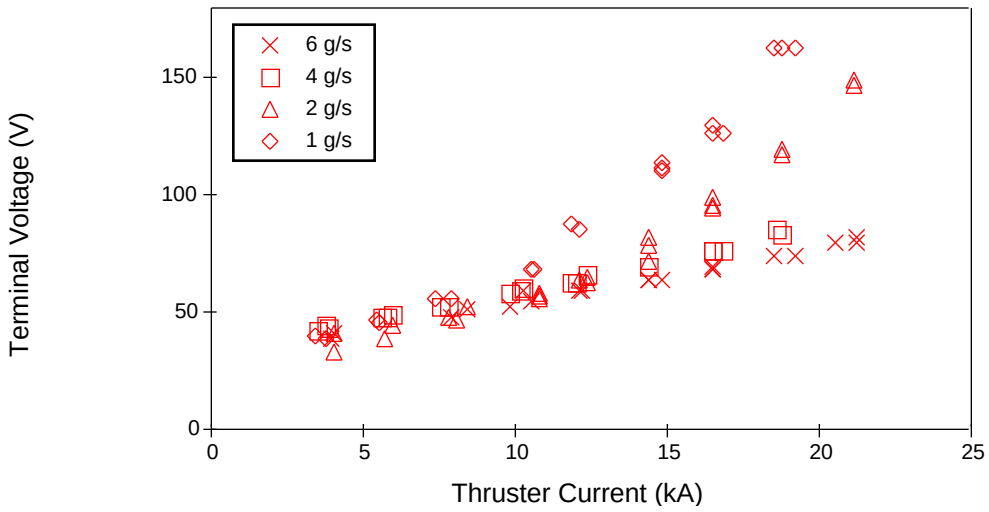

Figure IV.25: Thruster Voltage vs. Current for Helium.

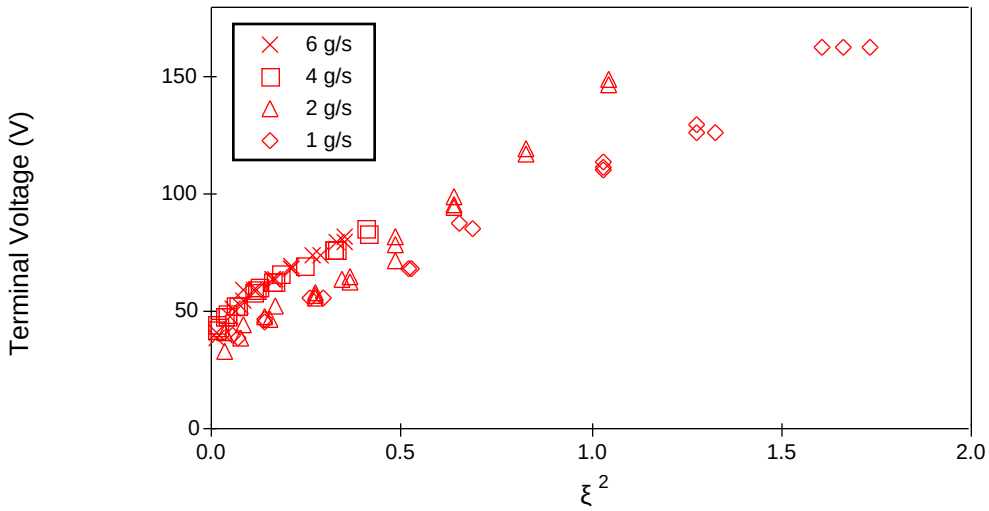

Figure IV.26: Thruster Voltage vs. ξ^2 for Helium.

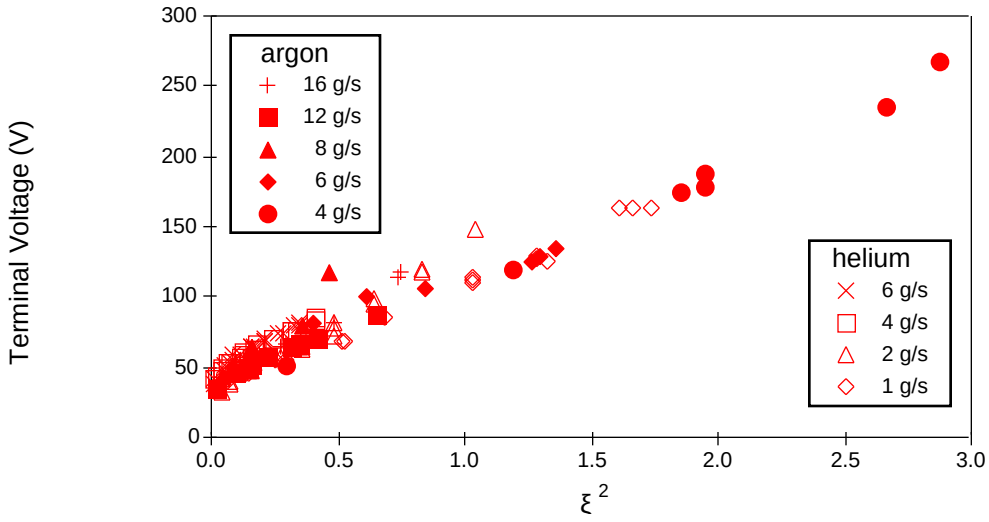

Figure IV.27: Thruster Voltage vs. ξ^2 for Argon and Helium.

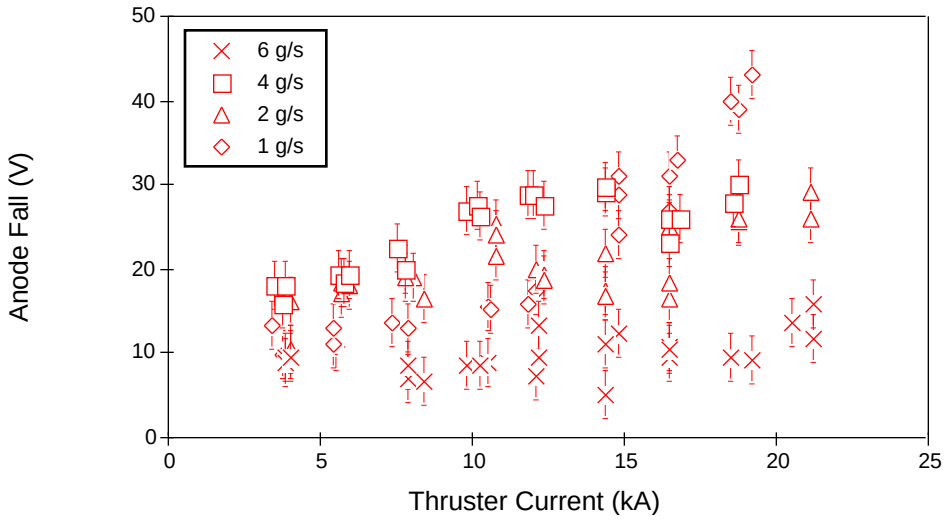

Figure IV.28: Anode Fall vs. Thruster Current for Helium.

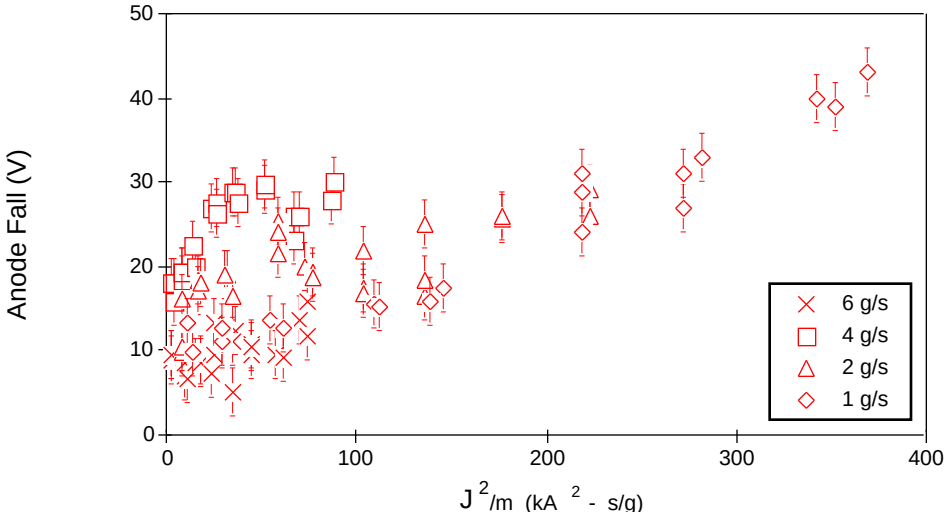

Figure IV.29: Anode Fall vs. $J^2/\dot{m}$ for Helium.

lowest anode falls were measured at the highest propellant flow rates (6 g/s), anode falls measured at relatively large mass flow rates (4 g/s) are almost as large as those measured at much lower mass flow rates for identical currents.

In Figures IV.29 and IV.30, the anode fall is shown as a function of $J^2/\dot{m}$ and ξ^2, respectively. The use of helium has allowed for a wide range of $J^2/\dot{m}$, varying from 2 to nearly 400 kA^2-s/g. For values of $J^2/\dot{m}$ and ξ^2 less than 100 kA^2-s/g and 0.5, respectively, there is a great deal of scatter in the data, with little dependence on mass flow rate. Above these respective values, however, the anode fall increases monotonically with both $J^2/\dot{m}$ and ξ^2. This is in sharp contrast to the behavior displayed with argon in which the anode fall plateaued at certain values of these parameters (cf. Figures IV.15 and IV.16).

Anode power fractions were estimated using the anode heat transfer equation (Equation I.3) presented in Chapter 1 in conjunction with triple probe (electron temperature) and floating probe (anode fall) data. Figures IV.31 and IV.32 show the estimated anode power fraction as a function of thruster power and $J^2/\dot{m}$, respectively. At thruster power

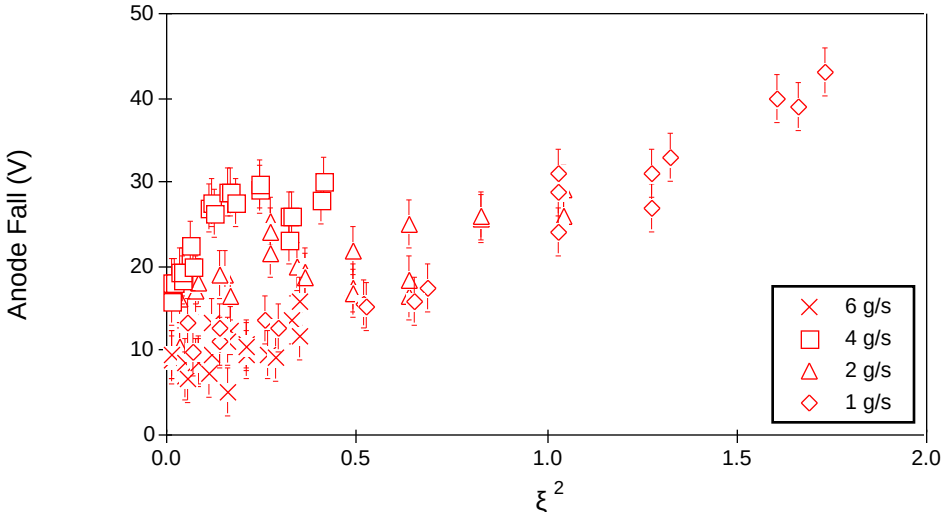

Figure IV.30: Anode Fall vs. ξ^2 for Helium.

levels below 1 MW and $J^2/\dot{m}$ less than 100 kA^2−s/g, the peak anode power fraction at a given thruster power level or value of $J^2/\dot{m}$ is up to 40% larger for the thruster operating with helium than with argon. This is primarily due to the lower terminal voltages associated with helium as the propellant. As is evident from the figures, the anode power fractions range from 0.7 at 150 kW to less than 0.3 at 3 MW. Once again the data exhibit little dependence on mass flow rate, particularly at the sub-megawatt power levels. At power levels below 1 megawatt, relatively high anode power fractions for a given level of thruster power are measured at intermediate propellant flow rates (2 and 4 g/s). Similar trends are apparent when the data are plotted versus $J^2/\dot{m}$, however, above $J^2/\dot{m}$ of 100 kA^2−s/g, the anode power fraction levels off to a value of approximately 0.3. When plotted against ξ^2(cf. Figure IV.33), the anode power fraction remains constant for ξ^2 above 0.5. This is in contrast to the argon data which showed a much more gradual leveling off of anode power fraction with ξ^2.

Using measured electron temperature and number density as well as measured magnetic field strength, the local electron Hall parameter was calculated for each condition in which the anode fall was measured. Figure IV.34 shows the anode fall as a function of

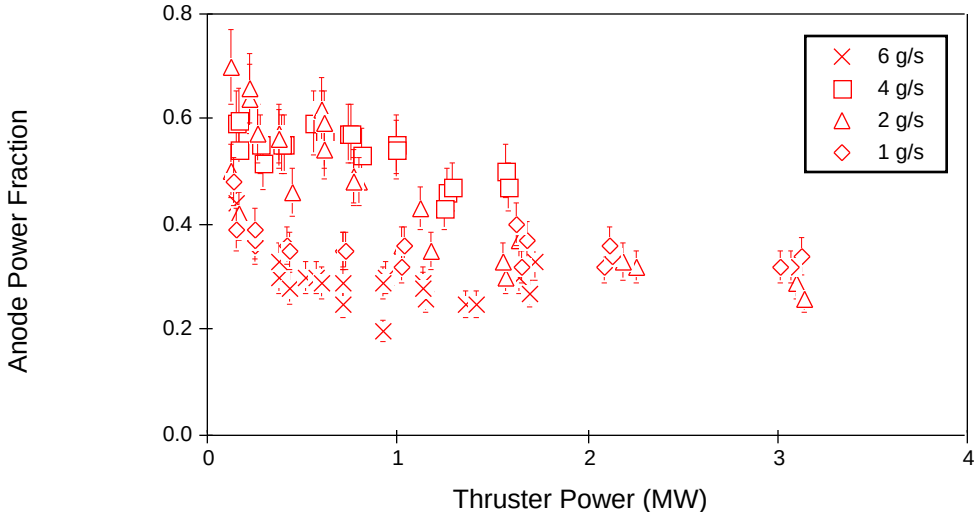

Figure IV.31: Anode Power Fraction vs. Thruster Power for Helium.

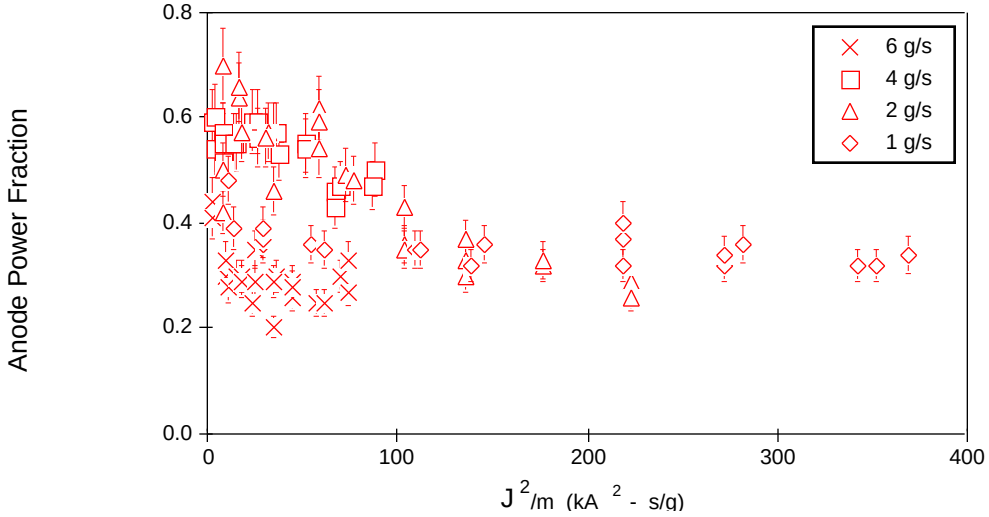

Figure IV.32: Anode Power Fraction vs. $J^2/\dot{m}$ for Helium.

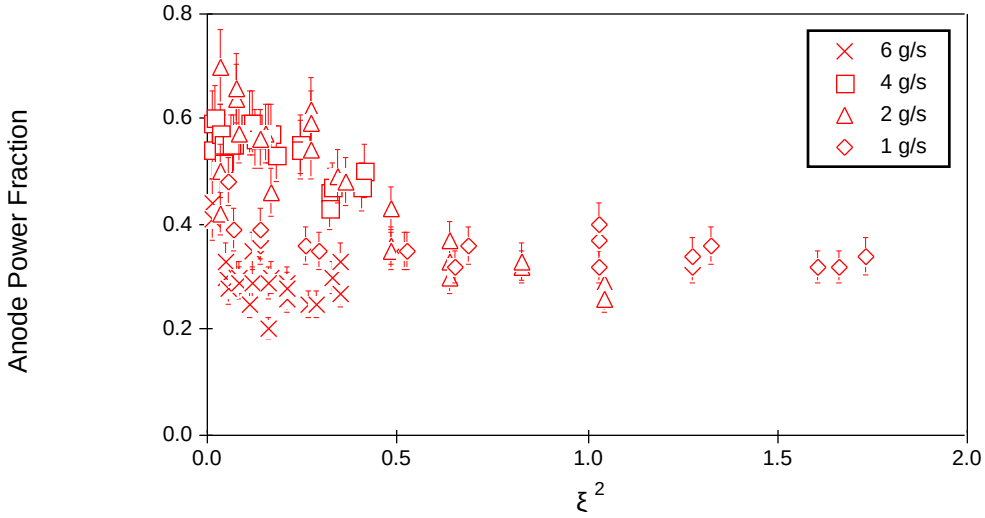

Figure IV.33: Anode Power Fraction vs. ξ^2 for Helium.

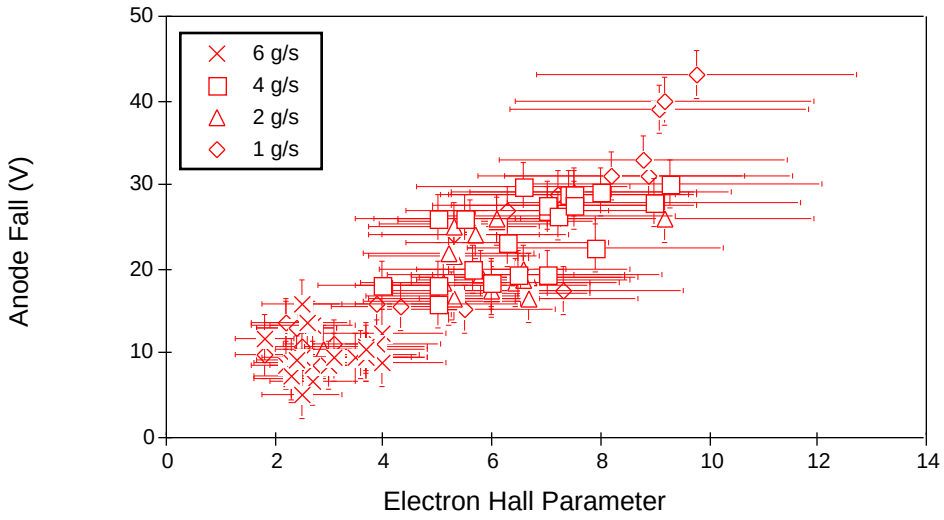

Figure IV.34: Anode Fall vs. Electron Hall Parameter for Helium.

calculated electron Hall parameter. As with argon, the figure shows a strong correlation between the anode fall and the electron Hall parameter for helium as well. The electron Hall parameter for helium ranged between 2 and 10, compared with a range of 2 and 8 for argon. The figure also shows that this correlation holds irrespective of mass flow rate as can be seen by the fact that conditions of high and low Hall parameter (anode fall) are represented at both large and small propellant flow rates. Thus, the electron Hall parameter is a major scaling parameter for the anode fall. Some interesting observations can be made from these experimental results.

- The anode fall increases monotonically with the electron Hall parameter[4]. As mentioned above, this trend had been suggested (although not rigorously shown) throughout the literature, however, its significance was never appreciated. As such, simple design options may exist to remedy the anode dissipation problem:

    1. Injection of a seed propellant of low ionization potential near the anode to reduce the electron Hall parameter by increasing the local ion number density.
    2. Judicious anode propellant injection to reduce the Hall parameter by increasing the ion number density via ionization.
    3. Use of an anode in the form of a moderately"High" pressure cavity ("Hollow Anode").
    4. Tailoring applied magnetic fields to either cancel local self-magnetic fields, thus reducing the cyclotron frequency, or to intersect the anode surface.

- Anode starvation models that do not take into account the restriction of anode current transport, due to the presence of a magnetic field may not be applicable to high powered MPD thrusters which operate with electron Hall parameters between one and ten.

The last item of the list (#4) is the approach taken in reducing the anode fall and is the subject of Chapter 5.

[4]calculated from the component of the magnetic field that is parallel with the anode.

IV.3.4 Determination of the Electron Hall Parameter from Measured Current Contours

A second method that was applied in determining the electron Hall parameter was to use measured current contours, electron temperatures and number densities, and field measurements in conjunction with Ohm's law to calculate the effective electron collision frequency. The motivation for this analysis was to determine if the electron Hall parameter (electron collision frequency) calculated using classical formulae matched that deduced from measured plasma and field parameters.

The basic approach of the analysis was to use measured current densities, electron number densities, electric fields and magnetic fields with Ohm's law to solve for the electron Hall parameter. Manipulation of Equation IV.3 yields the following equation for the electron Hall parameter:

$$\Omega = \frac{(1+\Omega^2) j_y B_z}{q n_e (\Omega(E_x + B_z v_y) + E_y - B_z v_x)}. \tag{IV.15}$$

Data presented in Chapter 3 that were collected within a 4 mm by 2 mm (axial by radial) region centered ∼3 mm from the anode surface (cf. Figure A.1) were used for the analysis. The radial current density (j_y) and the azimuthal magnetic field strength (B_z) were obtained from magnetic field probe measurements, and n_e was obtained from Langmuir probe measurements. The axial and radial electric fields (E_x and E_y, respectively) were obtained from floating probe surveys by assuming that the floating potential gradient is equivalent to the plasma potential gradient[5]. The magnitude of the flow velocities v_x and v_y, which turned out to have little impact on the results, were estimated with a model developed by Choueiri [66] in conjunction with Langmuir probe measurements to determine the plasma streaming angle (v_x/v_y).

Figure IV.35 shows the electron Hall parameter inferred from Equation IV.15 plotted against Hall parameters calculated via Equation IV.14, which only considers Coulomb collisions. As the figures show, there is virtually no agreement between the two methods of obtaining the electron Hall parameter. Since the magnetic fields used to calculate either set of Hall parameters are identical, the difference between the two sets is due to the discrepancy between inferred electron collision frequencies and those calculated

[5]Neglecting the variation in electron temperature between floating probe measurement sites.

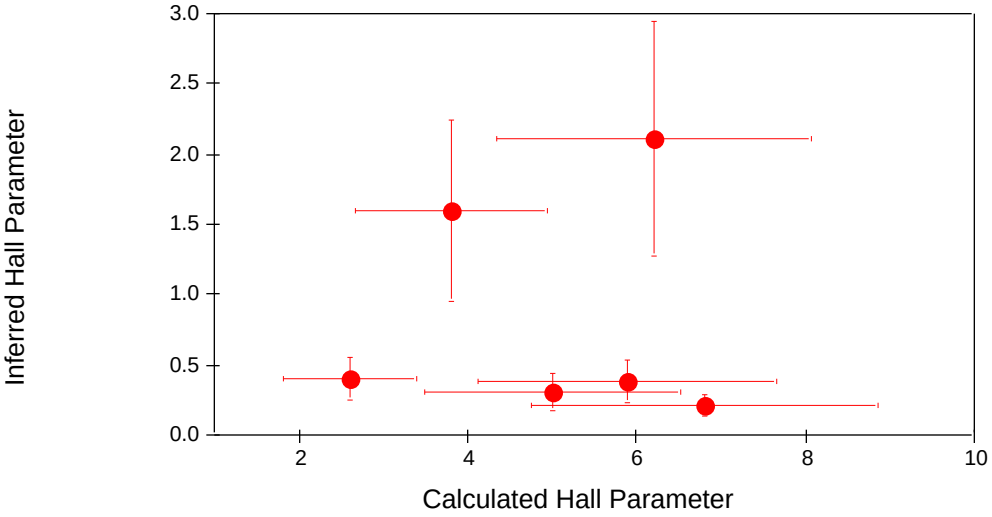

Figure IV.35: Inferred Hall Parameter vs. Calculated Electron Hall Parameter Considering only Coulomb Collisions.

assuming only Coulomb collisions (cf. Equation IV.11). Since Coulomb collisions dominate over electron-neutral collisions for ionization fractions above 1%, neglecting the latter cannot account for this discrepancy. The only other known phenomena which can account for this is scattering of electrons by waves.

Waves with oscillating electric fields of exponentially increasing amplitude (plasma instabilities) impede the passage of current carrying electrons within the plasma, resulting in anomalously high electron collision frequencies. As a result of these large electron collision frequencies the resistivity of the plasma is increased, necessitating the presence of large electric fields to maintain current continuity. Near the anode where the current density is relatively large, anomalous scattering of current carrying electrons by plasma instabilities can result in electric fields in excess of 5000 V/m.

Figure IV.36 shows the ratio of the inferred electron collision frequency calculated from Equation IV.15 (ν_e) to the electron-ion collision frequency calculated with Equation IV.11 (ν_{ei}) as a function of $J^2/\dot{m}$. As the figure shows, at low $J^2/\dot{m}$ the overall electron collision frequency is approximately three times larger than that calculated

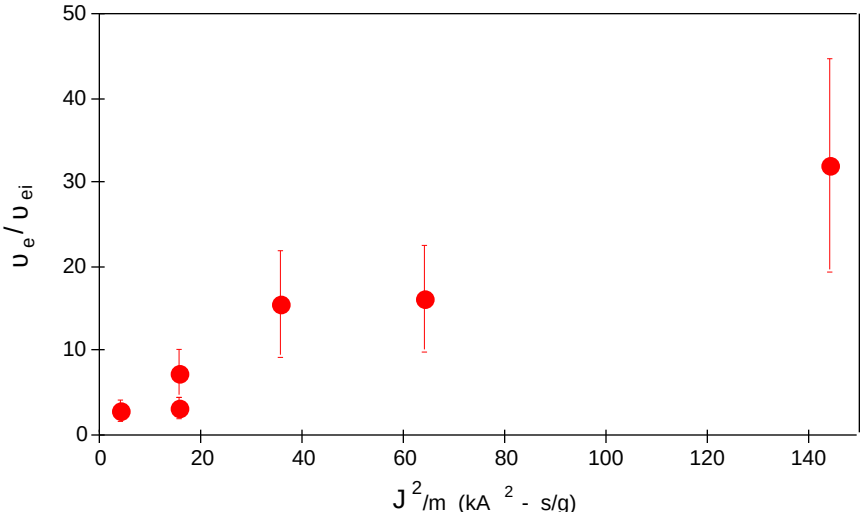

Figure IV.36: Ratio of Inferred to Calculated Coulomb Electron Collision Frequency vs. $J^2/\dot{m}$.

assuming only electron-ion collisions. As $J^2/\dot{m}$ is increased, the inferred collision frequency becomes substantially larger than the electron-ion collision frequency. For a $J^2/\dot{m}$ of 144 kA^2-s/g, the overall electron collision frequency is over thirty times larger than the Coulomb collision frequency. From the experimental data presented it is clear that for over much of the thruster operating range, anomalous effects are predominantly responsible for the dissipation of power in the plasma near the anode. Recent modeling results have shown that a correlation exists between the anomalous collision frequency and the electron Hall parameter calculated assuming only electron-ion collisions[43, 44]. A comparison of the modeling results of Reference [44] with experimental data obtained for this thesis is presented in Appendix A.

Chapter V

Anode Hall Parameter Reduction by Magnetic Field Cancellation

V.1 Introduction

The test of a method for decreasing anode losses by reduction of the electron Hall parameter in the vicinity of the anode surface is presented in this chapter. The approach is to decrease the local magnetic field by using the azimuthal component of the magnetic field produced by an array of permanent magnets imbedded beneath the anode surface. As a proof of concept, a standard benchmark thruster with an anode containing thirty six permanent magnets was tested. This device – the Magnetically Annulled Hall Parameter (MAHP) anode – was operated with argon and helium propellants at flow rates between 1 and 16 g/s and currents between 4 and 20 kiloamps. Though preliminary in nature, the experiment produced promising results. Incorporation of the MAHP anode led to thruster operation with significantly reduced anode falls, anode heating rates, and anode power fractions.

V.2 Background Information

In the previous chapter, the Hall parameter was shown to be a dominant scaling parameter for the anode fall. Recently, modeling results have shown that for configurations in which current carrying electrons must cross magnetic field lines to maintain current continuity, the anomalous collision frequency due to plasma microturbulence scales with the electron Hall parameter[43, 44]. Experimental corroboration of those findings is presented in Appendix A. Therefore, anode losses might be reduced if the plasma can be made less turbulent by decreasing the electron Hall parameter.

Attempts to reduce anode losses by increasing the electron collision frequency via the injection of propellant through or near the anode (i.e. decreasing the Hall parameter) has had some limited success[90, 45, 84]. In general, the anode fall is reduced somewhat with little or no effect on thrust. However, since these studies were performed on thrusters operating at low exhaust velocities (<20 km/s) in which electrothermal thrust contributions are significant, no conclusive verdict on the utility of anode propellant injection for MPD thrusters operating at large exhaust velocities is yet on hand. The difficulty in using propellant injection to reduce the Hall parameter is that in order for this injected mass to significantly increase the local electron collision frequency without degrading thruster performance, a substantial fraction of it needs to be ionized over a length scale commensurate with the anode fall region. Therefore, careful matching of the anode injection flow rate with thruster operating conditions is necessary to insure that this injected mass does not simply decrease the thruster specific impulse without significantly reducing anode power deposition. Criteria for determining adequate anode propellant flow rates are not readily apparent.

A more promising approach to decreasing the Hall parameter is to decrease the ambient magnetic field. In principle, if permanent magnets (or electromagnets) are arranged in the anode in such a manner that their magnetic field opposes the local field generated by the discharge current, the resulting reduction of the electron Hall parameter should lead to a decreased anode fall. In order to significantly reduce the Hall parameter, the cancellation field must be of the order of the current induced magnetic field. The impact of the magnetic field alteration near the anode on engine thrust will

be minimized if the cancellation field is limited to a small region near the anode. Ideally, the magnetic field generated by the imbedded magnets should be localized to within a distance comparable to the anode fall region (i.e. a few millimeters from the anode surface). Beyond this region, the cancellation field should be negligible in comparison to the ambient field.

An attempt was made to develop an anode with a cancellation field similar to that described above. Results of an experiment to test this concept is presented throughout the remainder of this chapter. Although the effect that this modified anode has on thruster performance, anode current conduction, and plasma transport properties near the anode is not fully understood, the promising results of this crude experiment suggest that this technique has potential for suppressing anode losses.

V.3 Experimental Investigation: Proof of Concept

V.3.1 MAHP Anode Design

The anode of a standard benchmark thruster has been modified to reduce the current induced azimuthal magnetic field in the vicinity of the anode surface and thereby reduce the Hall parameter at the surface. In principle, this device – the *Magnetically Annulled Hall Parameter* (MAHP) anode – can operate in steady or pulsed self-field MPD thrusters with currents from a few amperes to several tens of kiloamps for a variety of propellants and propellant flow rates so long as proper cancellation field matching is done. For this particular anode, the magnitude of the counteracting field at the anode produced by the permanent magnets varies with position, ranging from a few Gauss to 300 Gauss. Optimum cancellation is achieved when the current induced field is the same as the counteracting field.

The thruster consists of a standard aluminum cylindrical thrust chamber 5 cm deep with an inner diameter of 15.0 cm and an outer diameter of 18.8 cm. The MAHP anode is machined from an aluminum disc and is insulated with a thick nylon cover in order to restrict current collection to the lip (cf. Figure V.1). The uninsulated surface area of the MAHP anode is identical to that of the modified benchmark thruster anode.

Results of prior measurements show that the magnetic field at the midlip of the

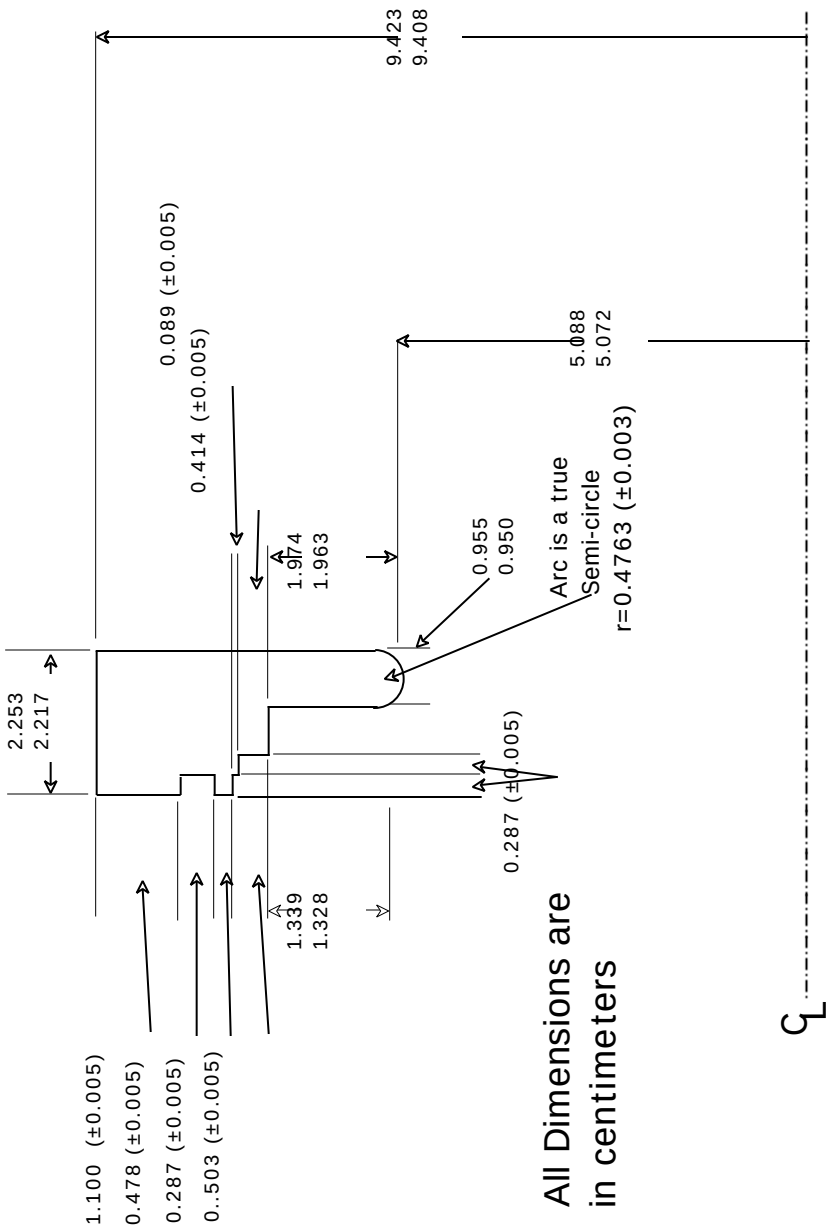

Figure V.1: Side View of MAHP Anode.

benchmark thruster anode varies from 200 to 1000 G. Therefore, the desired range of field cancellation strength from the permanent magnets is also within this range (200 to 1000 G). Cylindrical magnets (neodinium-iron-boron) nominally 0.64 cm in diameter and 0.32 cm high, with poles (N-S) on either face were selected on the basis of their small size and intense magnetic field. The magnitude of the magnetic field on either magnet face is approximately 3000 G.

To determine a satisfactory configuration of the permanent magnets, a calibration test rig was constructed in which several magnets were attached to the inner surface of a quartz cylinder to simulate the MAHP anode. The cylinder, with an inner diameter of 15 cm and a length of 8 cm, was clamped to a rotating table of a milling machine. A Hall probe was anchored to a hinged boom that was attached to the milling machine collar, allowing for precise magnetic field measurements to be made near the magnets. The Gaussmeter and Hall probe measure magnetic fields to within 1%. After several magnetic field surveys were made with the magnets oriented in a variety of configurations, a satisfactory arrangement was obtained.

Figure V.2 shows the front view of the anode with eight of its thirty six magnet passages. The gray portion of the figure illustrates the portion of the downstream anode face that is insulated from the discharge. The axis of each passage passes within 0.013 cm of the anode axis of symmetry. The centerline of each cylindrical passage is positioned once every 10 degrees in the azimuthal direction. A photograph of the uninsulated MAHP anode is shown in Figure V.3.

Figure V.4 shows a cross sectional view of the anode with magnet passage, insulating O-rings, and compression ring for the inner O-ring. Each magnet passage comes to within 0.32 cm of the midlip surface and 0.140 cm of the downstream anode face. The cylindrical passages are 0.68 cm wide, 4.02 cm deep, and flat at the base. The top of the passages are all threaded (5/16" 24) for a length of approximately 1.3 cm.

Each magnet is attached to the unthreaded end of a placement rod (cf. Figure V.5), with half of the rods having the north pole exposed while the remaining half having the south pole exposed. The magnets are arranged in an alternating pattern (N-S-N ... etc.). The magnetic field strength is adjusted by manipulating the depth of each element. Figure V.6 shows the static (zero thruster current) azimuthal magnetic field

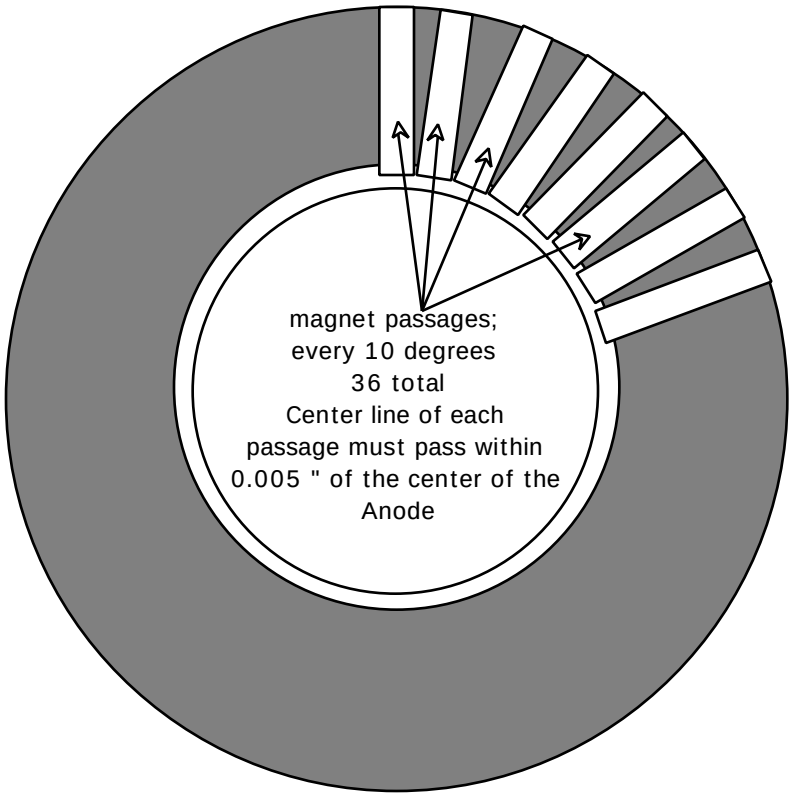

Figure V.2: Front View of MAHP Anode Structure.

Figure V.3: Photograph of MAHP Anode with Magnet Rod.

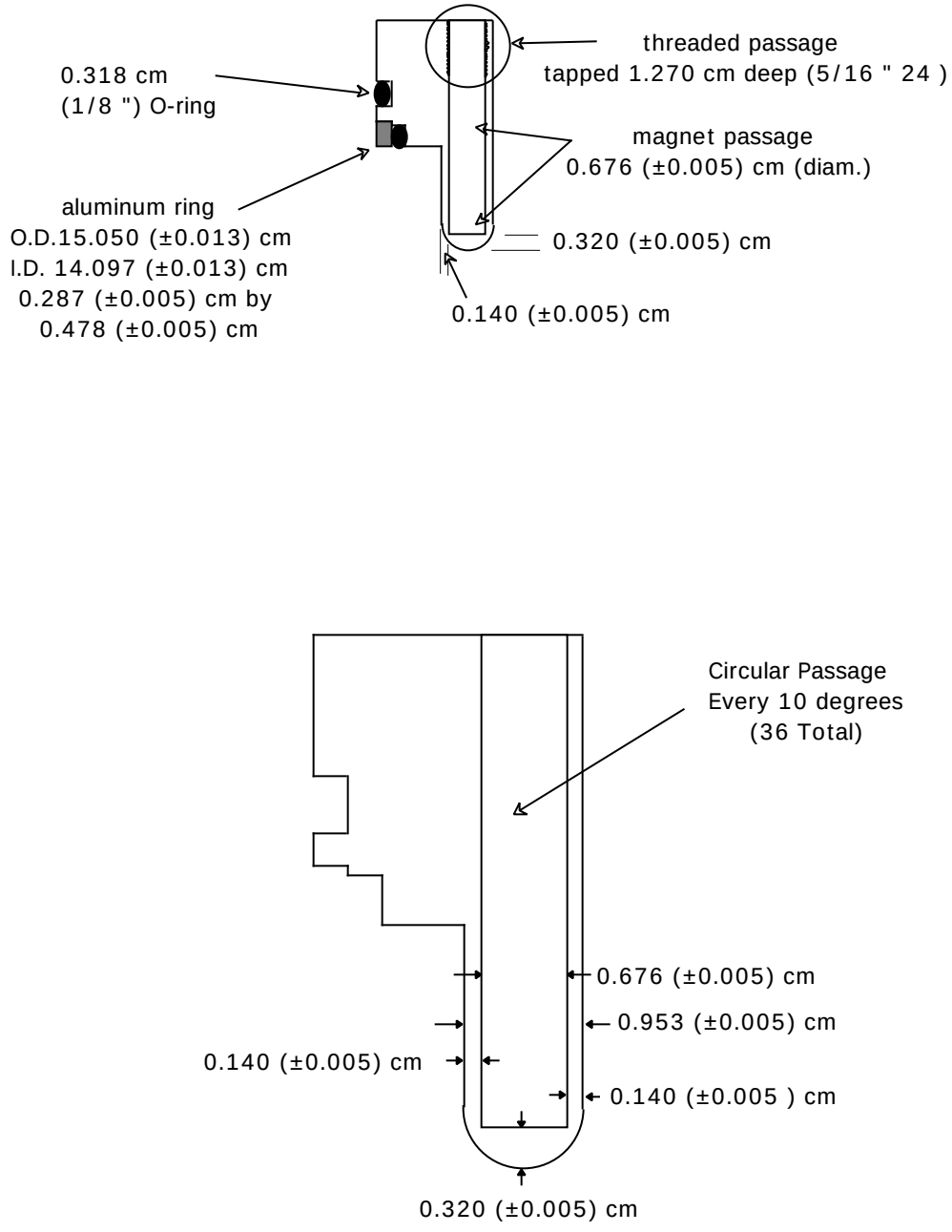

Figure V.4: Side View of MAHP Anode with Magnet Passage.

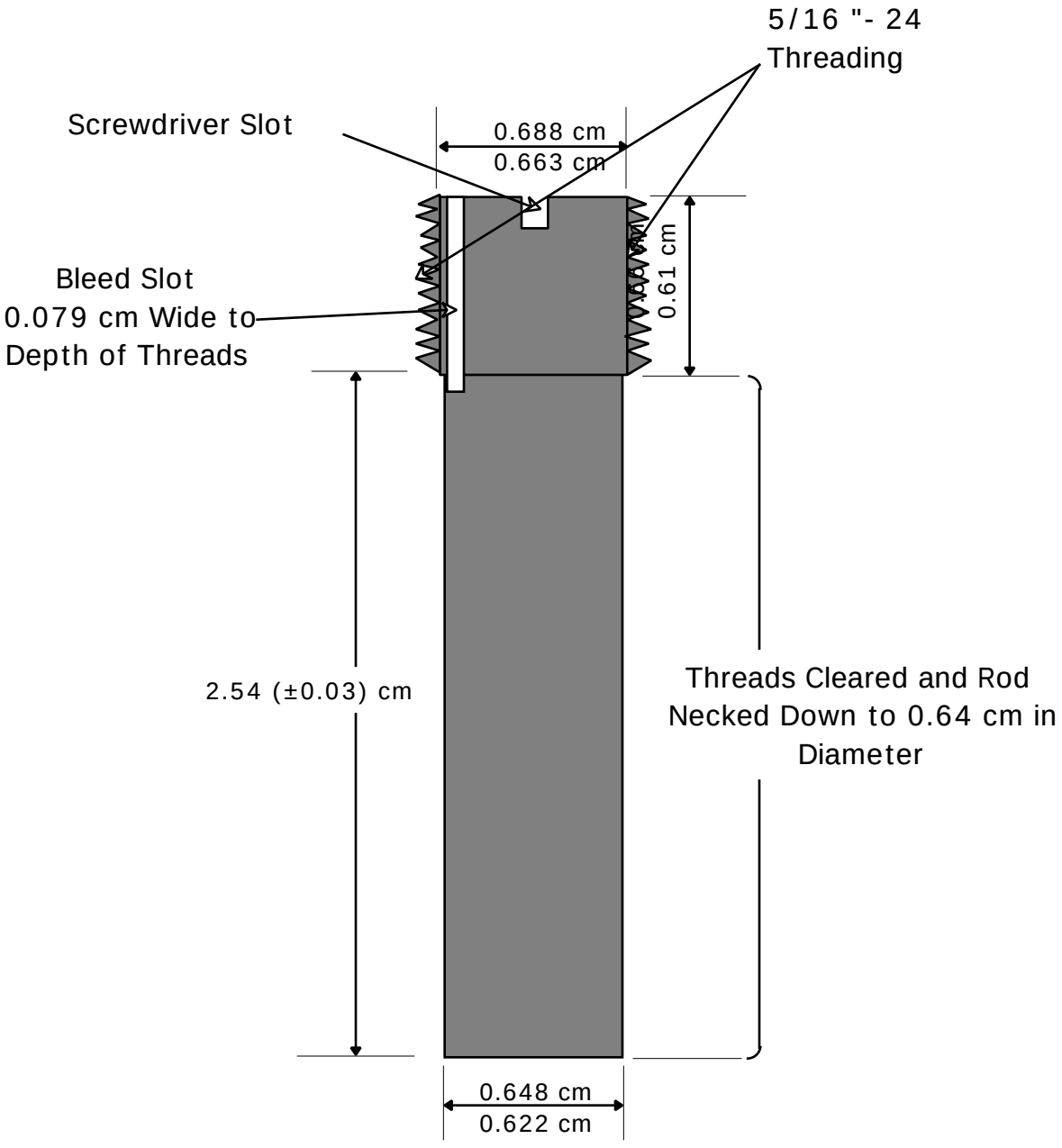

Figure V.5: Magnet Placement Rod.

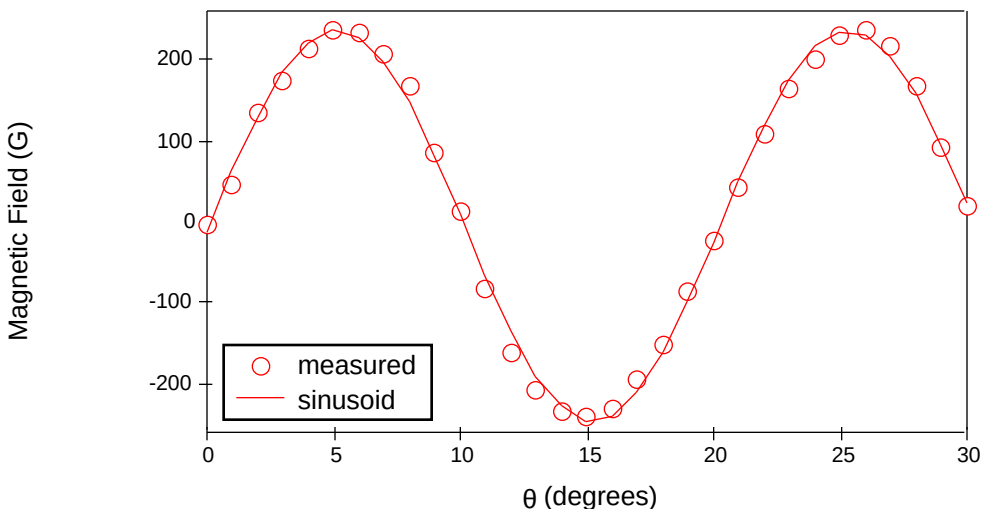

Figure V.6: Anode Surface Static Field Profile (1 mm radially inward from anode lip).

strength as a function of azimuthal angle. These measurements were taken 1 mm from the anode surface (midlip) with the Hall probe assembly described above. A least-squares curve fit is also presented to show the sinusoidal variation of the azimuthal field strength with angle. As the figure clearly illustrates, the alternating polarity of the magnets produces regions along the anode where the local azimuthal field generated by the current will either cancel or be reinforced. Peak magnetic field magnitudes 1 mm from the anode surface are approximately 250 Gauss.

Figure V.7 shows the static azimuthal field strength measured 1 mm from the anode midlip as a function of azimuthal angle (Theta) and axial position (Z). The line of peak values (Z=0) corresponds to data measured at the anode midplane (cf. Figure V.6). As the figure shows, the strength of the azimuthal magnetic field diminishes rapidly in either direction away from the midplane. The magnetic field profile is also symmetric in the axial and azimuthal directions.

In addition to azimuthal field components, the permanent magnets generate radial and axial magnetic field components as well. The interaction of these magnetic field

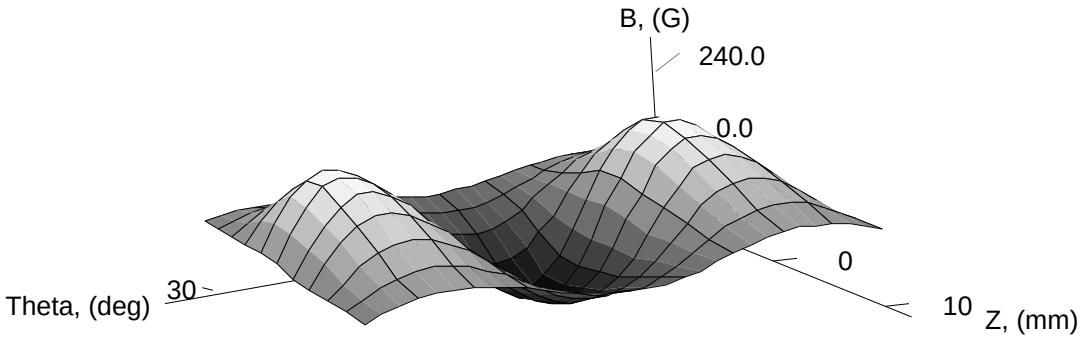

Figure V.7: Static Azimuthal Magnetic Field vs. Axial Position and Azimuthal Angle (1 mm from Anode Surface).

components with various current components (axial, radial, and possibly azimuthal) lead to complex flow conditions resulting from additional axial, radial and azimuthal force components. The presence of these components may have an adverse effect on thruster performance if they are significant over a large region of the thruster chamber. In the ideal situation, the influence of the MAHP anode's magnetic field should be only felt by plasma within the anode fall region (∼3-5 mm from the anode surface). To estimate the extent to which the MAHP anode's magnetic field is significant in comparison to the induced field, the radial variation of the MAHP anode static azimuthal magnetic field strength as a function of azimuthal angle was measured (cf. Figure V.8). Data collected 1 mm from the anode correspond to those displayed in Figure V.6. As the figure illustrates, the peak azimuthal magnetic field strength decreases by a factor of two over a span of 2 mm, and by a factor of five over 4 mm. A negligible azimuthal magnetic

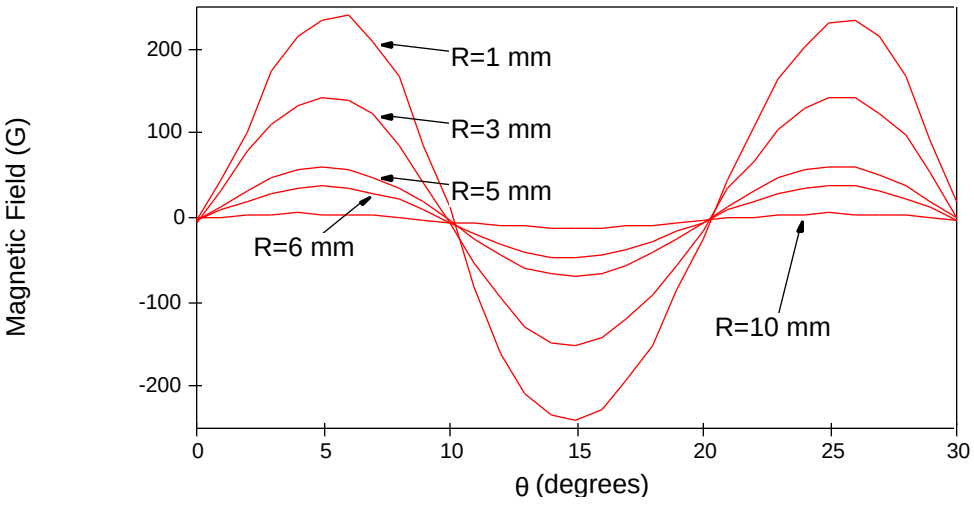

Figure V.8: Static Magnetic Field Radial Profile (along midlip).

field is measured 1 cm from the anode. The continuous radial variation of azimuthal field strength is presented in Figure V.9. As is evident from the figures, the magnetic field of the permanent magnets should have little effect on plasma more than 5 mm from the anode and no effect on plasma one or more centimeters from the anode lip. This implies that because of the small plasma volume affected by the permanent magnets, the thrust performance of the thruster is not expected to be significantly affected by the permanent magnets. In other words, the thrust of the engine should be largely unchanged since the vast majority of the plasma does not flow into the region in which the magnetic field is significantly affected by the permanent magnets.

In order to obtain a rough estimate of the actual magnetic field near the anode during a discharge, the static field data presented above were added to the previously measured azimuthal magnetic fields of the benchmark thruster (cf. Figure V.10). This rough calculation shows that the magnetic field generated by the permanent magnets causes the azimuthal component of the overall field 1 mm above the anode midlip to vary by almost 500 Gauss (by 300 Gauss 3 mm above the anode midlip). In fact, at low discharge currents the total azimuthal component of the magnetic field within cancel-

a)

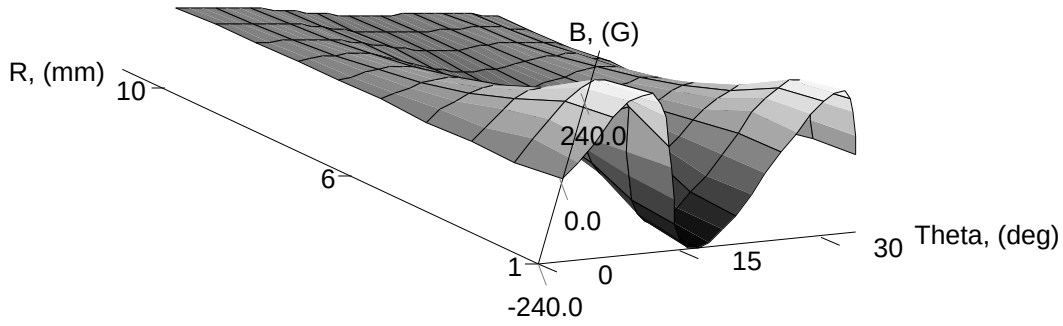

b)

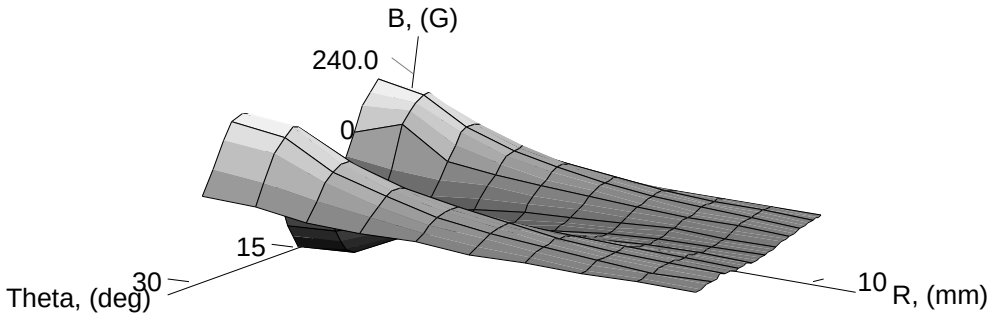

Figure V.9: Static Azimuthal Magnetic Field vs. Radial Distance from Anode and Azimuthal Angle.

a) 1 mm from anode surface

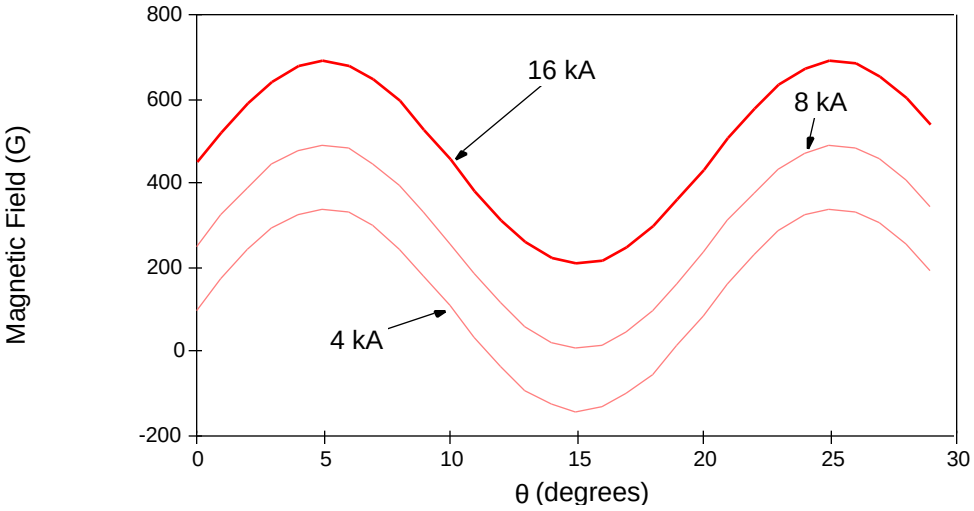

b) 3 mm from anode surface

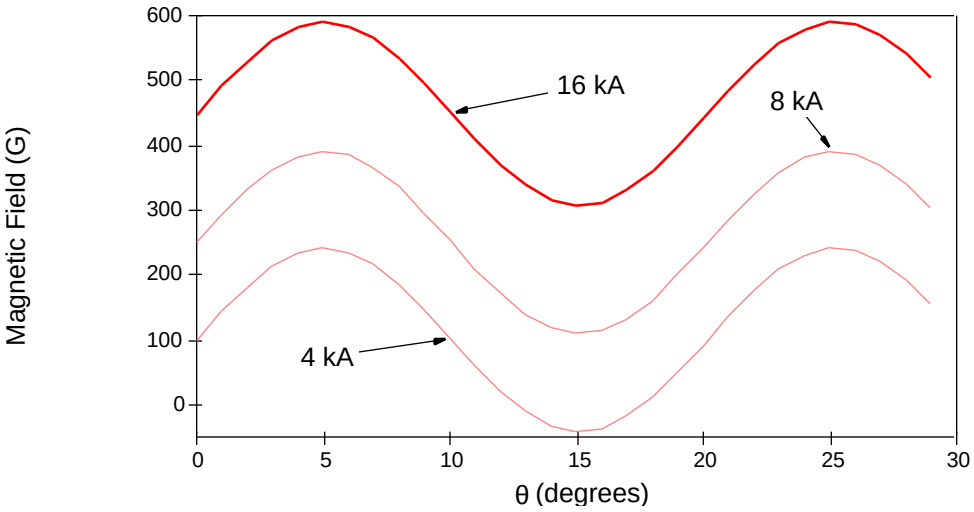

Figure V.10: Estimated Azimuthal Magnetic Field (at midlip) vs. Azimuthal Angle.

lation regions of the anode is estimated to be in the reversed direction of the azimuthal field in the enhancement zones[1]. The current should be concentrated within bands of relatively low magnetic field where cross field diffusion is easiest. Figure V.11 shows calculated (normalized) anode current density as a function of azimuthal angle along the anode midlip at thruster currents of 8 and 16 kA. The magnetic field distribution shown in Figure V.10 a was used with Ohm's law to calculate the current distribution. Values of electric fields, electron temperatures, and number densities used for the analysis were taken from probe data. As the figure shows, current is primarily transported to the anode through bands which coincide with maximum field cancellation (i.e. minimum ambient magnetic field strength). The analysis also predicts the anode current attachment at 16 kA to be more diffuse than at 8 kA. This is due to the fact that at 8 kA the magnetic field generated by the MAHP anode accounts for a larger fraction of the overall field strength than at 16 kA. Since at 16 kA the magnetic field near the anode remains somewhat large in either type of zone, the relative change in current density between the zones is smaller than at 8 kA. The actual current and flow patterns near the anode, however, are certain to be complex, the analysis of which is beyond the scope of this thesis.

V.3.2 Experimental Results

A series of experiments to test the new anode was performed with two primary goals:

1. To verify that reduction of the local Hall parameter by use of magnetic field cancellation leads to a decrease in the anode fall.

2. To map the general operating characteristics of the MAHP thruster, to permit comparison with standard or modified benchmark thruster behavior.

Figure V.12 shows the voltage current characteristics of the benchmark (no magnets) and the MAHP thruster (labeled "magnet"). Systematic and random errors are represented by the error bars. At low thruster currents and at the lower of the two mass flow rates for each propellant type, the terminal voltage of the MAHP thruster is

[1]It is almost certain that the discharge current pattern will adjust itself to prevent this from happening.

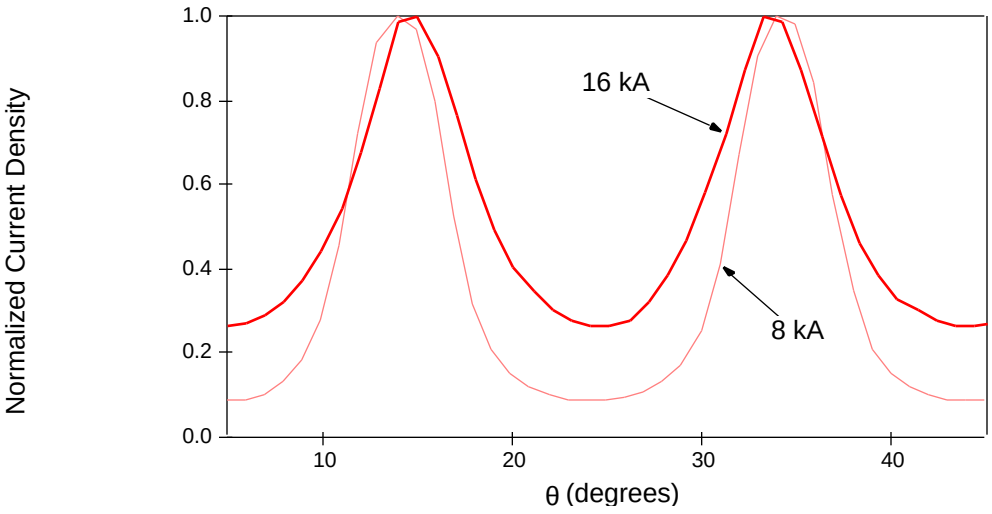

Figure V.11: Normalized Radial Anode Current Density vs. Azimuthal Angle (along midlip).

a few volts larger than that of the benchmark thruster. For these operating conditions, the magnitude of static magnetic field produced by the magnets, at the MAHP anode surface, is larger than the field generated by the discharge current. Above 10 kA, however, with argon propellant at both mass flow rates and helium at its lowest flow rate, the trends reverse with the MAHP thruster operating at terminal voltages 5 to 15 volts lower than the benchmark thruster. The terminal voltage characteristic of the MAHP thruster operating with helium at 4 g/s is similar to that of the benchmark thruster.

The magnetic field at locations of self-field cancellation and addition are shown in Figure V.13. These data, accurate to within 2%, were collected with a magnetic field probe (B-probe) positioned 3 mm from the anode midlip at adjacent cancellation and field addition zones (cf. Figure V.14). The presence of the field generated by the magnets are clearly shown in this figure. At all thruster operating conditions, the measured field strengths in the cancellation zones are less than those in regions of field addition. Moreover, with argon propellant the magnetic fields measured in enhancement regions are higher than the corresponding fields measured with the benchmark thruster.

a) argon

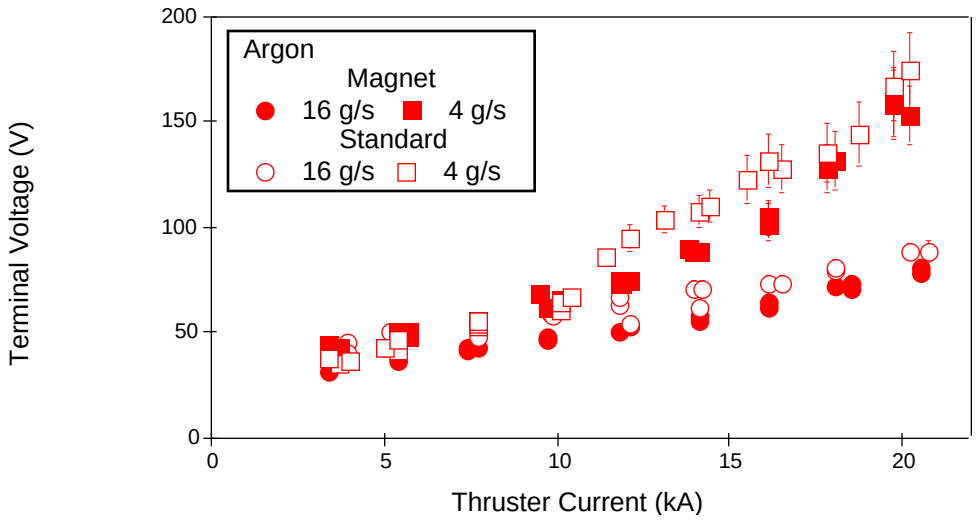

b) helium

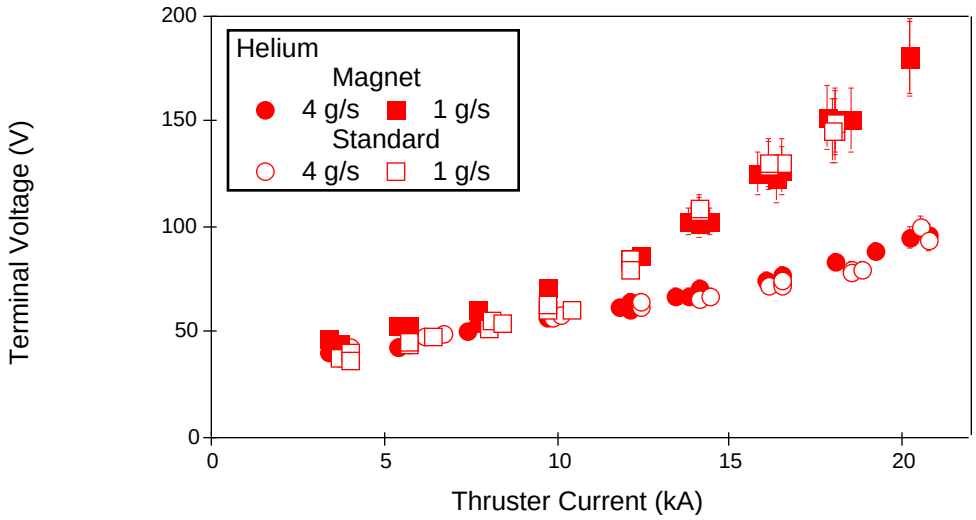

Figure V.12: Terminal Voltage vs. Thruster Current.

a) argon

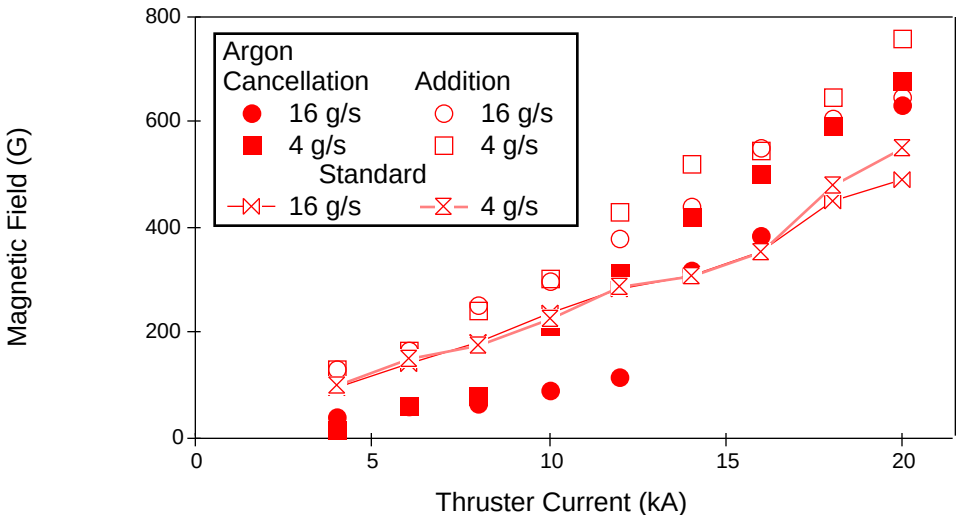

b) helium

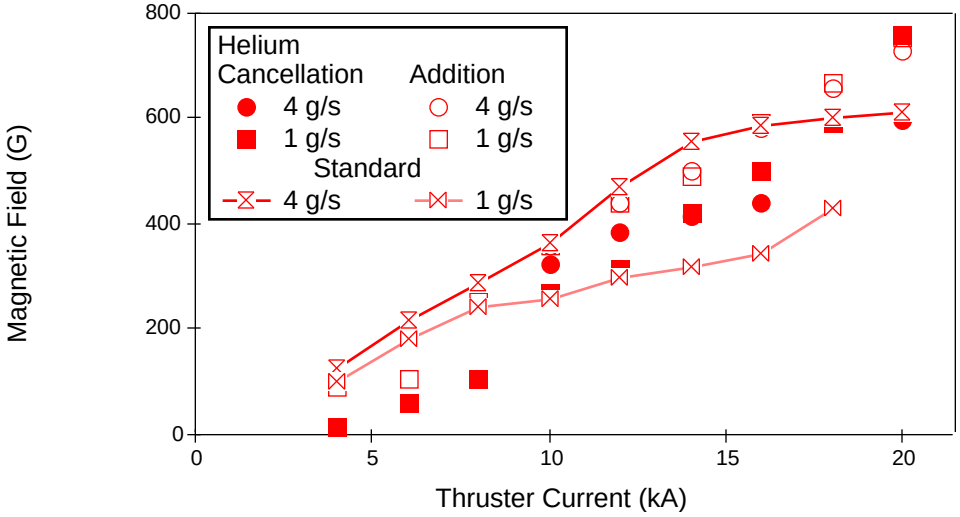

Figure V.13: Magnetic Field vs. Thruster Current.

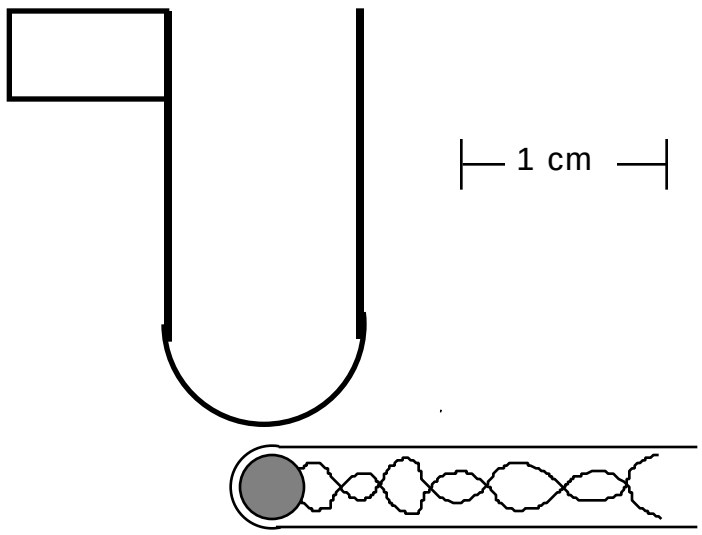

Figure V.14: Location of Magnetic Field Measurements.

At an argon flow rate of 4 g/s and for thruster currents above 10 kA, however, the measured field strengths in both the cancellation and addition zones are higher than the corresponding benchmark thruster values. Abrupt jumps in cancellation field strength are observed above 8 and 12 kA for argon flow rates of 4 and 16 g/s, respectively.

Similar behavior is exhibited with helium data. At currents below 10 kA, cancellation field data for both helium propellant flow rates are practically identical. However, with helium at 4 g/s and currents between 10 and 18 kA, the magnetic fields for the standard device are larger than those at either region of the MAHP anode. Furthermore, at currents below 10 kA, the magnetic fields in regions of field cancellation, are significantly lower than those of the benchmark thruster and at the adjacent zone of field addition. In general, at currents wherein the magnitude of the azimuthal magnetic field approaches that produced by the MAHP anode ($\sim$200 Gauss), the magnetic field at the cancellation zones abruptly increases. This clearly implies that a significant redistribution of current along the anode takes place at these transition conditions.

Figure V.15: Discharge of MAHP Anode (4 kA-4 g/s:argon).

To obtain qualitative information about the anode current pattern, unfiltered time integrated photographs of the discharge were taken at several conditions for helium and argon. These photographs, taken at thruster currents below and above the transition current (cf. Figures V.15 and V.16, respectively), show discrete azimuthal bands downstream of the midlip. As predicted, these bands, which presumably indicate regions of current attachment, are seen only (cf. Figure V.11) within field cancellation zones.

Figures V.17 and V.18 show the electron temperatures and ion number densities measured 2 mm from the anode midlip via triple probe for the MAHP and standard anode. The electron temperature and ion number density near the anode for both propellants and thrusters vary between 0.8 to 4 eV, and 5×10^{18} to 4×10^{20} m^{-3}, respectively. Temperatures and number densities for the modified anode are virtually identical in either zone (cancellation or addition). For operation at the highest mass flow

Figure V.16: Discharge of MAHP Anode (12 kA-4 g/s:argon).

rate of either propellant, the attenuation of the local magnetic field does not significantly affect the electron temperature. However, with helium at a mass flow rate of 1 g/s and at currents below 10 kA, the current where the abrupt jump in cancellation field strength is observed, the electron temperature for the MAHP anode is almost twice as high as in the benchmark thruster. The cause for this increased temperature is unknown. With the thruster operating on argon at 4 g/s, at currents above 12 kA the electron temperatures of the MAHP thruster are somewhat lower than corresponding values measured in the benchmark thruster.

In order for insulator ablation to affect the deposition of power to the anode by reducing the Hall parameter, the injected mass must be ionized within a few millimeters of the anode surface to significantly increase the electron collision frequency within the anode fall region. The presence of these additional ions would appear in triple probe

a) argon

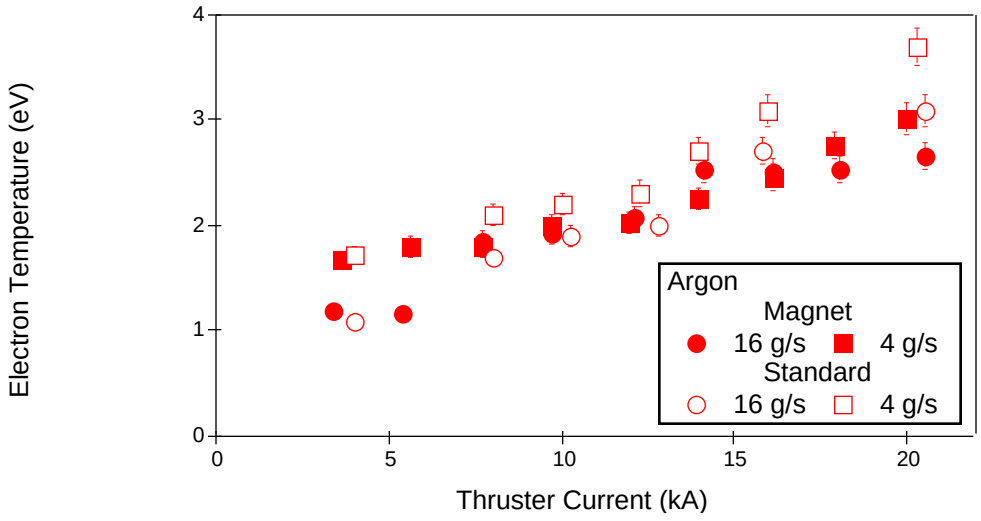

b) helium

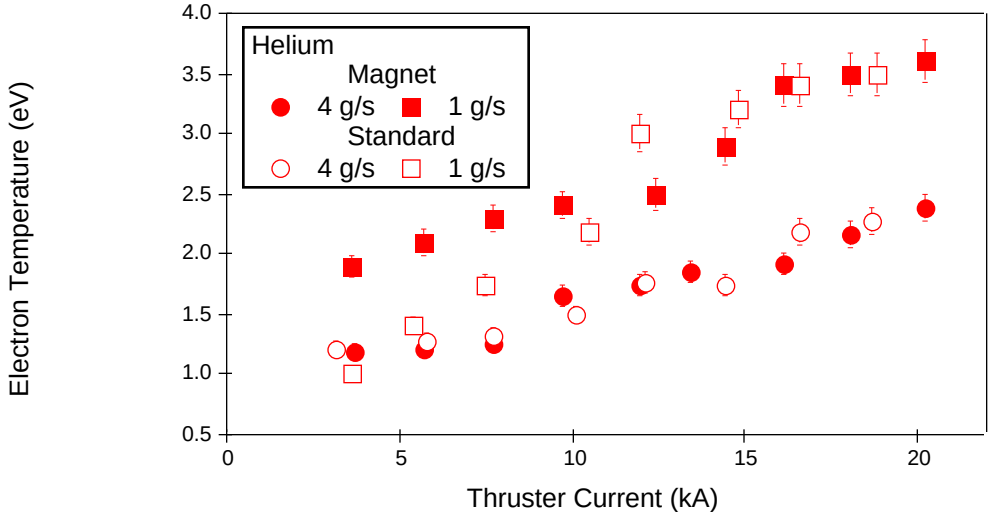

Figure V.17: Electron Temperature vs. Thruster Current.

a) argon

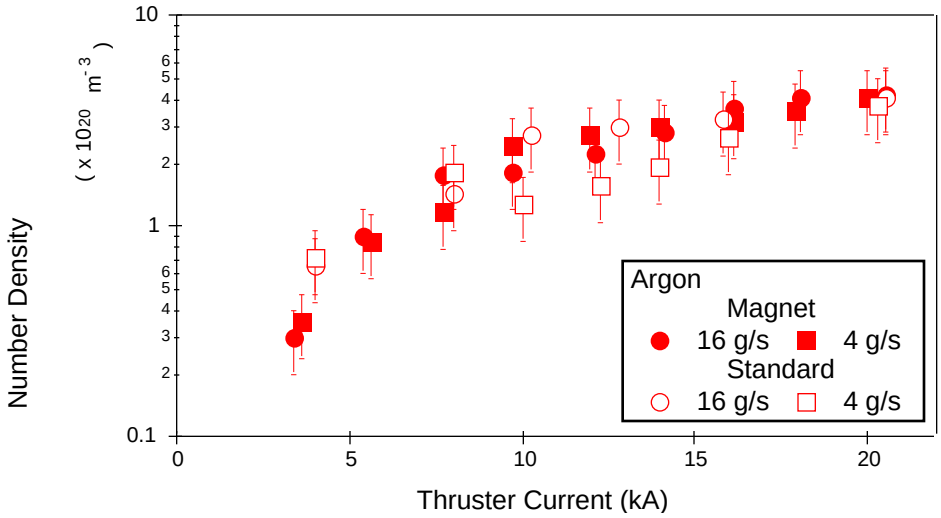

b) helium

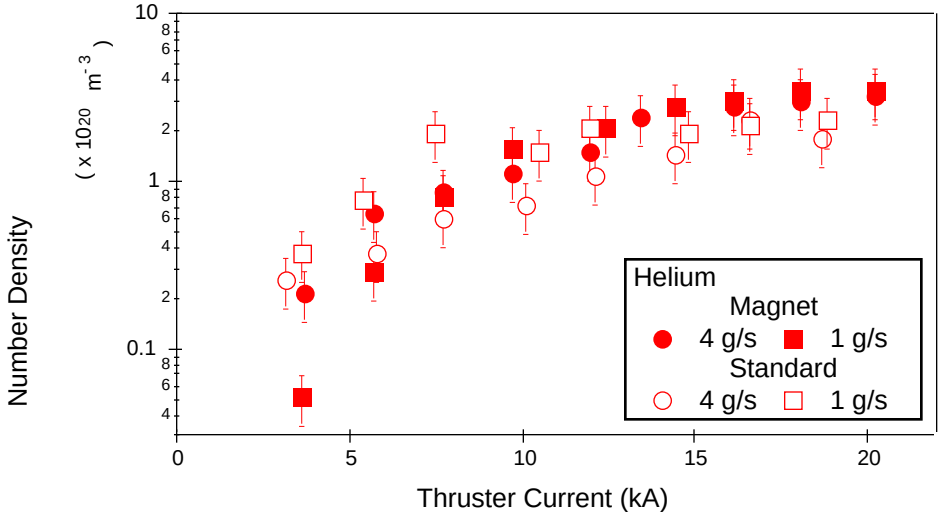

Figure V.18: Ion Number Density vs. Thruster Current.

measurements of ion number density. However, with the exception of the helium data at 4 kA-1 g/s, the number densities at the anode for either engine are virtually the same. Thus, the mass introduced by insulator ablation should not have significantly affected anode power deposition.

A floating probe was used to make plasma potential measurements throughout the anode region. Figure V.19 shows equipotential contours measured near the anode of the modified benchmark and MAHP thruster at a current of 16 kA and an argon propellant flow rate of 4 g/s. The cross in each figure is indicative of the positioning error of the probe ($\pm$1 mm). As the figure shows, the gradients of floating potential near the MAHP anode are considerable smaller than those of the benchmark thruster anode. Several azimuthal sites both in cancellation and addition zones of the MAHP anode were surveyed. Only a minor variation (5%) in floating potential gradient was observed from zone to zone. The floating potential measured 1 mm from the anode surface of either thruster is approximately 30 volts. However, the maximum floating potential measured one centimeter from the MAHP anode is 45 volts; considerably less than the 75 volts measured the same distance away from the modified benchmark thruster anode. This result is surprising since the magnetic field generated by the permanent magnets should be negligible 1 cm from the anode surface and so should have little influence on the plasma potential this far from the surface. Therefore, the effect of the MAHP anode on current collection close to the anode surface may be felt by the entire discharge.

Figure V.20 shows floating probe measurements in the vicinity of the MAHP anode at a thruster current of 8 kA and a helium propellant flow rate of 1 g/s. This figure is a compilation of data collected in both cancellation and addition zones. Again, there was negligible discrepancy (5%) between the data collected at either type of zone. Thus, the presence of the MAHP anode magnetic field does not appear to result in the establishment of strong azimuthal electric fields one or more millimeters from the anode surface. The floating potential near the anode surface is approximately 20 V while those measured 1 cm away reach a maximum value of 29 volts. For both argon and helium data, the maximum floating potentials are measured downstream of the anode midplane. The equi-potential lines in Figure V.20 tend to converge downstream of the anode midplane as well. This trend, however, is not exhibited in the argon data (cf.

a) Modified Benchmark Thruster

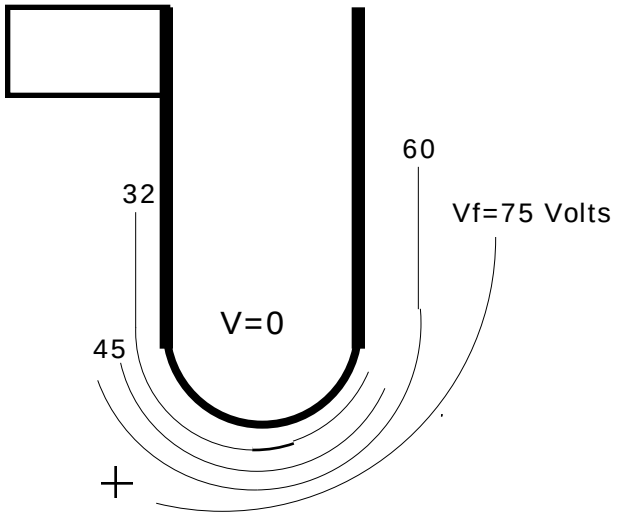

b) MAHP Thruster

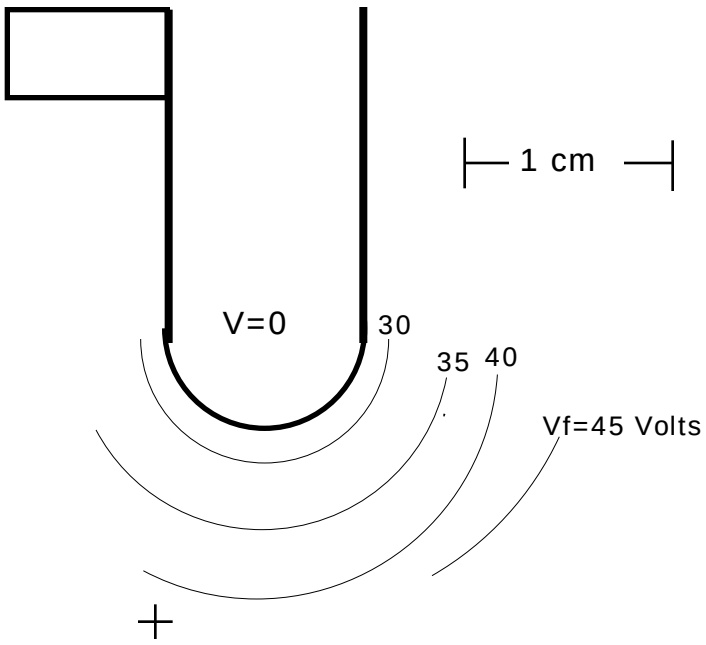

Figure V.19: Anode Floating Potential Profiles (16 kA-4 g/s: argon).

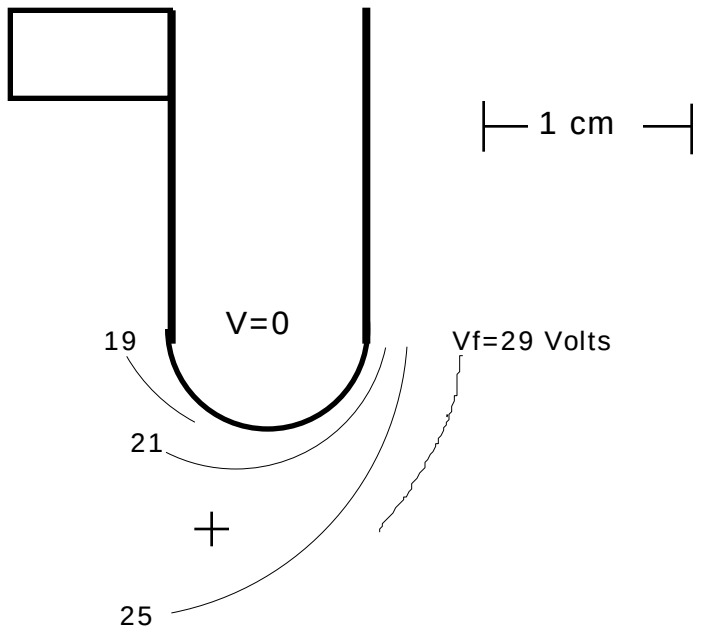

Figure V.20: Anode Floating Potential Profiles (8 kA-1 g/s: helium).

Figure V.19 b).

Figure V.21 shows anode fall measurements as a function of thruster current based on floating probe measurements taken 1 mm from the anode surface (cancellation zones). Electron temperatures obtained with the triple probe are used in converting probe floating potentials to plasma potentials. The anode fall varies by less than ± 3 V along the lip and ± 5 V between zones. With the thruster operating on argon at currents below 12 kA, the anode falls for the modified device are higher than those of the benchmark thruster. Above this current, however, the MAHP thruster shows marked improvement over the standard device. At 4 g/s, significant reduction of the anode fall is not observed until the thruster is operating at high current (20 kA). The current at which the new device shows improvement over the original thruster (for either argon flow rate) corresponds to that at which the jump in magnetic field occurs (cf. Figure V.13 a).

This implies that the redistribution of the current (i.e. attachment at the downstream portion of the lip) may have led to a decrease in the anode fall.

With helium as propellant, however, a slightly different picture emerges. At a mass flow rate of 4 g/s, the anode falls of the modified device are less than those of the standard thruster throughout the range of operation, again irrespective of zone type. At 1 g/s, the anode falls of the MAHP thruster are significantly lower than those of the standard thruster only at currents above 12 kA, significantly above the current where the magnetic field transition occurs (cf. Figure V.13 b).

In general, the utilization of permanent magnets to decrease the local magnetic field appears to have resulted in thruster operation with lower anode falls. The MAHP anode produces a reduction in the anode fall of up to 15 V (37%) with argon and 20 V (50%) with helium. Of primary interest, however, is its effect on anode power fraction. In Figure V.22, anode power fractions calculated from Equation I.3 are plotted as a function of thruster power for the MAHP and benchmark thrusters. With argon as propellant and at power levels less than 0.5 MW, the MAHP anode power fractions are higher than those of the original device, varying between 0.3 and 0.5. At 4 g/s, the anode power fractions of both thrusters are equal within a power range of 0.5 to 2 MW. Beyond 2 MW, the anode power fraction of the MAHP thruster falls to 0.23, a 25% improvement over the standard benchmark thruster. When using argon at 16 g/s, the MAHP thruster operates at lower anode power fractions for power levels above 0.8 MW. With argon at 20 kA and 16g/s (1.8 MW), the MAHP anode reduces the anode power fraction by over 40% (0.38 to 0.22).

During operation with 1 g/s helium, below 0.4 MW, the anode power fractions of the MAHP thruster are higher than those of the standard benchmark device by as much as 27% (0.51—0.37). At higher power levels, however, the MAHP anode provides sizable reductions of the anode power fraction (e.g. 37% at 3 MW). For operation with helium at 4 g/s, the MAHP anode results in reduced anode power fractions over the entire range of operation. At 18 kA-4 g/s (helium) for example, the MAHP anode reduces the anode power fraction by 45%, the most significant amount observed in the experiment.

Anode power fractions for both the MAHP and the modified benchmark thruster are shown as a function of $J^2/\dot{m}$ in Figure V.23. The trends of the previous figure

a) argon

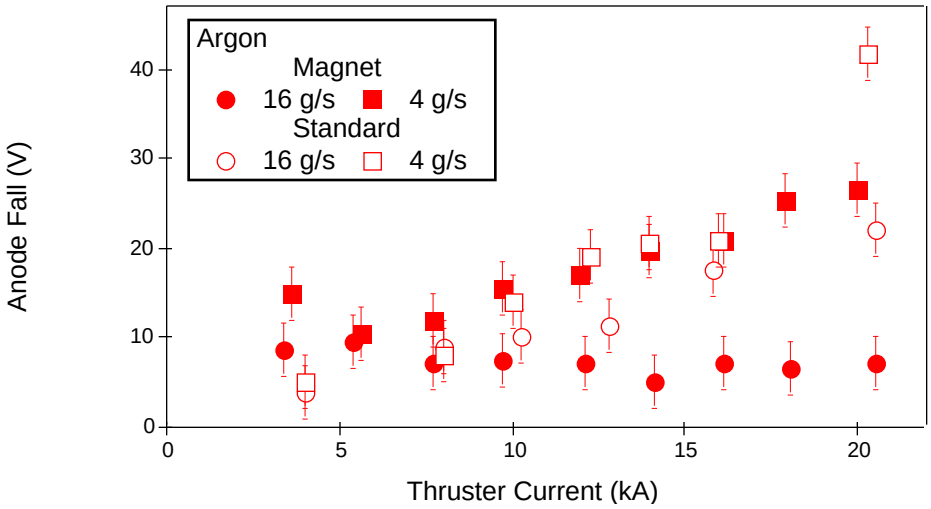

b) helium

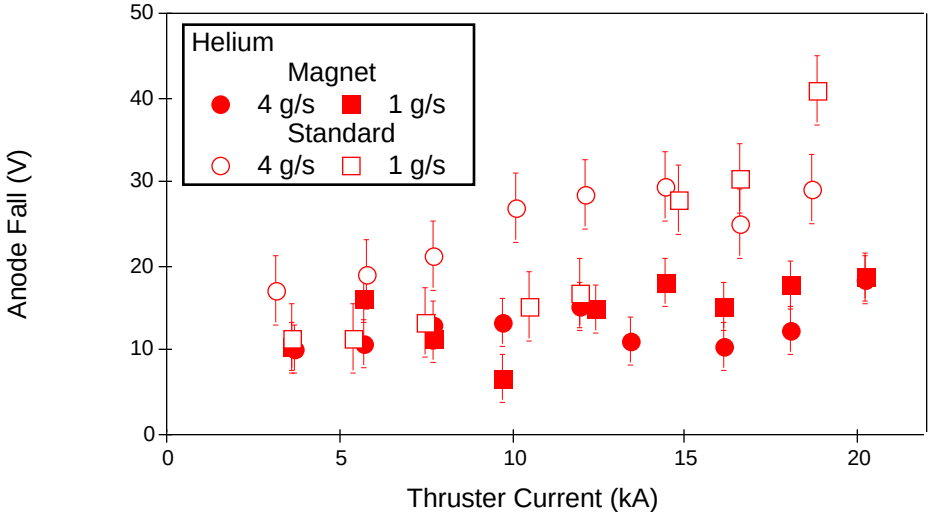

Figure V.21: Anode Fall vs. Thruster Current.

a) argon

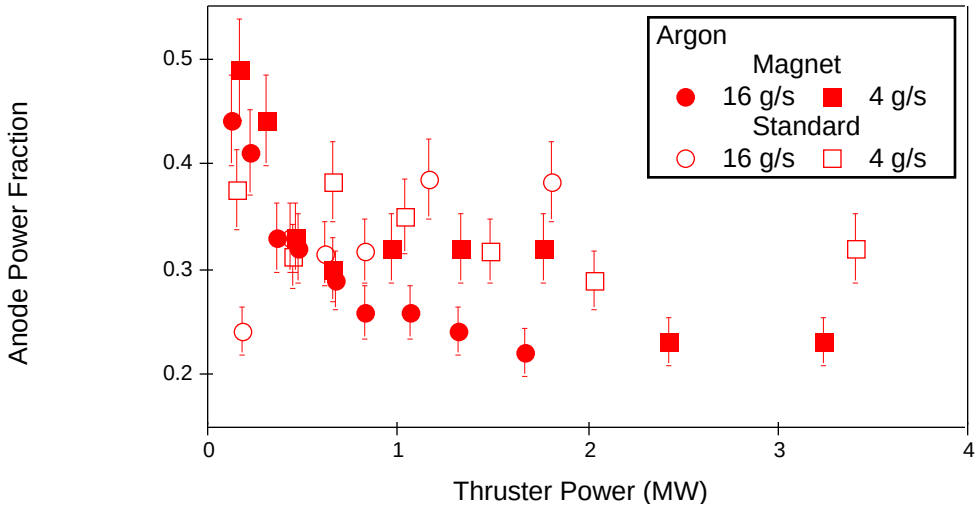

b) helium

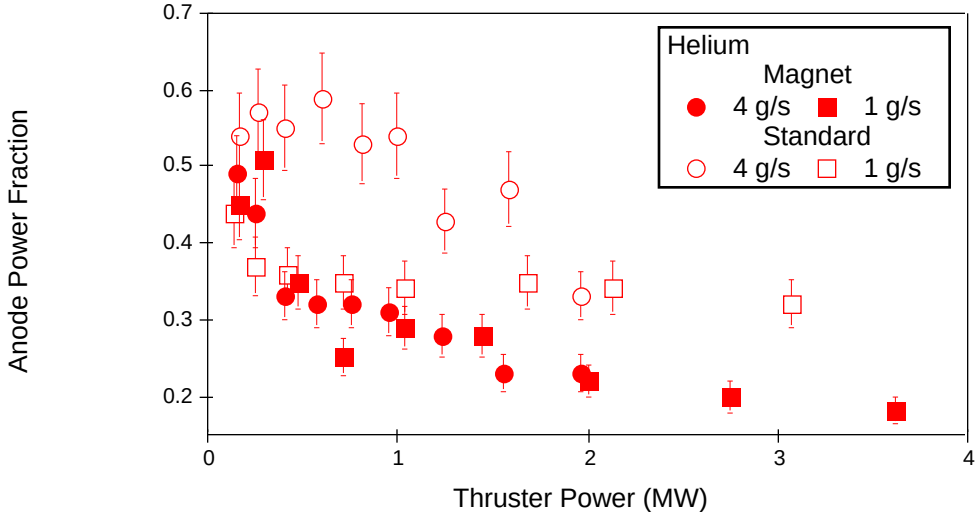

Figure V.22: Anode Power Fraction vs. Thruster Power.

(cf. Figure V.22) are evident in this figure as well. Using the Maecker thrust equation, which has been shown to be accurate for self-field MPD thruster operation in a regime in which most of its thrust is derived from electromagnetic forces ($J^2/\dot{m}$ above 55 and 135 kA^2-s/g for argon and helium propellants, respectively)[6, 66], the maximum specific impulse achieved in this study is estimated to have been 1600 seconds (16 km/s) for argon and 6400 seconds (64 km/s) with helium.

The principle function of the MAHP anode is to reduce the anode fall by decreasing the local Hall parameter. Figure V.24 shows the anode fall as a function of Hall parameter calculated from triple probe and B-probe data (cancellation zone) described above. As the figure illustrates, the correlation between the anode fall and the Hall parameter (cf. Figure V.24) appears in the MAHP anode data as well. Given the large error associated with these calculations (due primarily to uncertainty in number density estimates), it is difficult to determine to what extent the MAHP anode reduces the Hall parameter at the point of current attachment. Part b of the figure shows that the anode falls of the MAHP anode are lower than those of the benchmark anode even at conditions of large local Hall parameter (implying that the MAHP anode may have reduced the slope of the anode fall-Hall parameter characteristic). This trend is observed for operating conditions at which the current is blown downstream of the anode midlip. Assuming that the electron temperature and ion number density remain constant along the lip, an assumption which is supported by previous studies[19], the Hall parameter at the location of current attachment for these operating conditions will be significantly lower due to the lower magnetic fields measured there (cf. Figure V.25).

In summary, to decrease the anode fall, an attempt was made at reducing the electron Hall parameter near the anode by decreasing the local magnetic field. Although crude, this experiment yielded promising results that clearly demonstrate the concept's potential for decreasing anode losses for a variety of current carrying devices.

a) argon

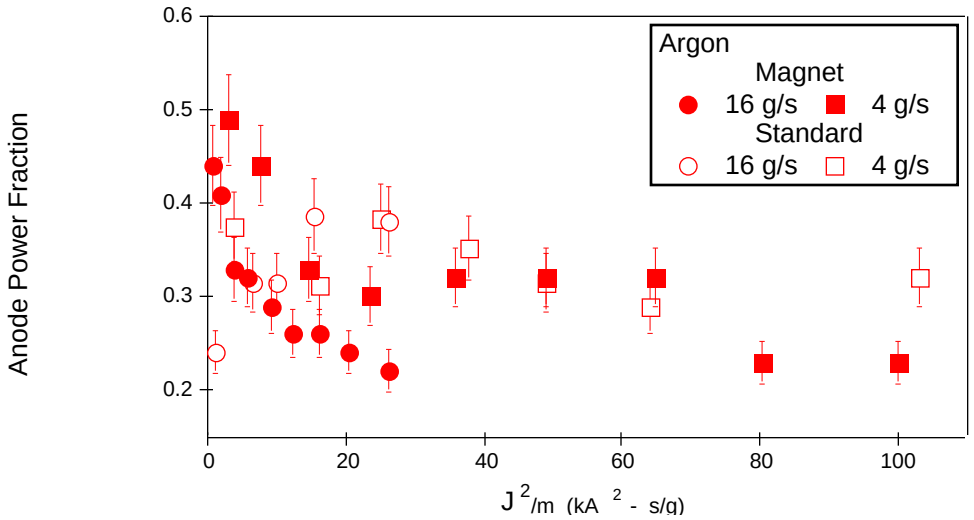

b) helium

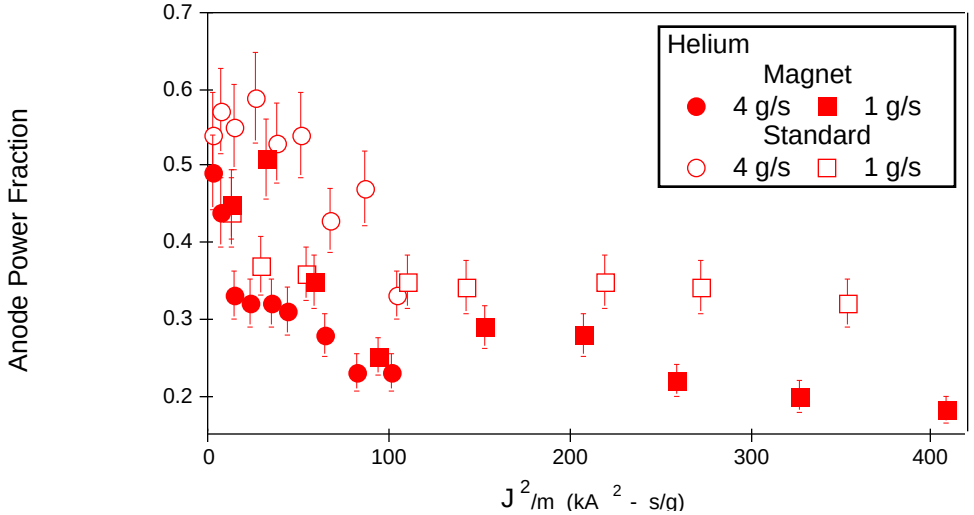

Figure V.23: Anode Power Fraction vs. $J^2/\dot{m}$.

a) argon

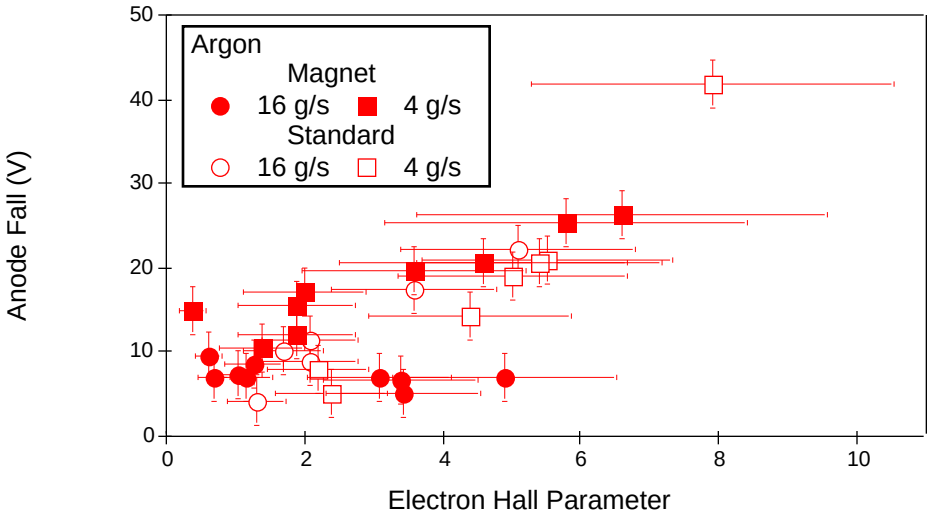

b) helium

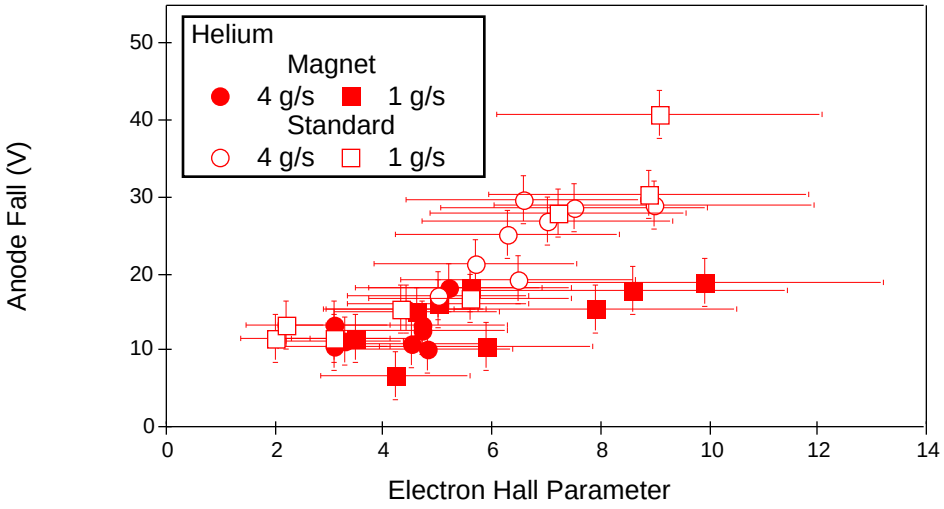

Figure V.24: Anode Fall vs. Electron Hall Parameter.

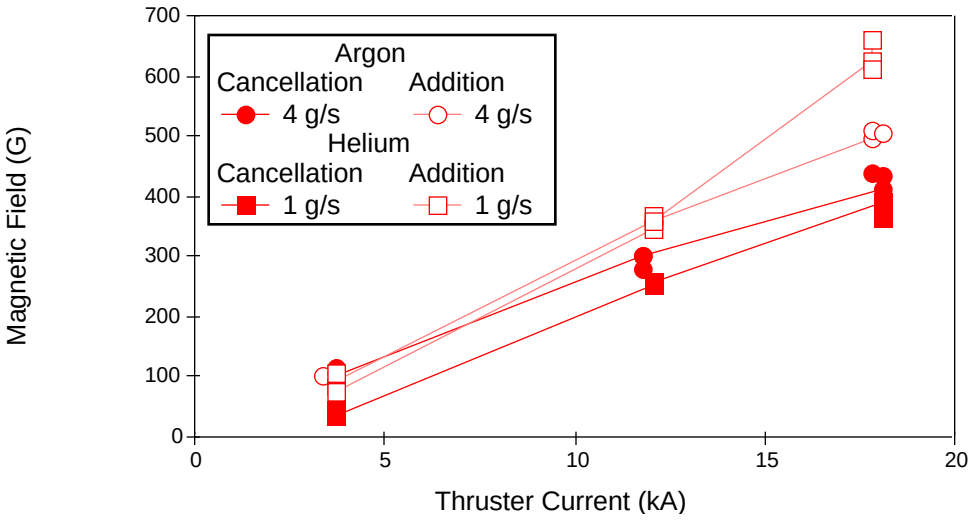

Figure V.25: Magnetic Field Measured Downstream of Lip.

Chapter VI

Summary and Concluding Remarks

VI.1 Summary

VI.1.1 Introduction

Anode power deposition was shown to be the dominant loss mechanism for MPD thrusters operating at power levels below a few megawatts. Both thermocouples imbedded within the anode, and Langmuir probes placed near the anode surface were used to determine anode heat fluxes. In general, anode power fraction decreased with increasing thruster power. With argon propellant, anode power fractions of 0.44 were measured at thruster power levels near 1 MW. At 6 MW however, the anode power fraction decreased to below 0.25. With helium propellant, the anode power fraction ranged from 0.7 at 150 kW, to less than 0.3 at 3 MW.

The anode fall was shown to be the dominant correlate of anode power deposition. Anode falls of almost 50 V were measured at thruster currents of 25 kA and 20 kA for argon and helium propellants, respectively. Negative anode falls were never measured in this investigation. Furthermore, the anode fall was found to correlate well with the electron Hall parameter calculated from electron temperature, number density, and magnetic field data obtained near the anode via probes. This led to the concept of reducing the anode fall by placing small magnets within the anode to decrease the

local magnetic field. Results of this experiment were encouraging. Incorporation of this modification led to reductions in the anode fall as high as 45%.

VI.1.2 Outline of Approach

The primary goal of this work was to develop engineering techniques for minimizing anode losses. To fulfill this goal, several milestones had to be accomplished.

- The means by which energy is transported to the anode had to be identified. This was necessary to create a foundation from which potential processes that govern anode power deposition could be identified.
- Trends in anode power deposition were established and suitable scaling parameters were identified. The determination of these controlling plasma state parameters is crucial for developing mechanisms for the control of anode heating rates.
- Finally, to reduce anode heating rates through manipulation of identified scaling parameters.

VI.1.3 Summary of Experiments and Findings

Anode power deposition in a standard benchmark thruster was first studied by imbedding several thermocouples within a hollowed section of the anode. By using a heat conduction model to infer anode heat fluxes from the response of the thermocouples, anode heating rates in excess of 1000 W/cm^2 were measured. Anode power fractions as high as 0.44 were measured at thruster power levels below 1 MW. At 6 MW however,the anode power fraction was below 0.2. In general, anode power fraction decreased with increased thruster power.

In addition, anode current density, electron temperature, ion number density, and plasma potential measurements were taken for the characterization of anode power deposition as a function of various plasma properties. Since the anode fall was shown to be the dominant mechanism for transferring heat to the anode of MPD thrusters, the major emphasis of the thesis was placed on studying this phenomenon.

Incorporation of electron temperature and current density measurements with anode heat flux measurements allowed for the deduction of the anode fall. For most thruster

operating conditions, the deduced anode falls compared favorably with those obtained by measuring the plasma potential near the anode surface with a floating probe. Large discrepancies exist between the two methods however, when the thruster operates at large values of $J^2/\dot{m}$ (>100 kA^2−s/g). The reason for this is thought to be due either to anode ablation or that the difference in potential between the anode and the plasma 1 mm away is not indicative of the potential energy that current carrying electrons deliver to the anode in the form of heat.

The observation that the anode fall is smallest at locations along the anode of high current density prompted the next phase of the experimental program; anode power deposition studies with an anode of reduced surface area. Current was allowed to flow only to the lip of the anode by applying a layer of aluminum-oxide to the remaining surface. Reducing the conducting surface area by 85% was predicted to lead to a two to four fold increase in anode current density at the lip. The diagnostics used in the first phase of the thesis were repeated with the modified anode. Although constricting the current to the lip resulted in a more uniform heat flux profile at the lip with roughly a three-fold increase in magnitude as well as in larger electric fields near the anode, no perceivable change in the anode fall or the terminal voltage was measured. Presumably, this was because the amount of increase in anode current density investigated was insufficient to significantly alter anode heating mechanisms.

For the next phase of the thesis, an extensive parametric study of the anode as a function of local plasma conditions was undertaken. The floating probe was used to measure anode falls, with both argon and helium propellants, of the modified benchmark thruster. In support of this endeavor, triple Langmuir and magnetic probe measurements were incorporated to acquire electron temperature, electron number density (setting n_e=n_i), and magnetic field data, respectively. This survey led to the primary contribution of the thesis, linking large anode falls to high electron Hall parameters in the ambient plasma. Further experimental evidence (cf. Appendix A) is introduced which suggests that the observed dependence of the anode fall on the Hall parameter may be a result of a current-driven plasma instability.

The last phase of the thesis was to test the hypothesis born out of the previous work by implementing experiments with a Hall parameter suppression anode. By imbedding

permanent magnets within the anode of a benchmark thruster, thus reducing the local Hall parameter in specific regions along the anode, a substantial decrease in anode losses was demonstrated. This crude first attempt at designing an anode which suppresses processes that lead to large anode heating rates had promising results.

VI.2 Conclusions and Suggestions of Future Work

VI.2.1 Conclusion

Strong experimental evidence has been presented which suggests that the electron Hall parameter is the primary scaling parameter of the anode fall. Plasma instabilities caused by wave particle interactions, have been identified as a possible mechanism for this dependence[43, 44]. Anomalously high electrical resistivities, measured in the plasma near the anode, support this conclusion (cf. Appendix A). However, none of the work presented herein offer any conclusive evidence that plasma instabilities are solely responsible for the deposition of power to the anode. Part of the power deposited to the anode may be due to a sheath. Modeling results of Appendix D suggest that the anode sheath may be the dominant source of the anode fall. However, the manner by which large axial currents (i.e. large Hall parameters) affect the anode sheath has not yet been established.

VI.2.2 Recommendations for Future Work

Although much progress has been made in developing schemes for reducing anode losses, a great deal of fundamental understanding of anode phenomena is still missing. The key question which is still unresolved is whether the anode fall is strictly a sheath effect or due to plasma instabilities fueled by the discharge current. As an approach to answering this question (i.e. sheath vs instability) and refining our understanding of anode processes in high current devices, the following research activities are suggested:

- Investigate the overall operating characteristics of the MAHP thruster. This includes measuring thrust and making electric and magnetic field measurements throughout interelectrode region of the thruster.

- The development of an advanced sheath model. The model should take into account magnetic field effects and should be coupled with a fluid code for the determination of suitable boundary conditions.
- Means should be developed for measuring electric fields and plasma potentials much closer than 1 mm from the anode surface. Spectroscopic means (e.g. Stark broadening) as well as planar Langmuir probes which poke through the anode surface (button probes) could be used to measure voltages within 0.1 mm of the surface.
- The identification of plasma instabilities near the anode (via Langmuir probe spectra) is a worthwhile activity which should be pursued.
- A model which describes electron diffusion across magnetic fields should be developed. This activity should be coupled with the instability work since the latter may determine the mode of diffusion (classical vs. Bohm).
- Mechanisms by which power dissipated in the plasma near the anode due to microinstabilities (i.e. anomalous resistivity) are deposited to the anode surface should be identified.

VI.3 Future Anode Designs

The research presented in this thesis has shown that the key to reducing anode losses in MPD thrusters may be to decrease the electron Hall parameter in the vicinity of the anode. Since the electron Hall parameter is simply the ratio of the electron gyrofrequency to the electron collision frequency, several approaches may be utilized to decrease the Hall parameter by either "decreasing the numerator (gyrofrequency)" or "increasing the denominator (collision frequency)."

First, as an extension to this work, the permanent magnets of the Hall parameter suppression anode should be replaced by small electromagnets. By having active control of the cancellation field, improved coupling between the suppression field and the induced field may be obtained.

Second, anode propellant injection may also serve as a means of decreasing anode loses. Proper coupling between the arc and the injected mass must be maintained to insure that the anode propellant does not decrease the performance of the thruster. However, if propellant is injected through an anode enclosure of relatively high pressure with a passage to pass current and propellant to the thrust chamber, the Hall parameter near the anode surface should be low by virtue of the large collision rates within the chamber. This device, called a hollow anode, is currently under investigation by the Air Force.

Lastly, if the anode surface intersects the magnetic field lines allowing the electrons to simply slide off field lines onto the anode surface, a reduction of the anode fall should incur. Studies conducted with applied-field MPD thruster utilizing tandem electromagnets wherein the angle of incidence of the axial magnetic field lines with respect to the anode surface were varied by adjusting the current levels of each electromagnet, found that minimum anode heating rates were measured when the axial magnetic field lines that trapped the bulk of the discharge current intersected the anode surface (i.e. when current carrying electrons reached the anode surface without crossing field lines)[90].

In short, the findings of this thesis open a whole new realm of possible anode designs which may lead to the operation of efficient MPD thrusters. The fact that manipulation of the magnetic field near the anode had a significant effect on anode heating rates suggests that the design of MPD thrusters with small anode heating rates are within our grasp. However, incorporation of one or more of the design themes presented herein are certain to make the appearance and operation of a future MPD thruster be quite different from those currently in use.

A Inferred Electrical Conductivity

A.1 Introduction

The question of whether anomalous effects (wave-particle interaction) play a significant role in the dissipation of power near the anode is still open to debate. For many years, researchers in the Soviet Union have concluded that large electric fields found near the anode of plasma thrusters are a result of plasma turbulence[69, 38, 39, 40, 41]. In non-Soviet literature, attempts to link dissipation of thruster power to turbulence has been scarce, with much of this work focused on identifying plasma instabilities through the analysis of terminal voltage [70, 71, 72] or Langmuir probe antenna data [43, 73]. More recently, electrostatic spectra taken near the anode of a benchmark thruster show evidence for the existence of the generalized lower hybrid drift instability [74] predicted by Choueiri [43]. Although these experiments have demonstrated that instabilities exist in the plasma of MPD thrusters at power ranges that span two orders of magnitude, virtually no direct measurements of anomalous transport properties (e.g. electrical conductivity) have been made. The sole exception is the work of Lovberg [75](1971), in which the electrical resistivity of the plasma in an applied-field quasi-steady MPD thruster was inferred from direct measurements of the local electric fields, magnetic fields, and current density. When compared to the resistivity predicted by classical formulae, he found that the inferred resistivity was several times (4.0 ± 1.5) larger. Lovberg concluded that this discrepancy was caused by "collective plasma phenomena" (i.e. plasma instabilities).

The goal of this appendix is to estimate the plasma electrical conductivity (resistivity) in the anode region of a benchmark MPD thruster by using an analysis that is similar in approach to that of Lovberg. Figure A.1 shows a diagram of the MPD thruster as well as the Cartesian coordinate system used for the analysis. Field (magnetic and electric) and current density data described in Chapter 3 are used to infer the electron collision frequency from Ohm's law. These inferred collision frequencies are then compared with those calculated from classical formulae.

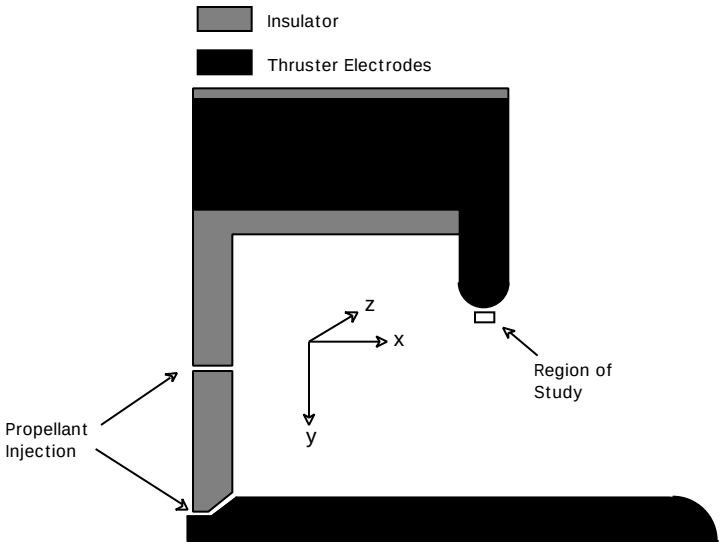

Figure A.1: Cross-sectional View of Benchmark Thruster Used for Experiment.

A.2 Analysis and Results

We begin by writing a form of Ohm's law (*generalized Ohm's law*) suitable for our purpose [76]

$$\mathbf{j} = \sigma_o(\mathbf{E} + \mathbf{v} \times \mathbf{B}) - \frac{\Omega}{|\mathbf{B}|}(\mathbf{j} \times \mathbf{B} - \nabla p_e) \tag{A.1}$$

where $\mathbf{j}$ is the current density vector, σ_o is the electrical conductivity, $\mathbf{E}$ and $\mathbf{B}$ are the electric and magnetic fields, respectively, $\mathbf{v}$ is the streaming velocity of the plasma (bulk velocity), and p_e is the electron pressure. The Hall parameter ($\Omega \equiv \omega_e/\nu_e$) is defined as the ratio of the electron cyclotron frequency (ω_e) to the *total* electron collision frequency (ν_e). For conditions of interest ∇p_e can be neglected (cf. Chapter 2) in the equation above. Equation A.1 then can be expressed by the following tensor [77]:

$$\mathbf{j} = \sigma_o \begin{pmatrix} \frac{1}{1+\Omega^2} & \frac{\Omega}{1+\Omega^2} & 0 \\ -\frac{\Omega}{1+\Omega^2} & \frac{1}{1+\Omega^2} & 0 \\ 0 & 0 & 1 \end{pmatrix} (\mathbf{E} + \mathbf{v} \times \mathbf{B}) \tag{A.2}$$

where the azimuthal current-induced magnetic field **B** defines the z axis of the Cartesian coordinate (Figure A.1). An axisymmetric current discharge is assumed allowing for the "z" components of **E**, **v**, and **j** to be neglected. After some algebra we arrive at two equations,

$$\sigma_o = \frac{(1+\Omega^2)j_x}{(E_x + B_z v_y) + \Omega(B_z v_x - E_y)} \tag{A.3}$$

$$\sigma_o = \frac{(1+\Omega^2)j_y}{\Omega(E_x + B_z v_y) + E_y - B_z v_x} \tag{A.4}$$

which relate the electrical conductivity to the "x" and "y" components of current. Since only one of these equations is necessary for the analysis, j_y, which represents the anode current density[1], is used to calculate σ_o through Equation A.4. The electrical conductivity σ_o is defined by the following equation:

$$\sigma_o = \frac{n_e q^2}{m_e \nu_e} \tag{A.5}$$

where n_e is the electron number density, q is the elementary charge, m_e is the electron mass, and ν_e is the *total* electron collision frequency. In order to be self-consistent (i.e. use the same electron collision frequency on both sides of Equation A.4), the electron Hall parameter used in Equation A.4 is calculated with the following relation:

$$\Omega = \frac{\sigma_o m_e \omega_e}{q^2 n_e} \tag{A.6}$$

where $\omega_e = qB/m_e$.

Table A.1 lists the field and current density data used for the analysis which were reviewed in Chapter 3. These measurements were made outside of the anode fall in a region 4 mm by 2 mm centered 2 mm from the anode (cf. Figure A.1). The magnitude of exhaust velocities is estimated from a model developed by Choueiri [66] which utilizes the "bJ^2" thrust law. The plasma streaming angle (v_x/v_y) was determined from Langmuir probe measurements. Neither the magnitude nor the direction (angle) of plasma streaming velocity had a perceptible influence on the outcome of the analysis.

The results of the analysis are presented in Table A.2 where Ω_{sh}, is the classical Hall parameter calculated with Equation IV.14 (Spitzer-Härm model) using Langmuir

[1]Both j_x and j_y were measured through the magnetic probe survey described in Chapter 3. Use of Equation A.3 does not alter the results presented here.

	j_y (A/cm^2)	E_x (V/m)	E_y (V/m)	B_z (T)	v_y (m/s)	v_x (m/s)
8kA-16g/s	70	800	1000	0.0192	-411	2359
8kA-4g/s	70	600	1500	0.0176	-410	4700
16kA-16g/s	160	2000	3000	0.0416	-820	4710
16kA-4g/s	200	3750	5000	0.0384	-1778	10084
24kA-16g/s	250	2500	6700	0.0624	-1229	6970
24kA-4g/s	220	4000	9000	0.0624	-2000	23000

Table A.1: Argon Field, Current, and Velocity Data.

	Ω_{exp}	Ω	σ_o (mho/m)	σ_{sh}/σ_o
8kA-16g/s	3.8	1.6	1062	2.4($\pm$1.0)
8kA-4g/s	2.6	0.4	484	7.2($\pm$2.5)
16kA-16g/s	6.2	2.1	1188	2.9($\pm$1.1)
16kA-4g/s	5.9	0.4	381	16.2($\pm$7.2)
24kA-16g/s	5.0	0.3	390	15.5($\pm$6.5)
24kA-4g/s	6.8	0.2	250	31.9($\pm$12.1)

Table A.2: Classically Calculated and Inferred Hall Parameters and Conductivities.

and magnetic probe data, Ω and σ_o are the inferred Hall parameter and electrical conductivity, respectively, calculated from Equations A.4 and A.6, and σ_{sh} is the electrical conductivity calculated from the Spitzer-Härm formula for the transverse electrical resistivity [76, 78]

$$\frac{1}{\sigma_{sh}} \equiv \eta_{\perp} = \frac{q^2\sqrt{m_e}\ln\Lambda}{3(2\pi)^{3/2}\varepsilon_o^2(kT_e)^{3/2}} \tag{A.7}$$

where ε_o is the permittivity of free space, k is Boltzmann's constant, T_e is the electron temperature, and Λ, the plasma parameter is given by

$$\Lambda = 9(\frac{4}{3})\pi n_e \lambda_e^3 \tag{A.8}$$

where the electron Debye length (λ_e) is calculated from

$$\lambda_e = \sqrt{\frac{\varepsilon_o kT_e}{n_e q^2}}. \tag{A.9}$$

As the table shows, the inferred plasma conductivity can be several times smaller than that calculated with Equation A.7, corroborating Lovberg's suspicion that non-classical phenomena, in some form, dictate plasma conductivity in MPD thrusters. In half of the cases studied, the inferred conductivity was over an order of magnitude smaller than the classical value. Most of the error associated with the analysis in calculating both classical and inferred conductivities results from electric field uncertainties due to the fidelity of the probe positioning system ($\pm$1 mm), the accuracy of the current density measurements ($\sim$20%), and the error in measuring electron number density and temperature (60 and 10%, respectively).

Figures A.2 and A.3 show the ratio of the calculated conductivities over the inferred values as functions of $J^2/\dot{m}$ and ξ^2, respectively. Although limited by the few data points and relatively large error bars, a strong trend is nevertheless apparent as the ratio increases drastically with both parameters.

Figure A.4 shows the ratio of classical to inferred conductivity as a function of measured electron Hall parameter (Ω_{sh}). The figure also presents anomalous conductivity ratios (anomalous to classical) obtained from the microinstability model developed by Choueiri[43, 44]. As the figure shows, qualitative agreement between the model and the experimental data is exhibited, implying that instabilities near the anode may play a

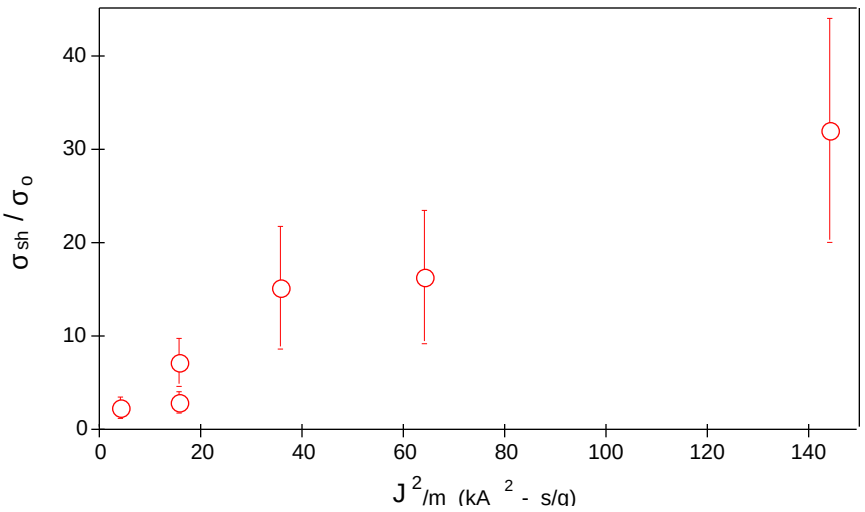

Figure A.2: Conductivity ratio vs. $J^2/\dot{m}$.

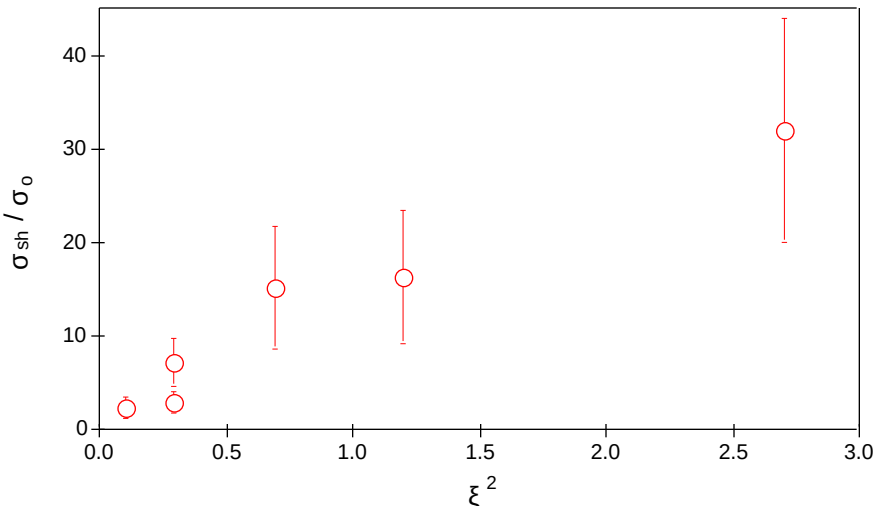

Figure A.3: Conductivity Ratio vs. ξ^2 .

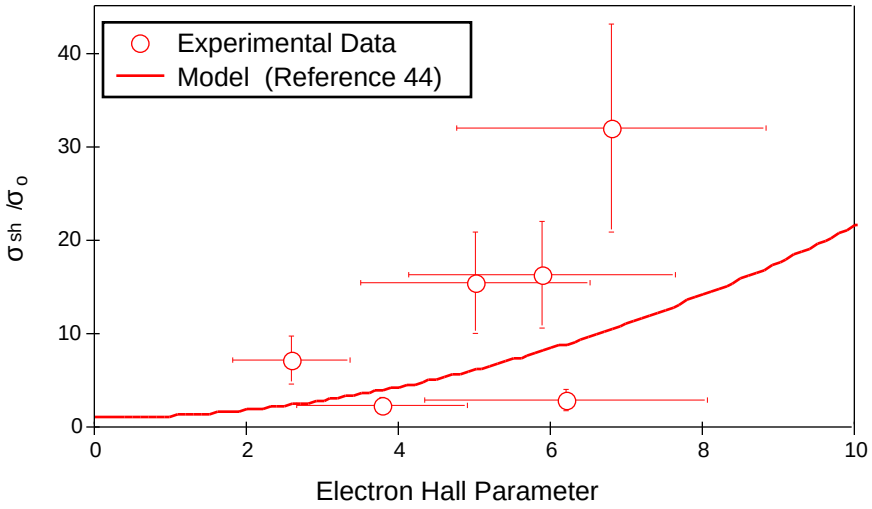

Figure A.4: Conductivity Ratio vs. Measured Hall Parameter.

role in establishing anomalously high resistivities. This statement is further supported by the fact that the instability which the model assumes has recently been shown to exist near the anode through analysis of Langmuir probe spectra[74].

B Anode Power Deposition in a Segmented Anode MPD Thruster

B.1 Abstract

Anode heat flux measurements of a water cooled segmented anode applied-field MPD thruster were made to investigate anode heat transfer phenomena. Pure argon and argon-hydrogen mixtures were used as propellants for a variety of thruster currents, propellant mass flow rates, and axial applied magnetic field strengths. The thruster was operated in two modes: with all four segments active, and with two of the segments floating. In addition, thrust and specific impulse were determined for each operating condition. The results of this work show that the heat flux to the anode increases monotonically with axial magnetic field strength and thruster current. Between 50 and 75% of the anode heat flux is transported by the current carrying electrons. Convective and radiative heat transfer account for the remaining portion of the power deposited in the anode. The addition of hydrogen to the argon propellant results in the reduction of the fraction of anode power deposited by the anode fall to a level equivalent to that of convection and radiation. Given the results of Langmuir probe measurements made a few centimeters downstream of the anode which show that T_e and n_i are insensitive to thruster operating condition, the Hall parameter is mainly determined by the strength of the applied magnetic field (cf. Equation IV.14).

B.2 Motivation for the Study

The results presented throughout the thesis suggest that the Hall parameter is the dominant scaling factor for the anode fall. This relation was found to hold true over a wide range of thruster power levels with two different propellants. Of primary concern, however, is the applicability of trends observed in quasi-steady thrusters to continuously operating devices. For the foreseeable future, multi-megawatt MPD thrusters will only be tested in pulsed forms. It is, therefore, important to determine what anode phenomena (if any) are inherent only to pulsed devices. To this end, it was felt that a comparison of trends in anode processes of the multi-megawatt quasi-steady device described throughout the thesis with the 100 kW steady thruster presented in this ap-

pendix would be useful in distinguishing steady and transient anode effects. However, the inability to run the steady device without an applied field complicates such a comparison. Nevertheless, trends found using an applied-field device were similar to those of the self-field quasi-steady thruster, including the scaling of the anode fall with the local Hall parameter. In this case, the Hall parameter was altered by varying the magnitude of the applied magnetic field.

B.3 Introduction

Numerous anode heat-transfer studies have been made using a variety of electrode geometries and plasmas in seeded MHD generators and accelerators[79, 80, 81, 82], free "burning" arcs[31, 83] as well as MPD thrusters[17]–[20],[22]–[25]. The goals of these studies were: 1) to establish a data base of anode phenomena; 2) to search for trends in anode processes; and 3) to assist in the design and verification of anode models. One approach frequently taken in MPD thruster anode research has been to divide the anode into independent segments whereby current and heat flux distributions can be obtained[21, 22, 32, 70, 71, 84]. Much of this work has been applied primarily to two types of steady-state thrusters; low power ($\sim$20 kW) MPD thrusters with strong axial applied magnetic fields (>1000 G) and propellant flow rates of approximately 20 mg/s, and high power (>100 kW) self-field MPD thrusters with propellant flow rates on the order of 1 g/s. There is, however, little information on anode power deposition in 100 kW class applied-field MPD thrusters with propellant throughputs of 0.1 g/s or less. Given the promising results of recent work[85], which shows the enhancement of thruster performance through use of applied magnetic fields, there is renewed interest in using 100 kW class applied-field MPD thrusters for applications ranging from payload orbit raising to unmanned planetary missions[12].

The primary goal of this portion of the research is to investigate the influence of thruster operating characteristics such as propellant selection, propellant flow rate, current, and applied magnetic field strength on anode power deposition in a 100 kW class MPD thruster. As a secondary goal, the trends in anode power deposition observed in quasi-steady thrusters are compared to those observed in the segmented anode device.

The segmented anode thruster used argon and argon-hydrogen mixtures as propel-

lant with mass flow rates between 50 and 150 mg/s. The thruster was operated at currents of 750 to 1250 A, with axial applied magnetic field strengths (measured at the cathode tip) between 300 and 800 G [2]. The anode of the thruster was composed of four water cooled copper segments. Current and heat flux to each segment were independently measured. Langmuir probes were employed to measure electron temperatures, which, with segment current and heat flux, permit an estimate of the local anode fall to be made. Thrust efficiency and specific impulse were measured over a broad range of discharge currents, propellant mass flow rates, and applied field strengths.

B.4 Experimental Apparatus

The applied-field thruster was tested in a vacuum facility at the NASA Lewis Research Center which consists of a cylindrical spool piece, 3 m in diameter and 3 m long, that was attached to a 7.6 m diameter, 21 m long vacuum chamber via a 3 m gate valve. Nineteen 81 cm diameter hydrocarbon oil diffusion pumps, backed by three roots blowers and two mechanical pumps, maintained tank pressures below 0.07 Pa (5×10^{-4} Torr) during thruster operation ($\sim$0.1 g/s argon). This tank pressure is below those shown to affect the operation of applied-field MPD thrusters[16]. Thruster power was supplied by a series-parallel network of Miller arc welding power supplies providing a maximum output of 3000 A at 130 V (390 kW). Power to the electromagnet was provided by an additional Miller unit capable of delivering up to 1500 A at 44 V. Power to the thruster and magnet was transferred through water cooled flexible copper cables.

Distilled and de-ionized cooling water for the thruster and magnet were provided by two closed-loop pump/heat exchanger assemblies each capable of supplying up to 0.8 liter/sec of water at pressures up to 1 MPa. Water flow rates were carefully monitored with calibrated turbine flow sensors capable of measuring flow rates accurately to within 3%. Additional descriptions of the Lewis test facility can be found in References [37, 86, 87].

[2] Based on computer models, the magnetic field at the anode face is expected to be within 20% of the fields measured at the cathode tip.

B.5 MPD Thruster Assembly

A schematic of the MPD thruster assembly used for this work is shown in Figure B.1. The assembly contains the thruster, magnet (not shown), current and water cooling lines, current sensors, water flow sensors, thermocouples, and assorted sensor signal and power lines (not shown). The entire assembly was placed on an inverted pendulum thrust stand. A large rectangular radiation shield made of stainless steel and tantalum protected the assembly from plume radiation.

The thruster used for this experiment (Figure B.2) featured an anode composed of four independent water cooled segments. Electrical and thermal isolation of each segment was provided by mica inserts, whose inner surfaces were recessed slightly for protection against the discharge. Each anode segment had an inner and outer diameter of 8.9 cm, and 12.7 cm, respectively, and was 2.2 cm long. The cooling water passage of each segment had a rectangular cross section measuring 1.6 cm by 0.6 cm with an anode wall thickness of 0.3 cm. Cooling water and current were provided to each segment through 1 cm O.D. copper tubing. All active segments were connected to a common 2.5 cm O.D. copper tube which also served as a plenum for the cooling water.

Mica insulation was also used to thermally insulate the first upstream (segment 1) from the the boron-nitride back plate. The exposed face of the exit anode segment (segment 4) was insulated with macor to restrict current attachment to the interior of the thruster chamber, ensuring that all segments had equal electrode surface areas. The segments were held together with eight stainless steel threaded rods which traversed through the segments and insulators 5.9 cm radially from the thruster centerline.

Propellant was injected through the backplate via twenty four 1.6 mm diameter holes at a radius of 1.9 cm, and through an annulus around the base of the cathode. An equal amount of propellant flowed through the holes and through the annulus. The cathode, constructed out of 2% thoriated tungsten, was 7.6 cm long and 1.8 cm in diameter and was held in place by a water cooled copper clamp located behind the propellant injector. Cooling water was passed through the cathode clamp prior to distribution to the anode segments. Water throughput for the entire thruster was approximately 0.4 liter/sec.

The electromagnet consisted of four planar elements each with an inner diameter

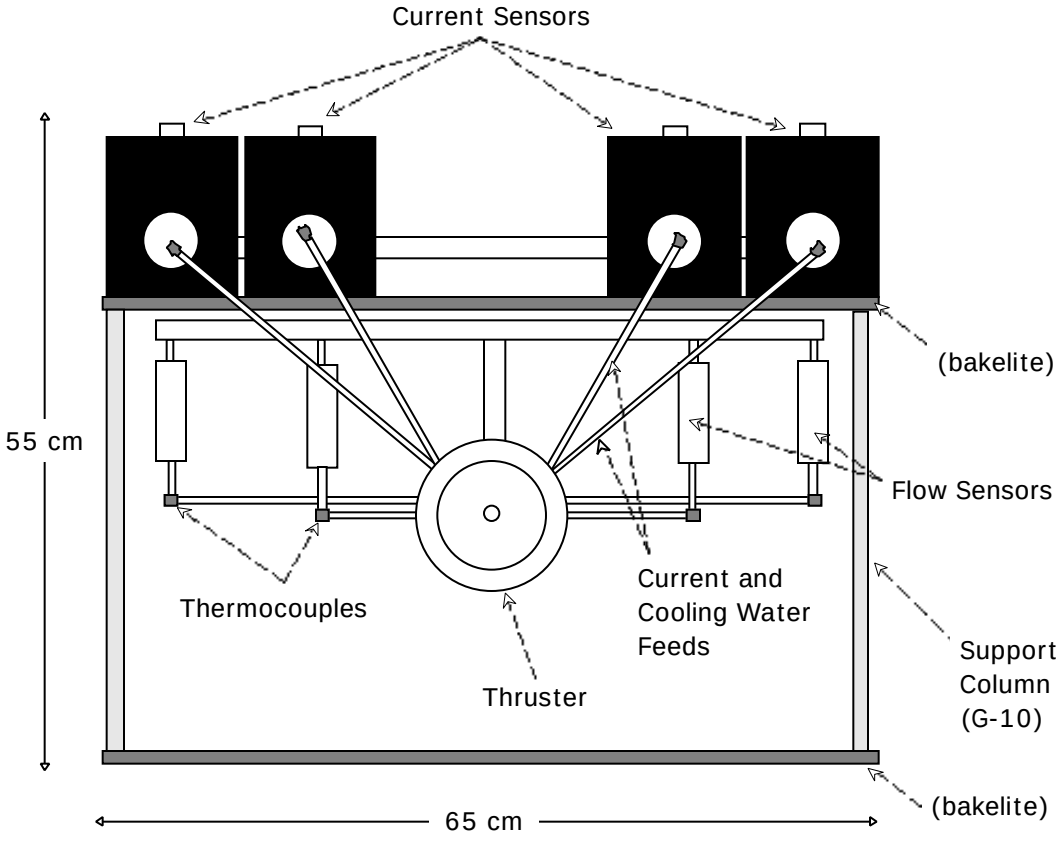

Figure B.1: MPD Thruster Assembly.

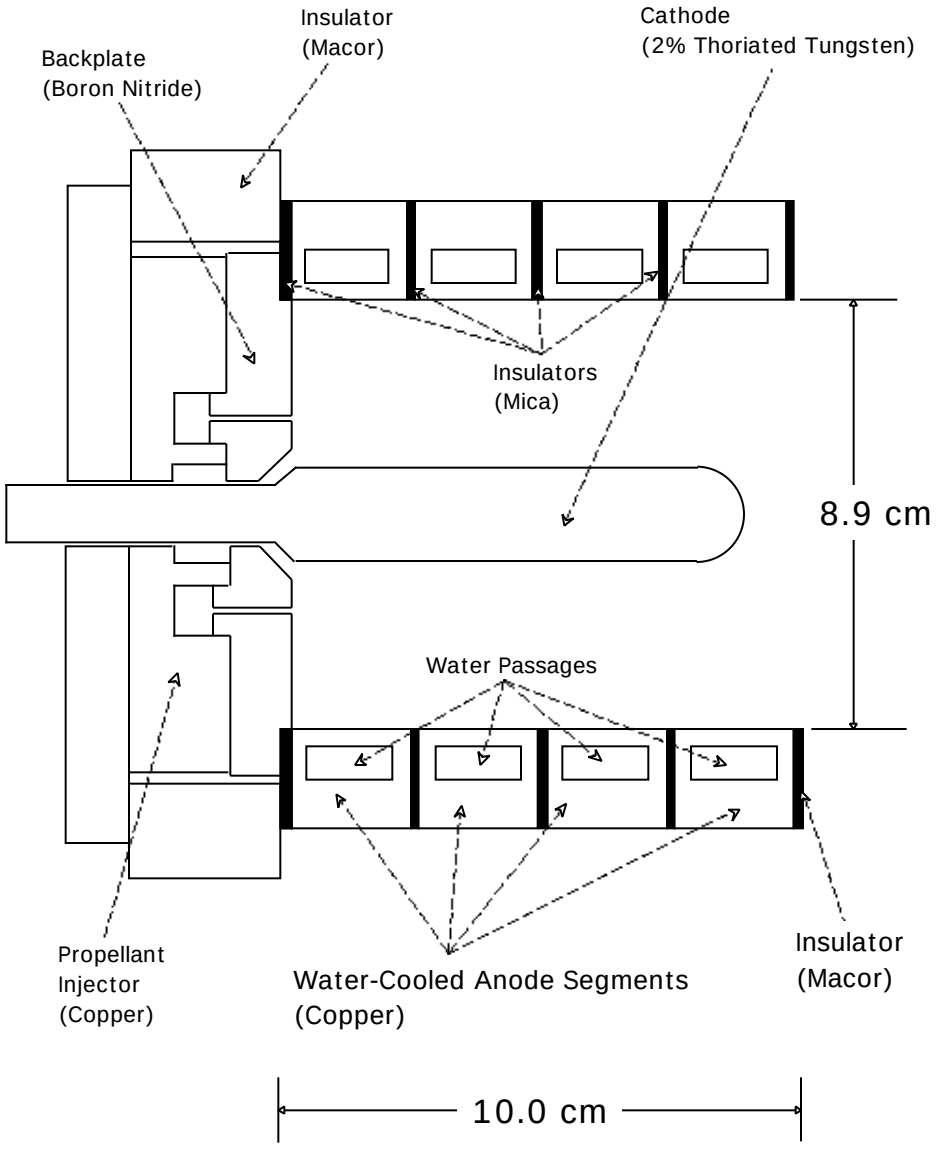

Figure B.2: Segmented Anode MPD Thruster.

of 14 cm and an outer diameter of 25 cm. Each element contained five turns of 1 cm O.D. copper tubing providing passage for water flow rates of up to 0.3 liter/sec. Each magnet element was aligned with a mica insulator. The magnet was designed to provide a magnetic field of up to 1000 G at the cathode tip for magnet currents up to 1200 A. A computer code was employed to predict the shape and magnitude of the field generated by this magnet. The predicted field profiles were similar to those produced by a solenoid of equivalent dimensions. Calculated and measured magnetic field strengths, at various locations within the thruster, compared quite favorably.

Cooling water flow rates for each segment were monitored with Omega FP-541 flow sensors which provided measurements accurate to within 1% (full scale). These plastic flow meters were also used to electrically isolate the anode and cathode current/cooling water supply lines from each other. Water temperature was measured with Type K thermocouples enclosed in 0.3 cm O.D. stainless steel sheaths that were concentric with the water passages. Cooling water temperature was monitored at the cathode clamp as well as at the magnet. Current to each segment was measured with F.W. Bell IF-5020P current sensors, to within 1% accuracy. Segment voltages, with respect to the cathode, were measured with isolation amplifiers accurate to within ± 0.5 V.

In addition to calorimetric measurements of anode power deposition, thrust, specific impulse, electron temperature and ion density profiles in the plume (via Langmuir probe) were obtained as well. A description of the Langmuir probe system and methods used for data reduction is presented in Reference [88]. Acquisition of all data and thruster operating parameters was performed by a Keithley System 500 driven by a Compaq personal computer.

B.6 Results

The primary goal of this work is to determine what influence the magnetic field has on anode power deposition. The primary advantage of applied field thrusters, in this respect, are their ability to operate at a variety of magnetic field strengths irrespective of thruster current. This offers the possibility of isolating magnetic field effects from other effects associated with discharge current level. A secondary goal is to see how anode power deposition in a multi-megawatt self-field quasi-steady MPD thruster differs from

that of a 100 kW applied-field steady device.

The thruster was operated at discharge currents between 750 to 1250 A with applied field strengths (measured at the cathode tip) between 300 and 800 G. The axial magnetic field strength at the anode is predicted to be of the order of that measured at the cathode tip. The self-magnetic field strength at the anode is at most 60 Gauss. Argon served as the primary propellant at mass flow rates of 100 and 140 mg/s. Attempts to run the thruster on pure hydrogen resulted in severe damage to the anode. Thus, argon-hydrogen propellant mixtures (up to 30% H_2 by *mass*) with flow rates between 50 and 150 mg/s were investigated. In an effort to quantify the dependence of convective and radiative power anode deposition on thruster operating conditions, two of the segments (1 and 2) were electrically isolated from the power source (Figure B.2).

Because of the dominance of the axial applied magnetic field over that induced by the current, the Lorentz body force acts primarily in the azimuthal direction, causing the plasma to rotate. The rotation of the plasma in applied-field thrusters has been observed experimentally[75, 89] and has been used to explain operating traits of these devices. Figures B.3 and B.4 show terminal voltage as a function of applied field strength for the thruster configured with 4 and 2 active (current carrying) segments, respectively. The linear dependence of the terminal voltage with magnetic field, a typical characteristic of applied-field MPD thrusters, has been attributed to the fact that the voltage drop due to the back-EMF (the product of the applied magnetic field strength and the azimuthal rotation velocity of the plasma) depends linearly on magnetic field strength[89]. Patrick et al.[95] have been able to correlate terminal voltage with magnetic field strength for several propellants through the following relation

$$V = V_o + U_c B r_a \tag{B.1}$$

where V is the terminal voltage, V_o is the voltage drop which accounts for ohmic and sheath voltage drops, U_c is the Alfvén critical velocity, B is the axial field strength "near but just downstream of the anode," and r_a is the anode radius. Fradkin found this relation to accurately fit terminal voltage data of a 20 kW lithium MPD thruster[89].

For the thruster of this study ($r_a \simeq$4.5cm) operating on pure argon as propellant (U_c $\simeq$8.7 km/s), the slope of the voltage characteristic predicted by Equation B.1 is 0.039,

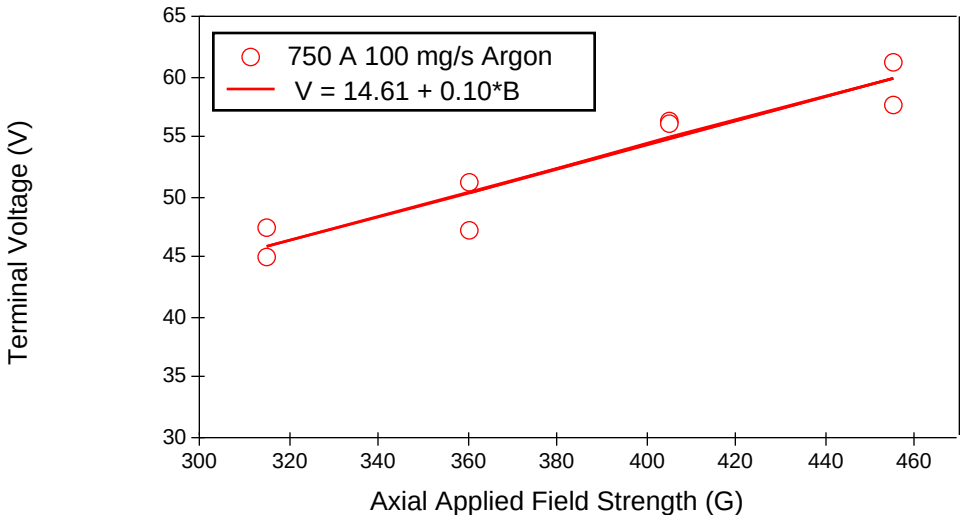

Figure B.3: Terminal Voltage vs. Applied Field Strength, (100 mg/s argon).

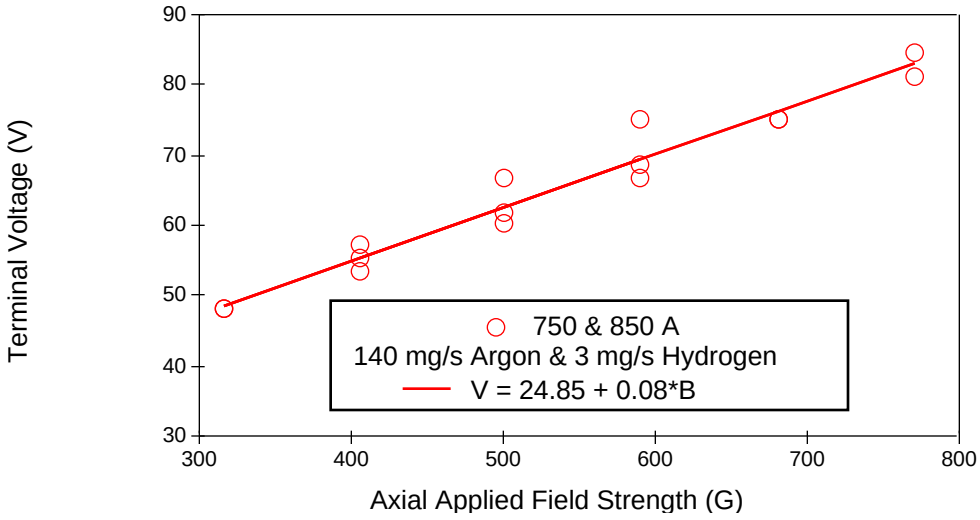

Figure B.4: Terminal Voltage vs. Applied Field Strength, (140 mg/s argon & 3 mg/s hydrogen).

which is 60% less than that measured experimentally (cf. Figure B.3). However, since the magnetic field a few centimeters downstream of the anode exit plane is expected to be half the field strength at the cathode tip, use of magnetic fields at this location results in better agreement with Equation B.1. This magnetic field value is appropriate since the plasma may not reach its terminal velocity until several centimeters downstream of the thruster exit plane. Because of the use of different propellant species (hydrogen and argon), such a comparison between data presented on Figure B.4 and Equation B.1 cannot be made [3]. However, the figure demonstrates that this dependence holds regardless of thruster current. The linear voltage-magnetic field characteristic was observed at all operating conditions.

Figures B.5 and B.6 show another characteristic commonly observed in applied-field MPD thrusters, namely that thrust varies linearly with the product of the thruster current and the magnetic field strength. The mechanism by which thrust in applied-field devices is enhanced by the axial field is not well understood. A common perception is that the kinetic energy locked in the azimuthal rotation of the plasma is converted to axial kinetic energy via the axial applied fields[89]. In his model, Fradkin assumes that perfect conversion of azimuthal to axial kinetic energy takes place due to the presence of a magnetic nozzle. His model is able to reproduce the observed trait of thrust being a linear function of the product of arc current and magnetic field strength at the anode face.

Thrust efficiency as a function of specific impulse for a number of propellant flow rates and mixtures at currents of 750 and 850 A is presented in Figure B.7. Thrust efficiency ranges from 6 to 11% with specific impulse between 700 and 1600 s. Peak thruster performance, in terms of both specific impulse and thrust efficiency, is achieved at a propellant mixture of 85 mg/s argon and 15 mg/s hydrogen.

Figure B.8 shows the distribution of current to the segments at three thruster currents and two applied field strengths where I/It is the fraction of thruster current that is carried by a segment. At these operating conditions 60 to 75% of the total input power is deposited into the anode. As the figure shows, most of the current is concentrated

[3] Because of the mixture of hydrogen and argon present calculation of the Alfvén critical velocity is not trivial.

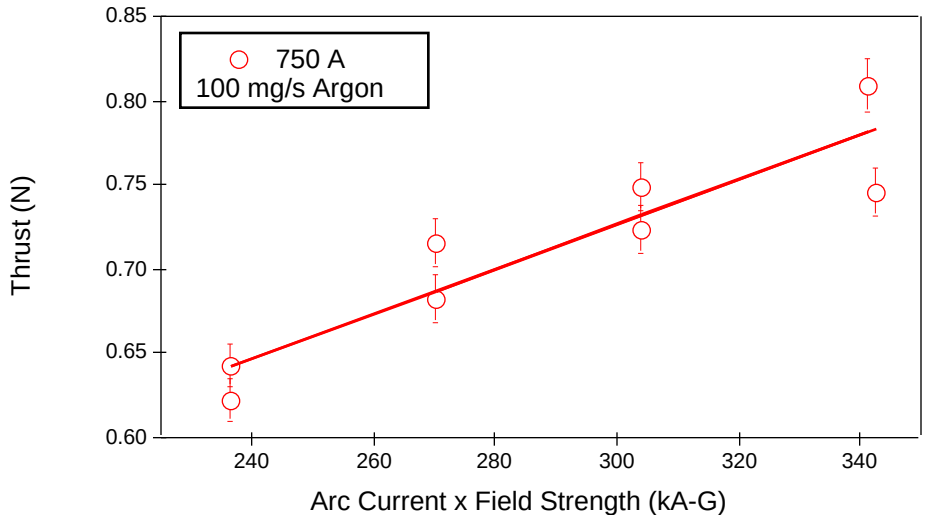

Figure B.5: Thrust vs. Arc Current × Applied Field Strength, (100 mg/s argon).

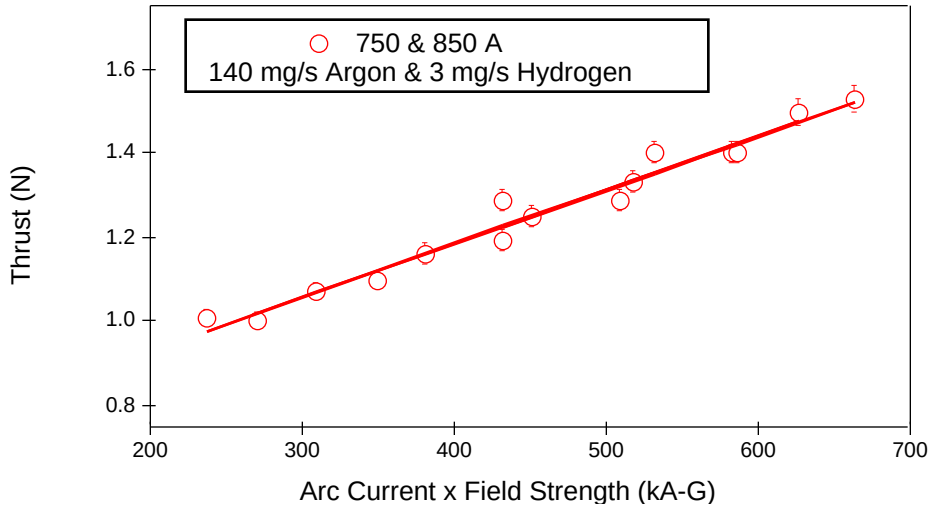

Figure B.6: Thrust vs. Arc Current × Applied Field Strength, (140 mg/s argon & 3 mg/s hydrogen).

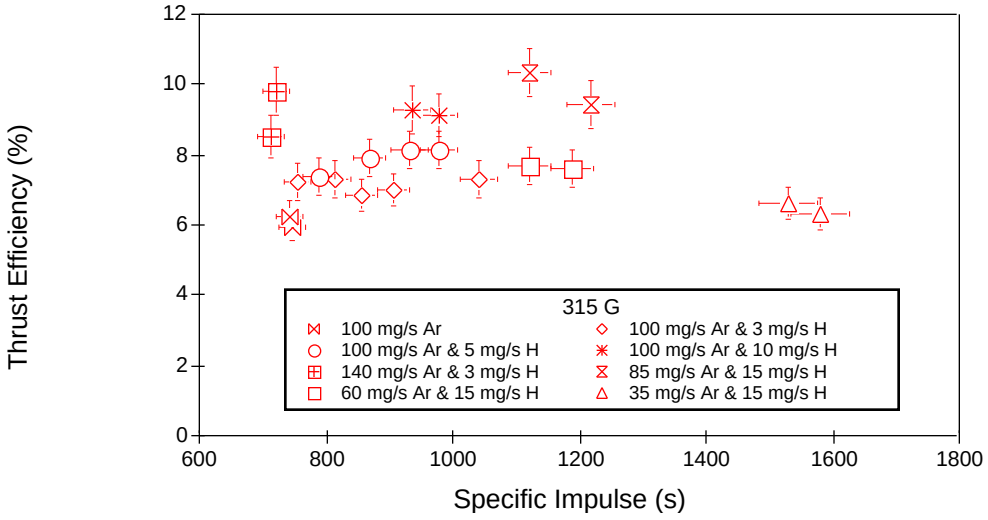

Figure B.7: Thrust Efficiency vs. Specific Impulse, (315 G).

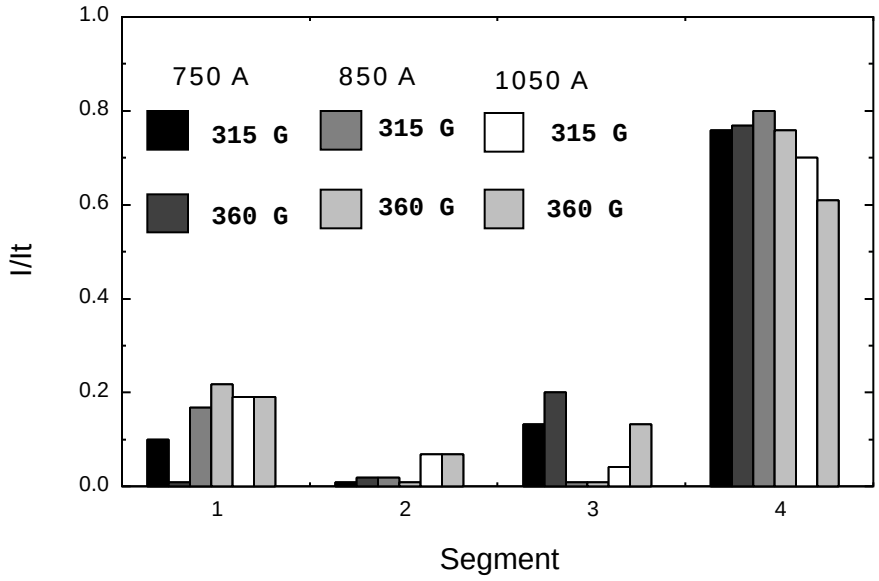

Figure B.8: Segment Current Distribution, (100 mg/s argon).

at the upstream and downstream most segments (1 and 4, respectively). Increasing thruster current results in a more diffuse current distribution. The uneven segment current distribution shown is characteristic of "bi-modal" axial current profiles seen in quasi-steady (self-field) MPD thrusters of similar geometries[91, 92]. This result is similar to that observed by Baksht et al.[93] and Schall[90] in which the intersection of magnetic field lines with the anode greatly enhanced current conduction. At the middle segments (2 and 3), the magnetic field lines are parallel to the anode, impeding current conduction. At the end segments (1 and 4) however, the magnetic field lines intersect the anode[37].

The contribution to anode heating from convection and radiation, while negligible for high power quasi-steady MPD thrusters characterized by anode heat fluxes of several kilowatts per square centimeter[19, 17, 25], can be important for 100 kW class steady-state thrusters with significantly lower levels of anode heat flux. This fact is illustrated in Figure B.9 which shows that a significant fraction of the power deposited to the anode (Pt) is absorbed by anode segments that do not receive a substantial amount of the arc current. P/Pt represents the fraction of anode power that is absorbed by each individual segment. It is estimated (Figure B.10) that for a cathode surface temperature between 3000 and 3200°K, up to 8 kW of cathode radiation is absorbed at the anode[94]. This corresponds to 10 to 25% of the total power deposited to the anode of a thruster operating at 100 kW.

Figure B.11 shows anode current and heat flux distributions as a function of applied field strength. An increase in field strength results in more current flow to the two downstream segments. In agreement with the anode heat flux equation presented in Chapter 1, it is also seen that the amount of heat absorbed at each segment is greatly influenced by the current. Although segment 2 receives only 1 or 2% of the current, it still accounts for 10% of the anode power. This further illustrates that convection and radiation, although negligible for multi-megawatt thrusters characterized by extremely large anode heat fluxes, are important modes of power deposition to the anode of 100 kW class thrusters, and can no longer be ignored in anode fall estimates which rely on anode heat flux data. For this reason, a series of tests was performed where the segments 1 and 2 (cf. Figure B.2) were electrically isolated from the power supply.

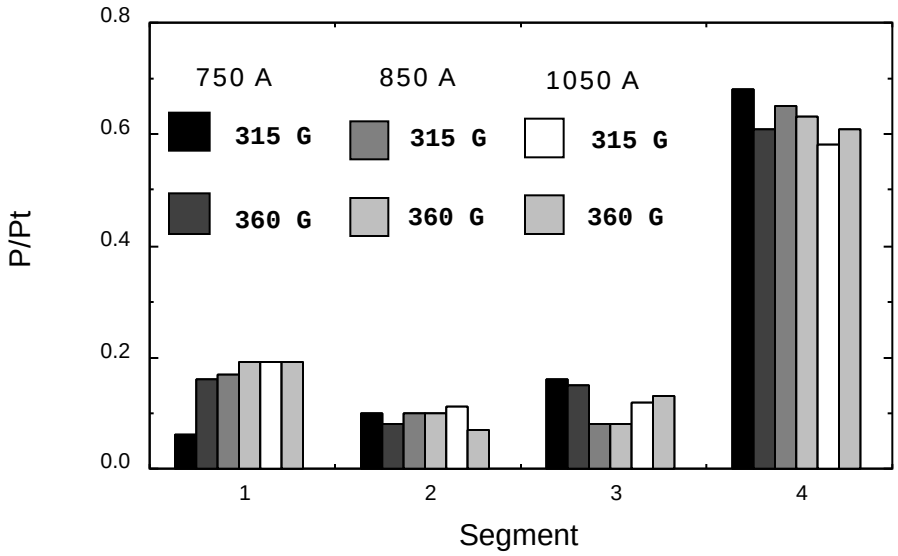

Figure B.9: Segment Heat Flux Distribution, (100 mg/s argon).

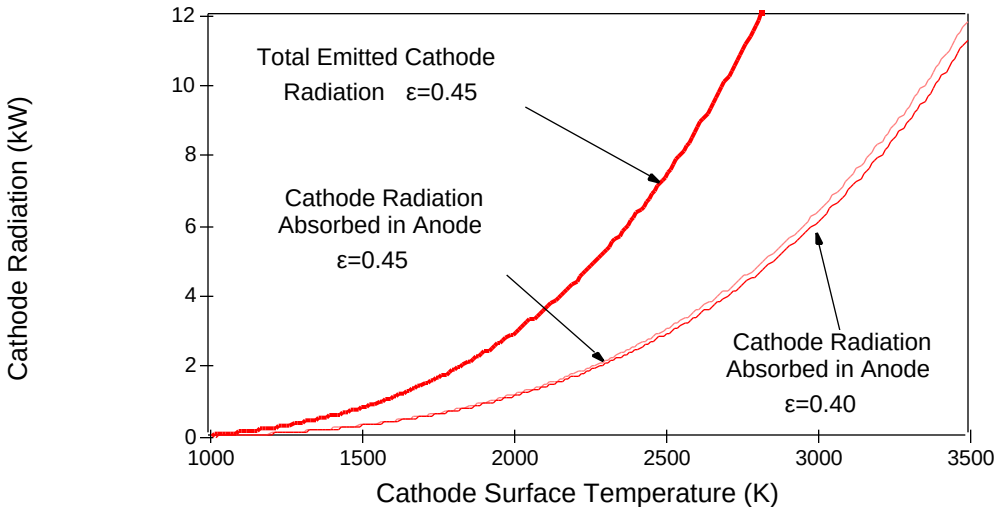

Figure B.10: Power of Cathode Radiation Absorbed by Anode.

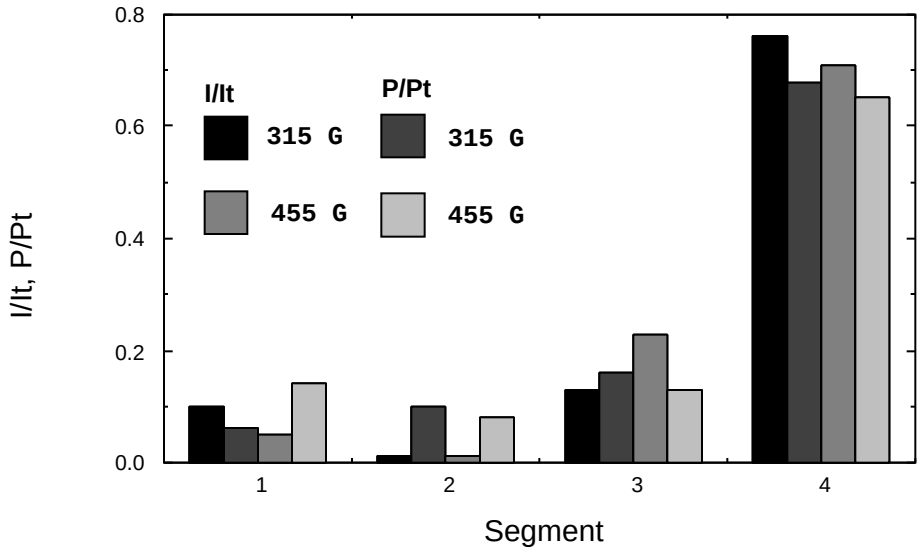

Figure B.11: Segment Current and Heat Flux Distribution, (750 A, 100 mg/s argon).

Current and heat flux distributions for the re-configured thruster are shown in Figure B.12. As the figure shows, the current and heat flux pattern has become less concentrated with increased field strength, a trend that was observed throughout the experimental program. It is also seen that the two floating segments each consume between 5 and 10% of the anode power, consistent with the amount absorbed by the segment (#2) that carried little current in our last case (Figure B.11). This implies that one is justified in using the heat flux to a floating electrode for the estimate of anode heating from convection and radiation. Restricting current flow to the two downstream segments results in higher terminal voltages which almost all appears as increased anode voltage. This effect can be seen in Figure B.13 which shows the terminal voltage and the characteristic anode voltage (Ua), defined as the total power consumed by the anode divided by the total current, as a function of applied field strength. Because of this, the thruster with four active segments has slightly better performance than the re-configured device. Although observed in other segmented anode studies[21], an

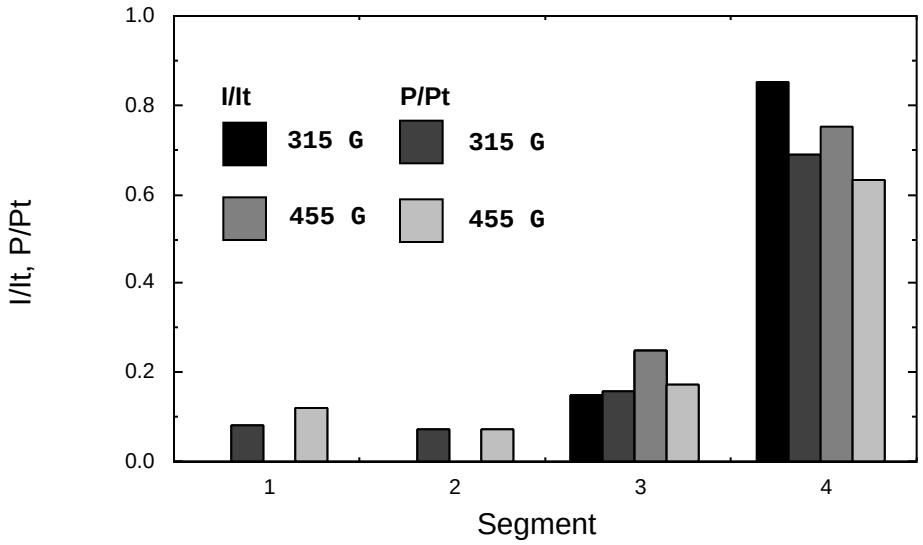

Figure B.12: Segment Current and Heat Flux Distribution, (2 active segments; 750 A, 100 mg/s argon).

explanation for this observation cannot be given at this time.

Figure B.14 illustrates the effect the addition of hydrogen propellant has on anode power fraction and thrust efficiency. As shown in the figure, the addition of hydrogen to argon reduces the fraction of input power that is deposited into the anode while slightly enhancing performance. Anode power fraction is reduced from 0.71 with pure argon to 0.55 with an argon-hydrogen mixture. At the same currents and field strengths, thrust efficiency typically increases from 7 to 10%. Increasing the mass flow rate (100 mg/s to 140 mg/s) of pure argon propellant had little impact on thrust efficiency or the anode power fraction. As seen in Figure B.15, over the range of investigation, anode power fraction and thrust efficiency are somewhat insensitive to thruster current. The power deposited into the anode increases linearly with current, in agreement with other studies[20].

Figure B.16 shows the variation of anode power fraction and thrust efficiency as a

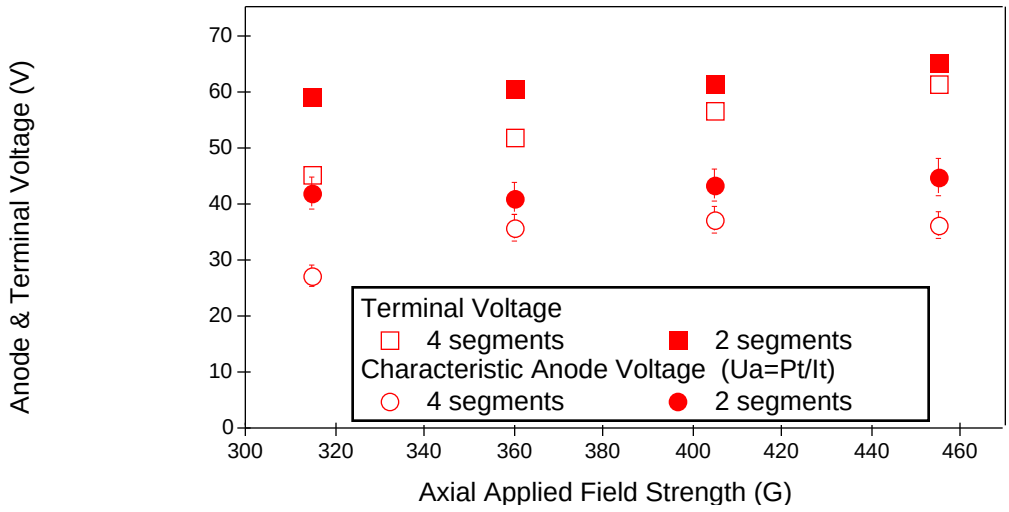

Figure B.13: Characteristic Anode Voltage and Terminal Voltage vs. Applied Field Strength, (750 A, 100 mg/s argon).

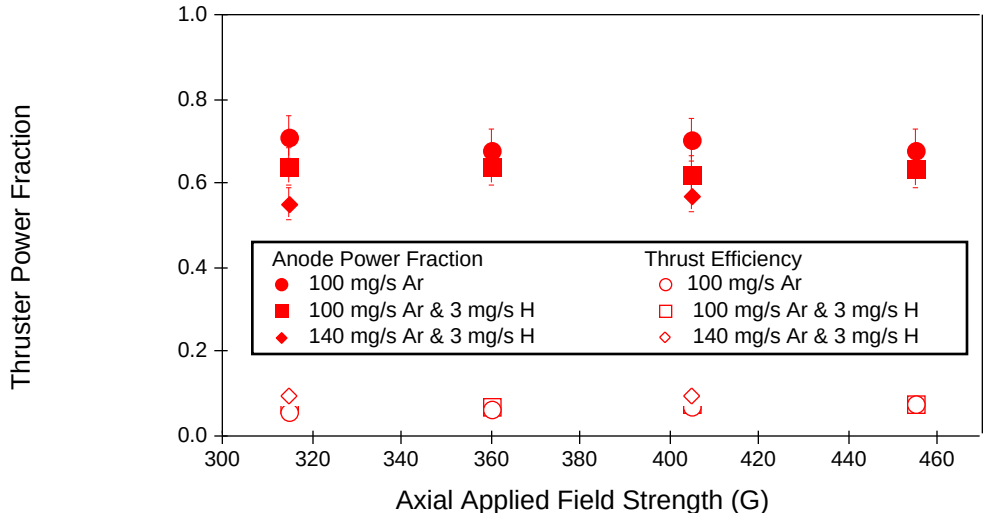

Figure B.14: Anode Power Fraction and Thrust Efficiency vs. Applied Field Strength.

function of hydrogen propellant mass fraction. Propellant flow rates presented in this plot vary from 140 mg/s argon with 3 mg/s hydrogen, to 35 mg/s argon with 15 mg/s hydrogen. The pure argon data correspond to a mass flow rate of 100 mg/s. As the figure clearly shows, the addition of a small amount of hydrogen improves thruster performance by increasing thrust efficiency and reducing the anode power fraction. However, above hydrogen propellant fractions of 10%, additional hydrogen results in declining performance. The figure also contains three points with total argon-hydrogen mass flow rates of 100 mg/s (0, 10, and 15% hydrogen mass fraction), indicating that, to a first order, this trend is independent of total mass flow rate.

Figures B.17 and B.18 show how power deposited to the floating segments through convection and radiation vary with applied field strength, thruster current, and hydrogen propellant fraction. As is seen in Figure B.17 a, power to the floating segments increases linearly with applied field strength. Through filtered photographic techniques, the cathode has been observed to become hotter with increasing magnetic field strength. Thus, part of this two-fold increase in segment power may be caused by an increase in emitted cathode radiation.

As shown in Figure B.17 b, above 850 A, heat flux to the segments increases linearly with current. As the current increases, the difference between the power absorbed at segments 1 and 2 also becomes larger. The effect of hydrogen propellant on convective and radiative anode heat transfer is presented in Figure B.18. Floating segment power remains constant for hydrogen propellant mass fractions up to 5%. Beyond this, there is a large increase in segment power and a large variation in power between segment 1 and segment 2. At a hydrogen mass fraction of 30%, 6 to 9 kW of power is deposited at each segment by convection and radiation. This magnitude of power is too much to be accounted for by cathode radiation alone (Figure B.10).

B.7 Estimated Anode Falls

The role of the anode fall in the transfer of power to the anode is a key issue in any study of anode phenomena. Two assumption were made in calculating the anode fall in this study:

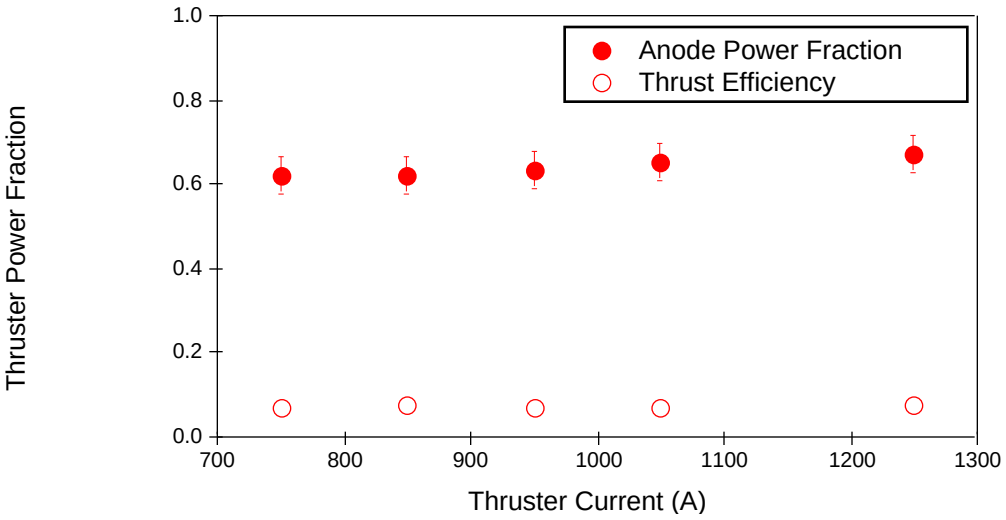

Figure B.15: Anode Power Fraction and Thrust Efficiency vs. Thruster Current, (315 G, 100 mg/s argon & 3 mg/s hydrogen).

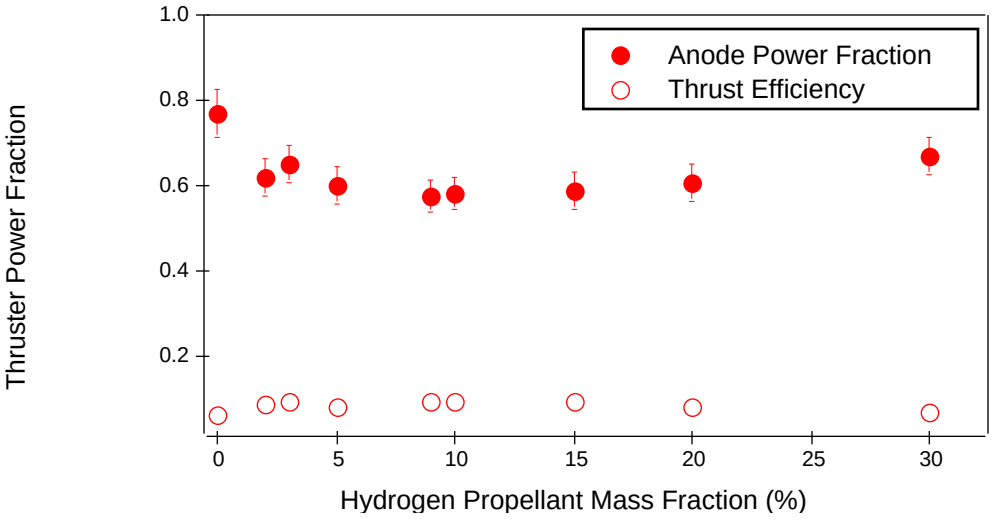

Figure B.16: Anode Power Fraction and Thrust Efficiency vs. Hydrogen Propellant Fraction, (850 A, 315 G).

a) 140 mg/s argon & 3 mg/s hydrogen

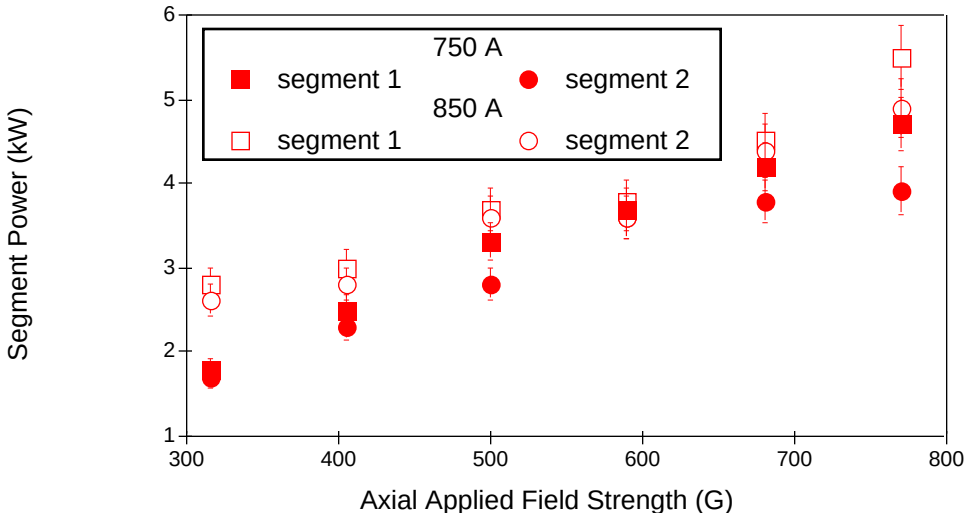

b) 100 mg/s argon & 3 mg/s hydrogen

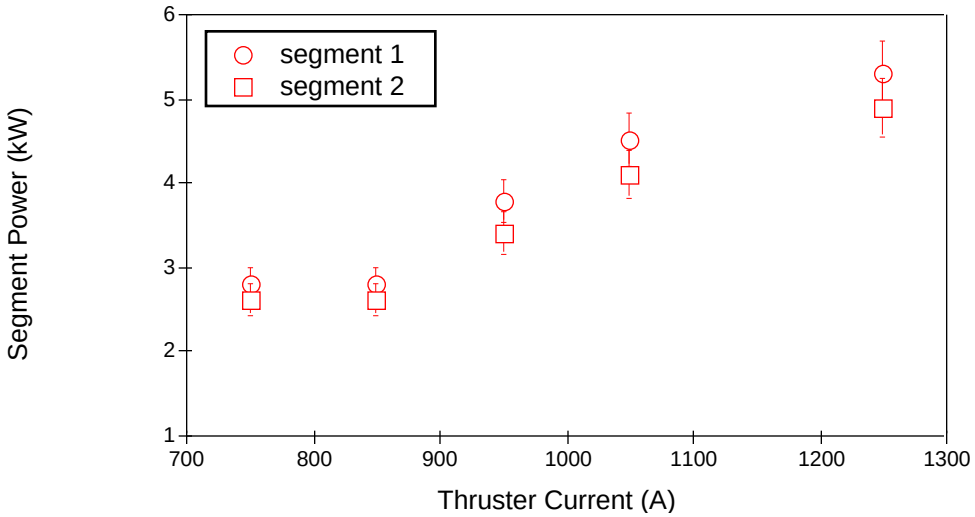

Figure B.17: Power Deposition to Floating Segments.

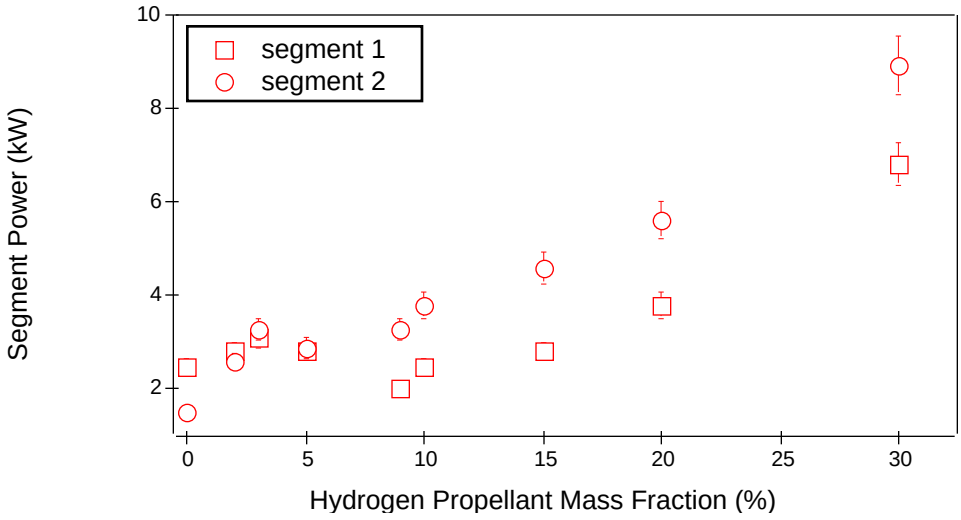

Figure B.18: Power Deposition to Floating Segments, (850 A, 315 G).

- Heat flux contributions from convection and radiation ($\dot{Q}_c + \dot{Q}_r$) to each current carrying segment were assumed to be the the mean of the fluxes measured at segments 1 and 2.

- An electron temperature of 1.3 eV (15,000 °K) was used for all calculations. This value was obtained from extrapolation of electron temperatures measured in the plume by Langmuir probes[88].

Figure B.19 shows electron temperature radial profiles measured 20 and 30 cm downstream of the anode face. As the figures indicate, the electron temperature is at its minimum value along the centerline (r=0 cm) and increases monotonically with radius in either direction. The large error bars at the radial extent of the survey are indicative of the large scatter of data measured in this region of the plume. At 20 cm from the anode face, the electron temperature varies from 0.6 eV near the center of the plume to 1.0 eV at either edge (Radius $\simeq$ 20 cm). At 30 cm from the anode face, the centerline electron temperatures are approximately 0.5 eV, however, the electron temperatures measured at the edges (Radius $\simeq$ 30 cm) are now 0.8 eV. Extrapolation of data obtained at these two

a)

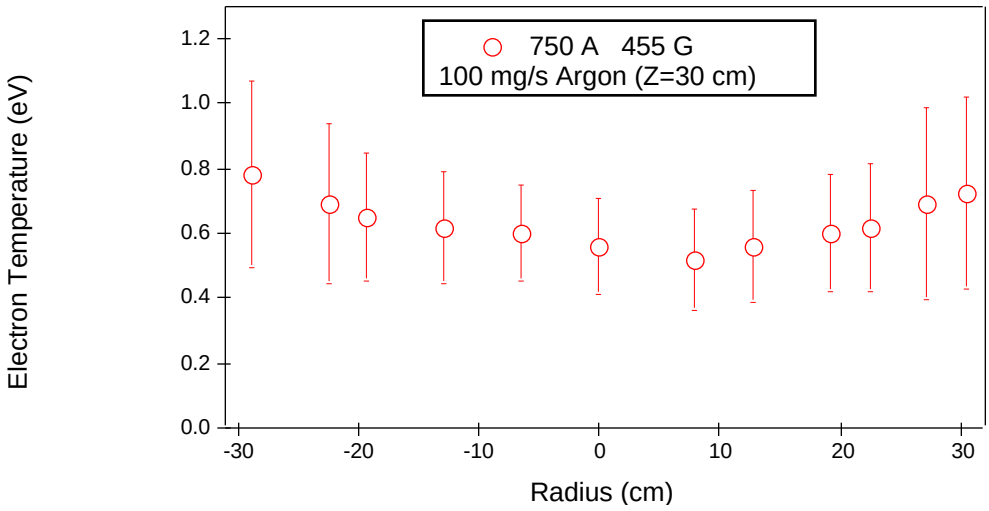

b)

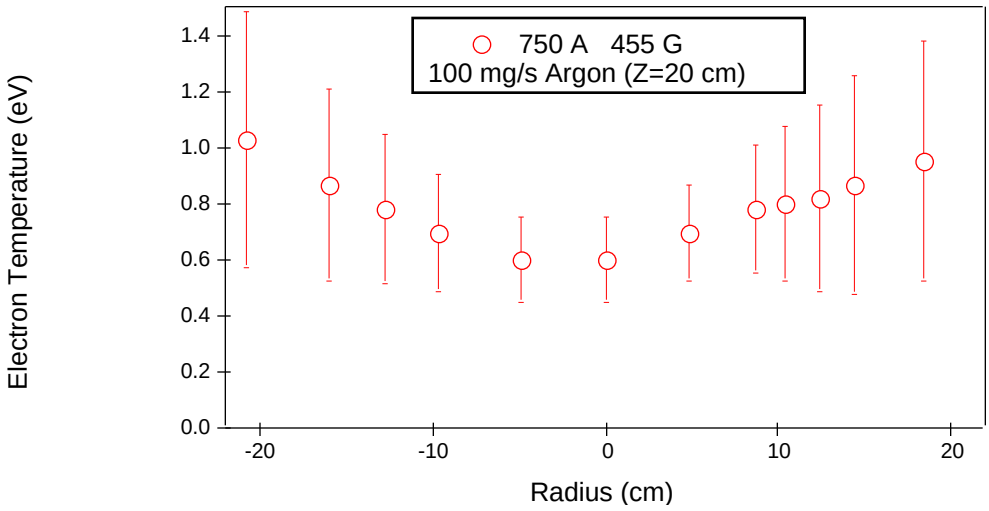

Figure B.19: Electron Temperature Radial Profiles, (750 A 455 G, 100 mg/s argon).

axial locations (by fitting the electron temperature data to an exponential[96]) yields electron temperatures at the anode exit plane of 1.2±0.4 eV.

Figure B.20 shows calculated anode falls and anode power fractions, for each energy transfer mode, as a function of magnetic field strength. Two means were used to calculate the anode falls: use of Equation I.3 with all the accompanying assumptions mentioned above (calorimetric) and employment of segment 3 as a floating probe (potential). The measured floating potential was corrected to plasma potential by using an electron temperature of 1.3 eV. As is illustrated in Figure B.20 a, the estimated anode falls of the two active segments are quite different. This difference becomes more pronounced at large values of applied field strength. Good agreement between the "calorimetric" and "potential" estimates of the anode fall exists only for segment 3, implying that axial as well as radial gradients of the electric field are present near the anode. Such axial gradients have been observed in quasi-steady devices of similar geometry as well[97, 36]. The anode heat flux from current carrying electrons, which includes contributions from the anode fall, work function, and electron thermal energy accounts for 60 to 70% of the total power deposited to the anode (Figure B.20 b). The anode fall alone accounts for 30 to 40% of the total thruster power (50 to 60% of the anode power). At increased field strength, the contribution to anode heating from convection and radiation increases to nearly that of the anode fall. The contributions from the work function and electron temperature represent approximately 8 and 5% of the thruster power, respectively.

Figure B.21 shows the dependence of the anode fall and anode heat transfer modes as a function of applied field strength for an argon-hydrogen mixture. As the figure shows, the anode fall for segment 2 remains constant while that of segment 4, as determined through calorimetry, increases with field strength. Although the anode fall increases with field strength, the thruster power fraction consumed by it remains constant (Figure B.21 b). The difference between "calorimetric" and "potential" fall estimates increases with field strength, implying that axial electric fields are sensitive to the magnetic field. Of special note is the fact that the contribution to anode heating from the anode fall is actually slightly less than that due to convection and radiation. The addition of a small fraction of hydrogen (<10%) tends to increase the overall arc voltage

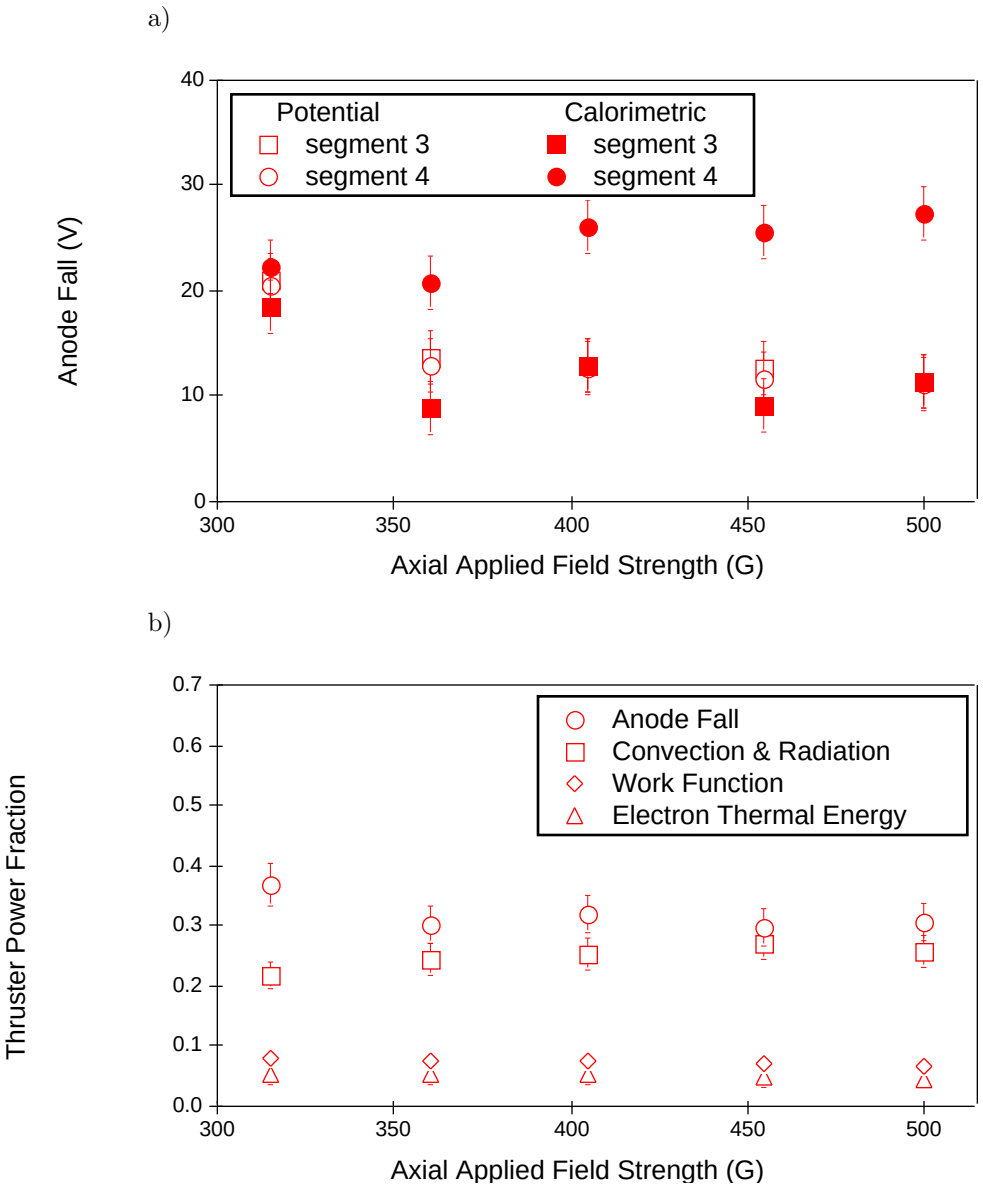

Figure B.20: Anode Fall and Anode Power Fraction Components vs. Applied Field Strength, (750 A, 100 mg/s argon).

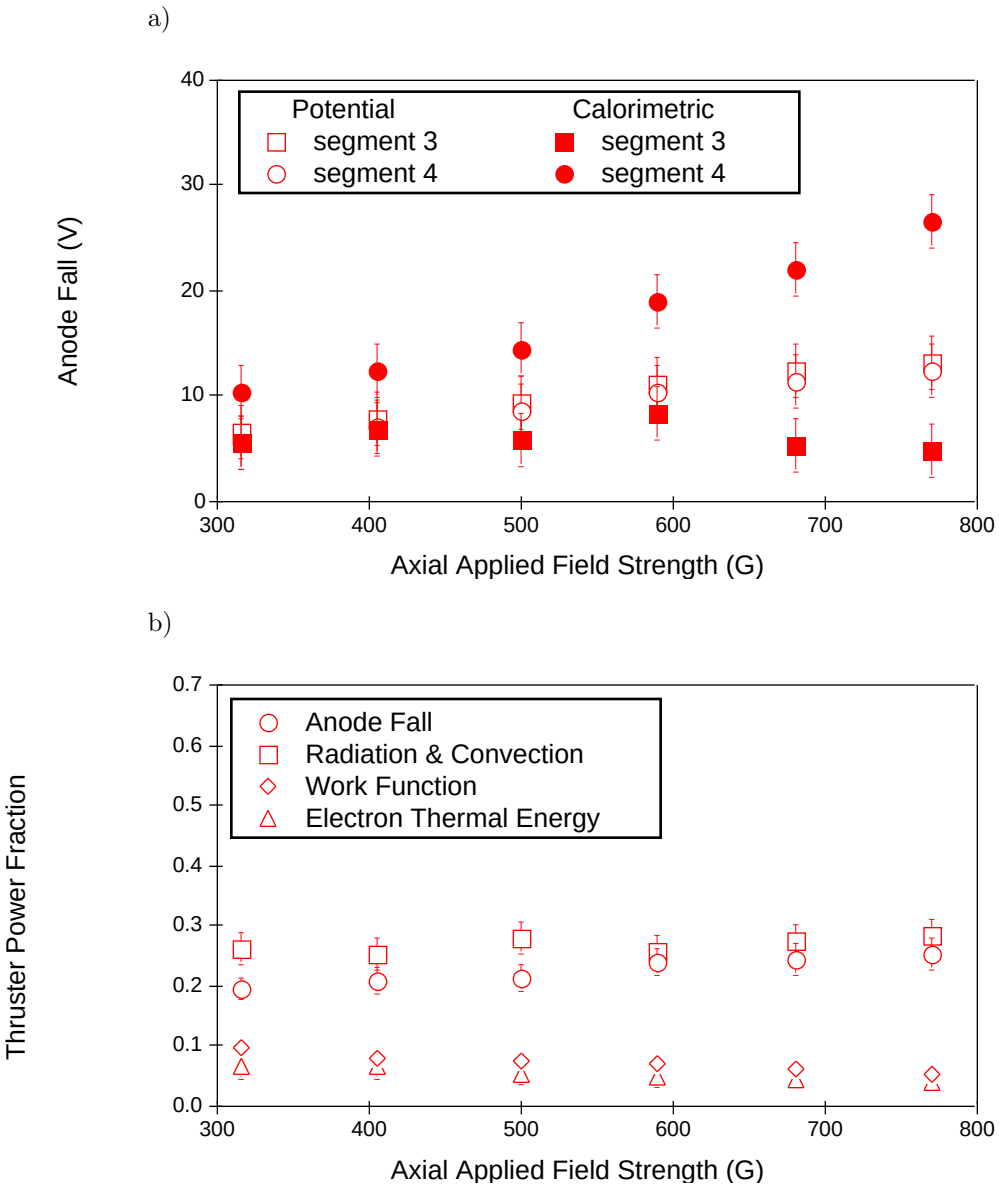

Figure B.21: Anode Fall and Anode Power Fraction Components vs. Applied Field Strength, (850 A, 140 mg/s argon & 3 mg/s hydrogen).

with a corresponding decrease of the anode power fraction. In addition, hydrogen also increased the magnitude, and in some cases the fraction of power deposited to the anode from convection and radiation[37].

Figure B.22 shows radial profiles of ion number density at two axial locations (Z=20 and 30 cm) for the thruster operating on 100 mg/s argon at an arc current of 750 A and an applied-field strength of 455 G. Since electron temperature and ion number density as determined from probe measurements do not vary appreciably (beyond the error bars) with thruster operating conditions (cf. Figures B.22–B.24), the change in the applied magnetic field, which is essentially the change of the total magnetic field since at the anode, the applied field is substantially larger than the self-induced field, is indicative of the variation of the Hall parameter. As such, the trend of increasing anode fall with Hall parameter, observed in Chapters 3 through 5 with quasi-steady thrusters, is also observed with applied-field steady thrusters operating at two orders of magnitude less power. For electron temperatures (1.3 eV), number densities ($\sim 1 \times 10^{19}$ m^{-3}) based on an extrapolation to the chamber[88]) and magnetic field strengths (300–1000 G) of interest, the electron Hall parameter ranges from 30 to 100. This implies that the electrons are highly magnetized and drift parallel with the anode for several gyroperiods before experiencing a collision with an ion.

Figure B.25 shows the dependence of the anode fall and anode power modes on thruster current for a mixture of argon and hydrogen propellants. As shown by Figure B.25 a, below a current of 1050 A, the anode fall, in both segments, increases linearly with current. Anode fall estimates based on floating segment potential measurements are directly between the calorimetrically determined values for segments 3 and 4.

Figure B.25 b shows that once again contributions from radiation and convection are on a par with those from the anode fall, all of which accounts for over 40% of the thruster power.

Figure B.26 shows the dependence of the anode fall and anode power fraction components with mixture ratios of argon and hydrogen propellants. Initially, the addition of hydrogen greatly reduces the anode fall of both active segments. Beyond 5% hydrogen propellant fraction however, the introduction of more hydrogen results in increased anode falls of both segments. In addition, the difference between calorimetrically de-

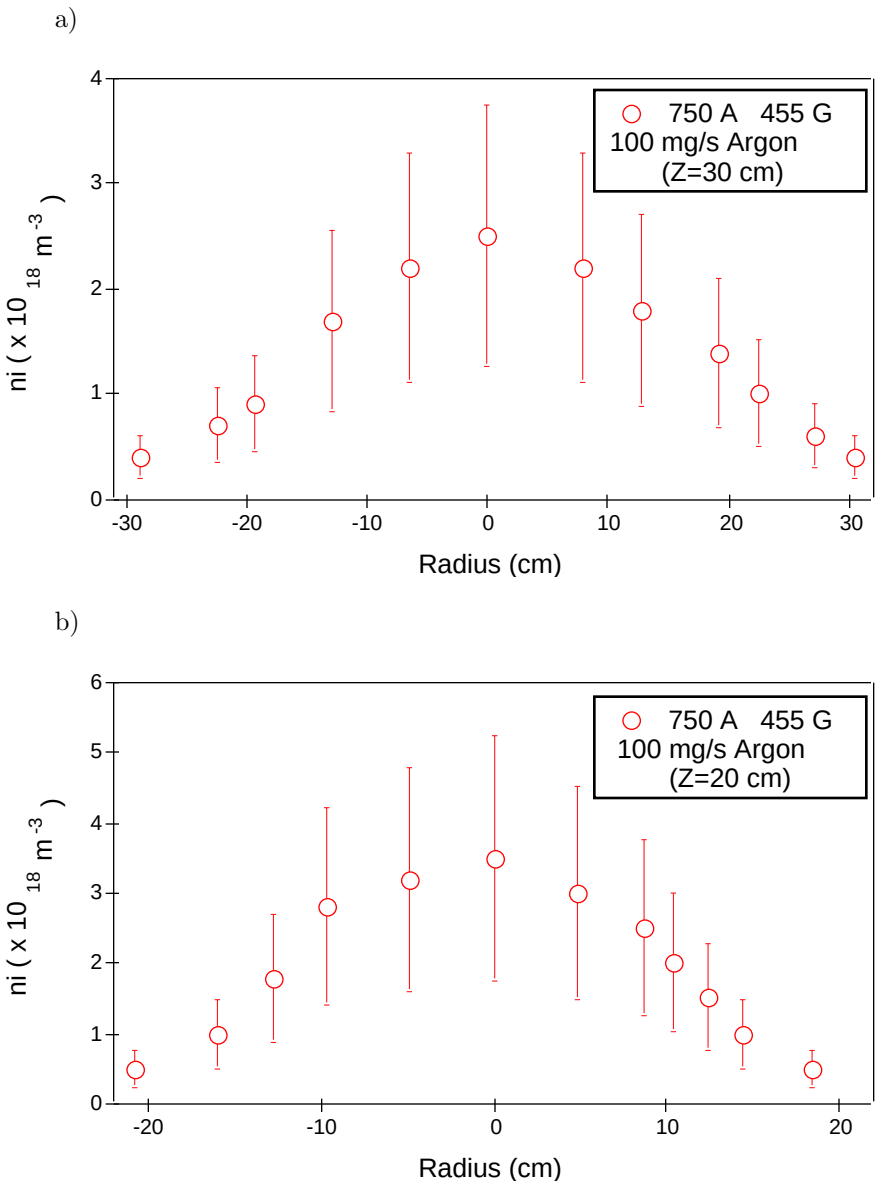

Figure B.22: Ion Number Density Radial Profiles. (750 A 455 G, 100 mg/s argon).

a)

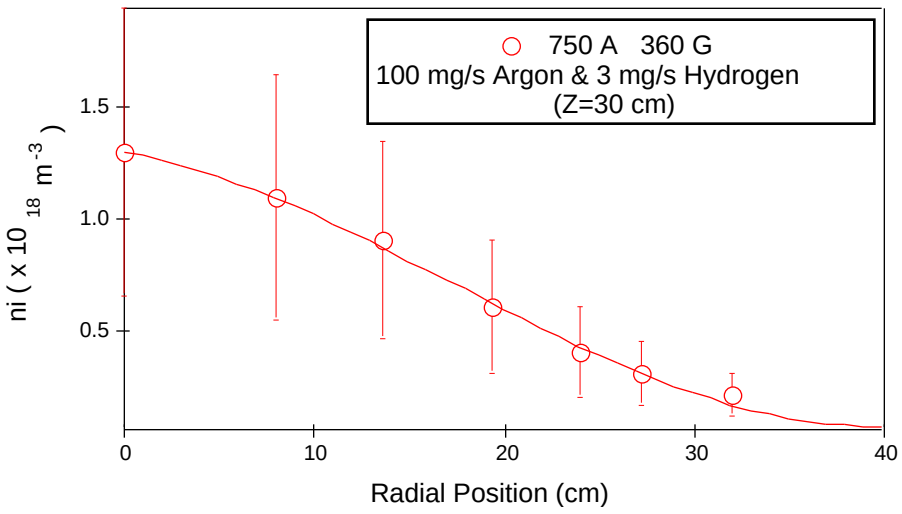

b)

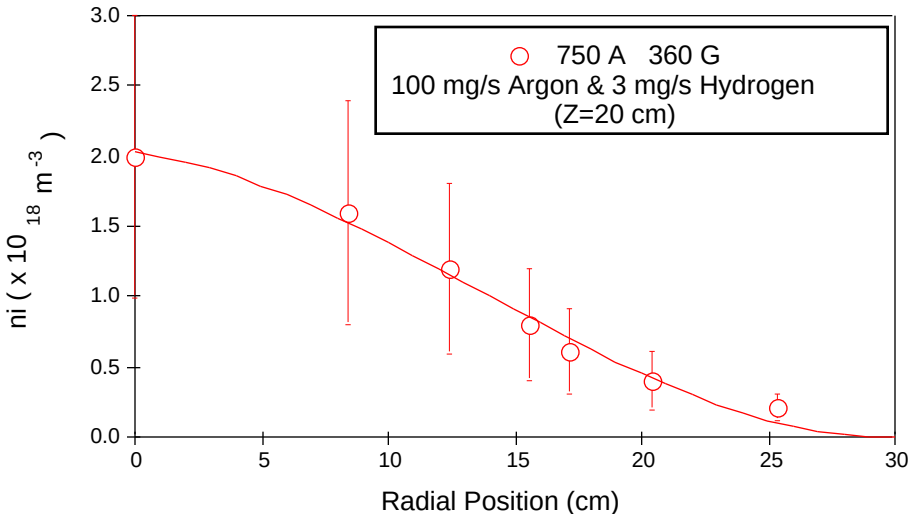

Figure B.23: Ion Number Density Radial Profiles. (750 A 360 G, 100 mg/s argon & 3 mg/s hydrogen).

a)

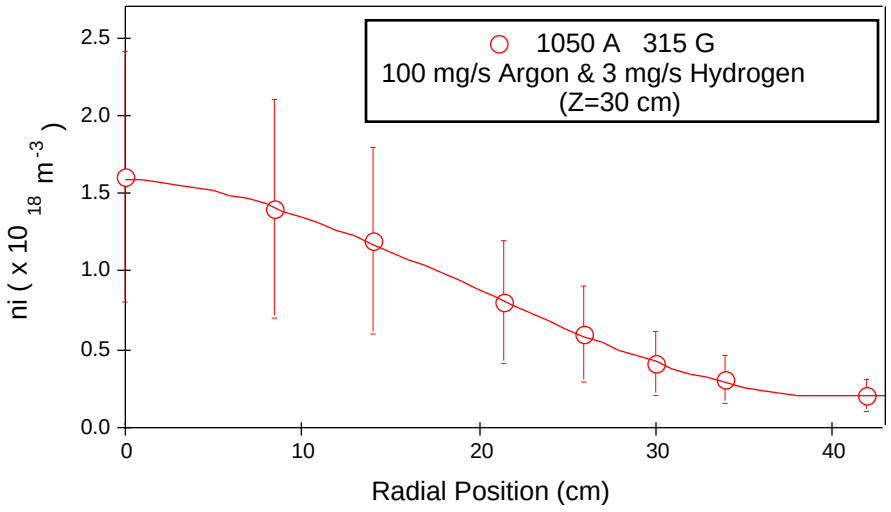

b)

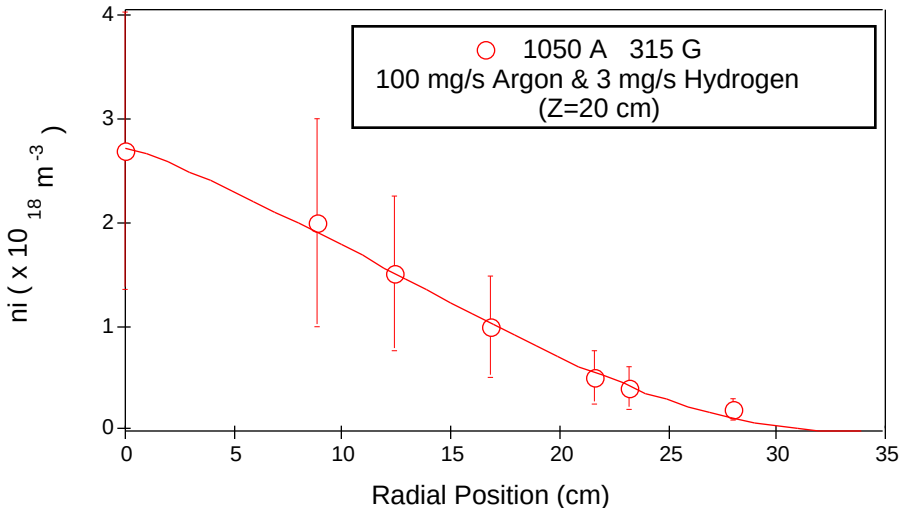

Figure B.24: Ion Number Density Radial Profiles. (1050 A 315 G, 100 mg/s argon & 3 mg/s hydrogen).

termined anode fall estimates and those measured by the floating segment, decreases with increasing hydrogen propellant fraction. Between hydrogen propellant fractions of 5 and 30%, the difference in the anode falls of segments 3 and 4 is less than 5 V. The behavior of the anode fall depicted in Figure B.26 a closely resembles that of the power input to the floating segments (cf. Figure B.18). Furthermore, in Figure B.26 b it is seen that the addition of hydrogen reduces the contribution of the anode fall to anode power deposition, to a level equivalent to that of convection and radiation.

B.8 Conclusions

In this appendix, calorimetric measurements of anode power deposition in a steady 100 kW applied-field thruster with a segmented anode were described. The thruster, which used argon and argon-hydrogen mixtures as propellants with mass flow rates between 50 and 150 mg/s, operated at currents between 750 and 1250 A and applied field strengths up to 800 G (measured at cathode tip). Results of this work show that the anode heat flux increases monotonically with applied field strength and thruster current, with the anode power fraction varying from 71% to 55%. Plume measurements of the electron temperature, extrapolated to the thruster chamber, are used with heat flux measurements to estimate the anode fall. In contrast to the results obtained with the quasi-steady thruster, the anode fall is not necessarily the dominant source of anode heating. Radiation and convection, as determined through heat flux measurements taken with floating anode segments, were found to contribute as much as the anode fall to anode heating for certain operating conditions. Furthermore, the anode fall was found to increase monotonically with increasing field strength. The observations that electron temperatures and number densities, measured in the plume, are insensitive to thruster operating conditions, and that the magnetic field at the anode is determined primarily by the applied magnetic field component, suggest that the Hall parameter is proportional to the applied magnetic field strength. Therefore, the monotonic increase of the anode fall with applied field strength corresponds to the monotonic increase of the anode fall with the electron Hall parameter. Thus, although the two thrusters are very different, an increase of the anode fall with electron Hall parameter appears to have been observed in both 100 kW class applied-field thrusters and in multi-megawatt

pulsed devices.

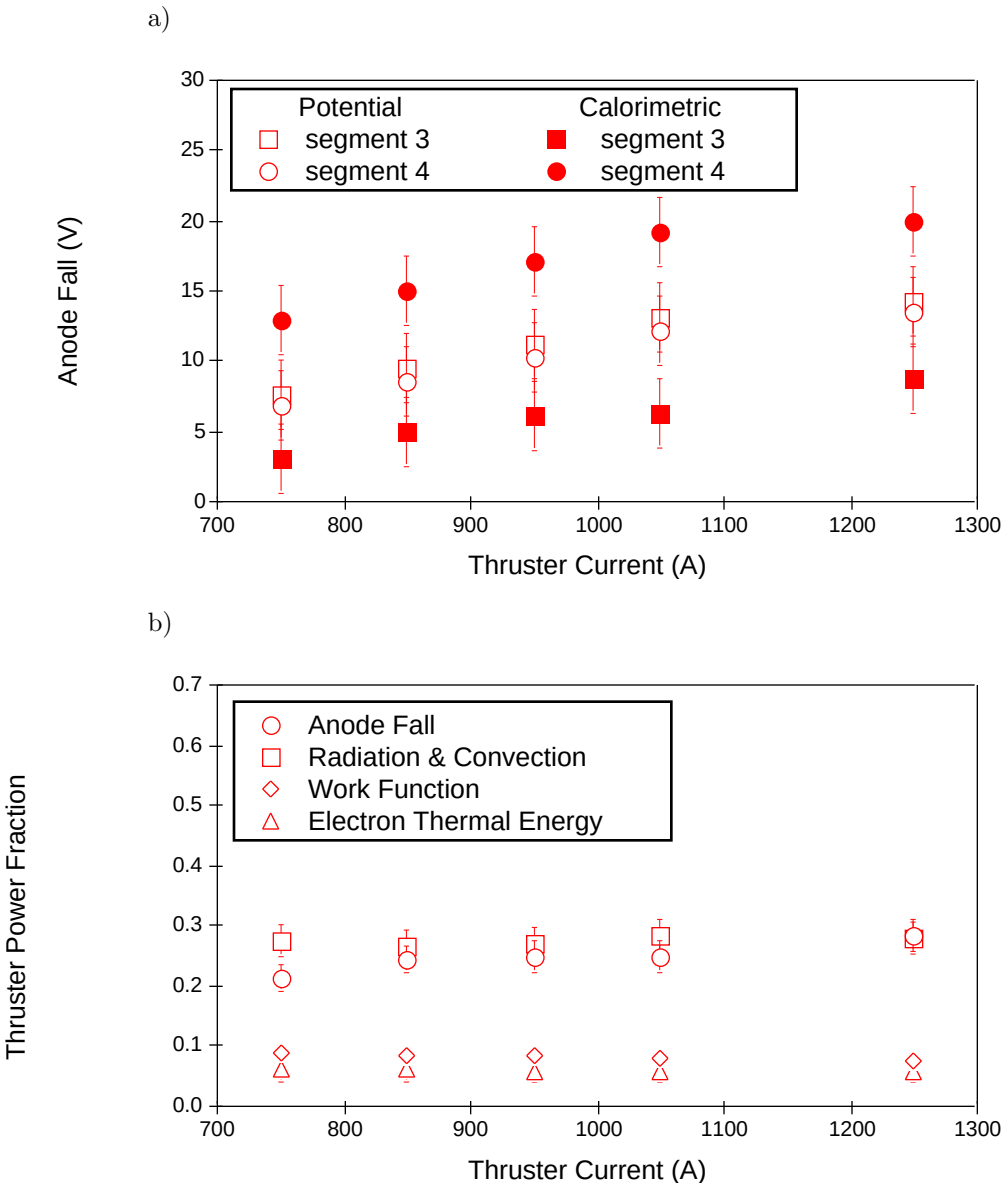

Figure B.25: Anode Fall and Anode Power Fraction Components vs. Thruster Current, (315 G, 100 mg/s argon & 3 mg/s hydrogen).

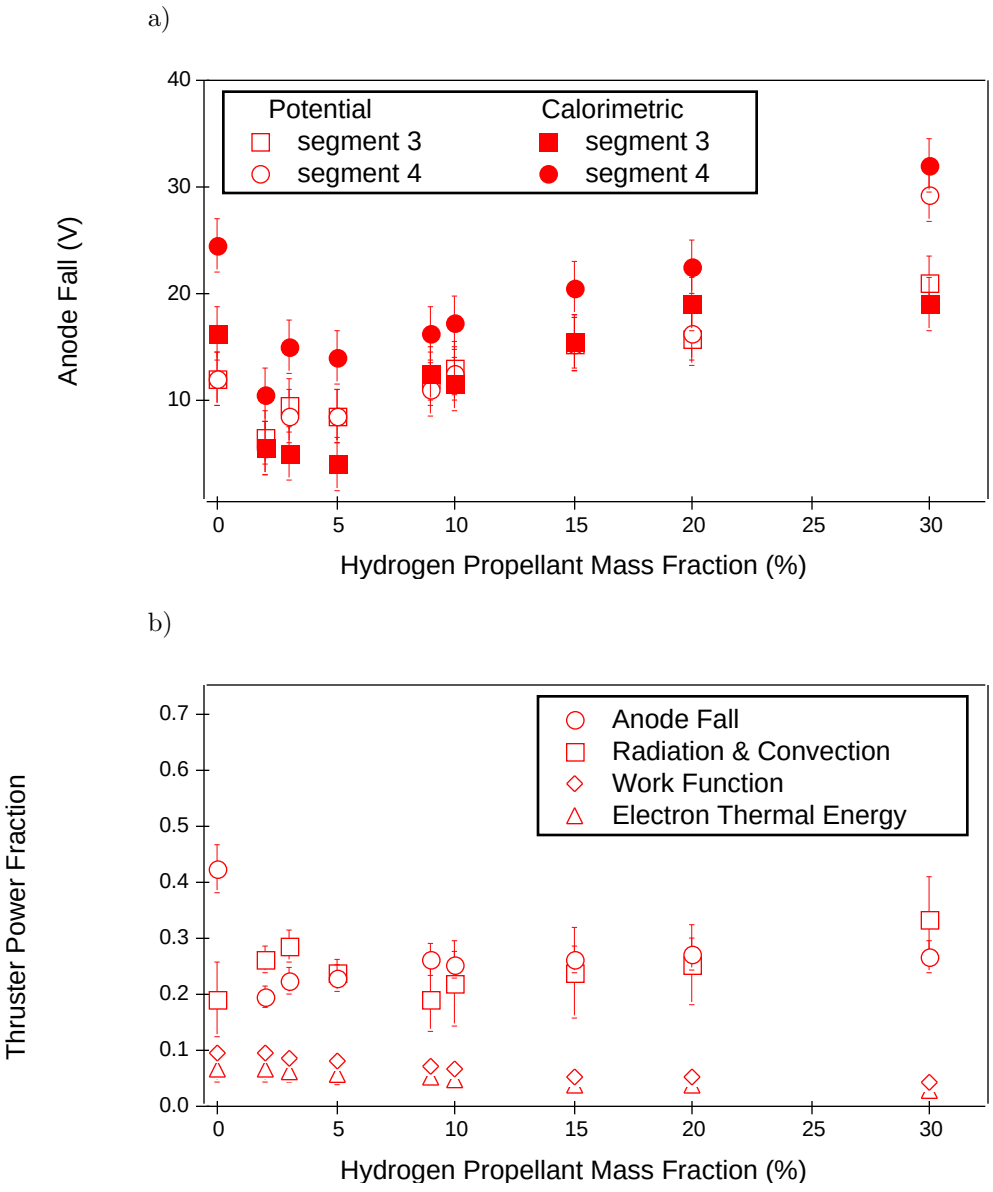

Figure B.26: Anode Fall and Anode Power Fraction Components vs. Hydrogen Propellant Mass Fraction, (850 A, 315 G).

C Heavy Particle Anode Heating

C.1 Introduction

As is shown throughout this thesis, the anode of multi-megawatt quasi-steady MPD thrusters is subjected to heating loads in excess of 5 kW/cm^2. In Chapter 1, contributions to anode heating from radiation ($\dot{q}_r$) and convection from heavy particles[4] ($\dot{q}_c$) were assumed to be negligible. Randolph[27], who has done extensive non-equilibrium modeling of the argon plasma in these devices, concludes that the radiative heat flux to the anode is at most a few watts per square centimeter. Simple calculations from both Saber[17] and Oberth[25] show the heat flux from plasma convection (electrons and heavy particles) to be 84 and 55 W/cm^2, respectively. A sophisticated numerical model which includes non-equilibrium ionization in the electrode-adjacent boundary layer of the straight coaxial thruster developed by King[98] predicts *heavy particle* electrode heat fluxes of approximately 60 W/cm^2. The complexity of this model severely limits its use in calculating heavy particle heating rates for a variety of ambient plasma conditions. The purpose of the model outlined in this appendix is to use a simple analytical means of estimating the heavy particle contribution to anode heating. No attempt is made to include anomalous transport quantities in the analysis.

C.2 Governing Equations

The first task in estimating convective heating rates is to calculate pertinent transport properties (i.e. viscosity and thermal conductivity). From kinetic theory[99, 100], the classical viscosity of a plasma is given by

$$\mu = \mu_H + \mu_e \simeq \mu_i + \mu_n + \mu_e \tag{C.1}$$

where μ is viscosity, μ_H (heavy particle viscosity) is the sum of ion viscosity μ_i and neutral particle viscosity μ_n, and μ_e is the viscosity due to the electrons. Because of its low mass, the electron contribution to viscosity can be neglected. Equation C.1 is now

[4] Since the contribution to anode heating from electrons are included in the anode heat flux expression that includes the current density multiplied by the anode fall, $\frac{5}{2}kT_e$, and ϕ, only heavy particles are considered for the estimate of the convective heat transfer rate to the anode.

rewritten as

$$\mu \simeq \mu_i + \mu_n = m_i \overline{C_i}(N_e \mathcal{L}_{iH} + N_n \mathcal{L}_{nH}) \tag{C.2}$$

where $\overline{C_i}$ is the mean thermal speed of the heavy particles ($T_i \simeq T_n$), $\mathcal{L}_{iH}$ is the mean free path of an ion colliding with another heavy particle (ion or neutral), and $\mathcal{L}_{nH}$ is the mean free path of a neutral encountering another heavy particle. For an ionization fraction of one or less ($n_i = n_e$), the mean free paths are given by the following equations[99, 100]:

$$\mathcal{L}_{iH} = \frac{1}{n_e Q_{ii} + n_n Q_{in}} \tag{C.3}$$

$$\mathcal{L}_{nH} = \frac{1}{n_n Q_{nn} + n_e Q_{in}} \tag{C.4}$$

where Q_{ii} is the Coulomb ion-ion collision cross section given by the following expression,

$$Q_{ii} = \frac{q^4 \ln \Lambda}{16\pi(\varepsilon_o k T_H)^2}, \tag{C.5}$$

Q_{in} is the ion-neutral cross section, and Q_{nn} is the neutral-neutral collision cross section. Combining the equations above and using the definition of the ionization fraction $\alpha = n_e/(n_n + n_e)$, we arrive at the following expression for the heavy particle viscosity,

$$\mu \simeq m_i \overline{C_i}\left(\frac{\alpha}{\alpha Q_{ii} + (1-\alpha) Q_{in}} + \frac{1-\alpha}{(1-\alpha) Q_{nn} + \alpha Q_{in}}\right). \tag{C.6}$$

Table C.1 gives typical cross sections for argon at conditions within the thruster. It is seen from Equation C.6 that when $\alpha \simeq 0$, the viscosity is determined by Q_{nn}. For $\alpha \simeq 1$, viscosity is determined primarily by Q_{ii}. With $\alpha \simeq 0$, $\mu \simeq 1 \times 10^{-3}$ kg-m/s, with $\alpha \simeq 0.5$, $\mu \simeq 1 \times 10^{-4}$ kg-m/s, and with $\alpha \simeq 1$, $\mu \simeq 1 \times 10^{-5}$ kg-m/s. Thus, thick boundary layers are present if the plasma is weakly ionized near the anode. Viscosities calculated with Equation C.6 compare favorably with transport coefficients evaluated by Devoto from Chapman-Enskog-Burnett expressions[102].

Treating the anode lip as a circular cylinder and defining the Reynolds number by

$$Re = \frac{\rho U \mathcal{D}}{\mu} \tag{C.7}$$

where $\rho \simeq (n_i + n_n) \times m_i$ is the mass density of the plasma ($\sim 10^{-5}$ kg/m^3), U is the flow velocity ($\sim$8700 m/s), $\mu \simeq 1 \times 10^{-5}$ kg-m/s (highly ionized free stream plasma), and $\mathcal{D}$ is the lip diameter ($\sim$1 cm), implies that boundary layer that forms at the lip is laminar

	Cross Section	References
Q_{ii}	$\sim 1 \times 10^{-17}$ m^2	[76, 99]
Q_{in}	$\sim 1 \times 10^{-18}$ m^2	[99, 101]
Q_{nn}	$\sim 1 \times 10^{-19}$ m^2	[99, 100]

Table C.1: Argon cross section data (kT_e=2 eV).

(Re$\simeq$85)[103]. To calculate the anode heating rate requires evaluation of the Nusselt number. The following empirical correlation, suitable for laminar boundary layers over circular cylinders with $1 < Re_D < 10^6$ and $0.7 < Pr < 500$, is used in obtaining the Nusselt number[94];

$$\overline{Nu}_D = 0.51 Re^{\frac{1}{2}} Pr^n (\frac{Pr_\infty}{Pr_s})^{\frac{1}{4}} \tag{C.8}$$

where Pr_∞ and Pr_s are the Prandtl numbers in the plasma free stream and at the anode surface, respectively, and n is a value which depends on the Prandtl number. If Pr$\leq$10, n=0.37, if the converse is true, n=0.36. The Prandtl number is defined by the following equation,

$$Pr = \frac{\mu C_p}{\mathcal{K}_H} \tag{C.9}$$

where C_p is the specific heat of the fluid at constant pressure and $\mathcal{K}_H$ is the thermal conductivity of the fluid. Since we are concerned only with the heavy particle heating of the anode, the "fluid" in this analysis will consist of only argon ions and neutrals. Because of the high mobility of electrons, the thermal conductivity of the heavy particle fluid will be significantly less than that of the entire plasma. Thus, values of thermal conductivity obtained from tables are not applicable for this analysis. The expression for $\mathcal{K}_H$ is given by[99],

$$\mathcal{K}_H = \frac{k^2 T_H}{m_i C_i} (\frac{\alpha}{\alpha Q_{ii} + (1-\alpha) Q_{in}} + \frac{1-\alpha}{(1-\alpha) Q_{nn} + \alpha Q_{in}}) \tag{C.10}$$

where k is the Boltzmann constant and T_H is the temperature of the heavy particles.

A rough estimate of C_p for the the heavy particle fluid was made by subtracting the contributions of the electrons,

$$C_{p_e} = \frac{5}{2} \frac{k n_e}{\rho} \tag{C.11}$$

from the equilibrium specific heat values of the entire plasma[104]. For a highly ionized argon plasma where $C_{p\,H} \simeq$1500 J/kg-°K[104], $\mu \simeq 1 \times 10^{-5}$ kg-m/s, and $\mathcal{K}_H \simeq 2.6 \times 10^{-3}$ W/m-°K, the Prandtl number for the heavy particles is approximately six. This value is two orders of magnitude larger than those calculated by Oberth or Saber because the electron contribution to thermal conductivity is not included in the present analysis. Since $Pr_\infty \leq$10 and assuming $\alpha \leq$1 near the anode surface so the $Pr_s \simeq Pr_\infty$, the Nusselt number ($\overline{Nu}_D$) is approximately equal to ten.

The following equation is used to calculate the anode heat transfer rate from the heavy particles[94],

$$\dot{q}_c = \overline{h}(T_\infty - T_s) \tag{C.12}$$

where the convective heat transfer coefficient $\overline{h}$ is given by the following expression,

$$\overline{h} = \frac{\overline{Nu}_D \mathcal{K}_H}{\mathcal{D}}. \tag{C.13}$$

For a fully ionized plasma, $\overline{h} \simeq$3 W/m^2 -°K, and for a weakly ionized plasma, $\overline{h} \simeq$100 W/m^2 -°K. Assuming, for an extreme case, that T_∞ =2 eV and $T_s \simeq$0 eV, convective heating rates to the anode are

$$\dot{q}_c \simeq 200 W/\mathrm{cm}^2$$

for $\alpha = 0$

$$\dot{q}_c \simeq 6 W/\mathrm{cm}^2$$

for $\alpha = 1$.

Using their numerical model, Subramaniam et al.[26] calculated heavy particle heating rates between 40 and 60 W/cm^2 at plasma conditions similar to those assumed in this analysis (i.e. kT_e=2 eV, n_e=1×10^{20} m^{-3}). These authors also find that the plasma remains highly ionized throughout the boundary layer with little variation in electron temperature. However, the temperature of the heavy particles decreases from its free stream value to the local electrode surface temperature. These predictions have been made by other authors as well[65].

In summary the simple analysis presented in this appendix yields heavy particle heating rates that agree with those predicted by more sophisticated models. The convective anode heating rates are predicted to be less than 200 W/cm^2 for a weakly

ionized plasma and approximately 10 W/cm^2 for a highly ionized anode boundary layer. Thus, for most operating conditions in which the boundary layer is expected to be highly ionized, the convective heating rates are at least two orders of magnitude less than the overall value.

D Anode Sheath Modeling

D.1 Introduction

Whether the anode fall is due to a sheath or anomalous resistivity is still a topic of debate. Over the last several decades substantial effort has been spent on modeling the interface of solid bodies with plasmas. Much of this work has focused on the accurate interpretation of voltage-current characteristics of Langmuir probes[52, 56, 105, 106, 107, 108, 109, 110, 111], the understanding of life limiting processes of cathodes for a variety of plasma devices[112, 113, 114, 115, 116, 117] and the walls of tokamacs[118, 119, 120, 121]. Relatively little effort, however, has been spent modeling anode sheath phenomena. The goal of this analysis is to determine if it is possible for a sheath at the anode of a MPD thruster to sustain voltage drops of 40 to 50 volts.

D.2 Governing Equations

The model presented in this appendix follows from those developed by Baksht et al.[113], Prewett et al.[116], and Goodfellow et al.[117]. Although the previous models treated the case of an electron repelling sheath (e.g. cathode or negatively biased Langmuir probe), this analysis is concerned strictly with anode sheaths that repel ions. To simplify the analysis, the presence of a pre-sheath is neglected. Inclusion of the pre-sheath, in general, would add an additional two or three volts to the results presented below. Before describing the governing equations, the assumptions of the model will be reviewed.

D.3 Model Assumptions and Algorithm

The sheath is considered so thin that collisions or magnetic gyro motions can be neglected. This assumption is justified by the fact that the thickness of a sheath is on the order of several debye lengths[52]. For plasmas characteristic of high powered MPD thrusters, the debye length is typically 1 μm while the electron mean free path and gyro radius are on the order of 1 mm. To be consistent with previous assumptions regarding the interpretation of Langmuir probe data, only singly ionized argon ions (ArII) are treated in the analysis. Given the electron temperatures and number densities near the anode, the number of ArIII ions is expected to be negligible in comparison

to the number of ArII ions. The random thermal energy of the electrons and ions are assumed to be much less than the change of potential energy within the sheath. Because of this, the electrons can be assumed to have a mono-energetic distribution while the ions are assumed to be Maxwellian. In the extreme case of zero temperature, the electron energy distribution function resembles a narrow spike shifted by the potential energy gained from the sheath. By assuming that the electron temperature is much less than the sheath voltage drop, we are stating that the spread of energies about the this shift point is not significant and can be modeled as a spike (zero temperature) without much error. In addition, the large ion repelling sheath potential tends to maintain a Maxwellian ion distribution since only a few energetic ions will be able to traverse the sheath barrier[113].

The basic equations governing the sheath include the ion momentum equation[122]

$$\frac{dn_i}{dy}kT_i + n_i qE = 0, \tag{D.1}$$

the continuity and momentum equations for the electrons

$$\frac{d}{dy}(n_e U_e) = 0 \tag{D.2}$$

$$-n_e m_i \frac{dU_e}{dy} = qEn_e, \tag{D.3}$$

and Poisson's equation

$$\frac{d^2\phi}{dy^2} = -\frac{q}{\varepsilon_0}(n_i - n_e). \tag{D.4}$$

E is the local electric field, U_e is the average electron (drift) velocity, and ϕ is the potential. The origin of the "y" axis is on the anode surface.

Combining Equations D.1 through D.4 leads to

$$\frac{d^2\eta}{d\xi^2} = -\frac{1}{1+2\lambda\eta} - e^{-\gamma\eta} \tag{D.5}$$

where the normalized variables

$$\lambda = \frac{kT_e}{m_e {U_e}^2}, \qquad \xi = \frac{y}{\lambda_d},$$

$$\gamma = \frac{T_e}{T_i}, \qquad \text{and} \qquad \eta = \frac{q\phi}{kT_e}$$

have been substituted.

Integration of Equation D.5 yields

$$\frac{d\eta}{d\xi} = -(\frac{2}{\lambda}[\sqrt{1+2\lambda\eta} - \sqrt{1+2\lambda\eta_{sh}}] + \frac{2}{\gamma}[e^{-\gamma\eta} - e^{-\gamma\eta_{sh}}] + (\frac{d\eta}{d\xi})^2_{sh})^{\frac{1}{2}} \tag{D.6}$$

where terms with "*sh*" subscripts are evaluated at the sheath edge. To evaluate quantities at this location Equation D.5, which can be written as

$$\frac{d^2\eta}{d\xi^2} = \mathcal{G}(\eta) \tag{D.7}$$

where $\mathcal{G}(\eta)$ represents the terms on the right hand side (RHS) of Equation D.5, is Taylor expanded about $\eta = 0$ resulting in the following:

$$\frac{d^2\eta}{d\xi^2} = \mathcal{G}_o + \frac{d\mathcal{G}}{d\eta}\eta + \frac{1}{2}\frac{d^2\mathcal{G}}{d\eta^2}\eta^2 + \ldots. \tag{D.8}$$

Since the potential is referenced to the voltage of the quasi-neutral plasma beyond the sheath, η near the sheath edge is assumed small. Therefore, near the sheath edge Equation D.8 reduces to

$$\frac{d^2\eta_{sh}}{d\xi^2} \simeq \frac{d\mathcal{G}}{d\eta}\eta_{sh} = (\gamma - \lambda)\eta_{sh}. \tag{D.9}$$

The constant $\mathcal{G}_o$ drops out because of the requirement that as y$\rightarrow\infty$ where $n_e \simeq n_i$, the RHS of Equation D.5 must approach zero. The solution of Equation D.9 is written as

$$\eta_{sh} = C_1 e^{+\sqrt{\gamma-\lambda}\xi} + C_2 e^{-\sqrt{\gamma-\lambda}\xi}, \tag{D.10}$$

where C_1 and C_2 are constants of integration. Consideration of the boundary requirement that η approaches zero as y$\rightarrow\infty$, shows that $C_1 = 0$. Therefore, the sheath edge conditions for Equation D.6 are as follows,

$$\eta_{sh} = Ce^{-\sqrt{\gamma-\lambda}\xi} \tag{D.11}$$

and

$$(\frac{d\eta}{d\xi})_{sh} = -\sqrt{\gamma-\lambda}Ce^{-\sqrt{\gamma-\lambda}\xi}. \tag{D.12}$$

The integration constant "C" is selected so that the magnitude of the sheath-edge electric field $(\frac{dV}{dy})_{sh}$ is of the same order as those calculated at pre-sheath boundaries in other studies[117].

Another boundary condition of interest in any sheath analysis is the Bohm velocity criterion[76]. For conditions of interest in the present analysis, this criterion may be written as

$$U_e > \sqrt{\frac{kT_i}{m_e}} \tag{D.13}$$

which is satisfied when $\lambda < 1/\gamma$. To obtain the variation of potential, electric field and particle densities throughout the sheath, Equation D.6 is numerically integrated. Once the potential distribution is determined, the electric field is calculated through Equation D.6. The charged number densities are calculated through the following equations: (mono-energetic electrons)

$$n_e = \frac{n_o}{\sqrt{1 + 2q\phi/kT_e}} \tag{D.14}$$

(Maxwellian ions)

$$n_i = n_o e^{-q\phi\gamma/kT_e} \tag{D.15}$$

where the number densities of the electrons and ions are assumed to be equal ($\simeq n_o$) at the sheath edge. In light of the large calculated electric fields at the sheath/pre-sheath interface, the equality of the two number densities is approximate at best.

The analysis described above has been implemented in a computer code written in BASIC. Experimental data for electron temperature and number density as functions of thruster current and propellant mass flow rate are used as boundary conditions at the entrance of the sheath. A sheath thickness of ten to fifteen Debye lengths (calculated from experimental data) is selected at the start of the computation. These heights are consistent with sheath thicknesses measured in glow discharges with electrostatic waves[123]. The code marches through the sheath from the cathode end towards the anode, numerically integrating the equations above. At each step, the voltage, electric field, and number densities are calculated. Marching continues until the prescribed thickness is reached. In addition to sheath thickness, the ion temperature (or specifically T_e/T_i) must be assumed as well. The code was tested by calculating sheath voltages of floating bodies. By setting the net current density at the surface equal to zero, the code successfully calculated sheath potentials, as a function of electron temperature, which correspond to those of floating bodies in argon and helium plasmas.

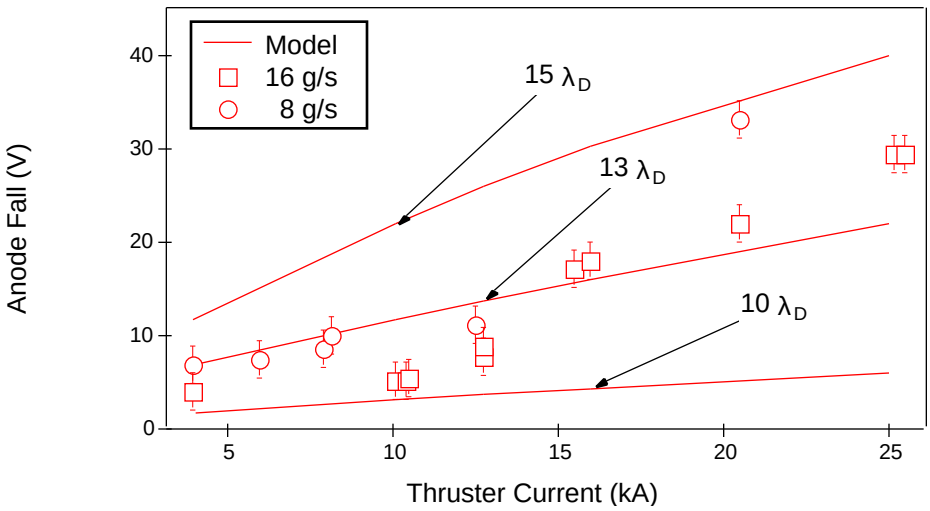

Figure D.1: Anode Fall vs. Current (T_e=T_i).

D.4 Results

Figure D.1 shows a comparison of measured anode falls and calculated anode sheath voltage drops as a function of thruster current at argon propellant mass flow rates of 8 and 16 g/s. Measured fall values are taken as anode fall measurements made 1 mm from the anode surface with floating Langmuir probes. As the figure shows, reasonable agreement exists between calculated sheath voltages and measured anode falls. Below 15 kA, calculations with sheath thicknesses of 10 and 13 Debye lengths corroborate experimental data. Above this current, however, agreement between experiment and the model requires calculations with sheath thicknesses of 13 or 15 Debye lengths.

Figure D.2 shows the dependence of the sheath voltage on temperature ratio. Since the ions are assumed to be Maxwellian, their temperature determines the number of ions that can penetrate the repelling sheath. When T_e/T_i is one or more, the ion temperature is not large enough to travel far into the sheath. As a result, for most of the sheath the electron number density is much larger than the ion number density. This condition leads to the establishment of large electric fields. In the case where the ion

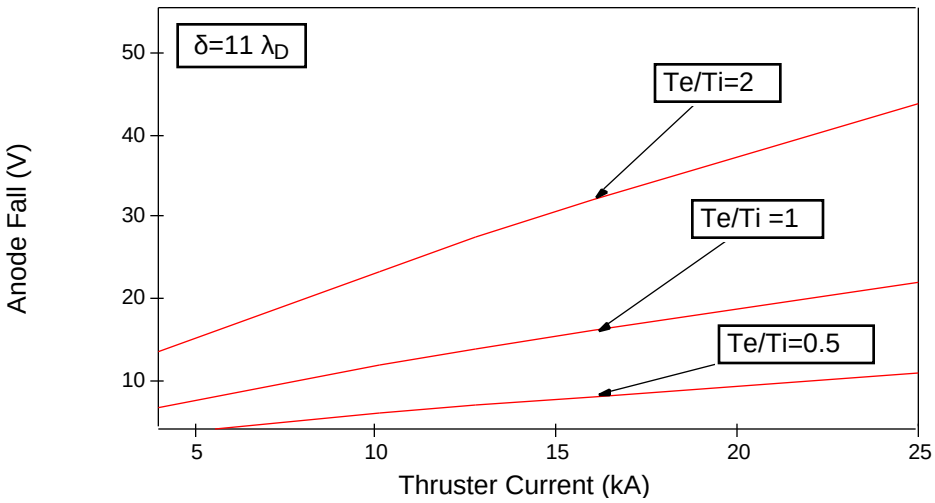

Figure D.2: Anode Fall vs. Current ($\delta = 11\lambda_D$).

temperature is higher then the electron temperature, the ions now have sufficient energy to accompany electrons through much of the sheath. The large disparity between the electron and ion number densities now exists over a much narrower region near the anode surface, resulting in lower overall sheath voltages. In cases where the ion temperature is much larger than the electron temperature, the sheath is unable to repel a sufficient number of ions to maintain a Maxwellian ion distribution at the sheath entrance, and the assumptions of the model are violated.

Anode fall as a function of distance within the sheath is shown in Figures D.3 and D.4 for argon flow rates of 8 g/s at thruster currents of 6 and 20 kA, respectively. The sheath thickness of either plot is selected so that calculated sheath voltages match measured anode falls. The fact that both sheaths are approximately 10 microns thick is due to the different electron temperatures and number densities at either operating condition. For either condition, the rise in potential is shallow through the first half of the sheath. Beyond this point, the voltage abruptly rises, increasing monotonically toward the anode. These calculations indicate that a thin electrostatic sheath at the

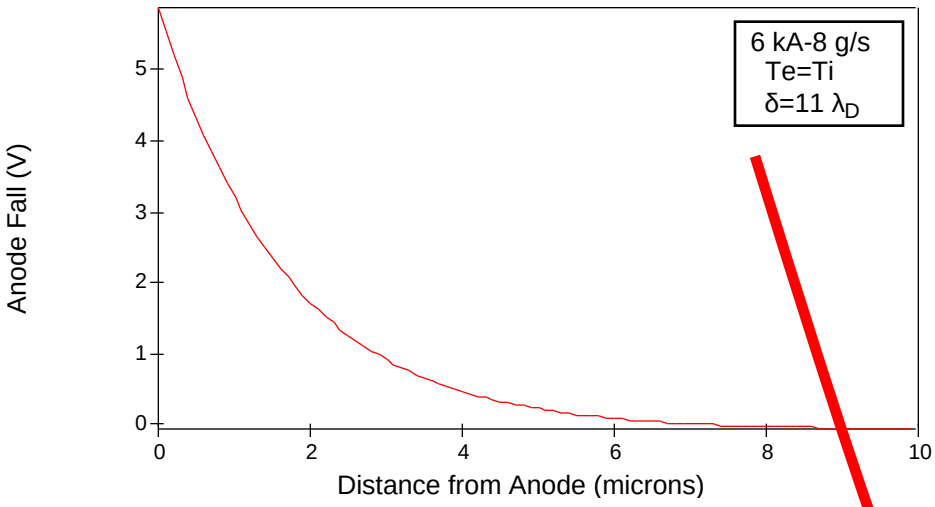

Figure D.3: Anode Fall vs. Distance from Anode Surface (6 kA-8 g/s).

anode is capable of producing voltage drops in excess of 40 V.

Figures D.5 and D.6 show electric field profiles throughout the sheath at the operating conditions of the last figures. The electric field at the sheath entrance of either condition is approximately 1×10^4 V/m. This field strength is within an order of magnitude of those measured several millimeters from the anode and are consistent with electric fields calculated within the pre-sheath by other researchers[117]. The peak electric field within the sheath is in excess of 10^7 V/m.

Figures D.7 and D.8 show normalized electron number density profiles near the anode surface within the sheath. As the figures illustrate, the electron number density decreases monotonically toward the anode surface. As the electrons are accelerated toward the anode by the electric fields, their number density decreases to maintain a constant electron flux. Therefore, the variation of electron number density is the inverse of the potential distribution. At the anode surface, the electron number density is approximately an order of magnitude less then that at the sheath entrance.

Ion number density profiles are shown in Figures D.9 and D.10. Because of the large

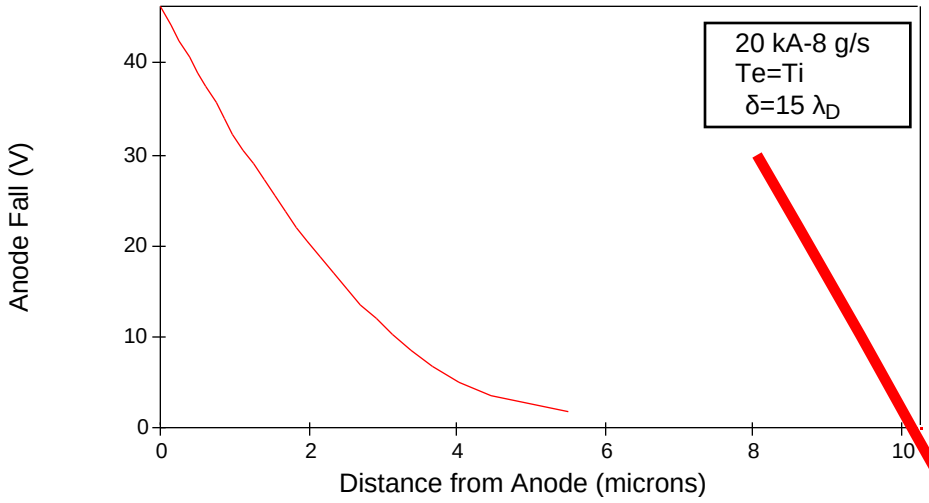

Figure D.4: Anode Fall vs. Distance from Anode Surface (20 kA-8 g/s).

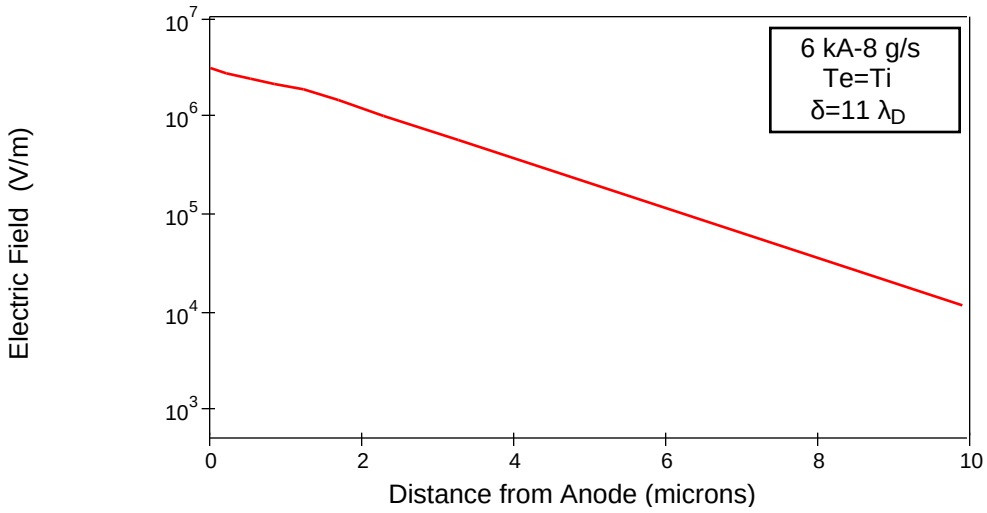

Figure D.5: Electric Field vs. Distance from Anode Surface (6 kA-8 g/s).

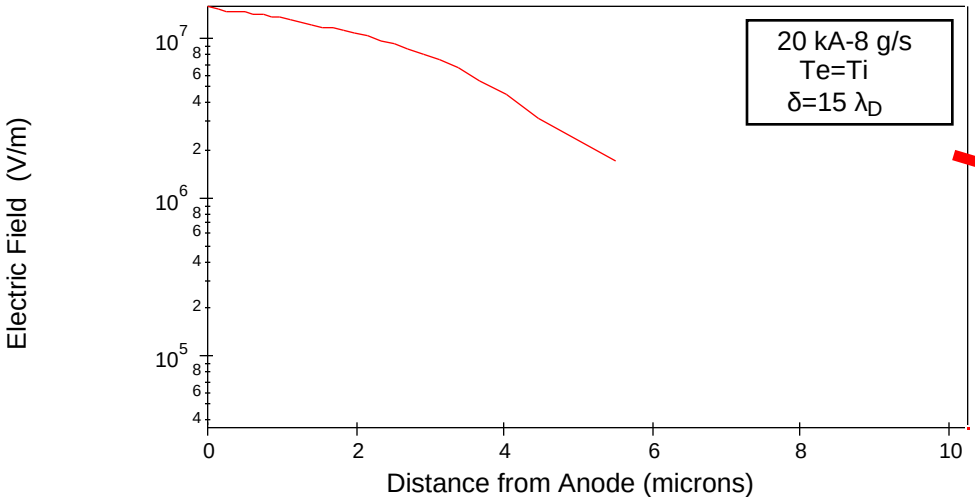

Figure D.6: Electric Field vs. Distance from Anode Surface (20 kA-8 g/s).

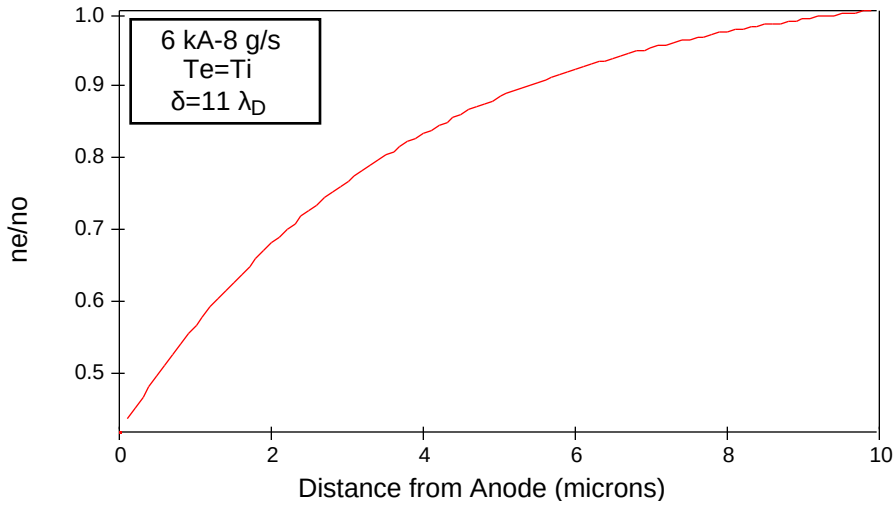

Figure D.7: Electron Number Density Profile (6 kA-8 g/s).

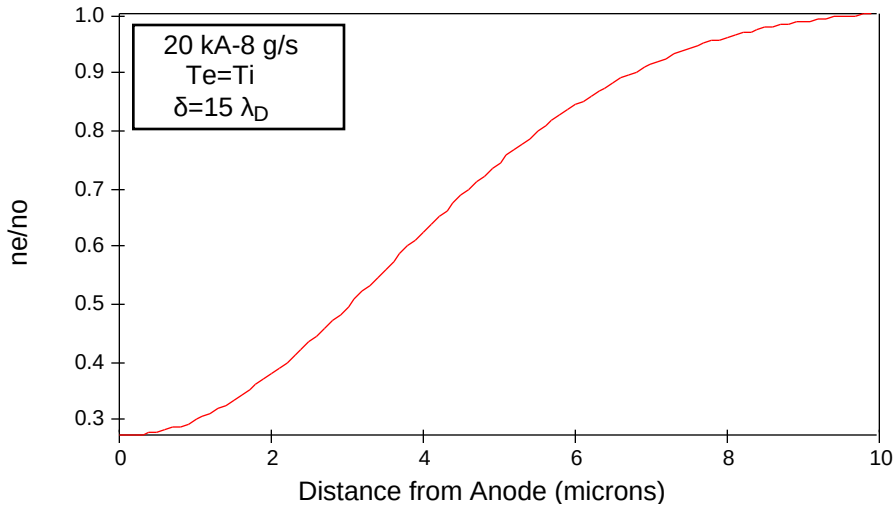

Figure D.8: Electron Number Density Profile (20 kA-8 g/s).

ion repelling electric fields, the ion number density decreases by more than three orders of magnitude within the anode sheath. At one micron from the anode surface, the ion number density is between 10 and 10^5 times smaller than the electron number density. This large difference in number density is the mechanism from which large electric fields are generated within the sheath.

In summary, a simple 1-D sheath model is outlined in this appendix to illustrate that the large voltage drops measured at the anode could be realistically produced by a sheath. Whether the anode fall is due to the sheath or to anomalous effects is still unknown. The results of this appendix and those of Appendix A imply that both phenomena may contribute to anode power deposition. More refined sheath models which take into account magnetic field effects which are certain to affect sheath boundary conditions, and detailed potential measurements taken less than one millimeter from the anode will be necessary to answer this question.

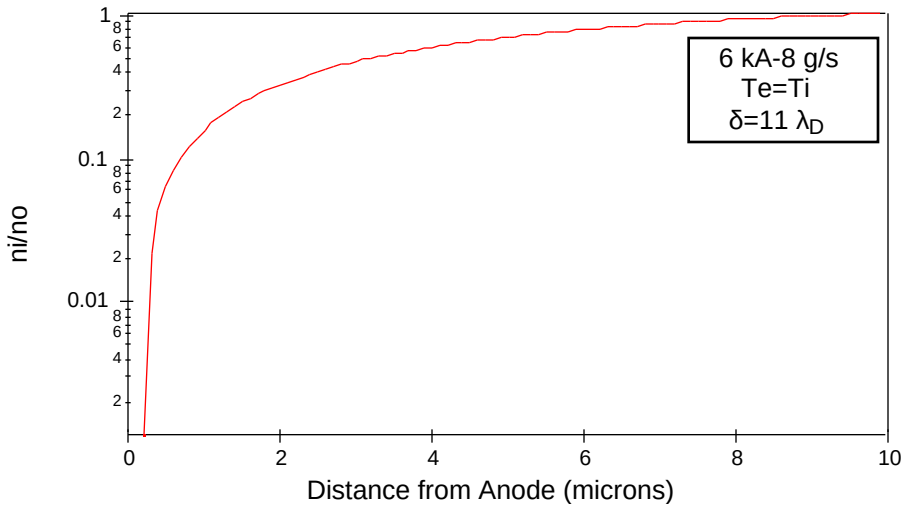

Figure D.9: Ion Number Density Profile (6 kA-8 g/s).

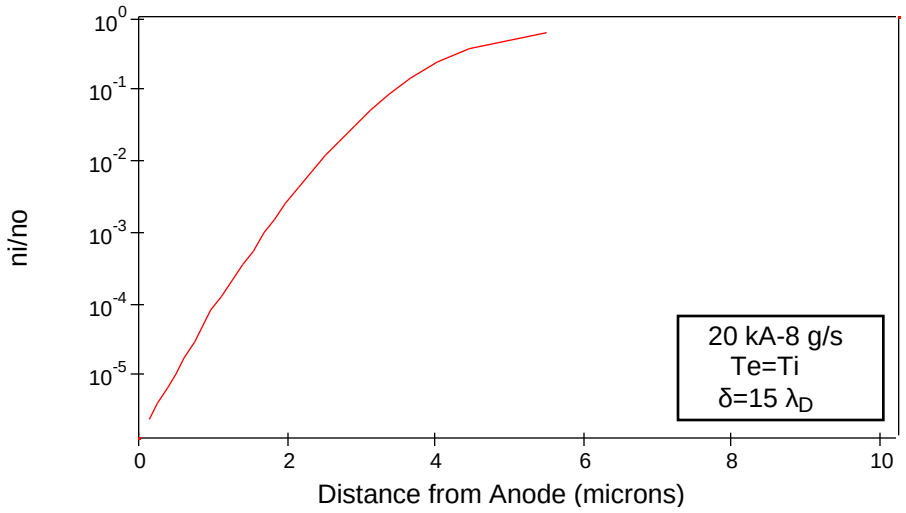

Figure D.10: Ion Number Density Profile (20 kA-8 g/s).

Bibliography

[1] Palaszewski, B.,"Electric Propulsion Parameters for Manned Mars Exploration,"1989 JANNAF Propulsion Meeting,Chemical Propulsion Information Agency, Laurel, Maryland, May 23–25, 1989.

[2] Garrison, P.W., Frisbee, R.H., Pompa, M.F.,"Ultra High Performance Propulsion for Planetary Spacecraft," FY'81 Final Report (unpublished), Jet Propulsion Laboratory JPL D-2123.

[3] Babb, G.R. and Stump, W.R.,"Comparison of Mission Design Options for Manned Mars Missions," *Manned Mars Missions,Working Group Papers*, edited by M.B. Duke and P.W. Keaton, NASA TM-89320, 1986, Vol. 1, Sec. 1-4, pp. 37-52.

[4] Garrison, P.W., and Stocky, J.F.,"Future Spacecraft Propulsion," J.Propulsion, Vol. 4, No. 6 Nov–Dec, 1988, pp 520-525.

[5] Buden, D.,"Nuclear Thermal Rocket Propulsion," AIAA-90-2755, 26^{th} *Joint Propulsion Conference*, Orlando, Florida, July 16–18, 1990.

[6] Jahn, R.G., Physics of Electric Propulsion, McGraw Hill Book Company, NY, 1968.

[7] Pivirotto, T., King, D., Deninger, W., and Brophy, J., "The Design and Operating Characteristics of a 30 kW Thermal Arcjet Engine for Space Propulsion," AIAA-86-1508, 22^{nd} *Joint Propulsion Conference*, Huntsville, Alabama, June 16–18,1986.

[8] Carney, L.M., and Sankovic, J.M., "The Effects of Arcjet Thruster Operating Conditions and Constrictor Geometry on the Plasma Plume," AIAA-89-2723, (NASA TM-102285), presented at the 25^{th} *Joint Propulsion Conference*, Monterey, California, July 10–12, 1989.

[9] Curran F.M., Bullock, S.R., Haag T.W., Sarmiento, C.J., and Sankovic J.M., "Medium Power Hydrogen Arcjet Performance," AIAA-91-2343, 27^{th} *Joint Propulsion Conference*, Sacramento, California, June 24–27, 1991.

[10] Patterson, M.J., "Performance Characteristics of Ring-Cusp Thrusters with Xenon Propellant," AIAA-86-90, 22^{nd} *Joint Propulsion Conference*, Huntsville, Alabama, July 16–18, 1986.

[11] Aston, G., Brophy, J., Garner, C., and Pless, L., "A Xenon Ion Propulsion Module for Enhanced Spacecraft Capability," AIAA-86-1393 22^{nd} *Joint Propulsion Conference*, Huntsville, Alabama, July 16–18, 1986.

[12] Hack, K.J., George, J.A., Riehl, J.P., and Gilland, J.H., "Evolutionary Use of Nuclear Electric Propulsion," AIAA-90-3821 *AIAA Space Programs and Technologies Conference*, Huntsville, Alabama, September 25–28, 1990.

[13] Hickman, J.M., Curtis, H.B., Kenny, B.H., and Sefcik, R.J., "Systems Analysis of Mars Solar Eletric Propulsion Vehicle," AIAA-90-3824 *AIAA Space Programs and Technologies Conference*, Huntsville, Alabama, September 25–28, 1990.

[14] Nakanishi, S., and Pawlik, E."Experimental Investigation of a 1.5 m diam. Kaufman Thruster," J.Spacecraft, Vol. 5, No. 7, July 1968, pp 801-807.

[15] King, D.Q., and Sercel, J.C.,"A Review of the Multi-Megawatt MPD Thruster and Current Mission Applications," AIAA-86-1437 22^{nd} *Joint Propulsion Conference*, Huntsville, Alabama, July 16–18, 1986.

[16] Sovey, J.S., and Mantenieks, M.M.,"Performance and Lifetime Assesment of Magnetoplasmadynamic Arc Thruster Technology," J.Propulsion, Vol. 7, No. 1 Jan–Feb, 1991, pp 71-83.

[17] Saber, A.J.,"Anode Power in a Quasi-Steady MPD Thruster," Dept. of Aerospace & Mechanical Sciences, Princeton University, 1974.

[18] Saber, A.J. et al. ,"Pulsed Electromagnetic Gas Acceleration," NASA NGLL 31-001-005 progress report (1 July–31 Dec. 1971), Dept. of Aerospace & Mechanical Sciences Semi-Annual Report 634r Princeton University, 1972.

[19] Gallimore, A.D., Kelly, A.J., and Jahn, R.G., "Anode Power Deposition in Quasi-Steady MPD Thrusters," AIAA-90-2668, 21^{st} *International Electric Propulsion Conference*, Orlando, Florida, July 18–20, 1990.

[20] Shih, K.T., Pfender, E., Ibele, W.E.,and Eckert, E.R.G.,"Experimental Anode Heat-Transfer Studies in a Coaxial Arc Configuration," AIAA Journal , Vol. 6, No. 8, Aug., 1968, pp. 1482-1487.

[21] Shih, K.T.,"Anode Current and Heat Flux Distributions in an MPD Engine," AIAA-69-244, *AIAA* 7^{th} *Electric Propulsion Conference*, Williamsburg, Virginia, March 3–5, 1969.

[22] Bose, T.K., and Pfender, E.,"Direct and Indirect Measurements of the Anode Fall in a Coaxial Arc Configuration," AIAA Journal, Vol. 7,No. 8, Aug., 1969, pp. 1643-1645.

[23] Shih, K.T., Pfender, E.,"Electrode Energy Transfer Mechanisms in a MPD Arc," AIAA Journal , Vol. 8, No. 2, Feb., 1970, pp. 211-215.

[24] Eckert, E.R.G., and Pfender, E., Advances in Heat Transfer, Vol. 2, Ed. Harnet, J.P., and Irvine, Jr. ,T.F., Academic Press, NY, 1967, pp. 229-316.

[25] Oberth, R.C.,"Anode Phenomenon in High-Current Discharges," Ph.D. Thesis, Dept. of Aerospace & Mechanical Sciences, Princeton University, 1970.

[26] Subramaniam, V.V, and Lawless, J.L., "Electrode-Adjacent Boundary Layer Flow in Magnetoplasmadynamic Thrusters", Carnegie-Mellon University Draft Report, 1987.

[27] Randolph, T.M., Personal Communication.

[28] Vainberg, L.I., Lyubimov, G.A., and Smolin, G.G., "High-Current Discharge Effects and Anode Damage in an End-Fire Plasma Accelerator," Sov. Phys. Tech. Phys., Vol. 23, No. 4, April, 1978, pp. 439-443.

[29] Dyuzhev, G.A., Shkol'nik, S.M., and Yur'ev, V.G., "Anode Phenomena in the High-Current Arc I," Sov. Phys. Tech. Phys., Vol. 23, No. 6, July, 1978, pp. 667-671.

[30] Dyuzhev, G.A., Shkol'nik, S.M., and Yur'ev, V.G., "Anode Phenomena in the High-Current Arc II," Sov. Phys. Tech. Phys., Vol. 23, No. 6, July, 1978, pp. 672-677.

[31] Merinov, N.S., Ostretsov, I.N., Petrosov, V.A., and Porotnikov, A.A.,"Anode Processes with a Negative Potential Drop at the Anode," Sov. Phys. Tech. Phys. , Vol. 21, No. 4, April, 1983, pp. 467-472.

[32] Hügel,H.,"Effect of Self-Magnetic Forces on the Anode Mechanism of a High Current Discharge,"IEEE Transactions on Plasma Science, Vol. PS-8, No. 4, Dec., 1980, pp. 437-442.

[33] Baksht, F.G., Moizhes, B.Ya., and Rybakov, A.B.,"Critical Regime of a Plasma Accelerator," Sov. Phys. Tech. Phys., Vol. 18, No. 12, June., 1974, pp. 1613-1616.

[34] Shubin, A.P., "Dynamic Nature of Critical Regimes in Steady-State High Current Plasma Accelerators," Sov. J. Plasma. Phys., Vol. 2, No. 1, Jan–Feb, 1976, pp. 18-21.

[35] Karkosak, J.J., and Hoffman, M.A., "Electrode Drops and Current Distribution in an MGD Channel," AIAA Journal , Vol. 3, No. 6, June, 1965, pp. 1198-1200.

[36] Kisov, A.Ya., Morozov, A.I., and Tilinin, G.N.,"Distribution of Potential in a Quasistationary Coaxial Plasma Injector," Sov. Phys. Tech. Phys., Vol. 13, No. 6, Dec., 1968, pp. 467-472.

[37] Gallimore A.D., Myers, R.M, Kelly A.J., and Jahn R.G., "Anode Power Deposition in an Applied-Field Segmented Anode MPD Thruster," AIAA-91-2343, 27^{th} *Joint Propulsion Conference*, Sacramento, California, June 24–27, 1991.

[38] Aref'ev, V.I., "Current-Driven Instabilities in a Strongly Inhomogeneous Plasma. I," Sov. Phys. Tech. Phys., Vol. 17, No. 7, Jan., 1973, pp. 1095-1102.

[39] Aref'ev, V.I., "Current-Driven Instabilities in a Strongly Inhomogeneous Plasma. II," Sov. Phys. Tech. Phys., Vol. 17, No. 7, Jan., 1973, pp. 1103-1107.

[40] Aref'ev, V.I.,"Plasma Acceleration in Crossed Electric and Magnetic Fields," Sov. Phys. Tech. Phys., Vol. 19, No. 4, Oct., 1974, pp. 446-454.

[41] Aref'ev, V.I. and Kirdyashev, K.P., "Excitation of High-Frequency Waves in a Plasma with an Accelerating Hall Sheath," Sov. Phys. Tech. Phys., Vol. 20, No. 3, 1975, pp. 330-334.

[42] Niewood, E.H., and Martinez-Sanchez, M., "The Hall Effect in a Numerical Model of MPD Thrusters," AIAA-91-099, 22^{nd} *International Electric Propulsion Conference*, Viareggio, Italy, October 14–17, 1991.

[43] Choueiri, E.Y.,"Electron-Ion Streaming Instabilities of an Electromagnetically Accelerated Plasma,"Ph.D. Thesis, Dept. of Mechanical & Aerospace Engineering, Princeton University, 1991.

[44] Caldo, G., Choueiri, E.Y., Kelly A.J., and Jahn R.G., "An MPD Code with Anomalous Transport," AIAA-91-102, 22^{nd} *International Electric Propulsion Conference*, Viareggio, Italy, October 14–17, 1991.

[45] Barnett, J.W.,"Operation of the MPD Thruster with Stepped Current Input,"Ph.D. Thesis, Dept. of Mechanical & Aerospace Engineering, Princeton University, 1985.

[46] Hoskins, W.A.,"Asymmetric Discharge Patterns in the MPD Thruster,"M.S. Thesis, Dept. of Mechanical & Aerospace Engineering, Princeton University, 1990.

[47] Clark, K.E.,"Quasi-Steady Plasma Acceleration,"Ph.D. Thesis, Dept. of Aerospace & Mechanical Sciences, Princeton University, 1969.

[48] Carslaw, H.S., and Jaeger, J.C., Conduction of Heat in Solids, 2^{nd} ed. , Clarendon Press, Oxford, 1959.

[49] Gilland, J., Air Force Report #74 (November 11 1985) Dept. of Mechanical & Aerospace Engineering, Princeton University, 1985.

[50] Lovberg, R.H., "Magnetic Probes," In *Plasma Diagnostic Techniques*, edited by Huddlestone, R.H. and Leornard, S.L., Academic Press, New York, 1965.

[51] Schott, L.,"Electric Probes", in Plasma Diagnostics, edited by Lichte-Holtgreven,W., John Wiley & Sons, Inc., NY, 1968, pp. 705.

[52] Chen, F.F., "Electric Probes," In *Plasma Diagnostic Techniques*, edited by Huddlestone, R.H. and Leornard, S.L., Academic Press, New York, 1965.

[53] Cambell, E.M., Semi-annual Report 634 z (1 July–31 December 1975) Dept. of Aerospace & Mechanical Sciences, Princeton University, 1976.

[54] Chen, S.L., and Sekiguche, T., "Instantaneous Direct-Display System of Plasma Parameters by Means of Triple Probe," Journal of Applied Physics Vol. 36, No. 8, Aug., 1965, pp. 2363-2375.

[55] Chung, P.M., Talbot, L., and Touryan, K.L., "Electric Probes in Stationary and Flowing Plasmas: Part 1 Collisionless and Transitional Probes",AIAA Journal Vol. 12, No. 2, Feb., 1974, pp.133-144.

[56] Laframboise, J., "Theory of Cylindrical and Spherical Probes in a Collisionles Plasma at Rest," ITIAS Report # 100, 1966. See also Rarefied Gas Dynamics, Vol. 2, edited by J.H. deLeeuw, Academic Press, NY, 1966.

[57] Peterson, E.W., and Talbot, L., "Collisionless Electrostatic Single-Probe Parameters by Means of Triple Probe," AIAA Journal, Vol. 8, No. 12, 1970.

[58] Tilley, D., "The Application of the Triple Probe Method to MPD Thruster Plumes,"AIAA-90-2667, 21^{st} *International Electric Propulsion Conference*, Orlando, Florida, July 18–20, 1990.

[59] Tilley,D., Report 1776.23 (January–February 1990 Report) Dept. of Mechanical & Aerospace Engineering, Princeton University, 1990.

[60] Boyle, M.J., Semi-annual Report 634 r (1 July–31 December 1971) Dept. of Aerospace & Mechanical Sciences, Princeton University, 1972.

[61] Gallimore A.D.,Report 1776.14 (January-February 1989) Dept. of Mechanical & Aerospace Engineering, Princeton University, 1989.

[62] Gallimore A.D.,Report 1776.11 (January-February 1988) Dept. of Mechanical & Aerospace Engineering, Princeton University, 1988.

[63] Bez, W., and Höcker, K.H., "Theorie Des Anodenfall I,"Zeitschrift Fur Naturforschung, Vol. 9a, 1954, pp. 72-81.

[64] Höcker, K.H., and Bez, W., "Theorie Des Anodenfall II,"Zeitschrift Fur Naturforschung, Vol. 10a, 1955, pp. 706-714.

[65] Dinulescu, H.A., and Pfender, E., "Analysis of the Anode Boundary Layer of High Intensity Arcs," Journal of Applied Physics Vol. 51, No. 6, June, 1980, pp. 3149-3157.

[66] Choueiri, E.Y.,Report 1776.14 (March 1987) Dept. of Mechanical & Aerospace Engineering, Princeton University, 1987.

[67] Alfvén, H., "Collision between a Nonionized Gas and a Magnetized Plasma,"Reviews of Modern Physics, Vol. 32, No. 4, Oct., 1960, pp. 710-713.

[68] Choueiri, E.Y., Kelly A.J., and Jahn R.G., "Manifestation of The Alfvén's Hypothesis of Critical Ionization Mechanism in the Performance of MPD Thrusters," AIAA-85-2037, 18^{th} *International Electric Propulsion Conference*, Alexandria, Va, 1985.

[69] Morozov, A.I., and Solov'ev L.S., "Plane Flows of Ideally Conducting Compressible Fluids with Hall Effect Considered," Sov. Phys. Tech. Phys., Vol. 9, No. 7, Jan., 1965, pp. 889-897.

[70] Auweter-Kurtz, M., Kurtz, H.L., Merke, W.D., Scharde, H.O., and Christian Sleziona, P.,"Self Field MPD Thruster Investigation,"FY'88 Final Report (unpublished), Institute für Raumfahrtsysteme, Universität Stuttgart, IRS-88-P-10.

[71] Auweter-Kurtz, M., Kurtz, H.L., Merke, W.D., Scharde, H.O., Christian Sleziona, P., and Wegmann, T.,"High Power Steady State MPD Thruster,"FY'89 Final Report (unpublished), Institute für Raumfahrtsysteme, Universität Stuttgart, IRS-90-P4.

[72] Kuriki, K. and Iida, H., "Spectrum Analysis of Instabilities in MPD Thruster," IEPC 84-28, 17^{th} *International Electric Propulsion Conference*, Japan Society for Aeronautical and Space Sciences, Tokyo, 1984.

[73] Tilley, D.L.,"An Investigation of Microinstabilities in a kW Level Self-Field MPD Thruster,"M.S. Thesis, Dept. of Mechanical & Aerospace Engineering, Princeton University, 1991.

[74] Diamant, K.D., Personal Communication.

[75] Lovberg, R.H., "Plasma Problems in Electric Propulsion," In *Methods of Experimental Physics, Plasma Physics*, edited by Lovberg, R.H. and Griem, H.R., Academic Press, New York, 1971, Volume 9, Part B.

[76] Chen, F.F., Introduction to Plasma Physics and Controlled Fusion, Volume 1: Plasma Physics, 2^{nd} ed. , Plenum Press, New York, 1984.

[77] Krall, N.A. and Trivelpiece, A.W., Principles of Plasma Physics, San Francisco Press, San Francisco, 1986.

[78] Spitzer, JR., L., Physics of Fully Ionized Gases, John Wiley & Sons, Inc., NY, 1962.

[79] Kerrebrock, J.L.,"Electrode Boundary Layers in Direct-Current Plasma Accelerators," Journal of Aerospace Sciences, Aug., 1961, pp. 631-643.

[80] High, M.D., and Felderman, E.J.,"Turbulent MHD Boundary Layers with Electron Thermal Non-equilibrium and Finite Rate Ionization," AIAA Journal , Vol. 10, No. 1, Jan., 1972, pp. 98-103.

[81] Karkosak, J.J., and Hoffman, M.A.,"Electrode Drops and Current Distribution in an MGD Channel," AIAA Journal , Vol. 3, No. 6, June, 1965, pp. 1198-1200.

[82] Kent James, R., and Kruger, C.H.,"Joule Heating Effects in MHD Generators Boundary Layers," AIAA Journal , Vol. 21, No. 5, May, 1983, pp. 679-686.

[83] Sanders, N.A., and Pfender, E.,"Measurements of Anode Falls and Anode Heat Transfer in Atmospheric Pressure High Intensity Arcs," J.Appl.Phys. , Vol. 55, No. 3, Feb., 1984, pp. 714-722.

[84] Kurtz, H.L., Auweter-Kurtz, M., Merke , W.D., and Scharde, H.O.,"Experimetal MPD Thruster Investigations," AIAA-87-1019,19^{th} *International Electric Propulsion Conference*, Colorado Springs, Colorado, May 11–13, 1987.

[85] Myers, R.M., Mantenieks, M.A., and Sovey, J.S., "Geometric Effects in Applied-Field MPD Thrusters," AIAA-90-2669, 21^{st} *International Electric Propulsion Conference*, Orlando, Florida, July 18–20, 1990.

[86] Sovey, J.S., Mantenieks, M.A., Haag T.W., Raitano, P., and Parkes, J.E.,,"Test Facility and Preliminary Performance of a 100 kW Class MPD Thruster,"1989 JANNAF Propulsion Meeting, Cleveland, Ohio, May 23–25, 1989.

[87] Haag, T.W.,"Design of a Thrust Stand for High Power Electric Propulsion Devices," AIAA-89-2829, (NASA TM-102372), presented at the 25^{th} *Joint Propulsion Conference*, Monterey, California, July 10–12, 1989.

[88] Myers, R.M., Wherle, D., Vernyl, M., Biaglow, J., and Reese, S., "A Preliminary Characterization of Applied-Field MPD Thruster Plumes," AIAA-91-2339, 27^{th} *Joint Propulsion Conference*, Sacramento, California, June 24–26, 1991.

[89] Fradkin, D.B.,"Analysis of Acceleration Mechanisms and performance of an Applied Field MPD Arcjet," Dept. of Aerospace & Mechanical Sciences, Princeton University, 1973.

[90] Schall, W., "Influence on Magnetic Fields on Anode Losses in MPD-Arcs,"AIAA-72-502, 9^{th} *International Electric Propulsion Conference*, Bethesda, Maryland, April 17–19, 1972.

[91] Wolf, M.J., Kelly, A.J., and Jahn, R.G., "A High Performance Magnetoplasmadynamic Thruster," IEPC 84-32, 17^{th} *International Electric Propulsion Conference*, Japan Society for Aeronautical and Space Sciences, Tokyo, 1984, pp. 206-212.

[92] Heimerdinger, J.D.,"Fluid Mechanics in a Magnetoplasmadynamic Thruster," Ph.D. Thesis, Dept. of Aeronautics & Astronautics, Massachusetts Institute of Technology, 1988.

[93] Baksht, F.G., Moizhes, B.Ya., and Rybakov, A.B.,"Critical Mode in a Coaxial Plasma Accelerator with External Magnetic Field," Sov. Phys. Tech. Phys., Vol. 21, No. 2, Feb., 1976, pp. 150-152.

[94] Incropera, F.P., and DeWitt,D.P.,Fundamentals of Heat Transfer, John Wiley & Sons, NY,1981.

[95] Patrick, R.M., and Schneiderman, A.M., "Performance Characteristics of a Magnetic Annular Arc," AIAA Journal, Vol. 4, No. 2, Feb., 1966, pp. 282-287.

[96] Myers, R.M., "Plume Characteristics of MPD Thrusters: A Preliminary Examination," AIAA-89-2832, (NASA CR-185130), presented at the 25^{th} *Joint Propulsion Conference*, Monterey, California, July 10–12, 1989.

[97] Tahara, H., Kagaya, Y., and Yoshikawa, T., "Hybrid MPD Thruster with Axial and Cusp Magnetic Fields," IEPC 88-058, *20th International Electric Propulsion Conference*, Garmisch-Partenkirchen, Germany, Oct. 3–6, 1988, pp. 333-341.

[98] King, D.Q.,"Magnetoplasmadynamic Channel Flow for Design of Coaxial MPD Thrusters,"Ph.D. Thesis, Dept. of Mechanical & Aerospace Engineering, Princeton University, 1981.

[99] Mitchner, M., and Kruger, Jr., C.H., "Partially Ionized Gases," John Wiley & Sons Inc., London, 1973.

[100] Vincenti, W.G., and Kruger, Jr., C.H., "Introduction to Physical Gas Dynamics," Robert E. Kreiger Publishing Company, Malabar, 1986.

[101] Massey, H.W.S., Burhop, E.H.S., and Gilbody, H.B., "Electronic and Ionic Impact Phenomena," Volume I:*Electrons with Atoms*, Oxford University Press, London, 1969.

[102] Devoto, R.S., "Transport Coefficients of Partially Ionized Argon,"Physics of Fluids, Vol. 10, No. 2, Feb., 1967, pp. 354-365.

[103] Schlicting, H., Boundary-Layer Theory, Seventh Edition, McGraw-Hill Book Company, New York, 1979.

[104] Brahinsky, H.S. and Neel, C.A.,"Tables of Equilibrium Thermodynamic Properties of Argon," Vol. I-IV, Arnold Engineering Development Center, AEDC-TR-69-19, March, 1969.

[105] Tonks, L. and Langmuir, I., "A General Theory of the Plasma of an Arc," Physical Review, Vol. 34, Sep., 1929, pp. 876-922.

[106] Allen, J.E., Boyd, R.L.F., and Reynolds, P., "The Collection of Positive Ions by a Probe Immersed in a Plasma," Proc. Phys. Soc. (London), B70 1957, pp. 297-304.

[107] Lam, S.H.,"A General Theory for the Flow of Weakly Ionized Gases," AIAA Journal, Vol. 2, No. 2, Feb., 1964, pp. 256-262.

[108] Lam, S.H.,"A Unified Theory for the Langmuir Probe in a Collisionless Plasma," The Physics of Fluids, Vol. 8, No. 1, Jan., 1965, pp. 73-87.

[109] Bienkowski, G.K.,"Electrostatic Sheath in a Weakly Ionized Plasma," The Physics of Fluids, Vol. 10, No. 2, Feb. , 1967, pp. 381-391.

[110] Cohen, I.M.,"Asymptotic Theory of Spherical Electrostatic Probes in a Slightly Ionized, Collision-Dominated Gas," The Physics of Fluids, Vol. 6, No. 10, Oct. , 1963, pp. 1492-1500.

[111] Goddard, R. and Laframboise, J.G.,"Total Current to Cylindrical Collectors in a Collisionles Plasma Flow," Planet Space Science, Vol. 31, No. 1, Jan. , 1983, pp. 275-283.

[112] Hu, P.N. and Ziering, S.,"Collisionless Theory of a Plasma Sheath near an Electrode," The Physics of Fluids, Vol. 9, No. 11, Nov. , 1966, pp. 2168-2179.

[113] Baksht, F.G., and Moizhes, B.Ya.,"Theory of the Sheath in a Low-Temperature Plasma," Sov. Phys. Tech. Phys. , Vol. 13, No. 4, April, 1968, pp. 540-549.

[114] Sander, K.F., "Theory of a Thick Dynamic Positive-Ion Sheath,"Journal of Plasma Physics, Vol. 3, part 3 1969, pp. 353-370.

[115] Hassan, H.A., and Thompson, C.C.,"Quasi-Ambipolar Diffusion in Arc Discharges in a Magnetic Field," Plasma Physics , Vol. 12, pp. 727-736.

[116] Prewett, P.D. and Allen, J.E.,"The Double Sheath Associated with a Hot Cathode," Proc. R. Soc. London, A. 348 1976, pp. 435-446.

[117] Goodfellow, K.D. and Murthy, S.N.B.,"Electrode Processes and MPD Thruster Operation," AIAA-88-3207, 24^{th} *Joint Propulsion Conference*, Boston, Massachusetts, July 11–13, 1988.

[118] Emmert, G.A., Wieland, R.M., Mense, A.T., and Davidson, J.N., "Electric Sheath and Presheath in a Collisionles, Finite Ion Temperature Plasma," The Physics of Fluids, Vol. 23, No. 4, April, 1980, pp. 803-812.

[119] Stangeby, P.C., "Plasma Sheath Transmission Factors for Tokamac Edge Plasmas," The Physics of Fluids, Vol. 27, No. 3, March, 1984, pp. 682-690.

[120] Kushner,M.J.,"Floating Sheath Potentials in Non-Maxwellian Plasmas," IEEE Transactions on Plasma Science, Vol. PS-13, No. 1, Feb., 1985, pp. 6-9.

[121] Chodura, R.,"Numerical Analysis of Plasma-Wall Interactions for an Oblique Magnetic Field," Journal of Nuclear Materials, Vol. 111-112, November–December, 1982, pp. 420-423.

[122] Montgomery, R.M., and Holms, R.A.,"Some Experiments in Radio-Frequency Diagnostics of Partially-Ionized Plasmas," In *Physico-Chemical Diagnostics of Plasmas: Proceedings of the Fifth Biennial Gas Dynamics Symposium*, edited by Anderson, T.P., Springer, and Warden Jr. , R.C., Northwestern University Press, Evanston, 1963.

[123] Jones, W.D., Doucet, H.J., and Buzzi, J.M., Linear Theories and Methods of Electrostatic Waves in Plasmas, Plenum Press, New York, 1985.